Fall 2018

Phenolic resin aerogels: The significance of inserting an oxidative ring-fusion aromatization step at the early stages of pyrolytic carbonization, and the application of these materials in CO_2 storage and separation

Hojat Majedi Far

Department: Chemistry

PHENOLIC RESIN AEROGELS: THE SIGNIFICANCE OF INSERTING AN OXIDATIVE RING-FUSION AROMATIZATION STEP AT THE EARLY STAGES OF PYROLYTIC CARBONIZATION, AND THE APPLICATION OF THESE MATERIALS IN CO_2 STORAGE AND SEPARATION

by

HOJAT MAJEDI FAR

A DISSERTATION

Presented to the Faculty of the Graduate School of the

MISSOURI UNIVERSITY OF SCIENCE AND TECHNOLOGY

In Partial Fulfillment of the Requirements for the Degree

DOCTOR OF PHILOSOPHY

in

CHEMISTRY

2018

Approved by:

Dr. Chariklia Sotiriou-Leventis, Advisor
Dr. Nicholas Leventis
Dr. Jeffrey G. Winiarz
Dr. Amitava Choudhury
Dr. F. Scott Miller

TO

MY PARENTS

PUBLICATION DISSERTATION OPTION

This dissertation consists of the following two articles that have been published for publication:

Paper I, pages 32–116, has been published in *RSC Advances*.

Paper II, pages 117–195, has been published in *Macromolecular Chemistry and Physics*.

ABSTRACT

Phenolic aerogels, prepared via polycondensation of phenolic monomers and formaldehyde, were converted to carbon aerogels at 800 °C/Ar followed by reactive etching under flowing CO_2. Previously, it was found that a lower-temperature air-oxidation of polybenzoxazine aerogels was necessary in order to obtain highly porous, isomorphic carbon aerogels with high carbonization yields. Using those findings as the point of departure, phenolic aerogels were oxidized at 240 °C/air prior to carbonization. During that air-oxidation step, phenolic aerogels based on phloroglucinol (1,3,5-trihydroxybenzene) undergo fusion of their aromatic rings, yielding 6-membered heteroaromatic pyryliums with pendant phenoxide ions. The resulting carbon aerogels have higher surface areas than other carbon aerogels not subjected to aromatization. Subsequently, carbon aerogels were studied for their CO_2 adsorption capacity at 273 K up to 1 bar, relevant to post-combustion separation of CO_2 from N_2. Carbon aerogels from phenolic resins were compared to carbon aerogels from Ishida's polybenzoxazine, and from a random copolymer of polyamide, polyurea, and polyimide. The results show that phenolic resin-derived carbons (containing phenoxide) adsorb more CO_2 than the latter, which contain N in addition to oxygen. Interestingly, resorcinol-formaldehyde-derived carbon aerogels uptook 14.8 ± 3.9 mmol g^{-1} CO_2, which is much higher than the values reported in the literature for other microporous materials. Opening of closed micropores and enlargement of micropore size, resulted in a multilayer coverage of micropore walls with CO_2. The high capacity for CO_2 was attributed to an energy-neutral reaction between surface phenoxides and CO_2.

ACKNOWLEDGEMENTS

I ought to profoundly thank my advisors, Dr. Chariklia Sotiriou-Leventis and Dr. Nicholas Leventis, who are wonderful sources of ideas and insights. One especially nice aspect of them is their ease of availability and engagement in research with students. Their caring regard for students makes them more than just advisors. I cannot thank them enough for all of their time and energy.

I would also like to thank Dr. Jeffrey G. Winiarz, Dr. Amitava Choudhury, and Dr. F. Scott Miller for serving as my committee members and their valuable suggestions.

I would like to thank Mr. Shannon D. Roark and Ms. Tina M. Balch, our secretaries, and Mr. Jonathon Sidwell, senior research specialist, for all their help and nice behavior. I especially thank Mr. Joseph A. Counsil, Research Engineer. Not only did he train me on the instruments, but he was also an amazing person to discuss various problems with related to instrumentation. I also thank Dr. Nathan Leigh and Mr. Dave Satterfield for their efforts in fixing some of the instruments.

I wish my father was alive to see this moment in my life, but I thank him for teaching me things that have helped me cope with problems in my life. My mother has been a great source of support and patience throughout my life. The rest of my family, my brothers and sisters, have also been very supporting and encouraging.

I would also like to thank all my colleagues: Dr. Abhishek Bang, Dr. Adnan Malik Saeed, Dr. Suraj Donthula, Parwani M. Rewatkar, Tahereh Taghvaee, Chandana Mandal, Rushi Soni, Shaheen ud Doulah, and Vaibhav Edlabadkar for their valuable discussions, assistance in the lab, and friendship.

TABLE OF CONTENTS

Page

PUBLICATION DISSERTATION OPTION iv

ABSTRACT v

ACKNOWLEDGEMENTS vi

LIST OF ILLUSTRATIONS xii

LIST OF SCHEMES xiv

LIST OF TABLES xv

LIST OF ABBREVIATIONS xvi

SECTION

1. INTRODUCTION 1

1.1. AEROGELS 1

1.2. ORGANIC AEROGELS 3

1.2.1. Other Types of Organic Aerogels. 8

1.2.2. Synthesis of Terephthalaldehyde-Phloroglucinol (TPOL) Aerogels. 9

1.3. POLYMERIC CARBON AEROGELS 10

1.3.1. Background. 12

1.3.2. The Importance of Ring Fusion Aromatization Step in the Carbonization of PAN Fibers and PBO Aerogels and Extension to Other Phenolic Resin Aerogels 14

1.3.3. Activation of Carbons. 25

1.4. CARBON AEROGELS IN CO_2 SEQUESTRATION AND GAS PURIFICATION 27

1.4.1. Background. 28

1.4.2. Solid CO_2 Sorbents..... 29

PAPER

I. AIR-OXIDATION OF PHENOLIC RESIN AEROGELS: BACKBONE REORGANIZATION, FORMATION OF RING-FUSED PYRYLIUM CATIONS, AND THE EFFECT ON MICROPOROUS CARBONS WITH ENHANCED SURFACE AREAS 32

ABSTRACT 32

1. INTRODUCTION 34

2. RESULTS AND DISCUSSION 37

2.1. MATERIAL SYNTHESIS. 37

2.2. PYROLYSIS PRODUCTS AT 240 ^{O}C/AIR VERSUS 240 ^{O}C/Ar 41

2.3. THE MECHANISM OF RING-FUSION AROMATIZATION 46

2.4. CHEMICAL TRANSFORMATIONS ALONG FURTHER PYROLYSIS OF RES-240(AIR) VERSUS RES 48

2.5. THE EVOLUTION OF MATERIAL PROPERTIES ALONG PYROLYTIC CARBONIZATION AND REACTIVE ETCHING 53

2.6. THE PYROLYTIC EVOLUTION OF THE NANOSTRUCTURE AND THE POROUS NETWORK..... 57

3. CONCLUSION..... 62

4. EXPERIMENTAL..... 63

4.1. MATERIALS 63

4.2. PREPARATION OF PHENOLIC RESIN AEROGELS (RES) 64

4.3. AIR OXIDATION OF RES AND PREPARATION OF RES-240(AIR) .65

4.4. CONVERSION OF AS-PREPARED RES AEROGELS, OR AIR-OXIDIZED RES-240(AIR) AEROGELS INTO CARBON AEROGELS C-RES-D-Θ AND C-RES-O-Θ 65

4.5. REACTIVE ETCHING OF C-RES-D-Θ AND C-RES-O-Θ CARBON AEROGELS INTO EC-RES-D-Θ AND EC-RES-O-Θ 65

4.6. METHODS 66

4.6.1. Physical Characterization 66

4.6.2. Chemical Characterization 66

4.6.3. Thermal Analysis 68

4.6.4. Structural Characterization 68

4.6.5. Pore Structure Analysis 68

ACKNOWLEDGEMENTS 80

SUPPORTING INFORMATION 81

REFERENCES 113

II. EXCEPTIONALLY HIGH CO_2 ADSORPTION AT 273 K BY MICROPOROUS CARBONS FROM PHENOLIC AEROGELS: THE ROLE OF HETEROATOMS IN COMPARISON WITH CARBONS FROM POLYBENZOXAZINE AND OTHER ORGANIC AEROGELS 117

ABSTRACT 117

1. INTRODUCTION 119

2. RESULTS AND DISCUSSION 123

2.1. CARBON AEROGEL SYNTHESIS AND CHARACTERIZATION 123

2.2. CO_2 UPTAKE BY THE CARBON AND ETCHED CARBON AEROGELS. 137

2.3. CO_2 UPTAKE CAPACITY AND THE MECHANISM OF ADSORPTION. 140

2.4. SELECTIVITY TOWARDS ADSORPTION OF CO_2 RELATIVE TO OTHER GASSES. 144

3. CONCLUSIONS 146

4. EXPERIMENTAL 147

4.1. MATERIALS 147

4.1.1. Gasses 147

4.1.2. Aerogel Synthesis 147

4.1.3. Carbonization 148

4.1.4. Reactive Etching with CO_2 148

4.2. METHODS 148

4.2.1. Drying Procedure 148

4.2.2. Oxidative Curing and Pyrolysis 149

4.2.3. CHN Elemental Analysis 149

4.2.4. XPS Analysis 149

4.2.5. Physical Characterization 150

4.2.6. Porosimetry and Gas Sorption Studies 150

4.2.7. Calculation of Isosteric Heats of CO_2 Adsorption (Q_{st}) 151

4.2.8. Calculation of Adsorption Selectivities 153

ACKNOWLEDGEMENTS 164

SUPPORTING INFORMATION 165

REFERENCES 188

SECTION

2. CONCLUSIONS 196

APPENDICES

A. PHENOLIC RESINS 199

B. C 1s XPS DATA 204

C. THE ANALYSIS OF VIRIAL FITTINGS APPLIED TO THE CO_2 ADSORPTION ISOTHERMS 212

BIBLIOGRAPHY 227

VITA 239

LIST OF ILLUSTRATIONS

Figure Page

SECTION

1.1. The schematic preparation of aerogels by sol-gel processing and some controllable polymerization parameters. 2

1.2. SEM images of silica (ρ_b = 0.200 g cm^{-3}) and RF (ρ_b = 0.160 g cm^{-3}) aerogels as shown 8

1.3. Preparation of carbon aerogels from organic aerogels and their main potential applications, which are derived from their outstanding properties as indicated. 12

1.4. Photographs and the corresponding SEMs of PBO aerogels, before and after aromatization at 200 °C/air and after carbonization at 800 °C/Ar. 19

1.5. Solid state ^{15}NMR spectra of PBO aerogels (with 5% w/w monomer concentration) obtained from heat-induced and acid-catalyzed pathways before and after aromatization (200 °C/air) step 21

1.6. Summary of materials characterization data for TPOL aerogels as indicated. 26

1.7. Contributions of the main greenhouse gas emissions in the atmosphere that have resulted in the global climate change 28

PAPER I

1. Representative differential scanning calorimetry (DSC) data for RES 70

2. Representative FTIR data for RES as-prepared, and after treatment as indicated by the sample names 70

3. O1s XPS data for TPOL and RF, and their air-oxidized versions as shown 71

4. Solid-state CPMAS ^{13}C NMR data for TPOL (A) and RF (B) and their pyrolyzed products at 240 ^{o}C under Ar or air, as shown 72

5. Elemental analysis data along pyrolysis under Ar towards porous carbons. 73

6. Solid-state ^{13}C NMR data for TPOL (A) and RF (B) along pyrolysis as shown. 74

7. O1s XPS data from the 800 ºC-carbonized C-TPOL-D-800 / C-TPOL-O-800 and C-RF-D-800 / C-RF-O-800 pairs (top and bottom, respectively). 75

8. Photographs and general materials characterization data along pyrolysis and reactive etching of the TPOL (A) and the RF (B) systems. 76

9. Representative SEM, N_2 sorption isotherms (77 K) and CO_2 sorption isotherms (0 ºC - insets) exemplified by the TPOL system as follows: Top: TPOL and TPOL-240(air); Middle: Carbonized C-TPOL-D-800 (red) and C-TPOL-O-800 (blue); Bottom: Etched samples corresponding to the samples in middle raw, EC-TPOL-D-800 (red) and EC-TPOL-O-800 (blue). 78

10. Pore size distributions in the meso and micropore range of samples as shown. 79

11. BET surface area data (upper curves, full symbols), and micropore surface area data (lower curves, open symbols) of all samples. 80

PAPER II

1. CHN analysis results for samples as shown. 154

2. Representative XPS data of samples as shown. 155

3. Photographs of PBO and RF aerogels along processing 156

4. Representative low and medium pressure N_2-sorption isotherms of samples as shown 157

5. Surface areas by medium pressure N_2-sorption of all carbon aerogels of this study as shown. 158

6. Representative adsorption isotherms by selected C and EC samples of CO_2 at two different temperatures (top); CH_4 at 273 K (middle); and, H_2 at 273 K (bottom) 159

7. Experimental and calculated CO_2 uptake from carbon aerogels of this study. 160

8. Representative isosteric heats of CO_2 adsorption (Q_{st}) on selected samples as a function of CO_2 uptake 161

9. Comparison of the isosteric heats of adsorption at zero coverage (Q_0) of all carbon aerogels of this study. 162

10. Relative selectivities at 273 K for the gasses shown of representative C- (top) and EC- (bottom) carbon aerogels derived from RF (red), PBO (yellow) and PA (blue) aerogels. 163

LIST OF SCHEMES

Scheme Page

SECTION

1.1. Base-catalyzed synthesis of RF and MF aerogels..... 4

1.2. Mechanism of base-catalyzed gelation of RF aerogels..... 6

1.3. Mechanism of acid-catalyzed gelation of RF aerogels 7

1.4. Proposed mechanism for the acid-catalyzed synthesis of TPOL aerogels 11

1.5. Proposed structures and SEM images of PAN aerogels at different stages of aromatization, carbonization, and graphitization as shown. 17

1.6. Synthesis of polybenzoxazine (PBO) aerogels via conventional heat-induced and acid-catalyzed (room temperature) methods. 18

1.7. Aromatized structure of polymeric PBO aerogels after curing at 200 °C/air 22

1.8. Structures of as-prepared RES aerogels and their air-oxidized products 23

PAPER I

1. The monomers of this study..... 36

2. Synthesis of acid-catalyzed phenolic aerogels (RES: TPOL, FPOL, RF, PF), air-oxidation, pyrolytic carbonization, and reactive etching. 39

3. Structures of as-prepared RES aerogels, and their air-oxidation products. 43

4. Oxidation mechanism of RES demonstrated with TPOL. 49

5. Idealized structure of carbons derived from pyrolysis of RES at 800 ºC showing two repeat layers of the graphitic core, one in red, one in blue. 52

PAPER II

1. Monomer precursors of the polymeric aerogels of this study (RES, PBO and PA)... 124

2. Synthesis of the carbon aerogels of this study and their activated forms 127

LIST OF TABLES

Table Page

SECTION

1.1. Classification of organic aerogels based on their precursors 9

PAPER II

1. Material Properties of Nanoporous Carbons and Etched Carbon Aerogels Derived from RES, PBO and PA Aerogels 130

2. Micropore Analysis and CO_2 Uptake 136

LIST OF ABBREVIATIONS

Abbreviation	Description
SCF	supercritical fluid
RF	resorcinol-formaldehyde aerogel
MF	melamine-formaldehyde aerogel
PF	phenol-formaldehyde aerogel
CF	cresol-formaldehyde aerogel
RF	resorcinol-furfural aerogel
PF	phenol-furfural aerogel
PBO	polybenzoxazine aerogel
TPOL	terephthalaldehyde-phloroglucinol aerogel
FPOL	phloroglucinol-formaldehyde aerogel
PAN	polyacrylonitrile
PUAC	polyurethane acrylates
PUNB	polyurethane-norbornenes
PA	polyamide
PI	polyimide
PUA	polyurea
PU	polyurethane
p-DCPD	polydicyclopentadiene
PI-ISO	polyimide from isocyanate route
PI-AMN	polyimide from amine route

EGDMA	ethylene glycol dimethacrylate
HDDA	1,6-hexanediol diacrylate
AIBN	Azobisisobutyronitrile
CA	carbon aerogel
CNT	carbon nanotubes
BO	Benzoxazine monomer
PBO-H	PBO via heat-induced polymerization of BO
PBO-A	PBO via HCl-catalyzed room temperature reaction
PBO-H-5-130	a-made heat-induced PBO with 5% w/w monomer concentration
PBO-A-5-RT	a-made HCl-catalyzed PBO with 5% w/w monomer concentration
PBO-H-5-200	cured heat-induced PBO with 5% w/w monomer concentration
PBO-A-5-200	cured HCl-catalyzed PBO with 5% w/w monomer concentration
C-PBO	PBO-derived CA pyrolyzed under Ar at 800 ^{o}C
EC-PBO	PBO-derived CA after etching under CO_2 at 1000 ^{o}C
RES	phenolic resin aerogels
POL	phloroglucinol
T	terephthalaldehyde
R	resorcinol
P	phenol
F	formaldehyde
RES-240(air)	RES aerogels pyrolyzed at 240 ^{o}C in air

RES-240(Ar)	RES aerogels pyrolyzed at 240 ^{o}C under Ar
C-RES-O-Θ	CA from RES aerogels via oxidation step, pyrolyzed under Ar at a given temperature Θ
C-RES-D-Θ	CA from RES aerogels via direct pyrolysis (without oxidation), pyrolyzed under Ar at a given temperature Θ
EC-RES-O-Θ	CA from RES via oxidation step and after reactive etching under CO_2 at 1000 ^{o}C
EC-RES-D-Θ	CA from RES via direct pyrolysis and after reactive etching under CO_2 at 1000 ^{o}C
C-PA	PA-derived CA pyrolyzed under Ar at 800 ^{o}C
EC-PA	PA-derived CA after etching under CO_2 at 1000 ^{o}C
MOF	metal organic framework
HCP	hyper crosslinked polymer
CMP	conjugated microporous polymer
PIM	polymer with intrinsic microporosity
PAF	porous aromatic framework
COP	covalent organic polymer
CTF	covalent triazine-based framework
MOP	microporous organic polymer
PPF	porous polymer framework
BILP	benzimidazol-linked polymer
TIPM	triisocyanate (tris(4-isocyanatophenyl) methane)
PMA	pyromellitic acid
EPA	environmental protection agency
CCS	carbon capture and storage, carbon capture and sequestration, or carbon control and sequestration

CFP	carbon filter process
SEM	scanning electron microscopy
XRD	X-ray diffraction
SAXS	small angle x-ray scattering
XPS	x-ray photoelectron spectroscopy
FTIR	Fourier transformed infrared spectroscopy
DSC	differential scanning calorimetry
MDCS	modulated differential scanning calorimeter
CP MASS ^{13}C NMR	cross-polarization magic angle spinning ^{13}C-NMR
CP TOSS ^{13}C NMR	cross-polarization total suppression of spinning sidebands ^{13}C-NMR
BET	Brunauer–Emmett–Teller method in the analysis of surface area from N_2-sorption porosimetry
BJH	Barret-Joyne-Halenda equation in the analysis of mesopore size distribution
HK	Horvath-Kawazoe method in the analysis of micropore size distribution
DFT	density functional theory in the analysis of micropore size distribution
DR	Dubinin-Radushkevich method in the analysis of micropore volume
Q_{st}	isosteric heat of adsorption
Q_o	Q_{st} at zero gas uptake

1. INTRODUCTION

1.1. AEROGELS

Aerogels are a unique class of highly porous solid materials with extremely low density. They can be up to 99% v/v air.[1–6] Due to their large open pores and high internal surface areas, they have numerous useful properties such as: extremely low thermal conductivity, low sound velocity, and high optical transparency. In most cases, they are amorphous materials by X-ray diffraction (XRD) techniques. Consequently, aerogels have attracted attention for potential applications such as: catalysts, sorbents, thermal insulators, energetic materials,[7,8] Cherenkov detectors, dielectric, electrodes for batteries and capacitors, etc.[9–13] However, due to their limited processing methods, their commercialization has been slow.[14,15]

Aerogels are prepared via sol-gel processing[16] of molecular precursors in organic solvents. The initial gel consists of a solid network filled with solvent. That pore-filling solvent is replaced by air via a process that is referred to as supercritical fluid (SCF) CO_2 drying. As a result, the porous texture of wet gel is retained in the dried aerogels. Figure 1.1 illustrates the general steps followed in the sol-gel processing of aerogels.

Depending on the choice of precursors (inorganic or organic), all aerogels fall into two main classes: inorganic and organic. The first inorganic silica-based gel was prepared by Ebelmen in 1846, by exposure to the atmosphere of a silane obtained from $SiCl_4$ and ethanol. In 1931, Kistler showed that the pore-filling liquid of a gel can be removed without destroying the gel network. Its long-time preparation was the reason that it took 30 years to become industrially applicable. Silica gel has become a widely investigated

inorganic material and numerous literature has been devoted to its rich chemistry and applications in fundamental sciences and high technology. Details about synthetic conditions and properties of silica aerogel can be found in the literature.[4,5,17–21]

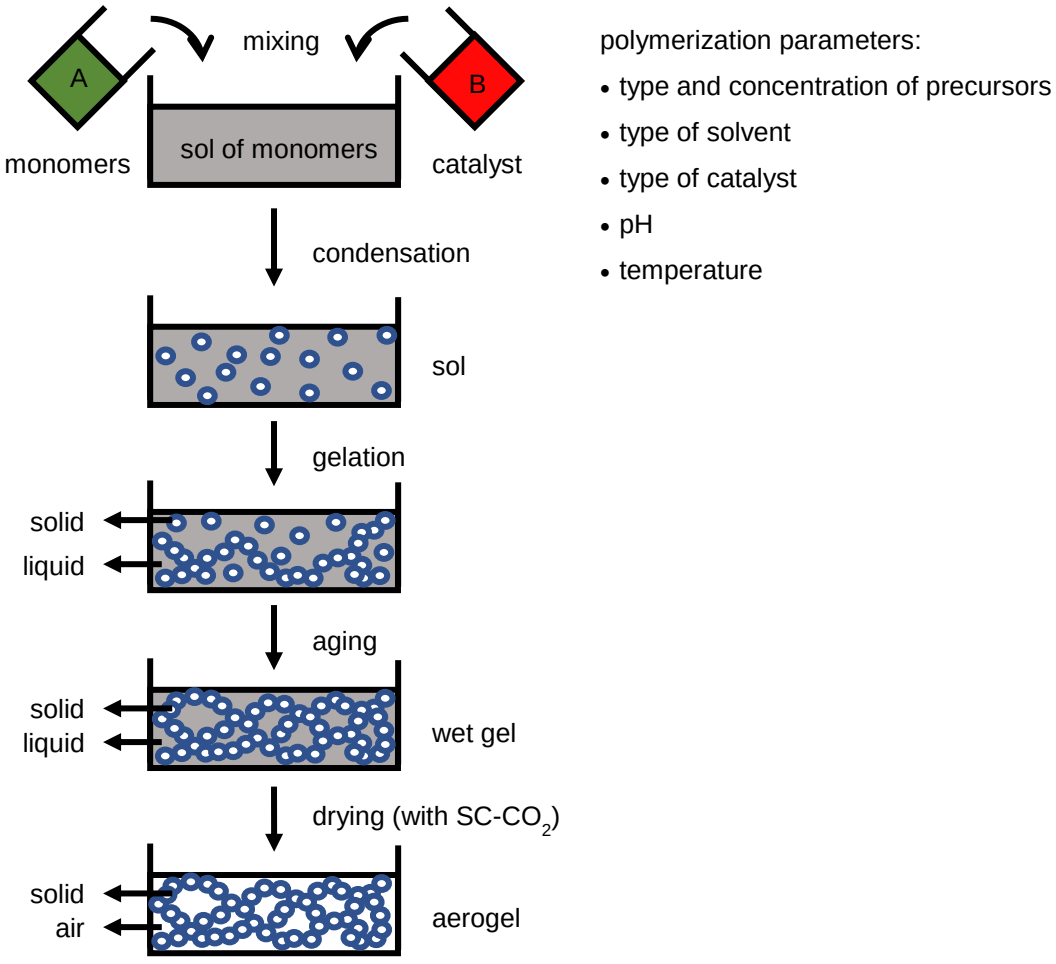

Figure 1.1. The schematic preparation of aerogels by sol-gel processing and some controllable polymerization parameters.

1.2. ORGANIC AEROGELS

Organic aerogels are highly crosslinked polymers, which are prepared by the sol-gel polymerization between purely organic monomers. They were first introduced by Pekala et. al. in 1987.[5,22] Those were resorcinol-formaldehyde (RF) and melamine-formaldehyde (MF),[23] which were synthesized from the polycondensation of resorcinol (1,3 dihydroxybenzene) or melamine (1,3,5-triazine-2,4,6-triamine) with formaldehyde under basic (often sodium hydroxide (NaOH), or sodium carbonate (Na_2CO_3)) conditions (Scheme 1.1). RF belongs to a large class of organic polymers, i.e., phenolic resins,[1] which are polycondensation products of phenolic compounds with aldehydes in the aerogel form.

In 2007, Mulik et. al. reported a one-pot acid-catalyzed synthesis of RF in acetonitrile, which proceeds faster (2 h at room temperature or 10 min at 80 °C) in comparison to Pekala's week-long base-catalyzed procedure. It was concluded that the acid-catalyzed gelation process yielded RF aerogels that were chemically (as evident by ^{13}C NMR) indistinguishable from those obtained via the usual base-catalyzed aqueous gelation process. Nevertheless, acid-catalyzed RF aerogels show a different morphology than their base-catalyzed analogues, which results from their different gelation mechanisms.[24]

The mechanisms involved in the base- and acid-catalyzed synthesis of RF aerogels are illustrated in Schemes 1.2 and 1.3, respectively. Resorcinol (R) has three reactive sites at 2, 4, and 6 positions of benzene ring and is more reactive than phenol, therefore, it can react with formaldehyde (F) at room temperature.

[1] For details about phenolic resins please refer to appendix A.

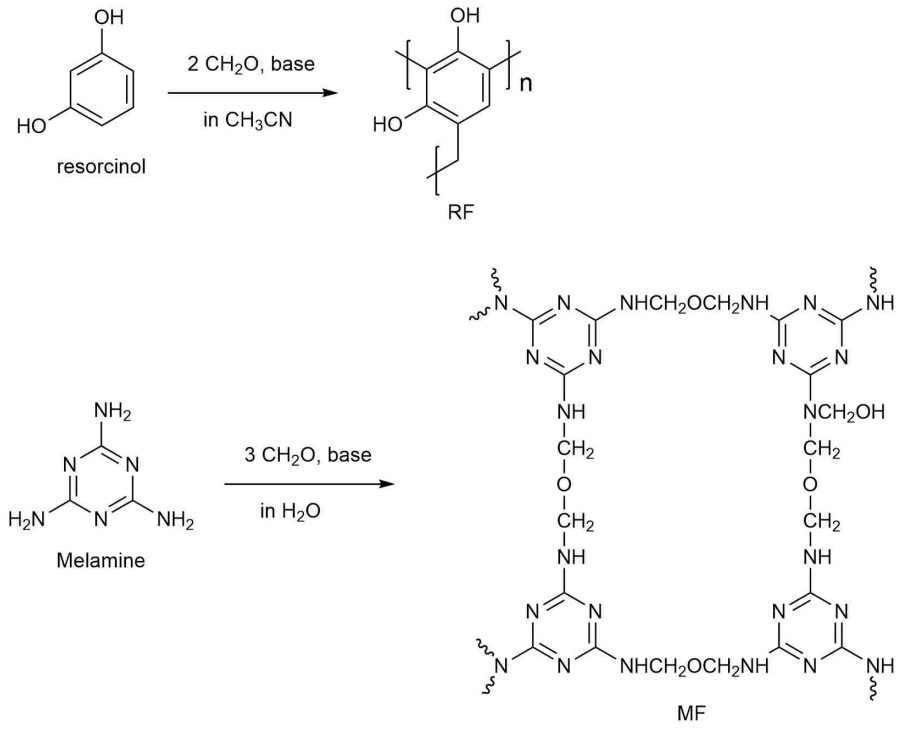

Scheme 1.1. Base-catalyzed synthesis of RF and MF aerogels.

As it is shown in Scheme 1.2, in the base-catalyzed gelation, the R anion is formed by deprotonation of resorcinol (1). Electron donation from positions 4 or 6 of R to the partially positively charged carbonyl carbon of formaldehyde leads to hydroxymethylation. Hydroxymethylation activates the ring further towards reaction with F leading to hydroxymethylation at position 4 (2). Subsequently, hydroxymethylated R at position 2 is deprotonated by the base, leading to the formation of unstable *o*-quinomethide intermediate (3), which reacts with the R anion and forms a compound with a methylene bridge (4). Because of the presence of active sites on R produced by deprotonation continuous condensation results in the formation of crosslinked RF polymer (5).

The acid-catalyzed reaction involves an electrophilic aromatic substitution in which, in contrast to the base-catalyzed one, F is first protonated by reacting with an acid (1). Afterwards, the protonated F is attacked by the π-system of R, leading to hydroxymethylation of R (2). Further, the acid helps in the protonation of the hydroxymethyl group followed by elimination of H_2O, a good leaving group, and formation of *o*-quinomethide intermediate (3). *o*-quinomethide can react with R (like in step 4 of the base-catalyzed reaction) or the π-system of another R can attack the protonated hydroxymethyled R to form methylene linkages (4). Finally, in the presence of excess R and F, additional condensations result in the formation of highly crosslinked RF network (5).[25]

Organic aerogels exhibit similar structures and properties to their inorganic counterparts. For example, RF aerogels are dark red, and their polymer network consists of interconnected particles ≤ 10 nm diameters similar to silica aerogels. Figure 1.2 compares the scanning electron microscopy (SEM) images of RF and silica aerogels, both consisting of primary particles of 10–12 nm in diameters, which are the building blocks of pearl-necklace-like secondary particles with 40–70 nm diameters.[22a] Those nanostructures give them special properties that can be superior in some cases to inorganic aerogels. For example, under ambient conditions, monolithic RF aerogels show a lower thermal conductivity of 0.012 W m^{-1} K^{-1} than silica aerogels (0.016 W m^{-1} K^{-1}). Another inimitable advantage of organic over inorganic aerogels is the capability of former to be used as carbon precursors. That will be discussed in detail in Section 1.4.[22c,26]

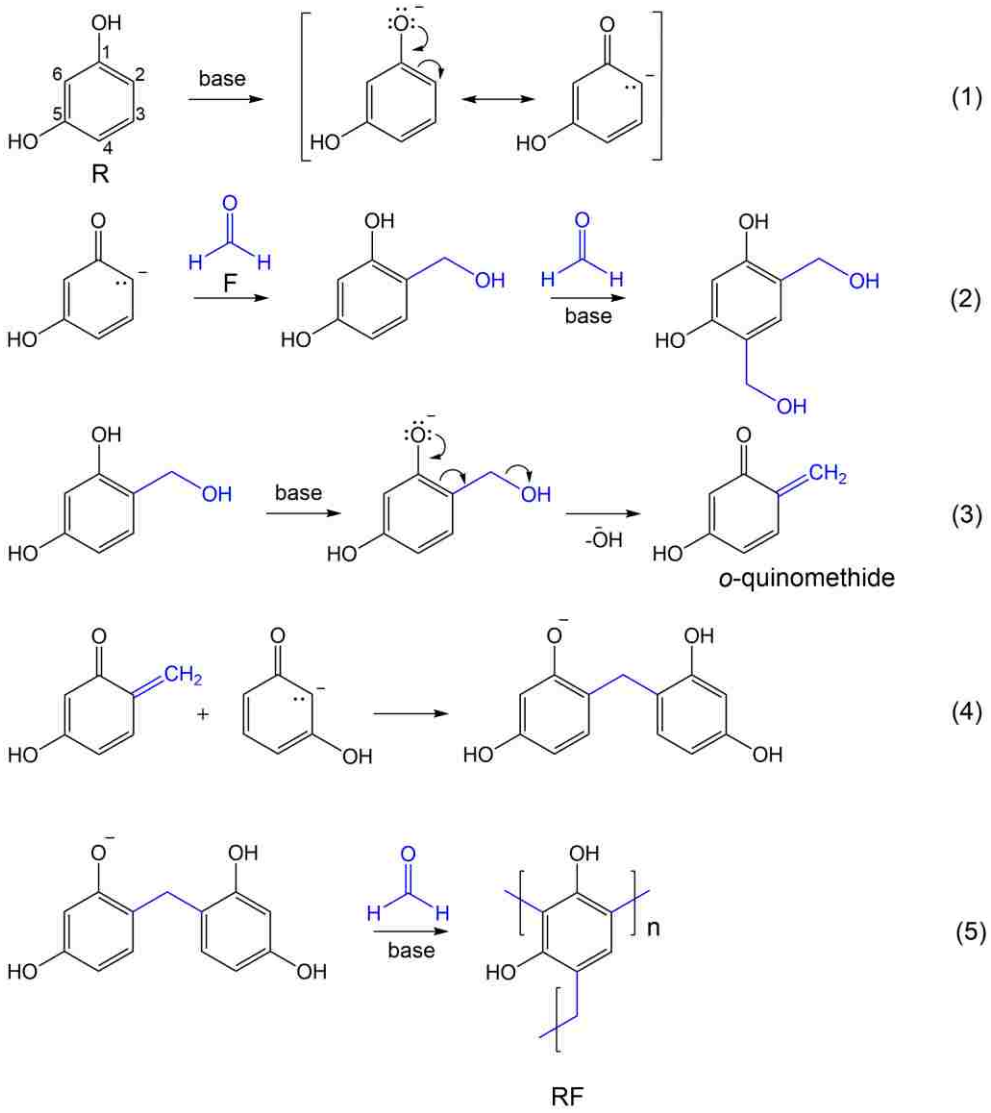

Scheme 1.2. Mechanism of base-catalyzed gelation of RF aerogels.

It is noted that combination of various polymerization conditions such as: monomers ratio, solvent, catalyst concentration, pH, and temperature greatly affect the physical and chemical characteristics of gels prior to drying (see Figure 1.1). These conditions can be fine-tuned so that the microstructure and properties of final aerogels are tailored accordingly.

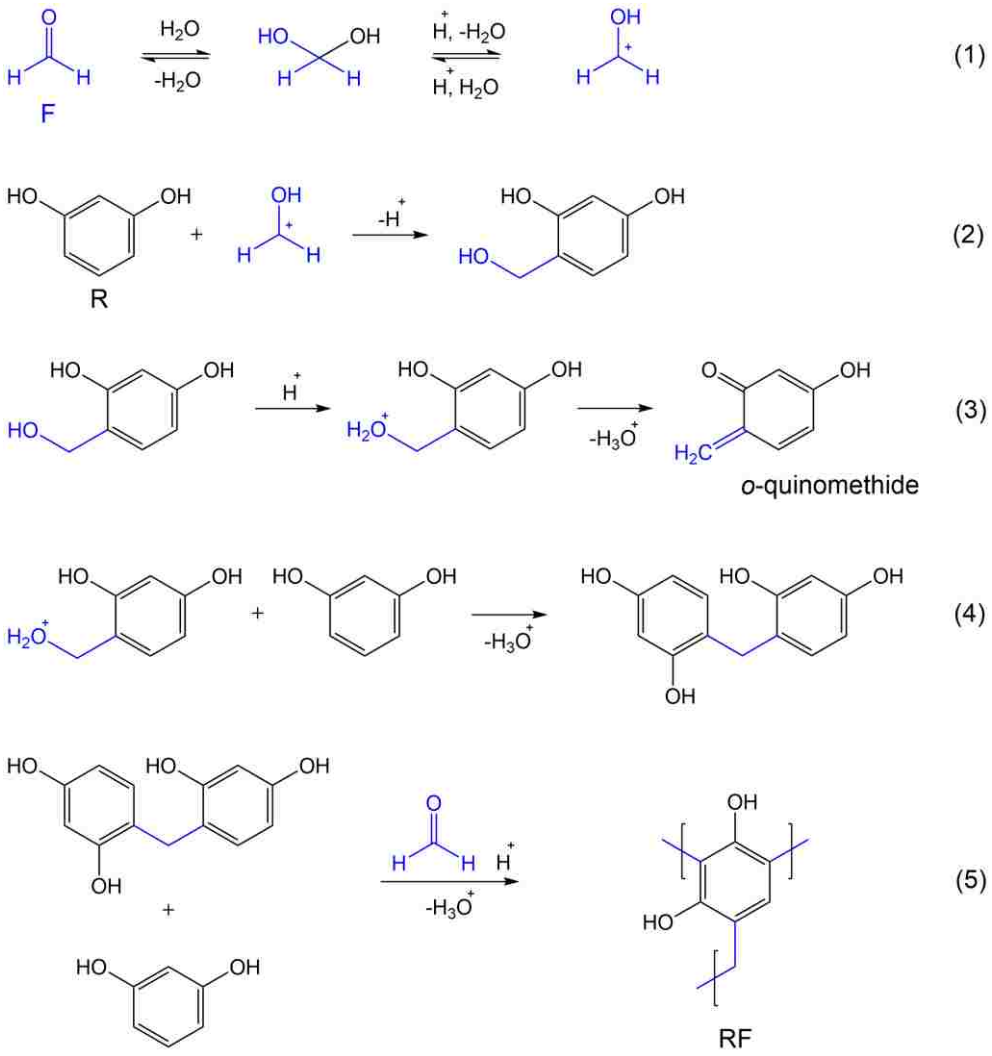

Scheme 1.3. Mechanism of acid-catalyzed gelation of RF aerogels.

For instance, for RF aerogels, changing the monomer concentration, clearly influences the density of the material by changing the degree of crosslinking. In the case of MF aerogels, the transparency of aerogels is essentially controlled by changing the pH of the initial sol.[5,23]

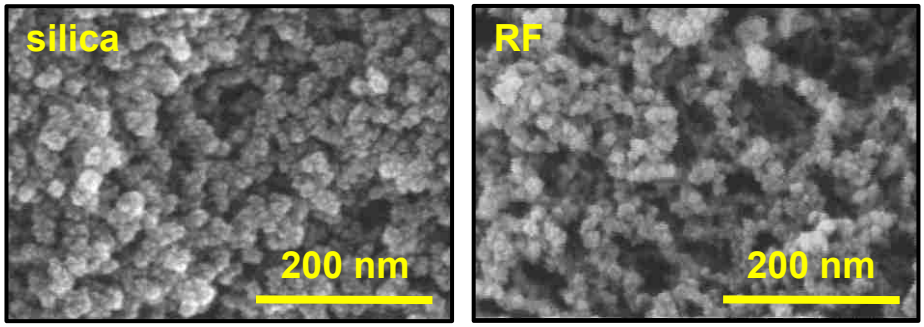

Figure 1.2. SEM images of silica (ρ_b = 0.200 g cm^{-3}) and RF (ρ_b = 0.160 g cm^{-3}) aerogels as shown. Note that at close bulk densities (ρ_b) both systems show similar particulate morphologies.

1.2.1. Other Types of Organic Aerogels. For many years, the term "organic aerogels'' was bound to RF aerogels. Further progress has been made to diversify organic aerogels based upon their chemical and porous structures. In addition to RF, many other phenolic resin types of organic aerogels such as: phenol-formaldehyde (PF),[27] cresol-formaldehyde (CF),[28] resorcinol-furfural (RF),[29] phenol-furfural (PF),[30] polybenzoxazine (PBO),[31] and more recently terephthalaldehyde-phloroglucinol (TPOL), and phloroglucinol-formaldehyde (FPOL) have been synthesized.[32] Organic aerogels are not limited to phenolic resins though. Organic chemists have taken the advantage of the rich organic reactions to develop many novel organic aerogels that are products of different functional groups. Those include: polyacrylates such as polyacrylonitrile (PAN),[33] and polyurethane acrylates (PUAC), polyurethane-norbornenes (PUNB),[34] polyamide (PA),[35] polyimide (PI),[36] polyurea (PUA),[37] polyurethane (PU),[38] and polydicyclopentadiene (*p*-DCPD),[39] each of which are being pursued for different applications such as suitable carbon precursors, thermal insulators, materials with excellent mechanical properties and stability, as core for armor plates, and shape memory aerogels. Table 1.1 summarizes all

organic aerogels that are obtained from the polymerization of phenolic monomers with aldehydes or other reactive (non-phenolic) starting materials.

1.2.2. Synthesis of Terephthalaldehyde-Phloroglucinol (TPOL) Aerogels. Just like the acid-catalyzed gelation mechanism of RF, the reaction of T with POL in acidic solution involves an electrophilic aromatic substitution (Scheme 1.4). In the

Table 1.1. Classification of organic aerogels based on their precursors.

Phenolic Aerogels	**Precursors**	**Organic Aerogels**
	Resorcinol (R) + Formaldehyde (F)	RF
	Phenol (P) + Formaldehyde (F)	PF
	Cresol (C) + Formaldehyde (F)	CF
	Resorcinol (R) + furfural (F)	RF
	Phenol (P) + furfural (F)	PF
	Bisphenol A + para-Formaldehyde (F) + Aniline	PBO
	Phloroglucinol (POL) + Terephthalaldehyde (T)	TPOL
	Phloroglucinol (POL) + Formaldehyde (F)	FPOL
Non-Phenolic Aerogels	Melamine (M) + Formaldehyde (F)	MF
	Acrylonitrile + Crosslinker[1] + Initiator[2]	PAN
	Isocyanate + Acrylates + Initiator[2]	PUAC
	Isocyanate + Norbornene Monomer + Initiator[2]	PUNB
	Isocyanate + Carboxylic Acid	PA
	Isocyanate or Amine + Anhydride	PI
	Isocyanate + Amine or Water	PUA
	Isocyanate + Alcohol	PU
	Dicyclopentadiene	*p*-DCPD

[1]ethylene glycol dimethacrylate (EGDMA) or 1,6-hexanediol diacrylate (HDDA)
[2]Azobisisobutyronitrile (AIBN).

presence of acid, the electrophile, T, is protonated and carries a positive charge (1). POL is a highly reactive multifunctional phenolic monomer in electrophilic aromatic substitution because of the electron donating resonance effect of the three -OH groups. The protonated T is attacked by the π-system of POL leading to the formation of hydroxymethylene bridges between T and POL. Subsequently, the protonation of hydroxyl group (2) creates a good leaving group ($-OH_2^+$), which cleaves further to form highly reactive *o*-quinomethide intermediates (3). The π-system of another POL can attack the protonated hydroxymethylene or the *o*-quinomethide to form methylene linkages, thus leading to condensation of 1 mol of T with two moles of POL (4). The same processes take place at other side of T and as a result of simultaneous addition and condensation reactions the crosslinked polymeric network of TPOL aerogels is formed (5).

The mechanism for the synthesis of FPOL aerogels follows the same steps as in the formation of TPOL aerogels, except T is replaced with F (formaldehyde, as the aldehyde) in the structure of FPOL system.

1.3. POLYMERIC CARBON AEROGELS

3D nanoporous carbons obtained by the pyrolysis (also referred to as carbonization) of organic aerogels (which are, in turn, prepared by sol-gel mixing of organic monomers as discussed in Section 1.2) are termed “carbon aerogels”.[27,40] Figure 1.3 depicts the typical step involved in the preparation of carbon aerogels from organic precursors, e.g., RF, or PF aerogels along with their potential applications.

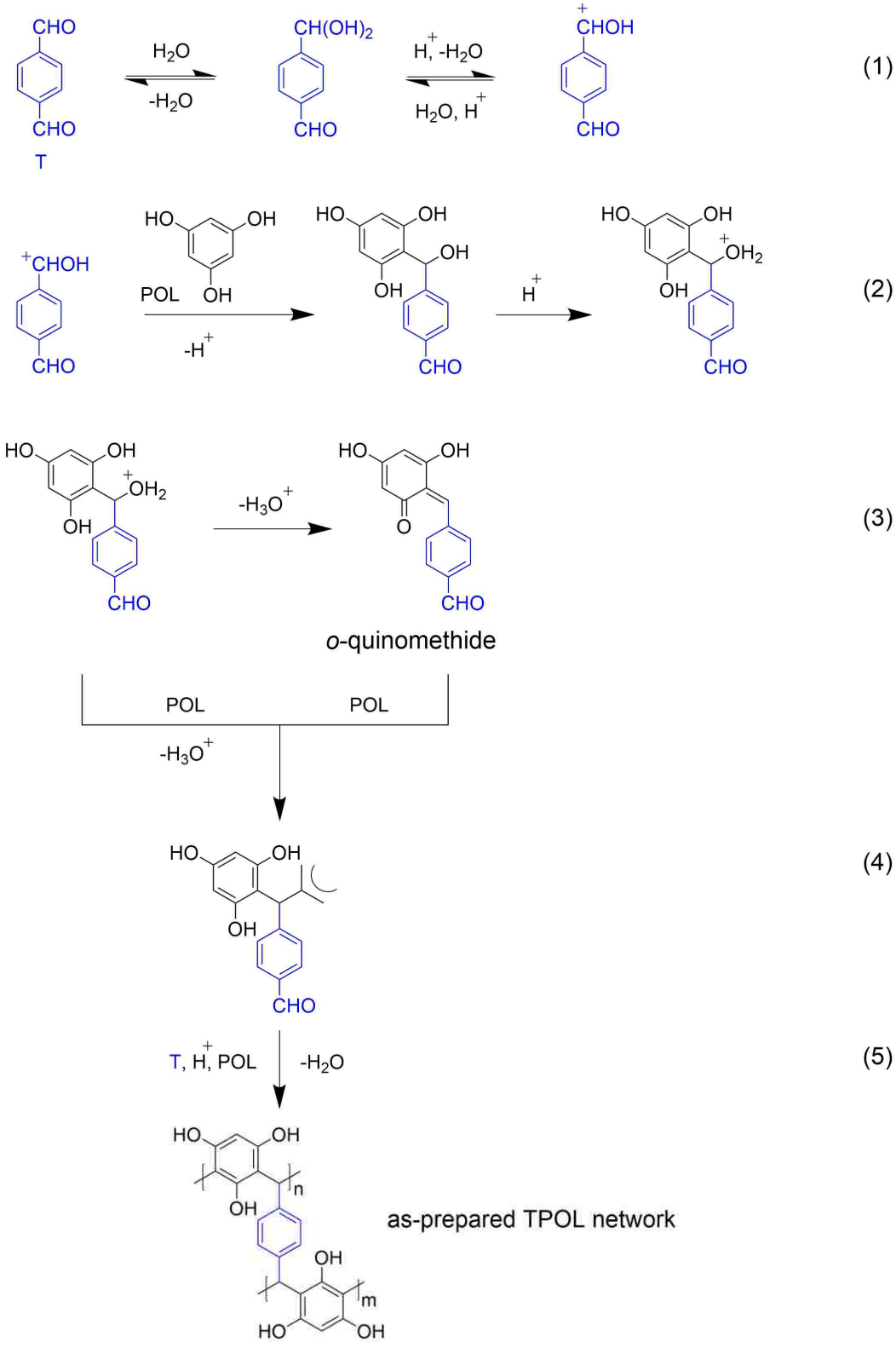

Scheme 1.4. Proposed mechanism for the acid-catalyzed synthesis of TPOL aerogels.

1.3.1. Background. The first and widely known carbon aerogel (CA) was produced by the carbonization of RF aerogel at the beginning of 1990's, 60 years after the discovery of the first aerogel based on silica gels. Indeed, tunable properties of RF aerogel, such as surface area, pore volume, and pore size distribution, allowed it to be a suitable precursor for preparing carbon aerogels.[41–48]

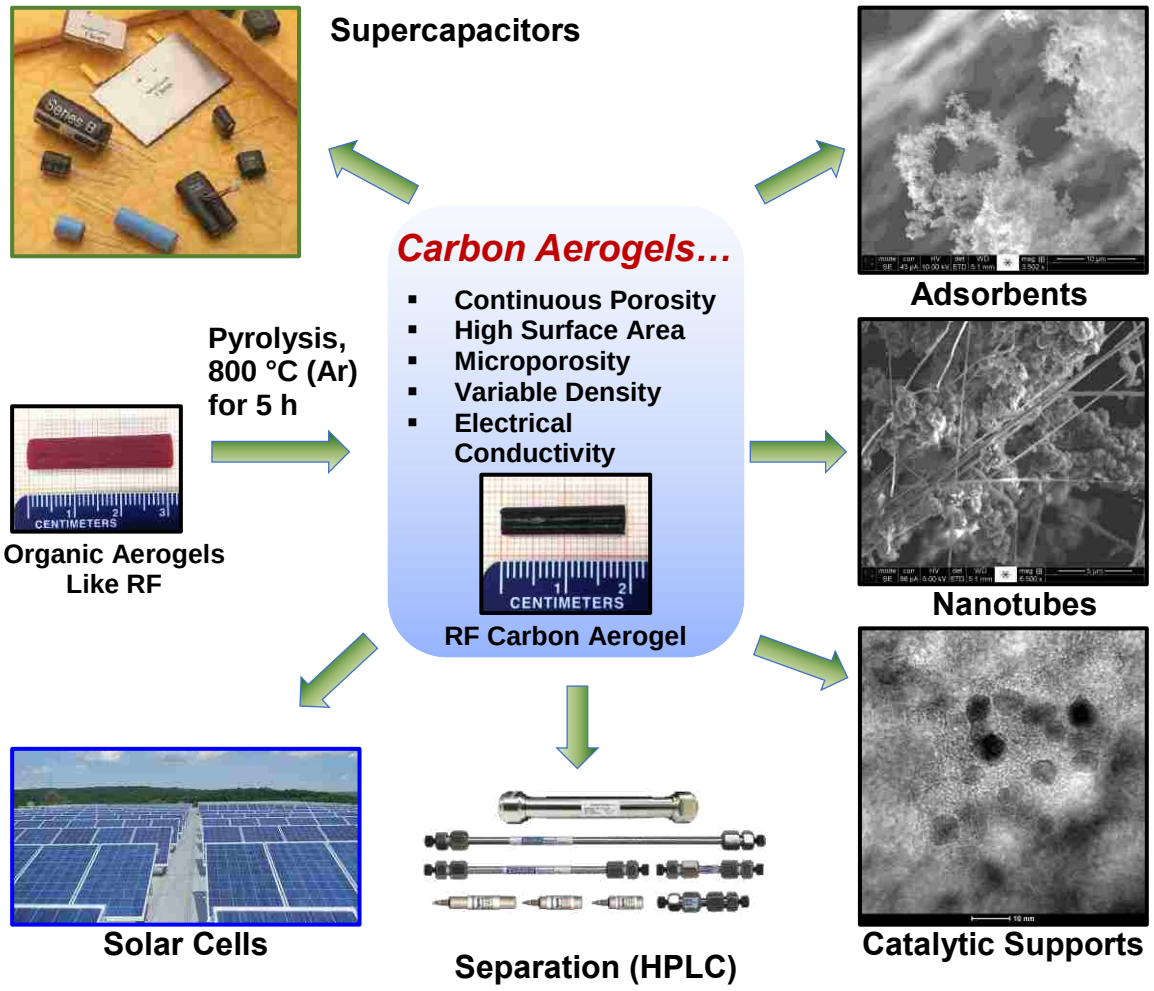

Figure 1.3. Preparation of carbon aerogels from organic aerogels and their main potential applications, which are derived from their outstanding properties as indicated.

The utility of CAs is derived from their exceptional properties in particular: high surface area and pore volume, low density, high electrical conductivity, and environmental compatibility (Figure 1.3).[49–51] CAs can be fabricated as monoliths, powders, microspheres, or thin films. Monoliths have some advantages over other forms of CAs. They show continuous structures and leverage a set of properties, due to their suitable geometry, better than other forms, thus, have emerged as useful media for novel technological applications. For example, microscopically, monolithic structure is described as 3D continuous hierarchical porosity, which usually leads to several distinct merits such as: low pressure drop, fast heat and mass transfer, high contacting efficiency, and easy to deal with. In addition, macroscopically, a monolith usually shows wider flexibility of operation as compared to the powder form.[52]

There are various types of porous carbons besides CAs. In general, they fall into the following classes: traditional activated carbons, renewable-resources-derived porous carbons, synthetic polymer-based porous carbons, porous carbon nanotubes (CNT), porous graphene composites, etc. CAs have the advantage that they can be prepared in bulk quantities via the facile sol-gel chemistry. However, their major issue is their long and sensitive drying process. That, in fact, can be sacrificed by considering their availability in unique shapes such as monolithic, films, etc., that cannot be obtained by other methods as mentioned before.[53,54]

All porous carbon nanomaterials show similar chemical structure consisting of conjugated carbons in sp^2 hybridization state, in which electrons are delocalized and serve as charge carriers, thus, responsible for electrical behavior of the materials.[53]

CAs have been viable candidates for energy storage materials, adsorbents, electrochemical double-layer capacitors/supercapacitors, materials for chromatographic packing, anodes in Li-ion batteries, electrodes in catalytic supports, for instance, in fuel cells, etc., some of which have already been commercialized (Figure 1.3).[55–59]

In the course of pyrolysis, the slow heat treatment (with) is used to convert the polymer or organic precursor to high-yield CA, which is essentially mostly carbon. Heating cycles and temperatures depend on the nature of the precursor. But, for most materials the heating is at slow rate (1–5 °C min^{-1}) and usually at temperatures of 800–1000 °C, which may be extended to 1300 °C.[60] It has to be noted that not every polymer can be converted to high-yield carbon. Typical carbonizable polymeric aerogels are phenolic resins, PAN and its copolymers as the main non-phenolic carbon precursors,[33,61] PA aerogels,[35,37c], PI,[36a,36c] PUA,[37b] and PU.[38b]

In general, to obtain high-yield carbon, the polymeric precursor must have: a) high molecular weight, b) high degree of aromaticity, and c) should not have more than one carbon atom between aromatic rings, otherwise, the polymer will turn into volatile molecules because of chain scission, and d) nitrogen should be in the ring structure and not in the chain. Other elements, if exist, do not affect the stability of the polymer but will result in lower carbonization yields.[62]

1.3.2. The Importance of Ring Fusion Aromatization Step in the Carbonization of PAN Fibers and PBO Aerogels and Extension to Other Phenolic Resin Aerogels. The pyrolysis of polymers, e.g., phenol-formaldehyde, had been studied before the emerge of organic aerogels. The structural changes during pyrolysis at successive temperatures were reported by means of measurements of diamagnetic

susceptibility, electrical conductivity, XRD, and infrared (IR) spectroscopy. Moreover, formation of gaseous compounds in the midst of pyrolysis were supported using chromatographic and mass spectrometry techniques.[63]

Among the most studied materials as carbon precursors, is PAN, the main source of carbon fibers for over a century. Extensive studies have been conducted to discuss the chemistry involved in the production of high performance carbon fibers from PAN polymers. In 1960's, it was found that if PAN fibers are treated in air before the main carbonization step, the resulting carbon fibers become stronger and stiffer.[64] After that, it became an accepted procedure worldwide to first cure PAN fibers in air at temperatures of 180–300 °C, followed by carbonization at temperatures above 800 °C in an inert environment (Ar or N_2) with a slow heating rate. Although the structure of the PAN fibers is still complicated, it is almost widely accepted that PAN fibers become oxidized and cyclization and aromatization are the main chemical changes that take place during curing step. Therefore, the structure of the carbon precursor needs to be selected wisely in order to enable the material to survive the high temperature carbonization step.[33,65]

However, the question remains as: what actually happens during that curing step that improves the yield and properties of carbons? As shown in Scheme 1.5, ordinarily, three steps are involved in the production of high-yield carbon from PAN-based fibers:

1. Stabilization, which occurs at temperatures of 180–300 °C in air. This step is crucial because the structure of final carbon is set in this step. As a result of oxidative aromatization happening in this step, cyclic structures are formed within the polymeric PAN network; hence, PAN becomes sustainable at high temperature processing (see next steps). The reactions occurring in this step

are exothermic and provide sufficient heat for the formation conjugated ladder chains between nitrile groups.

2. Subsequently, the aromatized (cyclized, or thermally stable) PAN fibers are subjected to a heat treatment at temperatures ≤ 1600 °C under inert atmosphere (Ar or N_2). During this step, separate conjugated polymeric networks become interconnected and form stacked conducting networks (Scheme 1.5).
3. Finally, the carbonized PAN fibers are graphitized at 2300 °C under inert gas to improve the stiffness of carbon fibers.[61,66,67]

It is possible to carbonize all graphitizable polymers by oxidizing the starting materials in the early stages of carbonization. Wislow (1958), prepared polystyrene polymers consisting of *m*-divinyl benzene, *m*-ethylvinyl benzene, and *m*-diethyl benzene. The copolymer was treated at 250 °C in air. The carbonization of that polymer at 450 °C resulted in black carbon with mass loss of only 45%. Hence, it was concluded that the oxidation stage could prevent chain degradation and fragmentation into small gaseous molecules.

Apparently, carbon yield is not affected by whether the polymer is thermosetting or thermoplastic, linear or crosslinked. However, the polymer has to be capable of undergoing cyclization (or ring-fusion aromatization) prior to the carbonization step.[68]

Another example in which the oxidative ring-fusion aromatization step is critical is in PBO aerogels. PBO aerogels are prepared from benzoxazine (BO) monomer, which is made by mixing bisphenol A (4,4'-(propane-2,2-diyl) diphenol), paraformaldehyde,

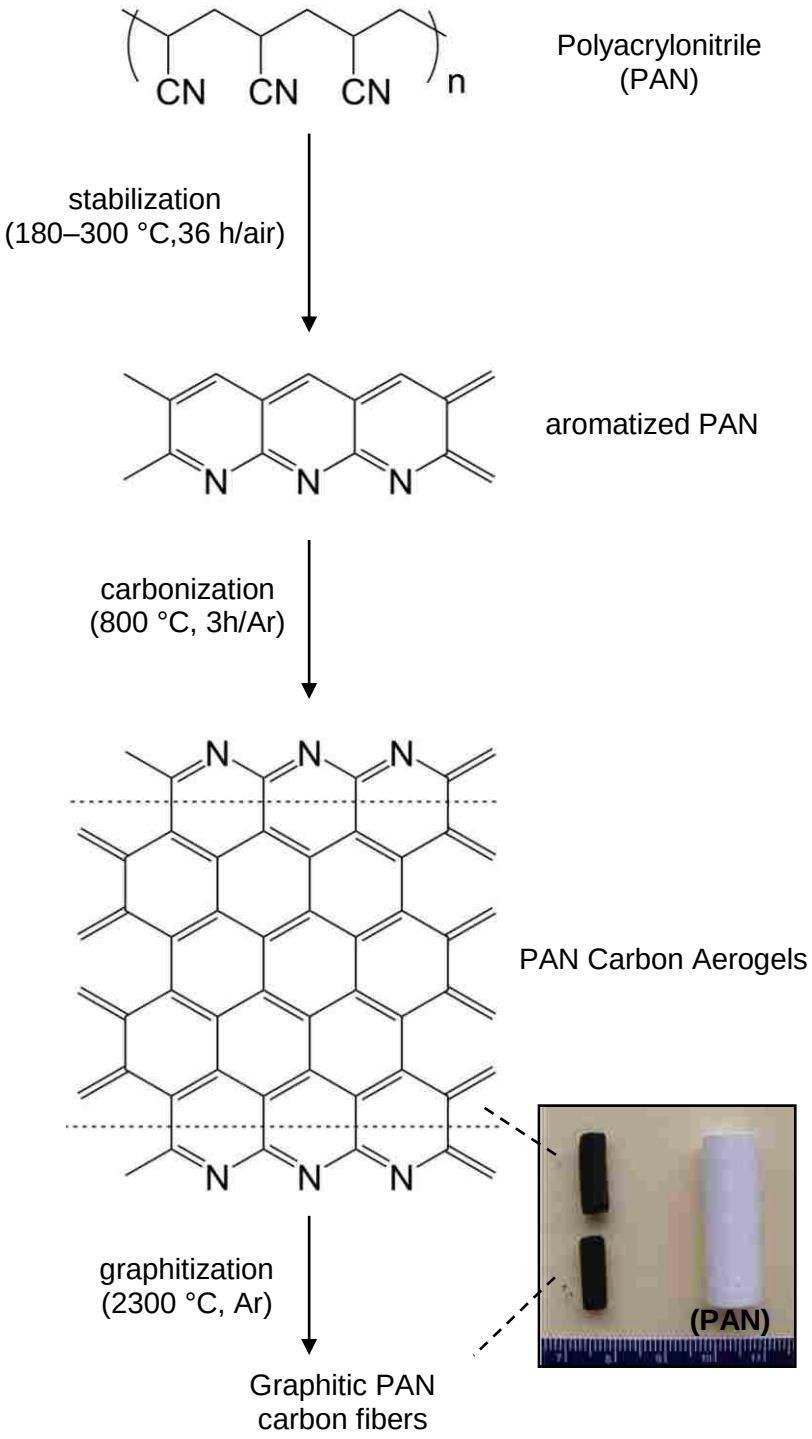

Scheme 1.5. Proposed structures and SEM images of PAN aerogels at different stages of aromatization, carbonization, and graphitization as shown. The physical appearances of as-prepared, CA, and graphitized PAN can also be seen in the photograph.

and aniline at 110 °C. The PBO is prepared traditionally via heat-induced (PBO-H) polymerization of BO in DMF.

Recently, monolithic PBO aerogels were synthesized over a wide density range via a new HCl-catalyzed (PBO-A) room temperature reaction, which is more time-efficient as compared to the heat-induced method. The advantage of acid-catalyzed vs the heat-induced process is that it imposes additional cross-linking in the para positions of

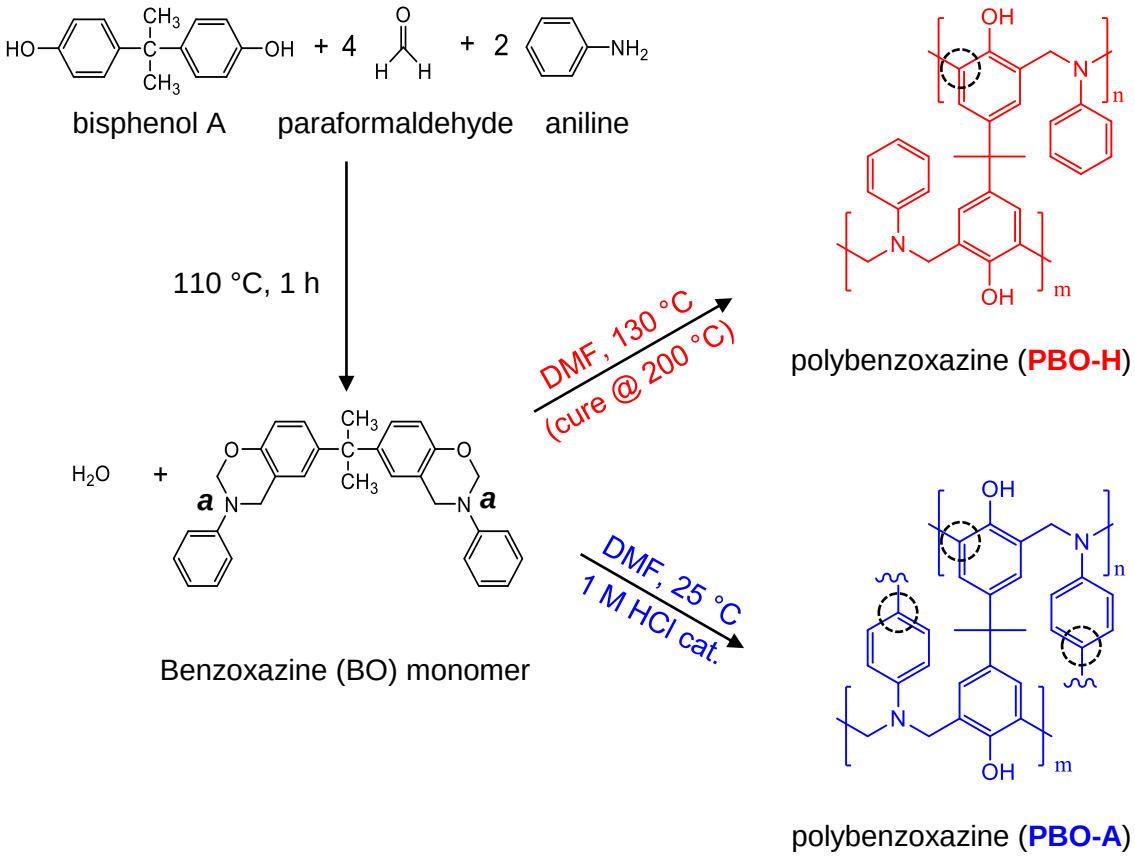

Scheme 1.6. Synthesis of polybenzoxazine (PBO) aerogels via conventional heat-induced and acid-catalyzed (room temperature) methods. Additional crosslinking centers are formed by using the time-efficient acid-catalyzed method.

the aniline as shown with circles in Scheme 1.6. That results in smaller particles, increased surface areas and reduced thermal conductivity.

CAs from PBO polymers were prepared by pyrolysis of the monolithic PBO aerogels at 800 °C under Ar for 5 h. It has been shown that high-yield isomorphic carbons (61%) from PBO are obtained only when PBO aerogels are first oxidized at 200 °C in air for 5 h. Otherwise, direct-pyrolyzed PBO polymers will result in carbons that are not nanoporous monoliths, as shown in Figure 1.4. The curing step oxidizes, aromatizes, and rigidizes the polymeric backbone. Hence, the CAs that are obtained from

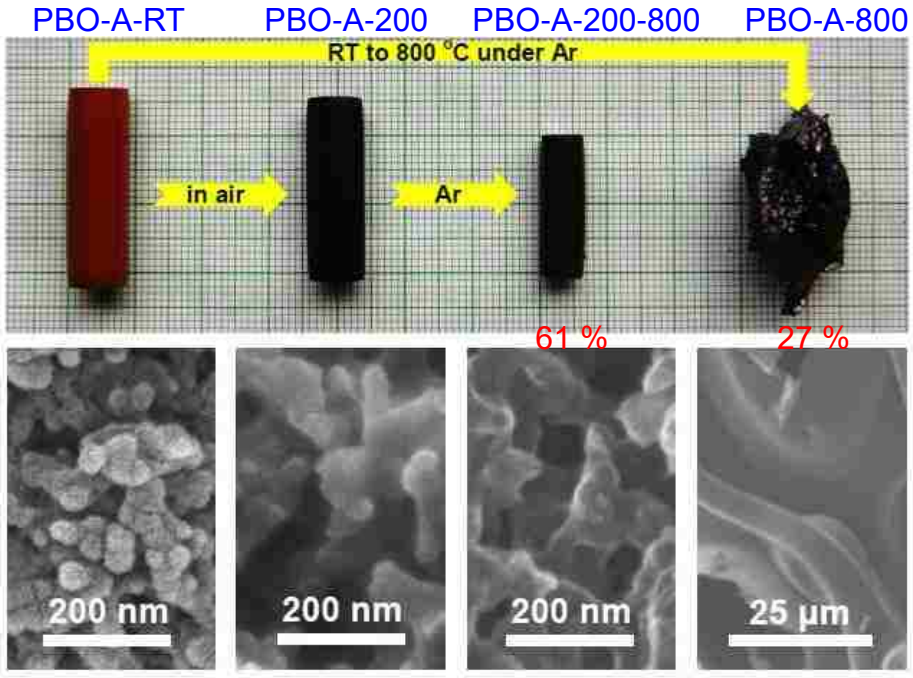

Figure 1.4. Photographs and the corresponding SEMs of PBO aerogels, before and after aromatization at 200 °C/air and after carbonization at 800 °C/Ar. Note that under direct pyrolysis, samples lose their morphology and porosity, while after aromatization isomorphic carbons with relatively high porosity and yields (61% from PBO) are obtained.

that route are extremely robust nanoporous materials with hierarchical porosities that range from micro- to meso- and to macropore sizes.[31]

The findings were supported by SEM, N_2 sorption, solid state ^{13}C NMR and ^{15}N NMR, small angle X-ray scattering (SAXS), FTIR, and thermogravimetric analysis (TGA). According to solid state ^{15}N NMR of PBO aerogels (Figure 1.5), the BO monomer contains only one type of N and shows a single sharp resonance at 62.8 ppm. On the other hand, the spectrum of as-prepared PBO-H showed two resonances close to one another, one at 64.2 ppm and another at 75.4 ppm. However, after curing the spectrum is quite different.

Also, the spectrum of as-prepared PBO-H was radically different than that of as-prepared PBO-A, showing, in addition to the peaks in the 60–70 ppm region, two more strong peaks, one at 293 ppm and another in the 128–135 ppm region. Also, the spectrum of partially cured A- samples (PBO-A-5-200) looks quite similar to that of as-made H-(PBO-H-5-130) samples. In conclusion, heat-induced polymerization is not a complete process. In fact, the 200 $^{\circ}$C/air curing step is an equalizer, through which the polymers from both routes become essentially the same. Thus, curing at 200 $^{\circ}$C in air causes ring-fusion aromatization, which evens out the H- and A- processes. The structure of aromatized PBO after air-curing is shown in Scheme 1.7.[69]

Now, the question is: can we induce ring-fusion aromatization similar to what was observed in PBO in other aerogels? In an attempt to generalize the concept of ring-fusion aromatization, the intriguing discoveries about the stabilization of PAN and PBO through the oxidative ring-fusion aromatization process (180–300 °C in air) were examined on four other polymeric aerogels. Those systems were phenolic resin types of organic

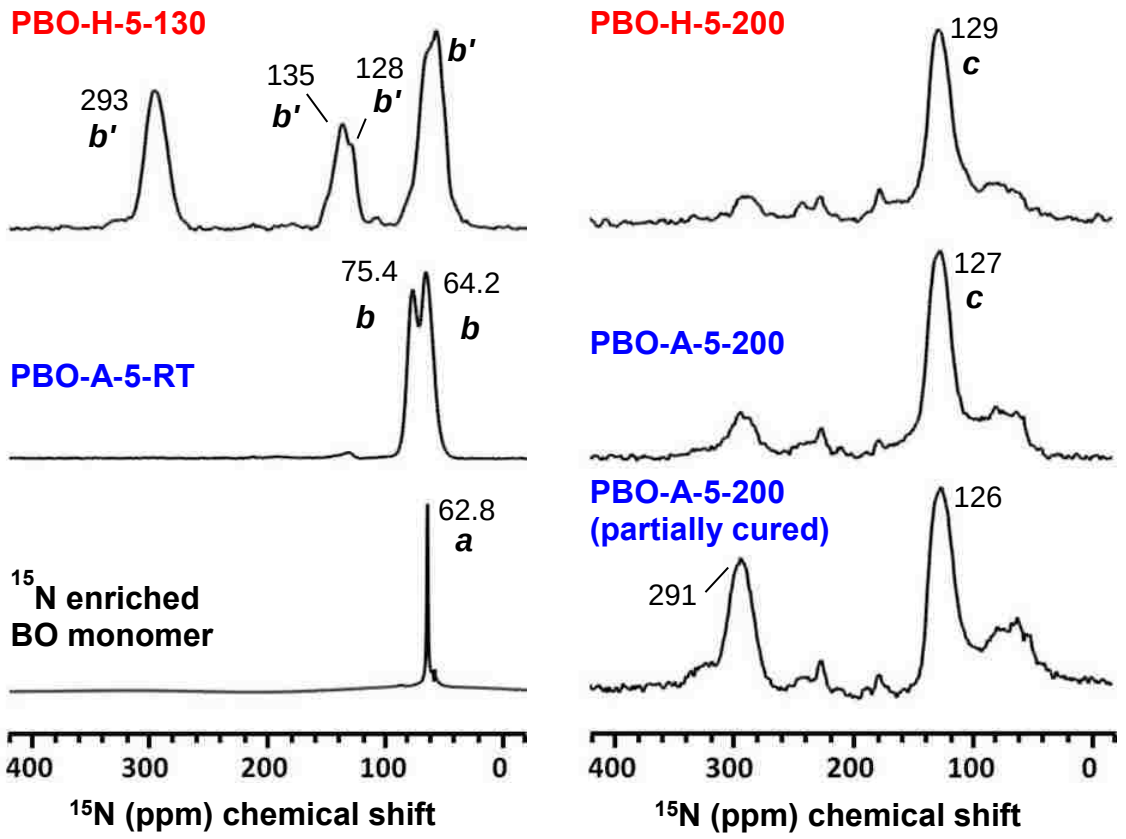

Figure 1.5. Solid state ^{15}N NMR spectra of PBO aerogels (with 5% w/w monomer concentration) obtained from heat-induced and acid-catalyzed pathways before and after aromatization (200 °C/air) step.

aerogels (RES), which were condensation products of three different phenols: phloroglucinol (POL), resorcinol (R), and phenol (P) with two aldehydes: terephthalaldehyde (T), and formaldehyde (F), as shown in Scheme 1.8. TPOL, FPOL, RF, and PF were prepared via HCl-catalyzed sol-gel polymerization in organic solvents. They exhibit high degree of cross-linking, high temperature stability, and high carbonization yields, thereby, they comply with the requirements for a suitable carbon precursor, as were discussed previously in Section 1.3.1.

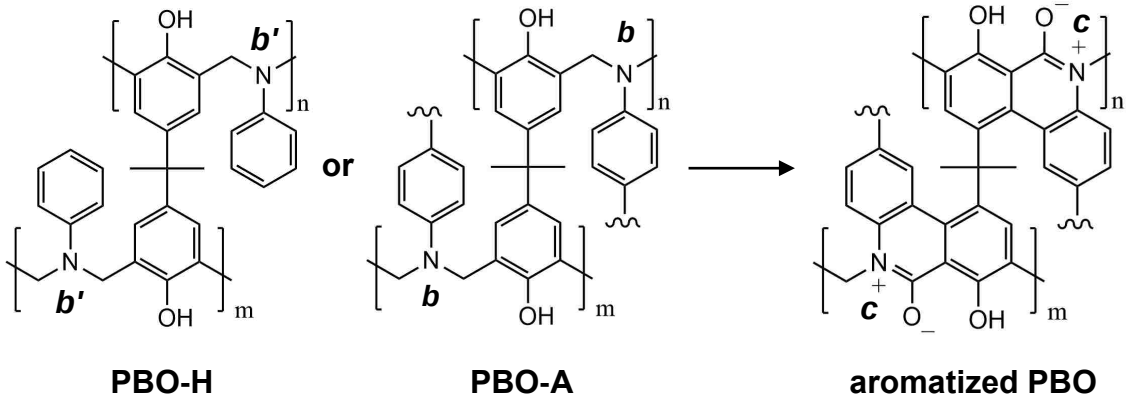

Scheme 1.7. Aromatized structure of polymeric PBO aerogels after curing at 200 °C/air.

Figure 1.6 shows the materials properties data of TPOL aerogels at various stages of pyrolysis. As can be seen, the samples are monolithic, highly porous, and particulate as examined by a combination of materials characterization techniques such as N_2 sorption porosimetry and SEM.

CAs from phenolic resin systems (C-RES-O) were prepared by pyrolysis of aerogel monoliths after inducing oxidative ring-fusion aromatization through heating at 240 °C in air for 5 h. For comparison purposes, samples were also directly pyrolyzed without undergoing the ring-fusion aromatization step, denoted as C-RES-D. The structural changes during the oxidation step along with the materials properties of carbons obtained at successive temperatures were monitored in parallel to the samples obtained via the direct-pyrolyzed route. The observations revealed that, in contrast to PAN and PBO, through the oxidation step, the carbonization yield does not change dramatically, and carbons obtained from both pathways are highly porous and

isomorphic. However, CAs from two of those polymers, i.e., TPOL and FPOL, had higher surface areas when compared to the direct-pyrolyzed samples.

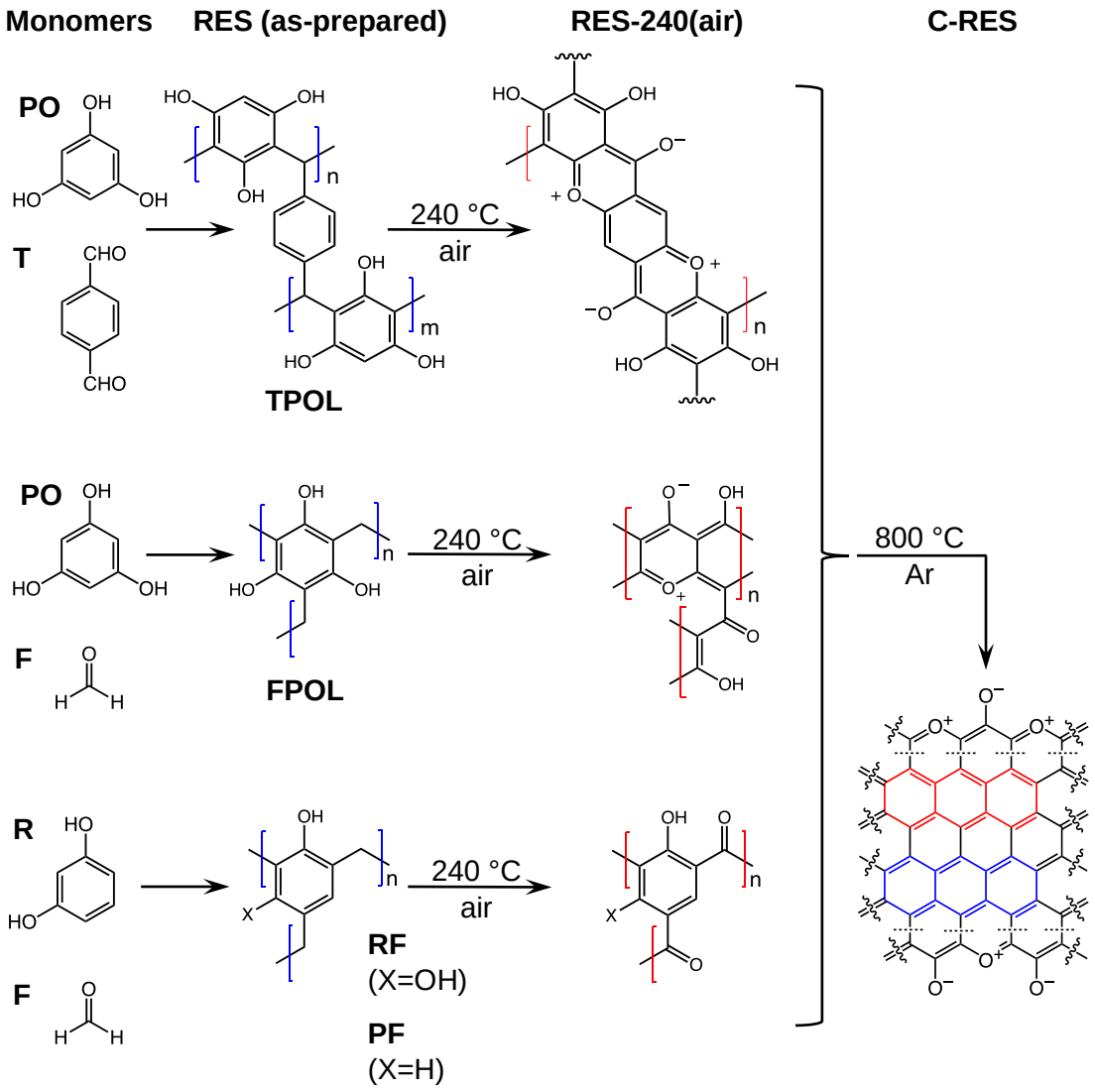

Scheme 1.8. Structures of as-prepared RES aerogels and their air-oxidized products. After carbonization at 800 °C/Ar they convert to a common structure.

Oxidation in air induced ring-fusion aromatization in those two systems as was confirmed with X-ray photoelectron spectroscopy (XPS), solid state ^{13}C NMR, FTIR, differential scanning calorimetry (DSC), and CHN analysis. It was then proposed that ring-fusion aromatization in TPOL and FPOL was analogous to the formation of nitrogen-bearing heterocyclic systems in PAN and PBO polymers, instead oxygen is involved as pyrylium (O^+) in fused 6-membered ring and phenoxide ($C–O^-$) as charge-compensating ion (see Scheme 1.8). RF and PF, on the other hand, did not show any ring-fusion aromatization under the same condition (240 °C/air 5h), and only oxidation took place in aliphatic regions ($-CH_2-$) of the polymer backbone. Their surface areas after carbonization were not different from the CAs obtained by the direct pyrolysis of as-prepared samples (C-RES-D).

Further studies of the carbonization of those four systems at successive temperatures pinpointed another interesting observation about their CAs. Regardless of their pyrolysis routes, either direct-pyrolysis or through oxidative route, and independent of their origin, samples eventually converged to a common structure at ≥ 600 °C consisting of fused aromatic repeat layers with pyrylium (O^+) and phenoxide ($C–O^-$) (see Scheme 1.8).

In conclusion, whenever early oxidative ring-fusion aromatization takes place, it is beneficial to the properties of final CAs. In PAN and PBO, it stabilizes the polymeric backbone and gives high-yield carbons that are stiffer. In PBO, it rigidizes the polymer network and is necessary for obtaining high-yield isomorphic porous CAs. In the case of TPOL and FPOL, it also rigidizes the polymer network and creates microporosity that results in CAs with higher surface areas than their directly-pyrolyzed counterparts.

1.3.3. Activation of Carbons. Carbons often show mass specific surface areas in the range of 200–1000 $m^2\ g^{-1}$, which can be further increased by an activation process. The activation can be carried out through either chemical or physical processes. In chemical activation, activated carbons are prepared by heating carbons or carbon precursors in concentrated acids (e.g., H_3PO_4) or bases (e.g., KOH), or in $ZnCl_2$ under inert atmosphere.[55,70] Physical activation, on the other hand, is a two-step process, which is performed using steam, CO_2, or combination of these two right after the carbonization step.[45] In both techniques, activated carbons show significant improvement on their surface areas due to the opening of closed pores and creating new microporosity.

Among those activation processes, CO_2 activation (or etching) has been found to be the most effective and simple method for producing high-surface area CA with uniform micropores. During CO_2 etching, carbon reacts with CO_2 according to the Boudouard equilibrium (Equation 1), which is basically a comproportionation reaction.[53,71]

$$C + CO_2 \rightleftharpoons 2\,CO \qquad (1)$$

Recently, etching was performed at 1000 °C under CO_2 on CAs obtained from anhydride (PI-AMN) and isocyanates (PI-ISO) polyimides. The BET surface areas of PI-AMN and PI-ISO increased to 417 and 1010 $m^2\ g^{-1}$, respectively. Also, etching improved the electrical conductivity of the latter by a factor of 70. The samples remained monolithic with mass losses of 20–40% relative to the samples before etching under CO_2.[36c]

TPOL (as-prepared)

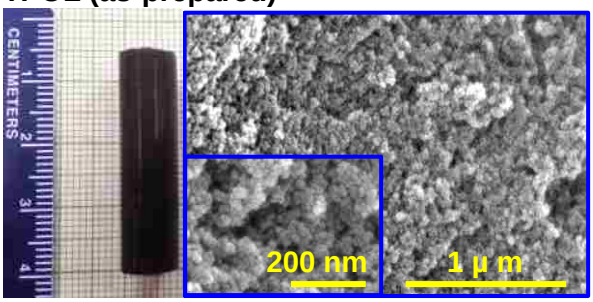

shrinkage = 32.2 ± 0.3%
ρ_b = 0.620 ± 0.009
ρ_s = 1.434 ± 0.006
Π = 56.8 ± 0.8
σ = 501
t-plot = 111

TPOL-240(air)

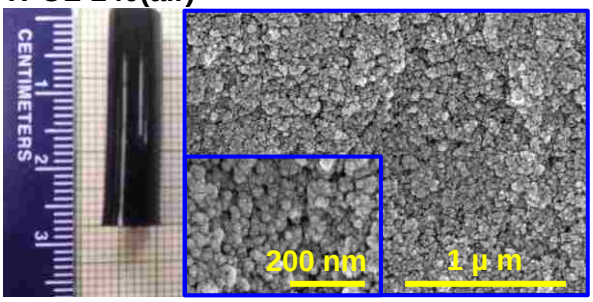

shrinkage = 46.1 ± 0.6%
ρ_b = 0.743 ± 0.014
ρ_s = 1.538 ± 0.007
Π = 51.7 ± 1.0
σ = 200
t-plot = 22

C-TPOL-O-800

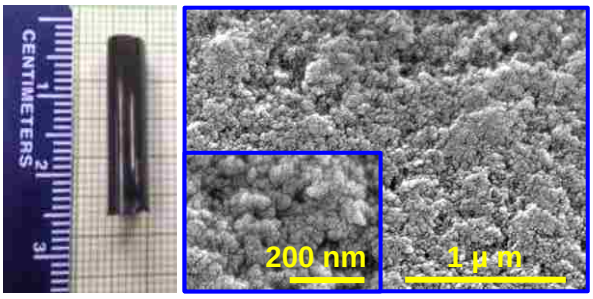

shrinkage = 52.8 ± 0.8%
ρ_b = 0.708 ± 0.039
ρ_s = 1.776 ± 0.007
Π = 60.1 ± 2.2
σ = 628 ± 46
t-plot = 349 ± 37

EC-TPOL-O-800

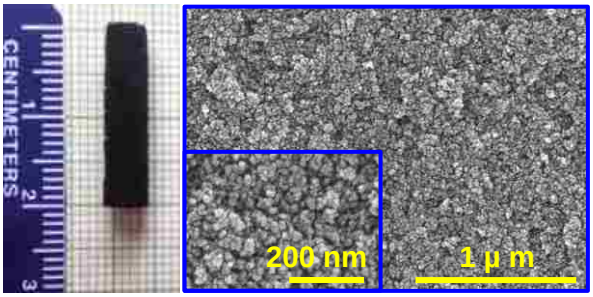

shrinkage = 60.2 ± 1.0%
ρ_b = 0.422 ± 0.054
ρ_s = 2.072 ± 0.008
Π = 79.6 ± 2.7
σ = 2568 ± 75
t-plot = 877 ± 48

shrinkage: with respect to mold
ρ_b: bulk density (g cm^{-3})
ρ_s: skeletal density (g cm^{-3})
Π: % porosity (v/v)
σ: total specific surface area (m^2 g^{-1})
t-plot: micropore surface area (m^2 g^{-1})

Figure 1.6. Summary of materials characterization data for TPOL aerogels as indicated. Samples remain monolithic throughout the pyrolysis steps.

Etching with CO_2 was also carried out on CAs from pyrolysis of polyamide-polyimide-polyurea random copolymers. The micropore surface areas of CAs after reactive etching were 4 × higher than their CAs parents, which resulted in an improved CO_2 adsorption capacity relevant to selective CO_2 sequestration applications.[72]

The same observations were made in the case of phenolic resin-based CAs. For example, in the case of TPOL samples, as shown in Figure 1.6, etching with CO_2 at 1000 °C increased the total surface area of CAs from 628 ± 48 to 2568 ± 75 m^2 g^{-1}. In addition, the micropore surface area increased from 349 ± 37 to 877 ± 48 m^2 g^{-1}, and micropore volumes doubled. Those samples are labeled as EC-TPOL-O-800.

1.4. CARBON AEROGELS IN CO_2 SEQUESTRATION AND GAS PURIFICATION

Industrial fuel gas emissions such as carbon dioxide (CO_2), methane (CH_4), nitrogen oxides (NO_x), carbon monoxide (CO), hydrocarbons, sulfur dioxide (SO_2), etc., have jeopardized human health, agricultural crops, and ecosystems by introducing greenhouse effect, resulting in the so-called global climate change.[73–75] As an example, burning of fossil fuels,[76,77] which supplies more than 85% of energy for industry, has contributed to the increase in the concentration of the greenhouse gases.[78] According to the EPA report on 2018, CO_2 is the source of over 76% of total greenhouse emissions, whereas CH_4 accounts to about 16%. Nitrous oxide (N_2O) contributes to about 6%, while other sources are responsible for near 2% of the global emission (Figure 1.7).[79] Consequently, the atmospheric CO_2 concentration has exceeded from the pre-industrial value of 280 ppm to nearly 405 ppm in 2018, and that of CH_4 has also doubled.[80]

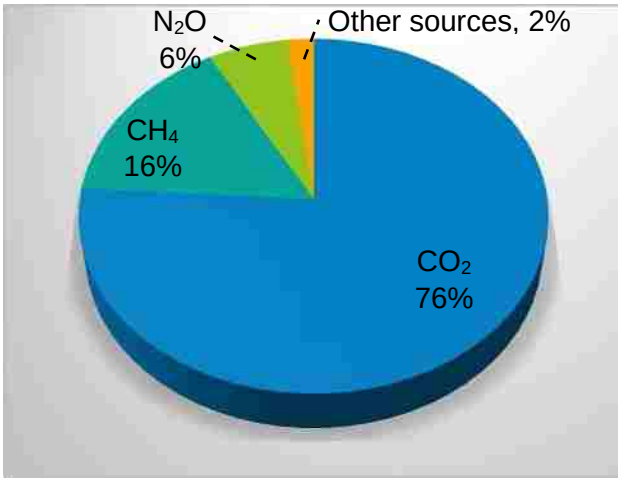

Figure 1.7. Contributions of the main greenhouse gas emissions in the atmosphere that have resulted in the global climate change.

1.4.1. Background. Developing renewable and clean energy technologies using hydrogen and methane seems to reduce the dependence on employing traditional energy sources.[80c] Alternatively, carbon capture and storage, or carbon capture and sequestration, or carbon control and sequestration (referred to as CCS) has been considered as an optional approach to reduce CO_2 concentration, which contributes significantly to global warming. CCS has attracted the most attention in which solid sorbents play an important role.[76] The term CCS is used to describe the process that captures CO_2 emission from large scale sources, such as power plants, storing and disposing it so that it will not return to the atmosphere.[78,81,82] Three viable techniques currently being investigated in CCS in large-point sources e.g., power plants include: 1) pre-combustion capture, 2) post-combustion capture, and 3) oxyfuel combustion.[76,78,83] Pre- and post-combustion processes have different technical and operational conditions. In the case of pre-combustion capture, CO_2 is separated from either CH_4 or H_2 at elevated temperatures,

e.g., 40 bars, and a temperature of around 40 °C, while for post-combustion process, CO_2 is captured from mostly N_2 at around atmospheric pressure and temperatures of 40–80 °C using chemical solvents.[75] In oxyfuel combustion, coal or gas in denitrified air is burned to yield only CO_2 and water.[78]

1.4.2. Solid CO_2 Sorbents. To date, three main technologies used to separate CO_2 from its emission sources include: the use of scrubbing solution, solid sorbents, and membranes. Among those, solid sorbents have been widely investigated recently in post-combustion method. The advantage of solid sorbents over other materials is that they are used in a larger temperature range and therefore yield less waste during cycling and also can be disposed without special environmental precautions.[76] For low-temperature applications various solid sorbents with different chemical compositions have been proposed. Those sorbents are primarily classified into two main classes of materials: traditional porous sorbents (i.e., activated carbon and zeolites) and novel polymer-based materials, which have attracted tremendous interest in the literature over the last few decades. Carbon-based materials, because of their low cost, high surface area, high amenability to pore structure modification and surface functionalization, and facile regeneration are among the most promising gas sorbents. For example, activated carbons have been used as filter materials in separation of gases or liquids; hence the term "carbon filter process (CFP)" has been widely used.[54] However, because of their weak interaction with CO_2, their uptake drops dramatically at elevated temperatures associated with postcombustion methods.[84] In contrast, polymer-based adsorbents, in addition to high surface area, possess synthetic diversity, light weight, and high thermal stability.[85] Most notable novel polymeric materials that have been proposed for atmospheric gas

sorption so far are: metal organic frameworks (MOFs),[86] hyper crosslinked polymers (HCPs),[87] conjugated microporous polymers (CMPs),[88] polymers with intrinsic microporosity (PIMs),[89] porous aromatic frameworks (PAFs),[90] covalent organic polymers (COPs),[91] covalent triazine-based frameworks (CTFs),[92] microporous organic polymers (MOPs),[93] porous polymer frameworks (PPFs),[94] and benzimidazol-linked polymers (BILPs).[95]

CAs have recently attracted attention in the literature for CCS in addition to their other energy-related applications.[54,72] They leverage the set of properties offered by each polymer- and carbon-based materials including: high surface area, hierarchical porosity, high thermal stability, tunable surface area and pore size, synthetic diversity, and ability to synthesize carbon materials with defined morphology in contrast to traditional porous carbons such as carbon blacks.[53] In addition, their wide flexibility of operation, e.g., preparation in various forms such as powders, films, composites, and monoliths has enabled them to emerge as a platform for a wide variety of novel technological applications.

Establishing a definite explanation for the CO_2 capture performance of solid sorbents based on their pore characteristics (size and shapes) and heteroatom functionality seems to be critical in designing a superior material for CCS applications. Different strategies have been proposed to increase the gas uptake in those sorbents including: 1) increasing surface area of the material, 2) increasing the average adsorbent-adsorbate interaction energy, and 3) tuning pore size, structure and particle shape to provide a preferential adsorption of a gas over others (referred to as selectivity), 4) surface modification via N-doping, amine modification, oxidation, fluorination, etc., and

5) synthesis of porous hybrid materials. Although high uptake is desired for designing a superior gas adsorbent, high selective adsorption of a gas over others is also required for practical applications, which is still a challenging research topic.[75,76]

The gas adsorption behavior of phenolic resin-derived monolithic carbon aerogels (C-RES) and their etched carbons (EC-RES) at temperatures and pressures close to the post-combustion process are fully investigated in Paper II of this dissertation. The results are compared in detail with carbons and reactivated carbons obtained from two nitrogen containing materials: PBO aerogels prepared via the acid-catalyzed route at room temperature,[31] and a random copolymer of polyamide, polyurea, and polyimide (PA) from the reaction of triisocyanate (tris(4-isocyanatophenyl) methane) (TIPM) with pyromellitic acid (PMA).[72] Choosing these materials allowed for a thorough investigation of their CO_2 uptakes qualitatively based on different chemical compositions and surface functionality (oxygen, nitrogen, and their derivatives ($-O^+$, $-O^-$, $-N^+$)) and quantitatively by comparing the adsorbent-adsorbate interactions from calculated heats of adsorption. Their advantage over other polymeric or carbon-based sorbents include the use of inexpensive monomers at room temperature without the need of a catalyst, in comparison to other polymers that require expensive catalyst. They are also stable at room temperature and are not as sensitive as MOFs to moisture.[96] An outstanding CO_2 uptake of 14.8 ± 3.9 mmol/g at 273 K and 1 bar is reported for low density reactivated resorcinol-formaldehyde carbon aerogel (EC-RF), which is higher than that of all porous CO_2 sorbents reported so far under the same conditions. That is attributed to the energy-neutral reaction of surface phenoxide ($C–O^-$) with CO_2 beyond monolayer coverage of micropores.

PAPER

I. AIR-OXIDATION OF PHENOLIC RESIN AEROGELS: BACKBONE REORGANIZATION, FORMATION OF RING-FUSED PYRYLIUM CATIONS, AND THE EFFECT ON MICROPOROUS CARBONS WITH ENHANCED SURFACE AREAS

Hojat Majedi Far, Suraj Donthula, Tahereh Taghvaee, Adnan Malik Saeed, Zachary Garr, Chariklia Sotiriou-Leventis* and Nicholas Leventis*

Department of Chemistry, Missouri University of Science and Technology, Rolla, MO 65409, U.S.A. *Correspondence: Tel.: 573-341-4391 (NL) 573-341-4353 (CSL). E-mail: leventis@mst.edu, cslevent@mst.edu

ABSTRACT

This paper is a thorough investigation of the chemical transformations during pyrolytic conversion of phenolic resins to carbons, and reports that all carbons obtained from main-stream phenolic resins including phloroglucinol-formaldehyde (**FPOL**), phloroglucinol-terephthalaldehyde (**TPOL**), resorcinol-formaldehyde (**RF**), and phenol-formaldehyde (**PF**) contain fused pyrylium rings and charge-compensating phenoxides. Those four phenolic resins were prepared via a fast HCl-catalyzed process as low-density nanostructured solids classified as aerogels, which, owing to their open porosity, allowed air circulation through their bulk. In that regard, the first step of this study was the air-oxidation of those phenolic resin aerogels at 240 ^{o}C. In **FPOL** and **TPOL** aerogels, that

air-oxidation step kicked off a cascade of reactions leading to ring-fusion aromatization and formation of pyrylium O^+-heteroaromatic rings in every repeat unit of the polymeric backbone. Despite the complexity of the process, those structural forms were well-defined, and were retained through pyrolytic carbonization (800 ^oC). Under the same conditions (240 ^oC/air), **RF** and **PF** aerogels did not undergo aromatization; instead, they just went through an autoxidation-like process that converted the $–CH_2–$ bridges between phenolic moieties into carbonyls (C=O). Importantly, however, upon further stepwise pyrolysis under Ar, by 600 ^oC all four systems (**TPOL**, **FPOL**, **RF** and **PF**), *irrespective* of whether they had been previously oxidized or not, converged to a common chemical composition. Thereby, carbon produced by pyrolysis of phenolic resins at 800 ^oC always contains fused pyrylium rings. All chemical analysis relied on FTIR, solid-state ^{13}C NMR, XPS and CHN analysis. The only and significant difference made by the low-temperature (240 ^oC) air-oxidation step was identified with the surface areas of carbons from aromatizable systems (**TPOL** and **FPOL**), which were higher than those from direct pyrolysis of as-prepared aerogels. Upon further reactive etching with CO_2, those surface areas went as high as 2778 ± 209 $m^2\ g^{-1}$. Those findings are directly relevant to high surface area carbons for gas sorption (e.g., capture and sequestration of CO_2) and ion exchange materials.

Air-oxidation at 240 ^oC, followed by pyrolytic carbonization, revealed that carbons from phenolic resins contain fused pyrylium rings and phenoxides.

TOC Graphic

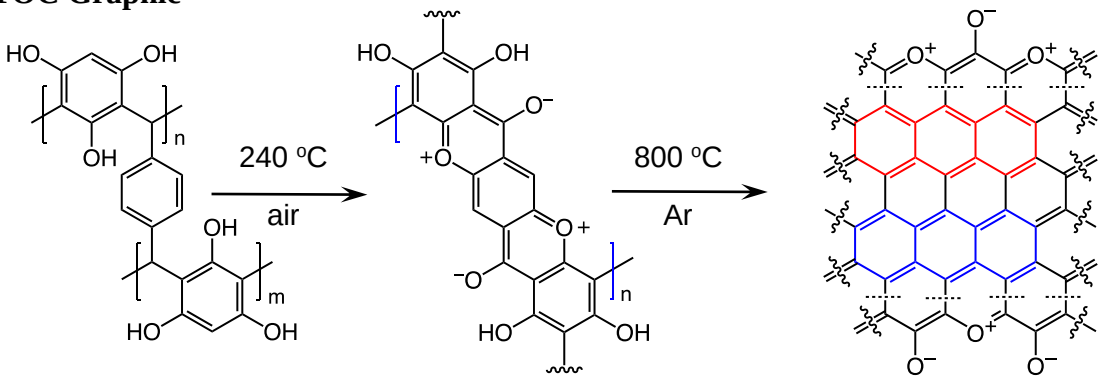

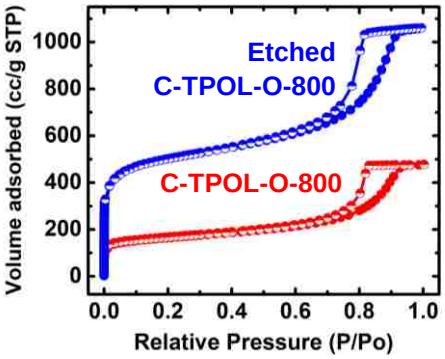

1. INTRODUCTION

Phenolic resins are the condensation product of phenol or phenol derivatives with formaldehyde.[1,2] If the reaction is run under sol-gel conditions, the reaction mixture turns into a gel, and if the pore-filling solvent is converted into a supercritical fluid that is vented off as a gas, phenolic resins take the form of highly porous, low-density, high surface area solids, classified as aerogels.[3,4] Pyrolysis of phenolic resin aerogels under inert atmosphere, and most notably those of resorcinol-formaldehyde (RF),[5–7] has been the primary source of carbon aerogels and xerogels.[8–10]

It is known that the high open porosity of aerogels allows gasses to diffuse through their bulk with near open-air rates.[11,12] That property is utilized in this report by

inserting an air-oxidation step at the early stages of pyrolysis (<250 ºC) of phenolic resin aerogels, and it is reported that certain of those materials undergo complete backbone aromatization yielding fused O^+-heteroaromatic pyrylium rings along their entire skeletal framework. Subsequently, by using those fully characterized fused aromatic ring systems as a new point of departure, it was found that *all* high-temperature (>600 ºC) pyrolysis products of mainstream phenolic resins include fused aromatic pyrylium rings, even without prior lower-temperature air-oxidation. However, phenolic aerogels that undergo air-oxidation-induced ring-fusion aromatization at lower temperatures, show a significant enhancement in the surface area of their carbons.

The impetus of this work stems from the pyrolytic carbonization of polyacrylonitrile (PAN), and of polybenzoxazines (PBOs). PAN is a linear polymer and the main source of graphite fiber for high performance fiber-matrix composites.[13,14] Direct pyrolysis of PAN under inert atmosphere leads to complete decomposition. Carbonization of PAN (yield: 70% w/w[15,16]) requires a prior air-oxidation step at 200-300 ºC that yields a new polymer consisting of a ladder-type structure with fused pyridine rings along its backbone.[17] Similarly, polybenzoxazines (PBOs) are a special type of phenolic resins with Mannich type bridges (–CH_2–N(R)–CH_2–) between phenolic rings, instead of the typical –CH_2– bridges in other phenolic resins.[18–20] PBOs are heat-resistant and are pursued as low-cost alternatives to polyimides. PBOs are also carbonizable, but curiously the carbon yield of PBO aerogels (up to 61% w/w) was much higher than that from PBOs in bulk form (27% w/w).[21] In analogy to PAN, the higher carbonization yield of PBO aerogels was traced to O_2-induced aromatization and formation of fused N^+-heteroaromatic pyridinium rings along the polymeric backbone.[22] It was concluded that

that process was facilitated by air circulating freely through the open porosity of PBO aerogels during a curing step up to 200 ^{o}C that, prior to that discovery, was thought only as necessary in order to complete polymerization of the benzoxazine monomer. The question then became whether oxidative ring-fusion aromatization could be forced upon more conventional phenolic resins, and if so, whether it would play a role in the carbonization process. That inquiry was pursued with aerogels derived from (Scheme 1) phenol (P), resorcinol (R) and phloroglucinol (POL) reacted

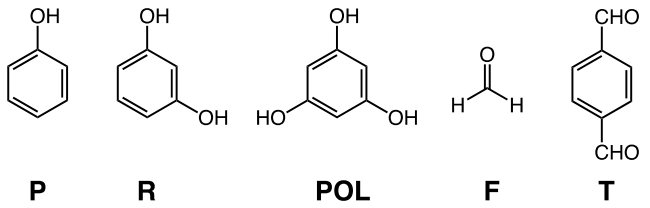

Scheme 1. The monomers of this study.

with formaldehyde (F), as well as with aerogels derived from POL reacted with terephthalaldehyde (T). Reflecting their chemical composition, those phenolic resin aerogels are abbreviated as **PF**, **RF**, **FPOL** and **TPOL**, respectively. Collectively, all those four types of resins in aerogel form are referred to as **RES**. Again, since the scope of this work was to explore chemical transformations in phenolic resins brought about by air-oxidation, working with **RES** was advantageous, because their open porosity allowed unobstructed air-circulation through their bulk. The chemical composition of the four model systems along pyrolysis was followed with XPS, solid-state ^{13}C NMR, FTIR and elemental analysis. The evolution of the skeletal framework and the pore structure was followed with SEM, and N_2-sorption porosimetry. It was found that at 240 ^{o}C in air all

four **RES** were oxidized, however only the two POL-systems, **FPOL** and **TPOL**, proceeded further to ring-fusion aromatization. Upon further pyrolysis under Ar, the chemical compositions of *all* four **RES**, either as-prepared, or after air-oxidation at 240 ^{o}C, converged at around 600 ^{o}C to a common chemical composition bearing two types of O: pyrylium O^{+}, and charge compensating phenoxide O^{-}. It was found that carbon aerogels from the aromatized versions of **FPOL** and **TPOL** had higher BET surface areas than carbons from direct pyrolysis of **FPOL** and **TPOL**. That property was magnified by reactive etching with CO_2 at 1000 ^{o}C. Possible applications of those carbons include gas sorption and ion-exchange based separations.

2. RESULTS AND DISCUSSION

2.1. MATERIAL SYNTHESIS

Aerogel synthesis and subsequent processing is summarized in Scheme 2. Processing details are described in the Experimental section. The exact formulations are given in Table S.I.1 (ESI, Appendix I). The gelation of **TPOL**, **FPOL**, and **RF** was carried out at room temperature. **PF** gelled at 80 ^{o}C. In order to ensure crosslinking among polymeric chains, which is a necessary condition for phase separation of nanoparticles and formation of the aerogel network,[23] the phenolic monomer-to-formaldehyde ratio for **PF**, **RF** and **FPOL** was set at 1:2 mol/mol. On the other hand, since T bears two –CHO groups, it can play the role of the crosslinker itself, thus the POL:T mol ratio was set at 2:1. All gelation reactions were catalyzed with aq. HCl. Using Kanatzidis' work on phloroglucinol-terephthalaldehyde porous polymers as a point of departure,[24] gelation of **TPOL** was carried out in 1,4-dioxane using a 16% w/w sol.

FPOL and **PF** were also gelled from 1,4-dioxane sols. In order to use our previous developed time-efficient, HCl-catalyzed gelation of **RF** as a reference,[25] gelation of that system was carried out in CH_3CN using much less concentrated sols (3.3% w/w). The R:HCl mol/mol ratio was the same as before (8.4), and gelation at room temperature occurred in 2 h, consistent with our previous report.[25] However, HCl-catalysis of the **TPOL** and **FPOL** sols was more efficient: gelation occurred in 1 min and 10 min, respectively, with a much lower catalyst concentration (POL:HCl ≈ 109 mol/mol). On the contrary, HCl-catalyzed gelation of **PF** was slow:[26] using the same P:HCl mol/mol ratio as in **RF** (8.4), gelation took 24 h at 80 ^oC. All four wet-gels were aged, solvent-exchanged with acetone and were dried with liquid CO_2 taken out at the end as a supercritical fluid (SCF). Post synthesis, **RES** aerogels were separated into two groups: The first one was pyrolyzed at 240 ^oC under Ar and the resulting samples are referred to as **TPOL-240(Ar)**, **RF-240(Ar)**, etc. The second group was pyrolyzed at 240 ^oC under air, and the corresponding samples are referred to as **TPOL-240(air)**, **RF-240(air)**, etc. Collectively, the two groups are referred to as **RES-240(Ar)**, and **RES-240(air)**, respectively. Next, as-prepared **RES** and **RES-240(air)** were pyrolyzed under Ar at 300 ^oC, 400 ^oC, 500 ^oC, 600 ^oC, 700 ^oC and 800 ^oC, using fresh samples at every successive pyrolysis temperature. That is, samples that were pyrolysed at a given temperature, were characterized as will be described below, and were stowed; they were not pyrolyzed under Ar again at any other temperature. The samples from those pyrolytic experiments

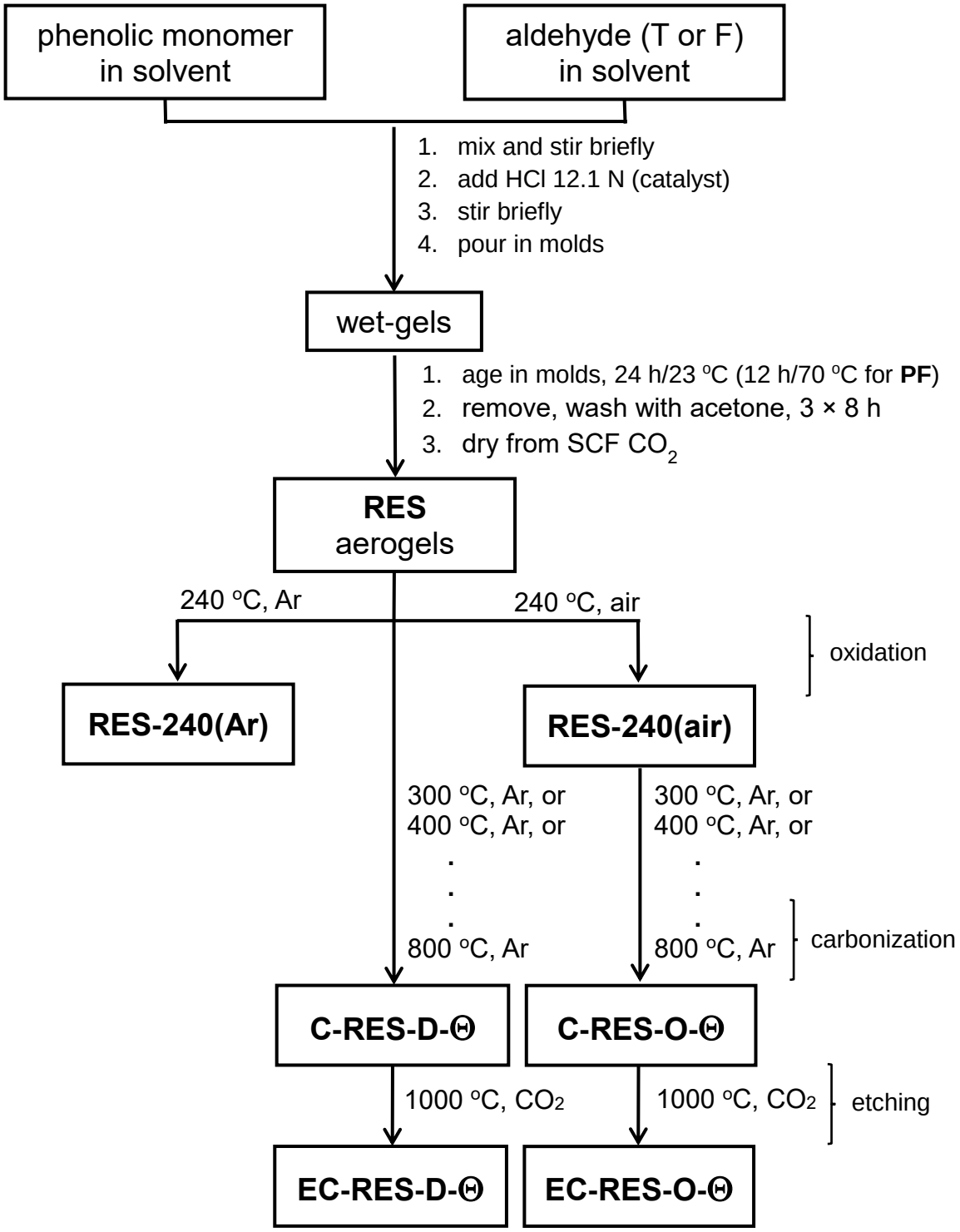

Scheme 2. Synthesis of acid-catalyzed phenolic aerogels (RES: TPOL, FPOL, RF, PF), air-oxidation, pyrolytic carbonization, and reactive etching. (D: Products from direct pyrolysis of as-prepared RES; O: Products from pyrolysis of oxidized samples: Θ: Pyrolysis temperature; C: Carbon; EC: etched carbon)

are abbreviated as **C-RES-D-Θ** and **C-RES-O-Θ**, where "C" stands as a reminder that those samples were obtained along carbonization; "D" stands for samples after Direct pyrolysis of as-prepared **RES**; "O" stands for samples obtained after prior Oxidation at 240 ^{o}C/air; and, "Θ" stands for the pyrolysis temperature. Finally, selected pyrolyzed samples, **C-RES-D-Θ** and **C-RES-O-Θ**, were subjected to reactive etching with CO_2 at 1000 ^{o}C, and are abbreviated as **EC-RES-D_**(or_**O)-Θ**, whereas "EC" stands for "etched carbon."

Certain key product yields along processing are cited in Table S.I.2 (ESI. Appendix I). First, the yields of the air-oxidation products were quite high (w/w): **TPOL-240(air)**, 90%; **FPOL-240(air)**, 74%; **RF-240(air)**, 82%; and, **PF-240(air)**, 100%. Next, the yields of the D route at the terminal pyrolytic temperature (800 ^{o}C) of this study were on average a little higher than the yields of the O route (% w/w vs. % w/w): **C-TPOL-D-800**/**C-TPOL-O-800**, 57/54; **C-FPOL-D-800**/**C-FPOL-O-800**, 54/50; **C-RF-D-800**/**C-RF-O-800**, 54/49; and, **C-PF-D-800**/**C-PF-O-800**, 61/49. However, by considering the errors in those yields (ESI, Table S.I.2), the definitive edge of the D-route in terms of carbonization yields was rather only with the **RF** and **PF** systems. It is noted further that the pyrolytic yields of **C-RES-O-Θ** declined only a little in the 300≤Θ≤600 ^{o}C range, compared with **C-RES-D-Θ**, whose yields declined steadily. This implies that the chemical changes brought about at 240 ^{o}C/air were stable for a few hundred ^{o}C afterwards. This point is important, because, as it will be shown in Section 2.3 below, above 600 ^{o}C, D and O processes converged chemically, thereby the chemical identity of the pyrolysis products at 240 ^{o}C/air dictates the common fate of all pyrolysis products afterwards.

2.2. PYROLYSIS PRODUCTS AT 240 ^{O}C/AIR VERSUS 240 ^{O}C/Ar

Differential scanning calorimetry (DSC) of the four **RES** up to 300 ^{o}C under N_2 showed no major heat exchanges. In air, however, all four **RES** showed strong exotherms with maxima in the 230–270 ^{o}C range (Figure 1 and ESI, Appendix II Figure S.II.1). Based on those data, quantitative pyrolysis of all as-prepared **RES** was carried out at 240 ^{o}C, as described above. Consistent with our previous findings with **RF**,[27] *all* **RES-240(Ar)** were chemically identical to as-prepared **RES** (see below). In contrast, **RES-240(air)** were chemically different from **RES**, and in fact they could be put in two groups: (a) **TPOL-240(air)** and **FPOL-240(air)**, and (b) **RF-240(air)** and **PF-240(air)**. Group (a), **TPOL-240(air)** and **FPOL-240(air)**, bore fused aromatic pyrylium ions on their polymeric backbones, Group (b) did not. Scheme 3 shows the structures of **RES** and **RES-240(air)** as inferred from the spectroscopic data below.

The FTIR spectra of all **RES-240(Ar)** (Figure 2 and ESI, Appendix III Figure S.III.1) were identical to those of as-prepared **RES**. On the other hand, while **RES-240(air)** retained at least some of the –OH groups of their parent **RES** (note the absorptions with maxima in the 3394–3436 cm^{-1} range), they also showed a new absorption in the 1723–1737 cm^{-1} range, which was assigned to C=O stretching, although those absorptions were not very strong by carbonyl standards. Pyrylium in-plane stretches were expected in the 1400–1650 cm^{-1} range,[28,29] which overlaps with the stretches of other aromatic rings, thereby that region was not interpretably useful. On the contrary, the region below 1000 cm^{-1} was quite informative, especially in the case of **TPOL-240(air)**. The OOP C-H bending at 833 cm^{-1} of the *para*-substituted ring of T,[30] which was clearly present in both **TPOL** and **TPOL-240(Ar)**, went missing from **TPOL-240(air)**, in

agreement with its involvement in a ring-fusion process (Scheme 3). Similarly, the out-of-plane C⋯⋯C bending[31,32] at 548 cm^{-1} was also missing from the oxidized product. In the latter region, the spectrum of **FPOL-240(air)** showed similar changes (see ESI, Figure S.III.1), consistent with ring fusion, while the spectra of **RF-240(air)** and **PF-240(air)** still showed the out-of-plane C⋯⋯C bending modes from isolated aromatic rings (see Figure 2 and ESI, Figure S.III.1).

XPS gave more direct evidence for the formation of pyrylium rings. O1s XPS spectra were obtained using compressed pellets made by mixing powders of the corresponding materials with Au dust (10% w/w), which dissipated electrostatic charges, and its $4f_{7/2}$ peak at 84.0 eV was used as an internal peak-position calibration standard. Three more compounds were also run in a similar fashion as external references: (a) 1-naphthol that gave a O1s peak from the phenolic –OH group at 531.97 eV; (b) sodium phenoxide that gave a O1s peak from the $–O^-$ group at 531.41 eV; and, (c) 2,6-diisopropyl-4-phenylpyrylium cation, which was available from other work in our laboratory,[33] and showed a O^+ peak at 534.26 eV. The O1s spectra of the three references are shown in ESI, Appendix IV Figure S.IV.1. The O1s XPS spectra of all as-prepared **RES** (Figure 3 and ESI, Appendic IV Figure S.IV.2) showed, as expected, the presence of only a single type of oxygen (with maxima in the 531.52-532.66 eV range), which was assigned to phenolic type –OH.[34–37] The XPS spectra of **TPOL-240(air)** and **FPOL-240(air)** showed three peaks: one at higher energies (533.62 eV and 535.24 eV, respectively), one more intense absorption in an intermediate energy range (532.64 eV and 533.45 eV, respectively), and one absorption at lower energies (531.39 eV and 531.61 eV, respectively). The intensity ratio of those three absorptions were 1:(1.4):1 in

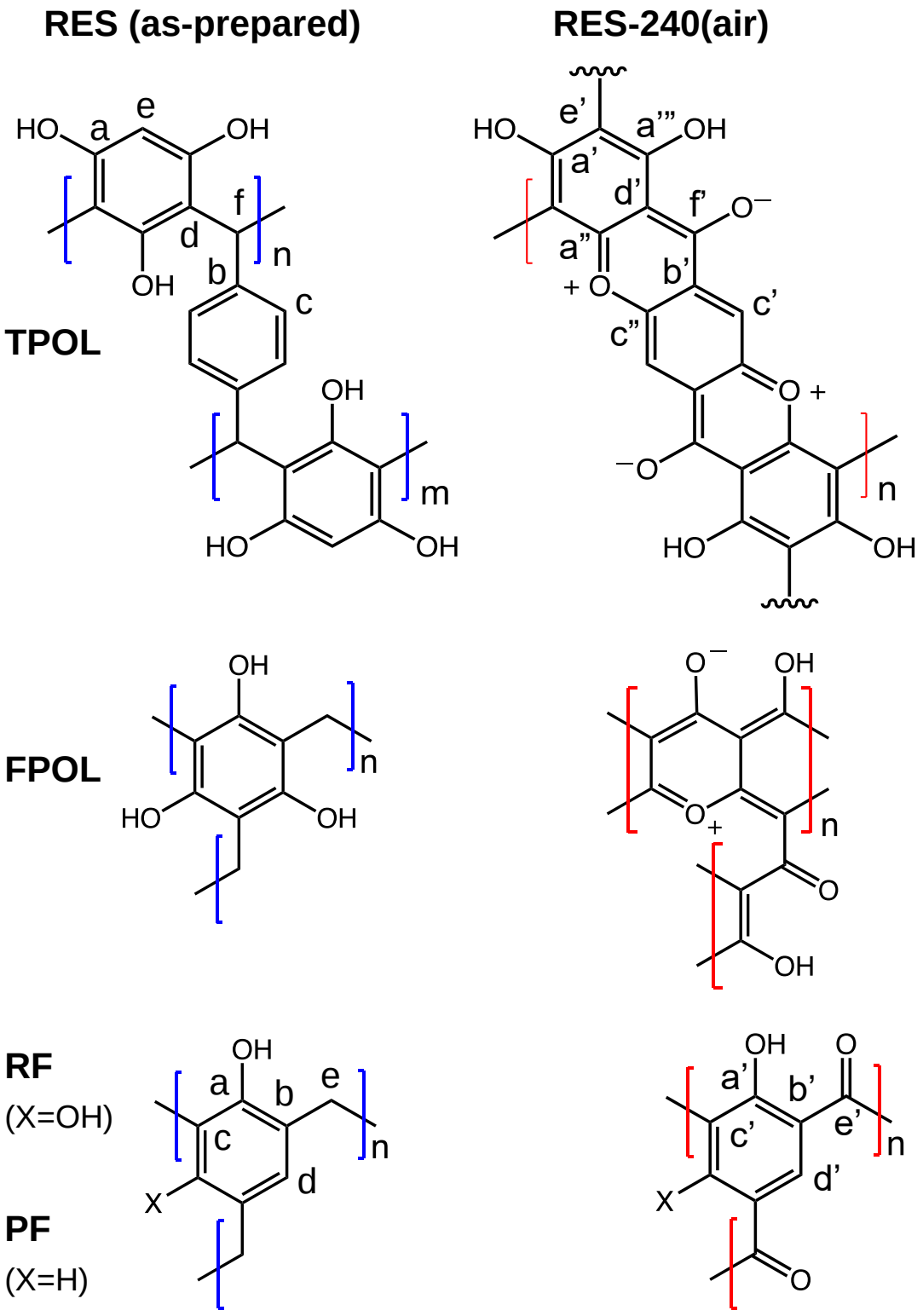

Scheme 3. Structures of as-prepared RES aerogels, and their air-oxidation products.

TPOL-240(air) and 1:(2.6):(1.3) in **FPOL-240(air)**. Based on literature values, and on direct comparison with the O1s XPS spectra of our three reference compounds (ESI, Figure S.IV.1), the high-energy absorptions of **TPOL-240(air)** and **FPOL-240(air)** were assigned to pyrylium O^+;[38] the intermediate range absorptions were assigned to phenolic type -OH;[34–37] and, the lower energy absorptions were assigned to $–O^–$,[39,40] perhaps overlapping with some C=O.[34–37] Importantly, each of the O1s XPS spectra of **RF-240(air)** and **PF-240(air)** consisted of only two absorptions, at 531.53/529.75 eV, and at 531.98/530.27 eV, respectively. Each of those high/low energy pairs were assigned to phenolic -OH and to C=O, and the relative ratios were 1.8 in **RF-240(air)** and 2.2 in **PF-240(air)**, i.e., they followed the trend of increasing phenolic –OH groups by going from **RF** to **PF**. Overall, the structures of Scheme 3 were all consistent with the O1s XPS data.

All solid-state CPMAS ^{13}C NMR spectra were run twice, once with a long cross-polarization (CP) contact time (3000 μs) and once with a shorter one (5 μs). The latter conditions forced carbons with no Hs to vanish. Figure 4A compares the spectra of **TPOL**, **TPOL-240(Ar)** and **TPOL-240(air)**; Figure 4B compares the spectra of **RF**, **RF-240(Ar)** and **RF-240(air)**. (Corresponding spectra for the **FPOL** and **PF** systems are shown in ESI, Appendix V Figure S.V.1, and they behaved pairwise similarly to the **TPOL** and **RF** systems, respectively.) For peak assignment refer to Scheme 3.

In agreement with DSC and FTIR, the ^{13}C NMR spectra of all **RES-240(Ar)** were similar to those of as-prepared **RES** aerogels. Using the aliphatic $\underline{C}H_2$ of the **RF** and **PF** as internal reference, the ratios of aromatic $\underline{C}$-H to $\underline{C}H_2$ in the as–prepared (and the 240 ^oC/Ar-treated samples) were approximately 0.5:1 and 1:1, respectively, consistent with the 1:2 stoichiometry of R (or P) and F in their sols. **FPOL** and **FPOL-240(Ar)** had no

aromatic C-H, as expected from complete reaction of F with POL at their 2:1 stoichiometric ratio in the sol. On the other hand, consistent with the T:POL stoichiometry in the sol, and the expected structure (Scheme 3) **TPOL** had only one type of aromatic C-H coming from POL (designated as "e") and only one type coming from T (designated as "c"). The aliphatic CH-to-"e"-to-"c" ratio was in the expected 1:1:2 value.

After pyrolysis at 240 ^{o}C/air, no **RES-240(air)** showed any surviving aliphatic carbons from the methylene or methyne bridges (–CH_2–, or –CH–) of the parent **RES**. All H-bearing aromatic carbons survived the oxidation process in both **RF-240(air)** and **PF-240(air)**, and the spectra of those two materials were similar to those of their parent **RES**, and most importantly to one another; in fact, in terms of chemical shifts the two spectra were almost identical (compare Figure 4B with ESI Figure S.V.1B). (It is noted in passing that the presence of two types of H-bearing aromatic carbons with about equal intensities in both **RF-240(air)** and **PF-240(air)**, –refer to the low contact-time CP spectra– is attributed to the random 2,2- and 2,4- connectivity in adjacent repeat units expected of the phenolic moieties along the main chain.[41]) Now, it is noted that in **PF-240(air)** some H-bearing aromatic carbons would have survived the oxidation process irrespective of ring-fusion aromatization, however, in **RF-240(air)** the *only* chance for aromatic H's to survive is when no ring-fusion aromatization takes place. The latter realization together with the similarity of the ^{13}C NMR, IR and XPS spectra of **RF-240(air)** and **PF-240(air)** render their structures similar to one another, and consistent with those shown in Scheme 3. On the contrary, as a result of ring-fusion aromatization the aromatic regions of **TPOL-240(air)** and **FPOL-240(air)** were more complicated than those of the corresponding as-prepared samples (Scheme 3). Based on the spectra of

FPOL and **FPOL-240(Ar)**, **FPOL-240(air)** was not expected and did not have any H-bearing carbons. On the other hand, the new broad downfield resonances of **TPOL-240(air)** at 189.5 and 174.2 ppm were assigned to the *ortho* (a´ and c´) and *para* (f´) carbons of the pyrylium ring, respectively. The *meta* carbons, d´ and b´, were expected significantly upfield, [42,43,44] and were assigned to the resonance at 97.9 ppm. Curiously, the only surviving Hs in **TPOL-240(air)** were those coming from T; that is, even the "e" carbon of as-prepared **TPOL** had lost its H, thereby fused-aromatic systems had to be head-to-tail connected to one another, as shown in Scheme 3. That type of connectivity was attributed to electrophilic aromatic substitution reactions of one polynuclear aromatic system to another - see next section and refer to Scheme 4C below.

2.3. THE MECHANISM OF RING-FUSION AROMATIZATION

The elementary processes during oxidation and ring-fusion aromatization are illustrated via the most complicated system of this study, **TPOL**, in Scheme 4. In **TPOL**, those processes take place in three stages. In Stage 1, bridging –CH– groups are converted to carbonyls following a route akin to autooxidation (Scheme 4A):[45,46] H-atom abstraction by O_2 is followed by addition of OOH groups at the benzylic positions; subsequently, homolytic cleavage of the O–OH bond and of the adjacent C-C bond yields H_2O_2, a carbonyl group at the previously bridging position, and a phenyl radical. In addition to creating carbonyls, that process breaks down the polymer chain at several places, and disrupts crosslinking. At that point, polymer chains are free to relax to new positions, in which phenyl radicals couple and establish a new crosslinked configuration that remains similar in terms of connectivity to, but is more compact than the original

TPOL. In Stage 2 (Scheme 4B), newly created carbonyl groups undergo 1,5-proton transfer tautomerization with the *ortho* OH groups of the POL moieties. In turn, tautomerized moieties undergo electrocyclic ring closure, to restore aromaticity. At that point, air (O_2) oxidizes the newly created ether bridges (–O– + O_2 ---> $–O^{\cdot+}–$ + $O_2^{\cdot-}$), and the byproduct of that oxidation (superoxide: $O_2^{\cdot-}$) acts as a Brønsted base, abstracts phenolic protons, and yields hydroperoxyl radicals ($HO_2^{\cdot}$). The latter abstract $H^{\cdot}$ atoms from the positions adjacent to $–O^{\cdot+}–$ and yield pyrylium rings.

FPOL goes through Stages 1 and 2, yielding ring-fusion aromatization to pyrylium in analogy to **TPOL** (see ESI, Appendix VI).

Based on the chemical characterization data of the previous section, **RF** and **PF** go through Stage 1, but oxidation stops there. It is noted, however, that in both of those systems the relative connectivity of at least one phenolic OH and the newly-formed bridging C=O is similar to that in **TPOL** and **FPOL**; thereby, in principle, both **RF** and **PF** could undergo 1,5-proton transfer tautomerization, and thus become ready for electrocyclic ring closure. Again, after ring closure, both of those systems should be able to continue along the reaction pathways of Stage 2 with $O_2^{\cdot-}$ and $HO_2^{\cdot-}$. But, they do not. It is speculated that Stage-1 oxidized **PF** and **RF** were unable to yield pyrylium, because the rings were not activated enough to undergo electrocyclic ring closure. On the contrary, the three OH groups of **FPOL** accommodate the loss of aromaticity involved with electrocyclic ring closure to the point that it is not very disfavored. A similar rationale holds true for **TPOL**.

Finally, **TPOL**, as opposed to **FPOL**, possesses hydrogen atoms in the “e” positions and continues with Stage 3, in which the tip of one fused aromatic system

undergoes an electrophilic aromatic substitution with another (Scheme 4C). Elemental analysis of **TPOL-240(air)** gave (% w/w): C: 64.71±0.16; H: 1.71±0.34; O: 33.26±0.07. (The %O was calculated via 100-(%C+%H).) The theoretical elemental composition calculated from the repeat unit shown in Scheme 3 (i.e., the end-product of Stage 3, Scheme 4C) was (% w/w): C: 64.2; H: 1.6; O: 34.2. The agreement between the experimental and theoretical elemental compositions is considered remarkable given the complexity of the processes and the fact that no "purification" of the pyrolysis products was possible in the conventional synthetic organic sense. It is noted further that if oxidation of **TPOL** had stopped at the end of Stage 2, the expected elemental composition would have been (% w/w): C: 63.8; H: 2.13; O: 34.0, i.e., markedly different from the experimental results.

2.4. CHEMICAL TRANSFORMATIONS ALONG FURTHER PYROLYSIS OF RES-240(AIR) VERSUS RES

The materials from the 240 ^{o}C/air oxidation process were used for further investigation along pyrolysis of **RES**. For that, as-prepared, as well as 240 ^{o}C/air-treated aerogels (**RES** and **RES-240(air)**, respectively) were pyrolyzed at 100 ^{o}C intervals, starting from 300 ^{o}C and ending at 800 ^{o}C (Scheme 2). At every pyrolysis temperature, we used fresh **RES** or **RES-240(air)** samples, as described in Section 2.1 above. The pyrolysis products are referred to as **C-RES-D**(or_**O**)-**Θ**. The evolution of the chemical composition was monitored with elemental analysis, solid-state ^{13}C NMR and FTIR. **C-RES-O-800** and **C-RES-D-800** were also characterized with XPS. Figure 5 shows the elemental analysis data of all four systems along pyrolysis. Dashed lines follow the pyrolytic evolution of the 240 ^{o}C/air oxidized samples (**RES-240(air)**); solid lines follow

the direct pyrolysis of as-prepared **RES**. All samples were analyzed three times, and in most cases error bars (one standard deviation) were within the respective symbols. The percent amount of oxygen was calculated via %O = 100 – (%C + %H). Relative to **RES**

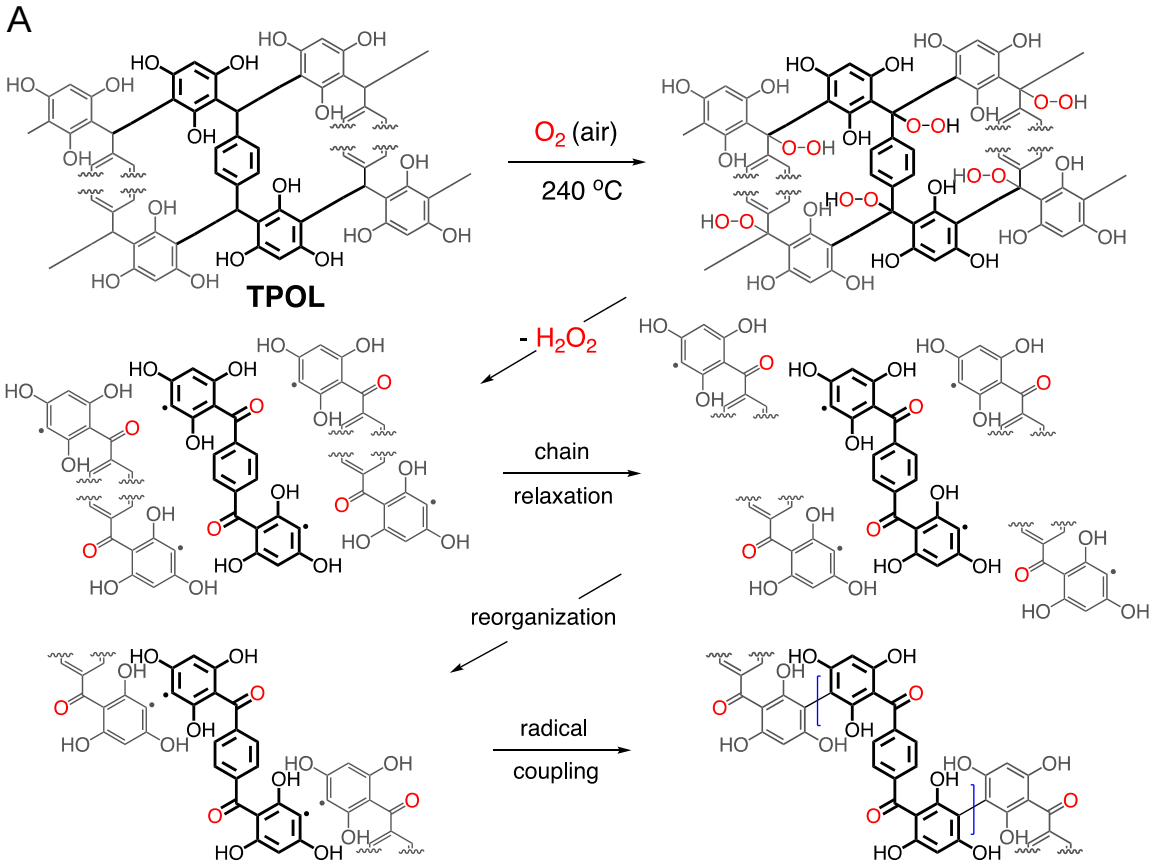

Scheme 4. Oxidation mechanism of RES demonstrated with TPOL, A. Stage 1: Initial oxidation leading to carbonyl group formation and change in connectivity along the polymer chain (Repeat unit shown in bold; adjacent units included in order to show connectivity.), B. Stage 2: Further oxidation and ring fusion aromatization (The Dewar-benzene-like canonical form in the first step was used for brevity.), C. Stage 3: Interchain coupling at the e'-positions of two adjacent repeat units.

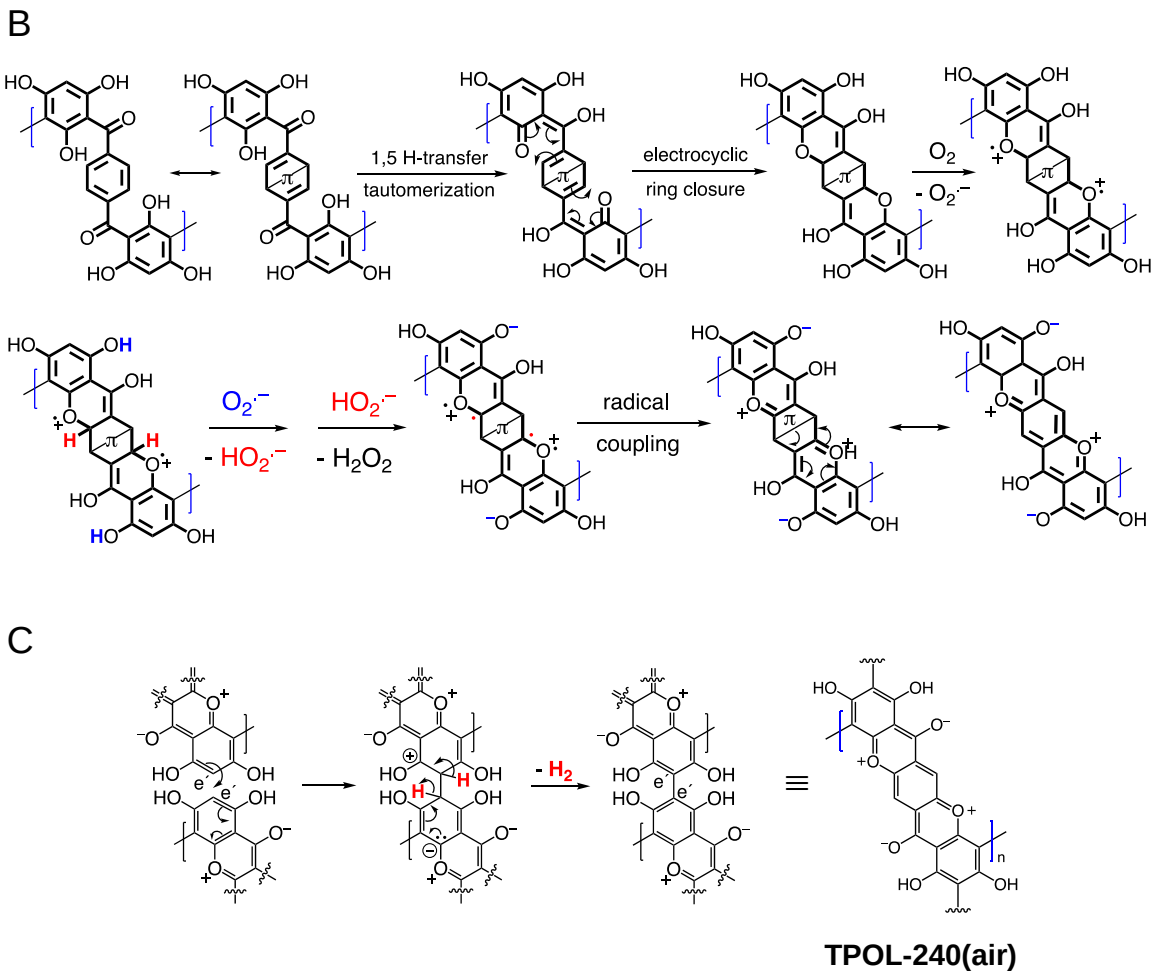

Scheme 4. Oxidation mechanism of RES demonstrated with TPOL, A. Stage 1: Initial oxidation leading to carbonyl group formation and change in connectivity along the polymer chain (Repeat unit shown in bold; adjacent units included in order to show connectivity.), B. Stage 2: Further oxidation and ring fusion aromatization (The Dewar-benzene-like canonical form in the first step was used for brevity.), C. Stage 3: Interchain coupling at the e'-positions of two adjacent repeat units. (Cont.)

and **RES-240(Ar)**, all **RES-240(air)** were deficient in H and richer in O, as expected. Between 300 ^{o}C and 500 ^{o}C **RES-240(air)** lost only a little additional H, while the amount of H in **RES** kept on decreasing steadily. At $\Theta \geq 600$ ^{o}C the C, H and O curves of

each **C-RES-D-Θ** / **C-RES-O-Θ** pair converged – practically coincided. By 800 ºC, *all eight materials*, independent of their **RES**-origin or the route (D or O), had produced carbons with the same, within error, CHO composition (C: 91.8 ± 1.8 % w/w; H: 0.64 ± 0.40 % w/w; O: 7.2 ± 1.7 % w/w; errors are spreads of triplicate analysis). The common chemical features of the converging structures were investigated with solid-state ^{13}C NMR and IR. The fate of oxygen was investigated with XRS.

Figures 6A and 6B show the CPMAS ^{13}C NMR spectra along the pyrolytic evolution of the **TPOL**/**TPOL-240(air)**, and the **RF**/**RF-240(air)** pair, respectively. Corresponding spectra for the **FPOL**/**FPOL-240(air)** and the **PF**/**PF-240(air)** pairs are shown in ESI, Appendix V Figure S.V.2. It is noted that the changes in the 300–600 ºC range in all four **RES-240(air)** were not as drastic as the changes observed after pyrolysis of the corresponding as-prepared **RES**. That suggests that the 240 ºC/air process accelerated the chemical changes that otherwise took place more progressively in the conventional pyrolytic carbonization of **RES** under inert atmosphere. Consistent with the elemental analysis data, by Θ=600 ºC the ^{13}C NMR spectra of *every* **C-RES-D-Θ** / **C-RES-O-Θ** pair had converged to a common spectrum. More importantly though, by Θ=600 ºC, spectra became identical not only pairwise, but in fact *all eight* spectra, independent of their **RES**-origin or the route (D or O), were also identical to one another. Similar observations were made from the evolution of the FTIR spectra showing again that the spectra of all **C-RES-D**(or_**O**)**-Θ** pairs became identical by 500 ºC or 600 ºC, depending on the **RES** (see ESI, Appendix III Figures S.III.2A-S.III.2D). At 800 ºC, the common FTIR spectrum of all eight **C-RES-D**(or_**O**)**-800** was quite simple, showing only two major absorptions at around 3396 cm^{-1} and 1619–1630 cm^{-1}.

Finally, Figure 7 shows and compares the high-resolution O1s XPS spectra of **C-TPOL-D**(and_**O**)-**800** (top) and of **C-RF-D**(and_**O**)-**800** (bottom). (The corresponding spectra of **C-FPOL-D**(and_**O**)-**800** and of **C-RF-D**(and_**O**)-**800** are shown in ESI, Appendix IV Figure S.IV.3.) The spectra of all eight **C-RES-D-800** and **C-RES-O-800** materials showed just two absorptions: one at 533.01–533.17 eV, which is consistent with the presence of pyrylium-type O^+, and a second one of similar intensity at 531.28–531.69 eV, corresponding to charge compensating O^-. (Please refer to the controls shown in ESI, Figure S.IV.1.) A common idealized structure for all pyrolysis products at 800 °C has been drawn by analogy to the structure of polyacrylonitrile-derived carbon at the same temperature range,[47–49] and is shown in Scheme 5. The fused aromatic ring core of the graphitic sheets is made up of "aromatic repeat layers." For example, the core of the structure of Scheme 5 consists of two such aromatic repeat layers color-coded in red and blue. Based on the average amount of O in all **RES**-derived carbons (7.2 ± 1.7 % w/w),

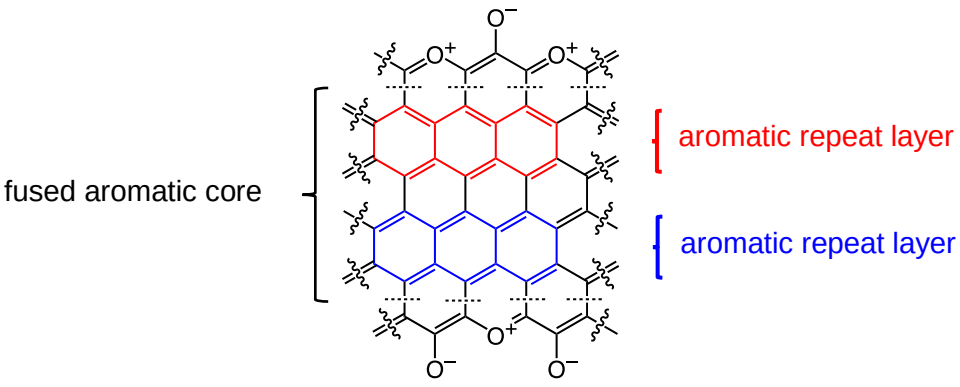

Scheme 5. Idealized structure of carbons derived from pyrolysis of RES at 800 °C showing two repeat layers of the graphitic core, one in red, one in blue.

it is calculated that on average the graphitic core of all **C-RES-D**(or_**O**)-**800** materials consisted of 6.5 aromatic repeat layers.

In summary, air-oxidation of **TPOL** and **FPOL** gave two well-defined products (**TPOL-240(air)** and **FPOL-240(air)** – Scheme 3) with extensive ring-fusion aromatization along their backbone that survived for several hundred ^{o}C afterwards. Second, all pyrolyzed carbons converged to a common chemical composition irrespective of: (a) the starting phenolic system, (b) whether we inserted an early oxidation step in the carbonization process, or (c) whether the particular phenolic system undergoes ring-fusion aromatization (**TPOL** and **FPOL**), or just a simple oxidation of the $–CH_2–$ bridges (case of **RF** and **PF**). By considering those points together, we have concluded that ring-fusion aromatization, with formation of pyrylium and charge compensating phenoxides, is the common converging point along pyrolysis of all four main-stream phenolic resins of this study. Reasoning by analogy, we speculate that this is the common converging point along carbonization of all phenolic resins. The question then became whether low-temperature oxidative aromatization was of any practical use, namely whether it makes *any* difference in the properties of the resulting carbons. That is discussed in the next section, in conjunction with the evolution of the material properties along carbonization, and high-temperature reactive etching with CO_2.

2.5. THE EVOLUTION OF MATERIAL PROPERTIES ALONG PYROLYTIC CARBONIZATION AND REACTIVE ETCHING

Bulk properties of interest include linear shrinkage, bulk density and porosity. Representative data exemplified with **TPOL** and **RF** are shown in Figure 8. Tables with primary materials characterization data along pyrolysis and reactive etching are given in

ESI, Appendix VII. Cumulative plots of shrinkage, bulk density and porosity along pyrolysis of all four **RES** are given in ESI, Appendix VIII.

Figures 8A and 8B show photographs of as-prepared **TPOL** and **RF**, after Ar or air treatment at 240 ^{o}C, after carbonization at 800 ^{o}C, and finally after reactive etching at 1000 ^{o}C. At all stages of pyrolysis, samples shrunk relative to the as-prepared materials, but remained monolithic. The relative linear shrinkage was quantified by the bar graphs shown next to the photographs. Most of the shrinkage occurred during aerogel preparation: both **TPOL** and **RF** shrunk 32–34% relative to the molds. Treatment at 240 ^{o}C/Ar caused only a small additional shrinkage: 6% for **TPOL**, 10% for **RF**. Air-oxidation at 240 ^{o}C (yellow bars) caused an additional shrinkage relative to **TPOL-240(Ar)** and **RF-240(Ar)** (7.5%, and 12.8%, respectively) – by that point, the cumulative shrinkage is clearly noticeable in the photographs. Beyond that point, i.e., from 300 ^{o}C to 800 ^{o}C, samples either by direct (D) pyrolysis of **TPOL** and **RF** (red bars), or by pyrolysis of their 240 ^{o}C/air oxidized (O) derivatives (blue bars) kept on shrinking more with increasing pyrolysis temperature, preserving though, for the most part, the higher shrinkage caused by the 240 ^{o}C/air oxidation step (yellow bars). Reactive etching at 1000 ^{o}C/CO_2 was conducted for all samples pyrolyzed at $\Theta \geq 600$ ^{o}C, and it caused only a small additional shrinkage relative to the respective parent carbons; said additional shrinkage is shown in Figure 8 with shaded segments on top of the regular pyrolysis bars. Thus, for example, considering samples from the terminal pyrolysis temperature of this study (i.e., at Θ=800 ^{o}C) the total shrinkage (from the molds) of **EC-TPOL-O-800** was 60.2 ± 1.0 % (vs. 52.8 ± 0.8 % for **C-TPOL-O-800**), while **EC-TPOL-D-800** shrunk less: 54.4 ± 0.4 % (vs. 53.4 ± 0.1 % for **C-TPOL-D-800**). Similarly, **EC-RF-O-800** shrunk 68.6 ± 1.1%

(vs. 66.8 ± 0.7% **C-RF-O-800**), while **EC-RF-D-800** shrunk again less: 59.1 ± 0.2% (vs. 56.2 ± 0.5% for **C-RF-D-800**). The shrinkage of the two remaining systems, **FPOL** and **PF**, followed the same trends as a function of the pyrolysis temperature (Θ) as **TPOL** and **RF** (see ESI, Figure S.VIII.1).

Reflecting the lower concentration of its sol, as-prepared **RF** was less dense (0.160 ± 0.006 g cm^{-3}) than **TPOL**, **FPOL** and **PF** (0.45–0.60 g cm^{-3}). That trend followed the samples throughout pyrolysis, except reactive etching. Now, within each **RES**, the bulk densities, ρ_b, of all pyrolysis products were higher than those of the as-prepared samples. Upon closer inspection of ESI, Figure S.VIII.2, in general ρ_b did *not* follow the upward trend observed with shrinkage as a function of Θ. Instead, the ρ_b of all **C-RES-O-Θ** varied randomly within narrow zones throughout the pyrolysis range. At Θ≤500 °C, the density of **C-TPOL-O-Θ** was slightly higher than the density of the D samples, but that trend got reversed at Θ≥600 °C (Figure 8A). Along pyrolysis of **FPOL**, **PF** and **RF** the densities of the O samples were always higher than the densities of the D samples, and remained near the levels attained at 240 °C/air (ESI, Figure S.VIII.2). In **FPOL** and **PF** in particular, the densities of the D samples kept on increasing with Θ, and by 800 °C the densities of the O and D samples had converged; on the other hand, no upward trend was noted in the densities of **C-RF-D-Θ** with Θ, thereby **C-RF-O-800** remained more dense than **C-RF-D-800** (Figure 8B). Probably reflecting a more significant percent mass loss (see pyrolytic yields in ESI, Tables S.I.2-S.I.5) than the small additional shrinkage during reactive etching, the densities of all etched samples were always lower than their parent carbons (notice the shorter shaded segments in the respective bars of Figure 8). In particular, the densities of **EC-RF-O-800** and **EC-TPOL-**

O-800 were nearly 50% lower than those of **C-RF-O-800** and **C-TPOL-O-800**. For **EC-FPOL-D**(or_**O)-800** and **EC-PF-D**(or_**O)-800**, the density difference from the corresponding C-samples was smaller, around 15–20%.

Percent open porosities, Π, were calculated from the bulk (ρ_b) and skeletal densities (ρ_s) via $\Pi = (\rho_s - \rho_b)/\rho_s$. Skeletal densities are tabulated in ESI, Appendix VII and are compared to one another in graph form in ESI, Appendix VIII Figure S.VIII.3. ρ_s-Values followed a common trend among all four **RES**: up to 500 ^oC, the ρ_s values of the O samples were higher than the ρ_s values of the D samples, then the two sets became equal and increased together from 1.2–1.3 g cm^{-3} to about 1.75–2.0 g cm^{-3} by 800 ^oC. Upon reactive etching, all ρ_s values increased again, moving in the 2.0–2.25 g cm^{-3} range. The last increase could be associated with closed micropores present in **C-RES-D**(or_**O**)-**Θ** that became accessible after etching. Closed porosity notwithstanding, along carbonization, open porosities, both with respect to one another, and within each **RES**, followed the expected general trend established by ρ_b (see Figure 8 and ESI, Figure S.VIII.4). Reflecting mass loss in excess of differential shrinkage, by going from the C- to the EC-materials, porosities increased, most dramatically in the **TPOL** samples (Figure 8A). Thus, although the porosities of the 800 ^oC-pyrolyzed D and O varieties of **TPOL**, **FPOL** and **PF** were all around 60% v/v, after reactive etching the porosities of **EC-FPOL-D**(or_**O**)**-800** and **EC-PF-D**(or_**O**)**-800** moved up in the 70–80% v/v range, while **EC-TPOL-D**(or_**O**)**-800** moved above the 80% v/v mark. (Owing, as discussed, to the lower starting density of **RF**, the porosities of **C-RF-D**(or_**O**)**-800** were already in the 83–87% v/v range, and the porosities of **EC-RF-D**(or_**O**)**-800**) moved up in the 92–93% v/v range.)

Despite all the preceding analysis, there was no aspect of the macroscopic material properties that could be clearly and uniquely identified with the early ring fusion aromatization process that takes place in the **TPOL** and **FPOL** systems. The closest we came to such a difference with oxidized systems was the large drop in the bulk density and the simultaneous increase in porosity by going from **C-TPOL-O-800** to **EC-TPOL-O-800**. However, that behavior was not observed in the **FPOL** system that also undergoes early ring fusion aromatization, and most importantly, even within the **TPOL** system itself, a similar drop in density and increase in porosity was also observed within the **C-TPOL-D-800** / **EC-TPOL-D-800** pair. Thus, we turned into the nanostructure and the porous network of **RES** as the last stop for possible differences induced by early oxidative ring fusion aromatization.

2.6. THE PYROLYTIC EVOLUTION OF THE NANOSTRUCTURE AND THE POROUS NETWORK

They were followed with SEM and N_2 sorption porosimetry. The microporosity of selected samples was also probed with CO_2 adsorption. Qualitatively, all systems behaved similarly, and typical primary data are exemplified with the **TPOL** system in Figure 9. Data in similar format for the **FPOL**, **RF** and **PF** systems are shown in ESI, Appendix IX.

All samples, at all stages of processing, consisted of smaller particles (arrows in Figure 9) aggregating to larger ones (dashed circles), which in turn agglomerated to larger entities, and so on. The smallest particles discernible in SEM were on the order calculated for primary particles using gas sorption and skeletal density data (see ESI, Tables S.VII.1–4). Generally, there was an increase in size of primary particles in **RES-**

240(air) (most pronounced in **TPOL-240(air)**, where the particle size increased >2×, from 8.4 nm to 18.4 nm) followed by a gradual decrease till **C-RES-D_**(or**_O**)**-800**. The primary particle size at that temperature was 5–7 nm in all pyrolyzed systems, irrespective of the D or O route. After reactive etching at 1000 ºC, the most noticeable effect was that **EC-RES-D_**(or**_O)-800** had more empty space.

At *all* stages of processing, all N_2 sorption isotherms of **RES**, **RES-240(air)**, **C-RES-D_**(or**_O**)**-800** and **EC-RES-D_**(or**_O)-800** (Figure 9 and ESI, Figures S.IX.1–3) were Type IV with broad saturation plateaus indicating that we are dealing with mesoporous materials. (Plateaus, albeit narrower, were observed even with the lower-density **RF** system – see ESI, Figure S.IX.2.) At low partial pressures (P/P_o), all N_2 sorption isotherms showed a quick rise that became more pronounced in the carbonized samples (**C-RES-D_**(or**_O**)**-800**), and even more pronounced in the carbonized and etched samples (**EC-RES-D_**(or**_O**)**-800**). That rapid increase in the volume of N_2 adsorbed indicated microporosity that was confirmed and quantified with CO_2 adsorption experiments (see Insets in the isotherm frames of Figure 9 and ESI, Figures S.IX.1–3): as the volume of N_2 adsorbed at low P/Po increased, the total uptake of CO_2 increased too.

The pore-size distributions along processing, of pores with sizes <300 nm are exemplified with the **TPOL** and **RF** systems in Figure 10. Mesopore size distributions were obtained with the BJH method;[50] micropore size distributions were obtained with the DFT method on the CO_2 adsorption data.[51,52] Data for the two other two systems, **FPOL** and **PF**, are shown in ESI, Appendix X Figure S.X.1. In general, the behavior of **RF** and **PF** was almost identical to one another, while the behavior of **FPOL** was intermediate between that of **TPOL** and of **RF**/**PF**. A first observation in Figure 9 is that

the pore size distribution of as-prepared **TPOL** was different from that of the other three **RES**, implying an already quite rigid structure. By going from **TPOL** to **TPOL-240(air)** the mesopore size distribution moved to smaller diameters, while the micropore size distribution became more resolved. Both of those changes were consistent with molecular relaxation, contraction and further rigidization in a new, more compact molecular arrangement as described by the mechanism of Scheme 4. After ring fusion aromatization neither the mesopore, nor the micropore size distribution was affected by carbonization: the distribution profiles in **C-TPOL-D**_(or**_O**)**-800** were practically the same as in **TPOL-240(air)**. After etching, the smallest micropores were lost, the larger micropores became a little more narrow, and the mesopores remained unaffected. Now, it is noted that the pore size distributions of the carbonized and etched **EC-TPOL-D**_(or**_O**)**-800** and **EC-RF-D**_(or**_O**)**-800**, and for this matter of all **EC-RES-D**_(or**_O**)**-800,** were practically identical irrespective of the system or the process (D or O), consistent with the common terminal pyrolytic fate of all **RES**. More importantly, however, the molecular flexibility of as-prepared **RF** and **PF**, that followed them in their oxidized structures, **RF-240(air)**, **PF-240(air)**, accounted for conformational minima right from the beginning, yielding microporous structures similar to those obtained from **TPOL** only after the chain relaxation processes described in Scheme 4. Consistent with those conclusions, the **FPOL** system, being more flexible than **TPOL**, realized a conformation minimum right from the as-prepared stage, just like **RF** and **PF**, thus its micropore profile was resolved just like in the latter two. However, **FPOL** undergoes oxidative ring fusion aromatization just like **TPOL** (see ESI, Appendix VI). That process imposes contraction and

rigidization, which in turn is expressed by the mesopore profile of **FPOL-240(air)** (and above) moving to smaller pores.

Similarities or differences in the pore size distributions notwithstanding, the absolute pore volumes that correspond to those distributions paint a complementary view of the effects brought about by ring fusion aromatization, and pave the way towards explaining differences in surface areas. The micropore volumes (tabulated in ESI, Appendix VII) were extracted from the CO_2 adsorption isotherms by assuming slit-pore geometry and using the Horvath-Kawazoe method.[53] Micropore volumes in all **RES** were very small to begin with (<0.08 cm^3 g^{-1}), and generally decreased even further in **RES-240(air)**. The largest such decreases were observed with the aromatizable systems: from 0.07 cm^3 g^{-1} to 0.04 cm^3 g^{-1} in **TPOL**/**TPOL-240(air)**, and from 0.08 cm^3 g^{-1} to 0.06 cm^3 g^{-1} in **TPOL**/**TPOL-240(air)**. The largest decrease in the **TPOL**/**TPOL-240(air)** pair agrees with the molecular contraction expected from Scheme 4. Upon carbonization at 800 °C, the micropore volumes increased to 0.10–013 cm^3 g^{-1} in all **C-RES-D**_(or_**O**)-**800**. Upon further reactive etching, the micropore volumes exactly doubled in all **EC-RES-D**_(or_**O**)-**800** (all in the 0.22–0.27 cm^3 g^{-1} range), except in **EC-RF-D**_(or_**O**)-**800**, where the micropore volume increased 3.5× (to 0.44 cm^3 g^{-1}). Interestingly, in all **RES**, the sum of pore volumes in the range of 1.7–300 nm (by N_2 sorption) and of micropores (by CO_2 adsorption) was about equal to the total pore volume calculated from bulk and skeletal density data via $V_{Total} = (1/\rho_b)-(1/\rho_s)$, meaning that all materials lacked any significant macroporosity.[54] (All relevant values are cited in ESI, Tables S.VII.1–4.) What is important to look at though, is the $V_{micropore}$:V_{Total} ratio, which can be calculated directly from the $V_{micropore}$ and V_{Total} data shown in ESI, Tables S.VII.1-4. After

carbonization, but before etching, the percent micropore volumes of both **C-PF-D**_(or**_O**)-**800**, and especially of **C-RF-D**_(or**_O**)-**800**, were consistently behind the values of the corresponding **C-TPOL-D**_(or**_O**)-**800** and **C-FPOL-D**_(or**_O**)-**800**. Curiously, after carbonization and etching the percent micropore volume of **EC-PF-D**_(or**_O**)-**800** (16.25% and 18.2%, for D and O respectively) seemed to have caught up with those of **EC-TPOL-D**_(or**_O**)-**800** (11.6% and 13.8%), and those of **EC-FPOL-D**_(or**_O**)-**800** (19.7% and 24.1%, for D and O respectively). On the other hand, the percent micropore volumes of **EC-RF-D**_(or**_O**)-**800** (6.8% and 8.0%, for D and O respectively) were consistently behind. Perhaps, that the out-of-line behavior of **EC-PF-D**_(or**_O**)-**800** was related to the resilience of **C-PF-D**_(or**_O**)-**800** to etching (refer to the etching yields in ESI, Table S.I.2).

It is speculated that the trend towards higher micropore volumes in the aromatized systems is directly related to the molecular rigidization that fixes the relative position of the polymeric chains. In systems that cannot be aromatized by an early oxidation step (**RF** and **PF**), later aromatization (recall all systems converged chemically above 600 ºC) may compete with other processes, e.g., melting of polymeric segments, which may have reduced microporosity. Most probably related to the link between higher micropore volumes and early oxidative ring-fusion aromatization, BET surface areas of carbons derived from **TPOL-240(air)** and **FPOL-240(air)** were consistently about 20% higher than the surface areas of carbons derived by direct pyrolysis of as-prepared **TPOL** and **FPOL** (Figure 11). That edge identified in the surface areas of **C-TPOL-O-Θ** and **C-FPOL-O-Θ** over **C-TPOL-D-Θ** and **C-FPOL-D-Θ** followed the samples through etching. As shown in Figure 11, considered as groups, the BET surface areas of **EC-**

TPOL-O-(600≤Θ≤800) and **EC-FPOL-O-(600≤Θ≤800)** were higher than the BET surface areas of **EC-TPOL-D-(600≤Θ≤800)** and **EC-FPOL-D-(600≤Θ≤800)**. The highest surface area was recorded for **EC-TPOL-O-600** and was equal to at 2778 ± 209 m^2 g^{-1} (see ESI, Table S.VII.1). Micropore surface areas (using the Harkins and Jura method[55,56]) are included in Figure 11, and for carbonized samples they were about 50% of the BET surface areas. The micropore surface areas of the carbonized and etched samples were between 30% and 50% of their BET surface areas. On the other hand, both the BET and the micropore surface areas of carbons and etched carbons from **RF-240(air)** and **PF-240(air)** were at all levels indistinguishable from those via direct pyrolysis of **RF** and **PF** (Figure 11). Although in absolute terms the BET surface areas of the carbonized **RF** and **PF** systems were in the same range as those from **TPOL** and **FPOL**, their micropore areas were generally lower.

3. CONCLUSION

Aerogels became an enabling tool for the study of the carbonization process of four main-stream phenolic resins. It was found that low-temperature (240 ^oC) oxidation of **FPOL** and **TPOL** aerogels with air circulating through their bulk caused ring-fusion aromatization and formation of pyrylium heteroaromatic rings along their skeletal backbone. Other phenolic resins like **RF** and **PF** got oxidized too, but their oxidized forms did not proceed with aromatization at 240 ^oC. Eventually, upon further pyrolysis, either as-prepared samples, or samples from a prior 240 ^oC/air oxidation step, converged to a common carbon structure that includes fused pyrylium rings, and charge-compensating phenoxides. It is surprising that although pyryliym has been identified in

biochar,[38] it has been missed among the pyrolysis products of phenolic resins.[41] The closest prior studies ever came to pyrylium had been to claim saturated five- and six-membered rings with oxygen between aromatic rings.[57–61] On the hindsight, it seems that key to our findings was the fact that we compared the oxidative behavior of several systems of increasing complexity, which turned out to be beneficial, because it allowed us to track the fate of aromatic carbons using solid-state ^{13}C NMR. Whenever an early oxidative ring-fusion aromatization could take place (cases of **TPOL** and **FPOL**), its effect was to rigidize the polymeric structure and create microporosity that contributed towards carbons with higher surface areas than those obtained by direct pyrolysis of as-prepared materials. Those findings are directly relevant to high surface area carbons for gas sorption (e.g., capture and sequestration of CO_2[62]) and for ion-exchange materials via the fixed O^+ and O^- sites on the carbon backbones, as has been proposed for biochar bearing pyrylium moieties.[38]

4. EXPERIMENTAL

4.1. MATERIALS

All reagents and solvents were used as received without further purification. Terephthalaldehyde (T), phloroglucinol (POL), 12.1 N hydrochloric acid, and 1,4-dioxane were purchased from Acros Organics U.S.A. Resorcinol (R), formaldehyde (F, 37% w/w aqueous solution methanol stabilized), and acetonitrile (ACS reagent grade) were purchased from Aldrich Chemical Co. Phenol (P, crystals/certified ACS grade) was purchased from Fisher Scientific. Syphon grade CO_2 and ultra-high purity argon were

obtained from BOC Gases, Murray Hill, N.J. supplied locally by Ozarc Gases. Liquid nitrogen was purchased from Airgas, Rolla, Mo.

4.2. PREPARATION OF PHENOLIC RESIN AEROGELS (RES)

All formulations and gelation points are listed in ESI, Appendix I Table S.1. In a typical procedure, the predetermined amount of the phenolic monomer was dissolved in 2/3 of the predetermined amount of the appropriate solvent. Dissolution of POL in 1,4-dioxane was assisted by heating and stirring for 5 min at 70 ^{o}C under N_2. In the case of **TPOL**, T was also mixed with POL and the two reagents were dissolved in 1,4-dioxane together as just described. In the cases of the three formaldehyde-based aerogels (**FPOL**, **RF**, **PF**), the appropriate amount of the commercially available formaldehyde solution was added at room temperature to the solution of the phenolic compound. (In the case of **FPOL**, the POL solution was allowed to cool back to room temperature before adding the formaldehyde solution.) Subsequently, the predetermined amount of the catalyst (12.1 N HCl) was dissolved in the remaining 1/3 of the predetermined amount of solvent, and the acid solution was added to the phenolic compound/aldehyde solution at room temperature to form the sol. All sols were stirred briefly and were poured in polypropylene molds (either polypropylene Scintillation Vials General Purpose, 6.5 mL, Sigma–Aldrich Catalogue No. Z376825, 1.27 cm inner diameter; or, Wheaton polypropylene Omni-Vials, part No. 225402, ~1 cm in diameter). The molds were sealed with their caps, wrapped with Parafilm^{TM}, and were kept for 24 h for gelation and aging. **TPOL**, **FPOL** and **RF** gelled at room temperature and aging was carried out at the same temperature. Gelation of **PF** was carried out at 80 ^{o}C (24 h); **PF** wet-gels were aged at 70

^{o}C (12 h). Wet-gels were washed with acetone (3 × 8 h, using 4× the volume of the gel each time), and were dried in an autoclave with CO_2 taken out at the end as a supercritical fluid.

4.3. AIR OXIDATION OF RES AND PREPARATION OF RES-240(AIR)

RES aerogels were placed in a conventional convection oven at 240 °C for 5 h, and turned from brown or red to dark brown.

4.4. CONVERSION OF AS-PREPARED RES AEROGELS, OR AIR-OXIDIZED RES-240(AIR) AEROGELS INTO CARBON AEROGELS C-RES-D-Θ AND C-RES-O-Θ

Aerogel monoliths, including as-prepared and those treated at 240 °C in air, were pyrolyzed in a tube furnace under flowing high purity Ar (300 mL min^{-1}) at 300 ^{o}C, 400 ^{o}C, 500 ^{o}C, 600 °C, 700 °C, or 800 °C for 5 h. The temperature of the furnace was increased to the target temperature Θ at 2.5 °C min^{-1}. New samples were used at each pyrolysis temperature. At the end of the heating period, cooling was controlled also at 2.5 °C min^{-1} under continuous flow of Ar. As-prepared **RES** aerogels pyrolyzed at a target temperature Θ are designated as **C-RES-D-Θ**. Air-oxidized aerogels, **RES-240(air)**, pyrolyzed at a target temperature Θ are designated as **C-RES-O-Θ**.

4.5. REACTIVE ETCHING OF C-RES-D-Θ AND C-RES-O-Θ CARBON AEROGELS INTO EC-RES-D-Θ AND EC-RES-O-Θ

Either **C-RES-D-Θ** or **C-RES-O-Θ** aerogels prepared at Θ=600 °C, Θ=700 °C, or Θ=800 °C were pyrolyzed further at 1000 °C for 3 h under flowing CO_2 (300 mL min^{-1}). For this, at the end of the 5 h pyrolysis-under-Ar period, the temperature of the furnace

was increased to 1000 ^{o}C, the gas was switched to CO_2 and pyrolysis continued for the prescribed time. At the end of this period, the flowing gas was switched back to Ar and the tube was cooled back to ambient temperature at 2.5 °C min^{-1}.

4.6. METHODS

Drying of acetone-exchanged wet-gels with supercritical fluid (SCF) CO_2 was carried out in an autoclave (SPIDRY Jumbo Supercritical Point Dryer, SPI Supplies, Inc. West Chester, PA). Samples submerged in acetone were loaded into the autoclave cooled at 14 ^{o}C. The pressure vessel was closed and liquid CO_2 was allowed until it displaced all acetone, which was then drained out. Liquid CO_2 was allowed in the vessel several more times until acetone was extracted out of the pores of the samples completely. The criterion for the latter was that CO_2 released from the vessel formed dry ice powder. At that point, the temperature of the autoclave was raised to 40 ^{o}C and SCF CO_2 was vented off as a gas.

4.6.1. Physical Characterization. Bulk densities (ρ_b) were calculated from the weight and the physical dimensions of the samples. Skeletal densities (ρ_s) were measured using helium pycnometry on a Micromeritics AccuPyc II 1340 instrument.

4.6.2. Chemical Characterization. CHN elemental analysis was conducted with a Perkin-Elmer Model 2400 CHN Elemental Analyzer, calibrated with acetanilide, urea, *trans*-stilbene, benzophenone, and glycine.

Infrared (FTIR) spectra were taken in KBr pellets, on a Nicolet-FTIR Model 750 spectrometer.

Solid-state CPMAS ^{13}C-NMR spectra were obtained with samples ground into fine powders on a Bruker Avance III 400 MHz spectrometer with a carbon frequency of 100 MHz, using a 7 mm Bruker MAS probe at a magic angle spinning rate of 5 kHz, with broadband proton suppression, and CP TOSS pulse sequence. The Total Suppression of Spinning Sidebands (TOSS) pulse sequence was applied by using a series of four properly timed 180º pulses on the carbon channel at different points of a cycle before the acquisition of the FID, after an initial excitation with a 90º pulse on the proton channel. The 90º exitation pulse on the proton and the 180º excitation pulse on carbon were set to 4.2 μs and 10 μs, respectively. Under those conditions, spectra of all **RES**, **RES-240(Ar)** and **RES-240(air)** were taken twice, once with the cross-polarization contact time set at 3000 μs and once at 5 μs. Solid-state ^{13}C NMR spectra were referenced externally to glycine (carbonyl carbon at 176.03 ppm). Chemical shifts are reported versus TMS (0 ppm).

XPS data were obtained with a Kratos Axis 165 Photoelectron Spectroscopy System. Samples for XPS were prepared by mixing powders of the aerogels (like those prepared for solid-state NMR) with Au powder (10% w/w) and pellets were compressed like those used for FTIR. (For highly conductive samples, the amount of Au powder could be reduced to 5% w/w.) Such pellets were placed flat on a conductive carbon tape that was then adhered to stainless steel sample holders. Samples were introduced into the analysis chamber one at a time and the chamber was evacuated at 10^{-8} Torr or lower. No ion sputtering was carried out on any of the samples. An Al monochromatic source at 150 watts was used for excitation. A charge neutralizer was used to reduce the effects of differential or sample charging. The analysis area was 700×300 microns. Elemental

quantification calculations were based on broad survey results from single sweeps at higher sensitivity (Pass Energy=80), and were carried out with Kratos Axis Vision processing software and its appropriate relative sensitivity factors for the particular XPS system. High resolution elemental scans where carried out at a lower sensitivity (Pass Energy=20), using multiple sweeps to improve the signal-to-noise ratios. Deconvolution of C1s and O1s spectra of the samples were performed with Gaussian function using OriginPro 8.5.1 software.

4.6.3. Thermal Analysis. Differential Scanning Calorimetry (DSC) was conducted both under N_2 and in air with a TA Instruments Modulated Differential Scanning Calorimeter (MDCS) Model 2920 calibrated with a sapphire standard. Samples were used as powders (4–8 mg), and the MDSC instrument was run from -30 to 300 °C at 10 °C min^{-1}.

4.6.4. Structural Characterization. Scanning electron microscopy (SEM) was conducted with Au-coated samples on a Hitachi Model S-4700 field-emission microscope.

4.6.5. Pore Structure Analysis. The pore structure was probed with N_2-sorption porosimetry at 77 K using either a Micromeritics ASAP 2020 or a TriStar II 3020 version 3.02 surface area and porosimetry analyzer. Before porosimetry, samples were outgassed for 24 h under vacuum at 80 °C. Data were reduced to standard conditions of temperature and pressure (STP). Total surface areas, σ, were determined via the Brunauer-Emmett-Teller (BET) method from the N_2-sorption isotherms. Micropore surface areas were calculated via t-plot analysis of the isotherms using the Harkins and Jura Model.[55,56] Pore size distributions were determined with the Barret-Joyne-Halenda (BJH) equation applied

to the desorption branch of the N_2-sorption isotherms.[50] Micropore analysis was conducted either with N_2-sorption at 77 K using a low pressure transducer (0.1 Torr) on the Micromeritics ASAP 2020 surface area and porosity analyzer, or with CO_2-sorption up to 760 torr (0.03 relative pressure) at 273 K (ice-water bath) using the Micromeritics Tristar II 3020 version 3.02 mentioned above. Micropore size distributions were calculated from the CO_2 adsorption data using a DFT model,[51,52] and micropore volumes were obtained using the Horvath-Kawazoe (HK) method,[53] applied on the same data. Average pore diameters were calculated using the $4\times V_{Total}/\sigma$ method, where V_{Total} is the total pore volume per gram of sample, and can be calculated either via $V_{Total} = (1/\rho_b) - (1/\rho_s)$ or from the single highest volume of N_2 adsorbed along the adsorption isotherm (at $P/P_0 \sim 1$). Average pore diameter values, calculated with V_{Total} by both methods, are cited herewith; the two values converge for mostly mesoporous materials.

Electronic supplementary information (ESI) available: Appendix I: Formulation of RES, gelation times and pyrolytic yields. Appendix II: Differential scanning calorimetry of the four RES. Appendix III: FTIR data. Appendix IV: High-resolution O1s XPS data. Appendix V: Solid-state CPMAS ^{13}C NMR data. Appendix VI: Air-oxidation mechanism of FPOL. Appendix VII: Tables with cumulative materials characterization data of all samples. Appendix VIII: Cumulative shrinkage, bulk and skeletal density, and porosity data in graph form. Appendix IX: SEM, N_2 sorption and CO_2 sorption analysis data. Appendix X: Additional meso and micropore size distribution data.

CONFLICTS OF INTEREST: There are no conflicts to declare.

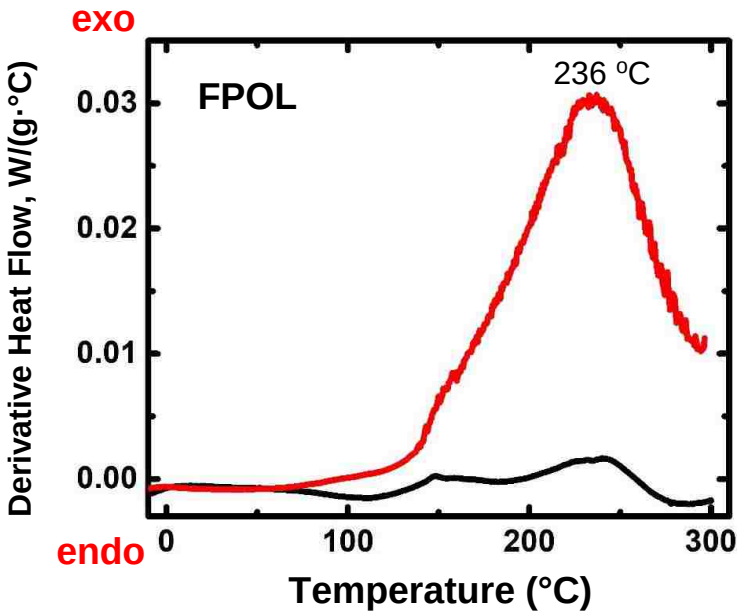

Figure 1. Representative differential scanning calorimetry (DSC) data for **RES**. Black line: under N_2; Red line: in air. (For **TPOL**, **RF** and **PF**, see ESI, Figure S.II.1.)

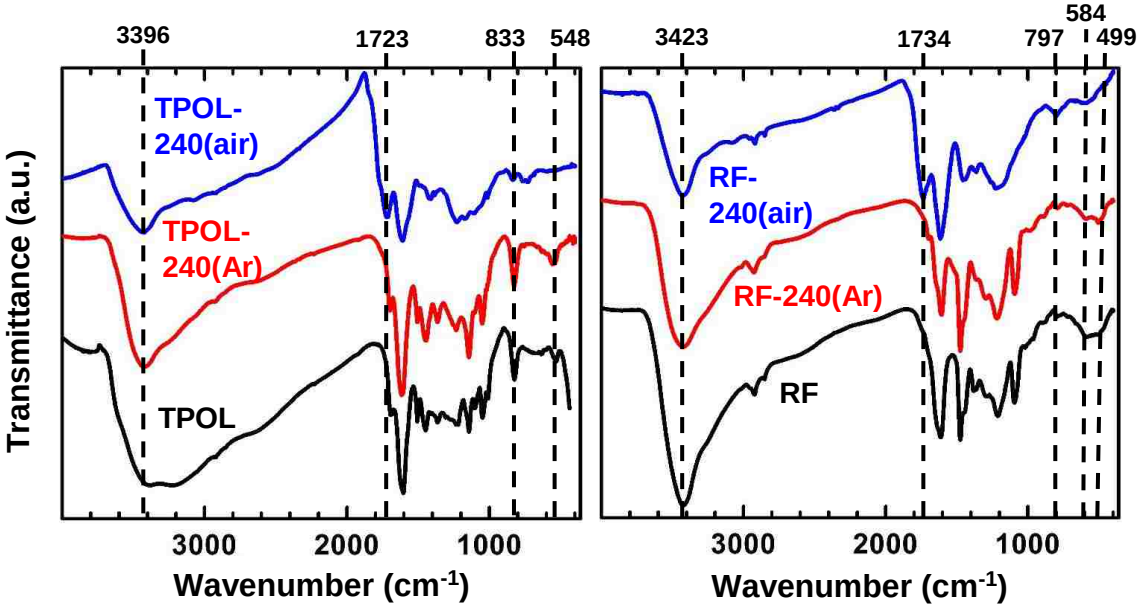

Figure 2. Representative FTIR data for **RES** as-prepared, and after treatment as indicated by the sample names. (For **FPOL** and **PF** see ESI, Figure S.III.1.)

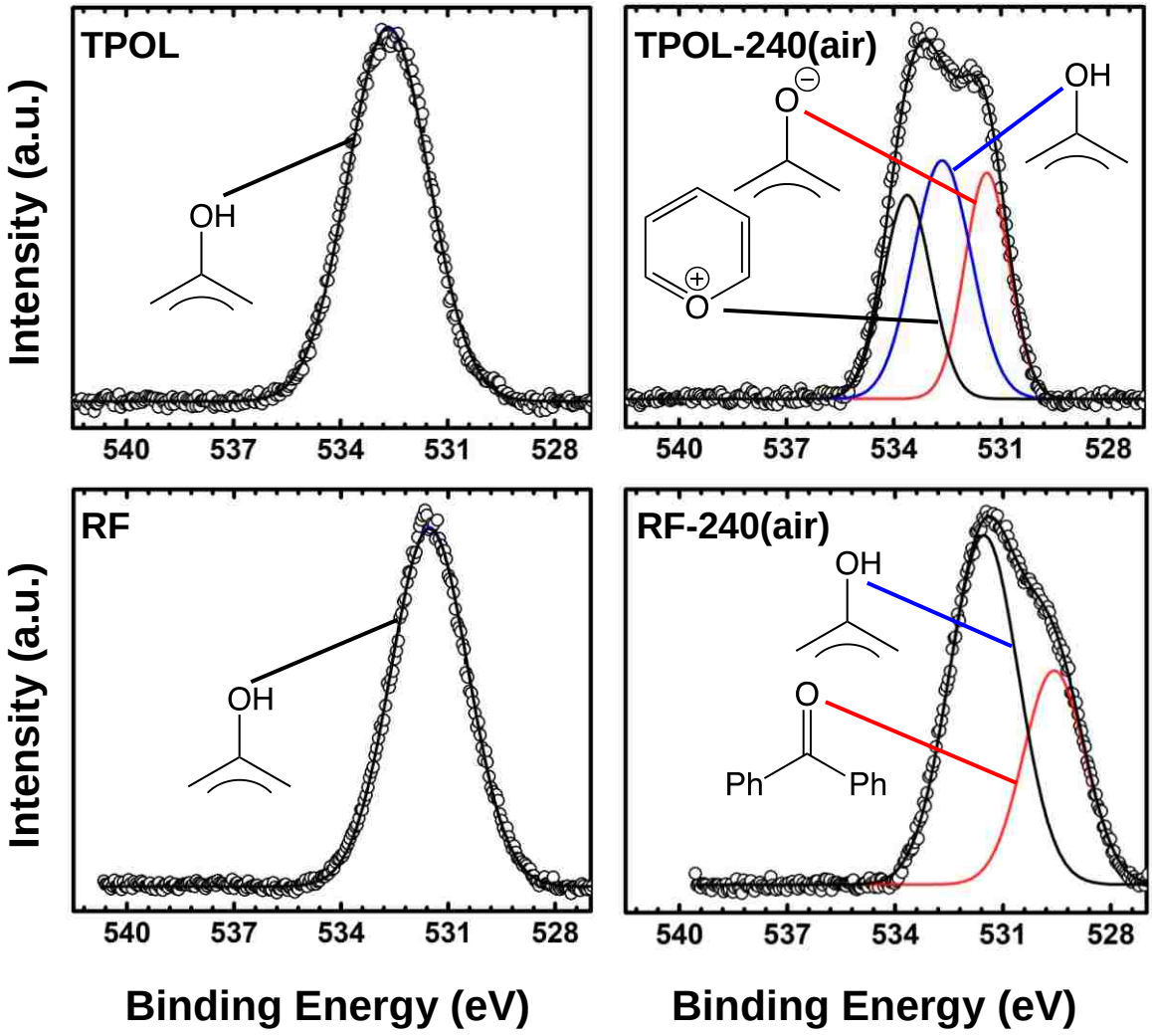

Figure 3. O1s XPS data for **TPOL** and **RF**, and their air-oxidized versions as shown. (The spectra of **FPOL** are similar to **TPOL**, and of **PF** are similar to **RF** – see ESI, Figure S.IV.2.)

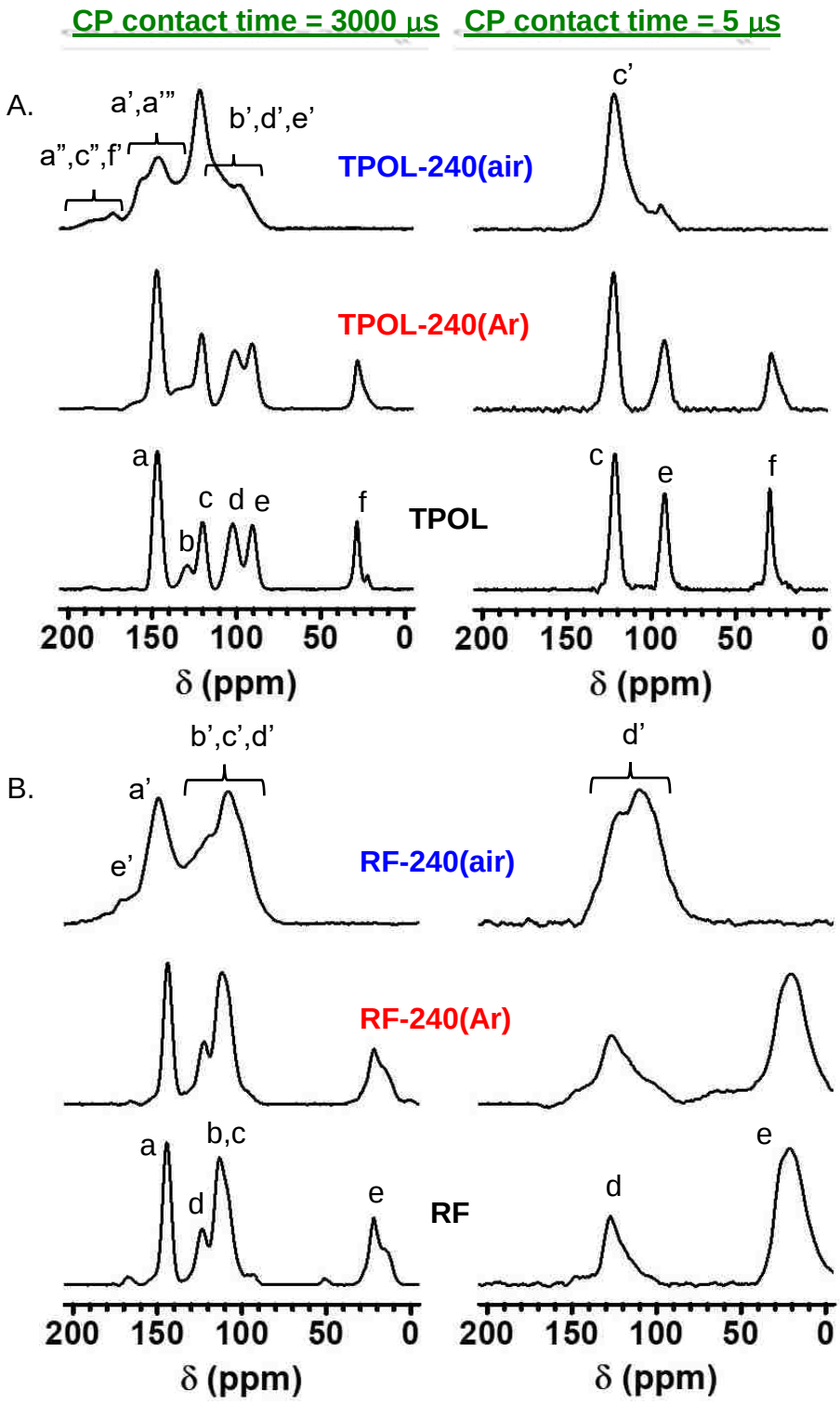

Figure 4. Solid-state CPMAS ^{13}C NMR data for **TPOL** (A) and **RF** (B) and their pyrolyzed products at 240 ^{o}C under Ar or air, as shown. (Similar spectra for **FPOL** and **PF** are shown in ESI, Figure S.V.1.)

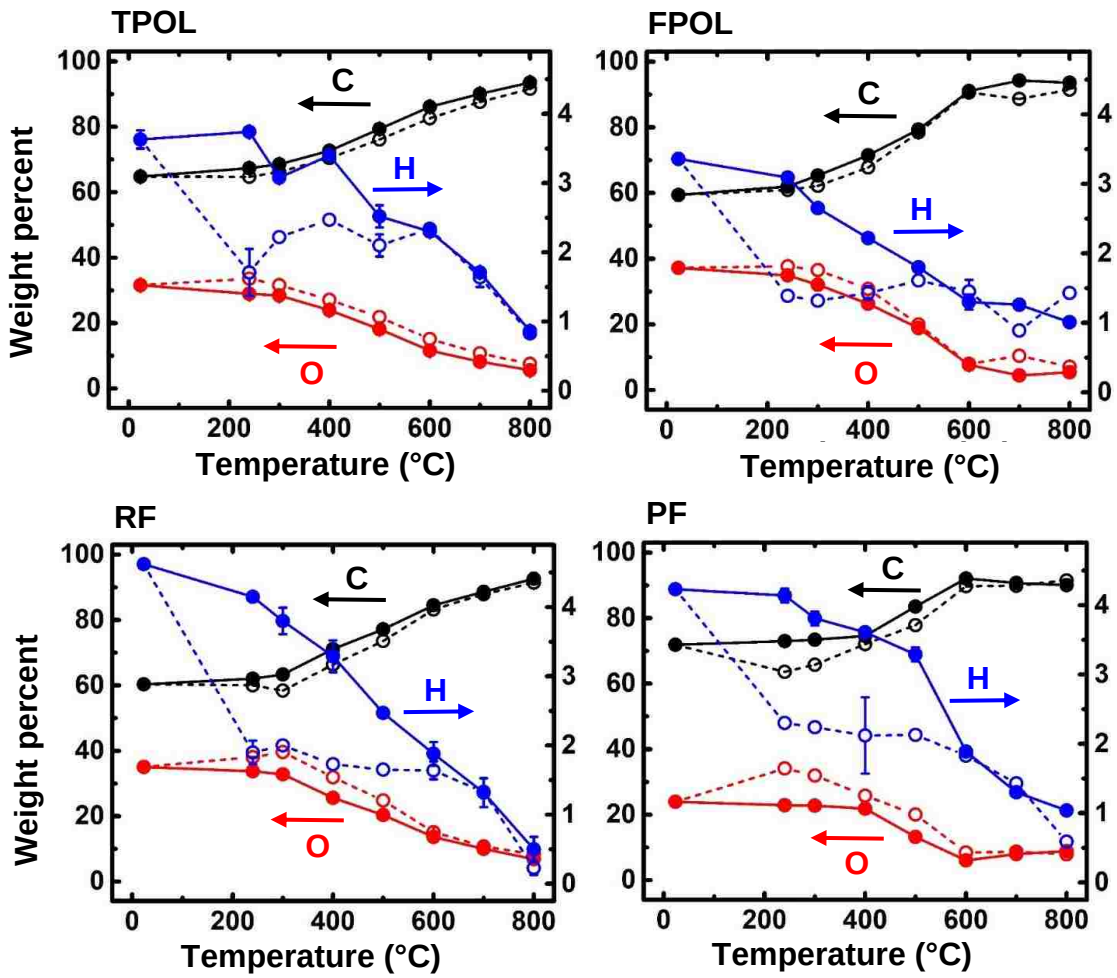

Figure 5. Elemental analysis data along pyrolysis under Ar towards porous carbons. Solid lines: Pyrolytic evolution of elemental composition of as-prepared RES. Dashed lines: Pyrolytic evolution of samples treated at 240 ºC/air (**RES-240(air)**). (% Weight of O by difference.)

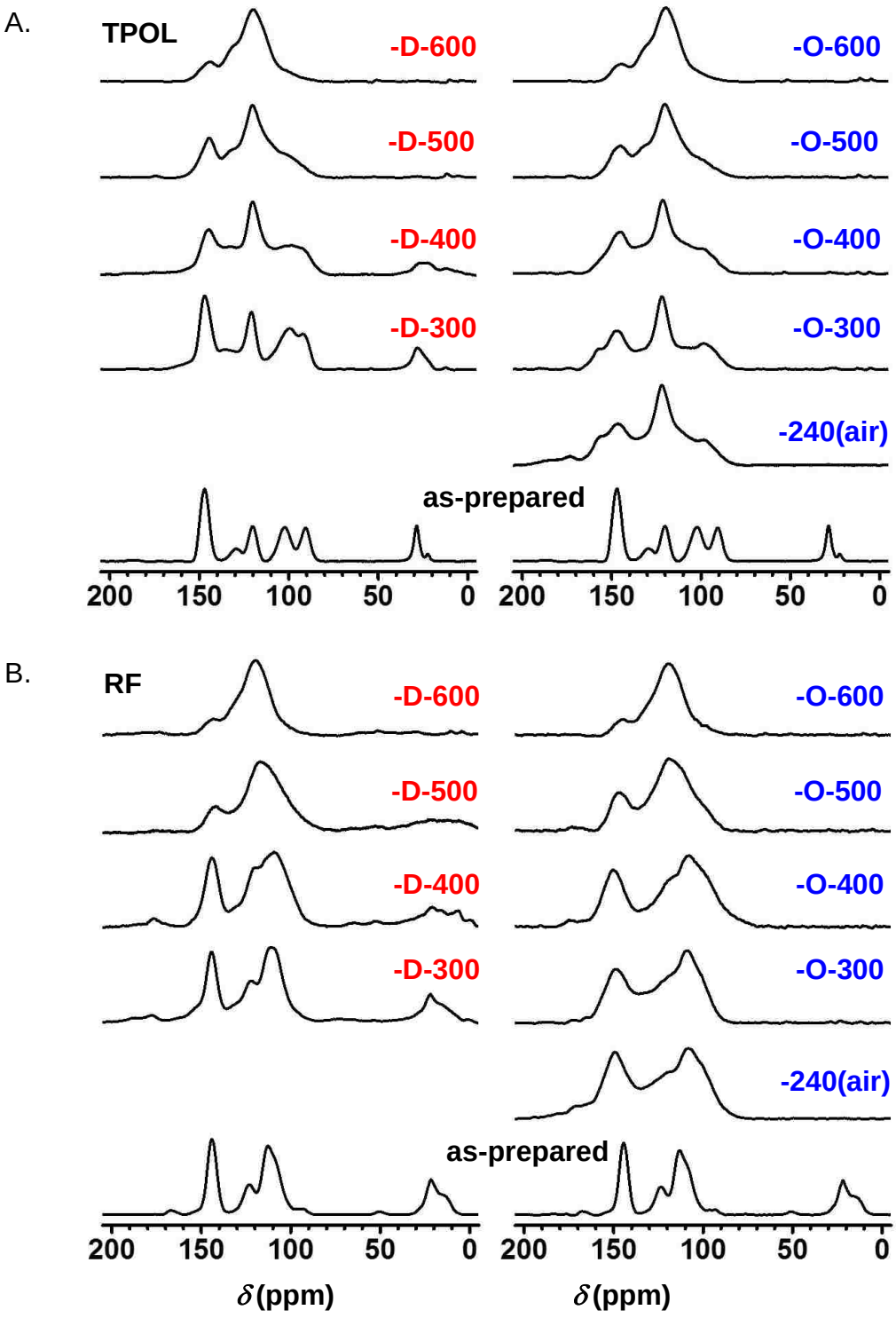

Figure 6. Solid-state ^{13}C NMR data for **TPOL** (A) and **RF** (B) along pyrolysis as shown. D designates samples from pyrolysis of **TPOL** and **RF** as-prepared. O designates samples from pyrolysis of **RES-240(air)** (i.e., sample treated at 240 °C/air). (Similar spectra for **FPOL** and **PF** are given in ESI, Figure S.V.2.)

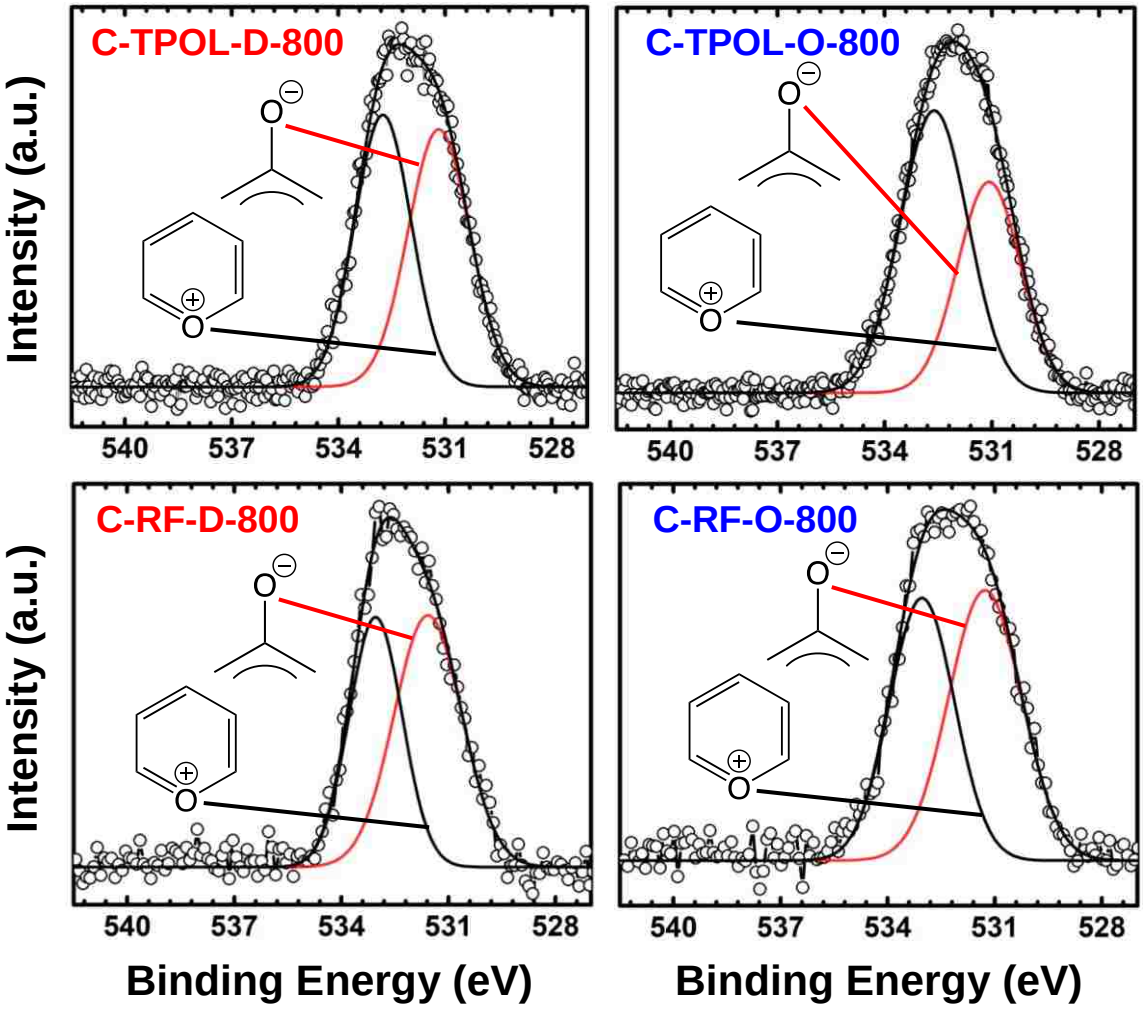

Figure 7. O1s XPS data from the 800 ºC-carbonized **C-TPOL-D-800** / **C-TPOL-O-800** and **C-RF-D-800** / **C-RF-O-800** pairs (top and bottom, respectively). (Similar data for the **FPOL** and **PF** systems are given in ESI, Figure S.IV.3.)

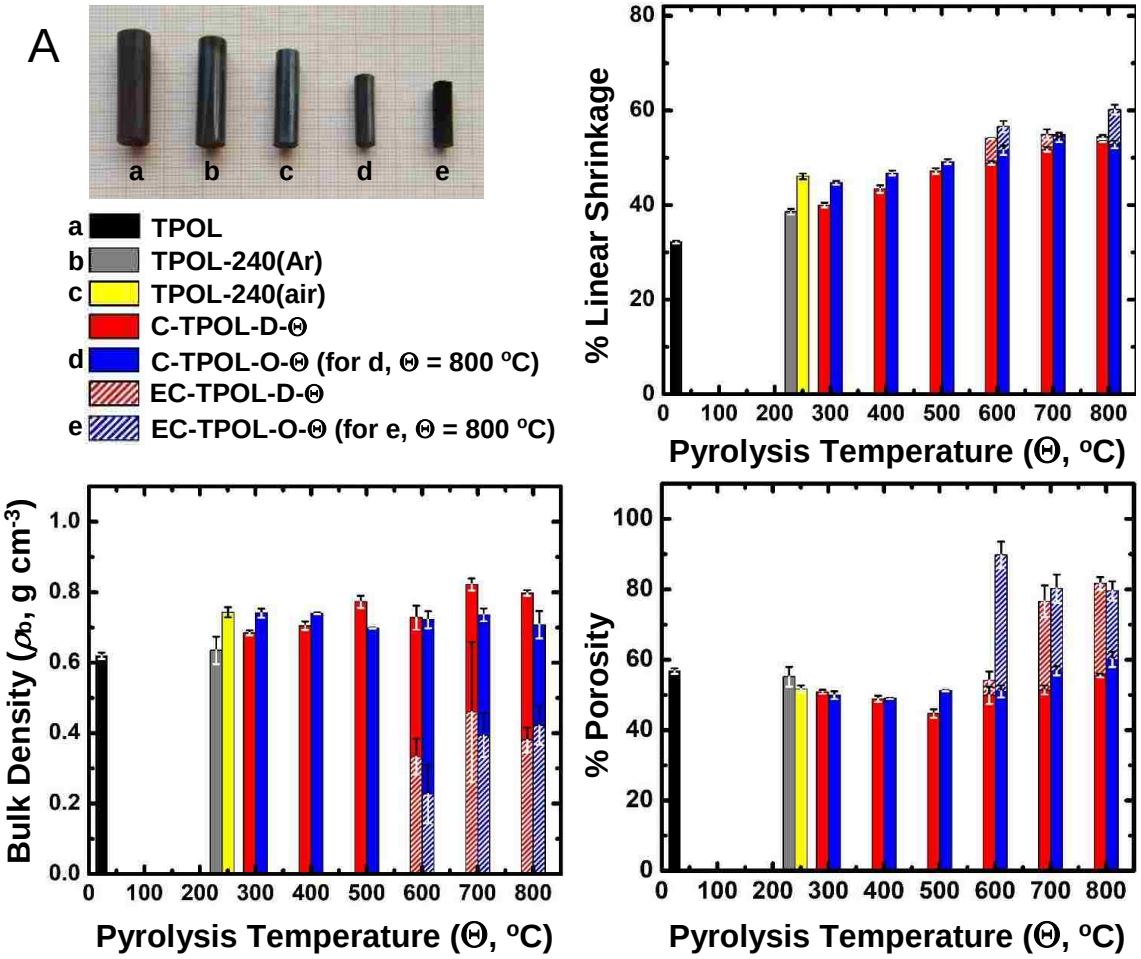

Figure 8. Photographs and general materials characterization data along pyrolysis and reactive etching of the **TPOL** (A) and the **RF** (B) systems. Linear shrinkage is relative to the molds. D refers to products from direct pyrolysis of as-prepared **RES**. O refers to products from pyrolysis of 240 °C/air-oxidized samples. Θ: pyrolysis temperature. Shaded segments of the bars indicate the values after reactive etching at 1000 °C of samples having been carbonized at Θ.

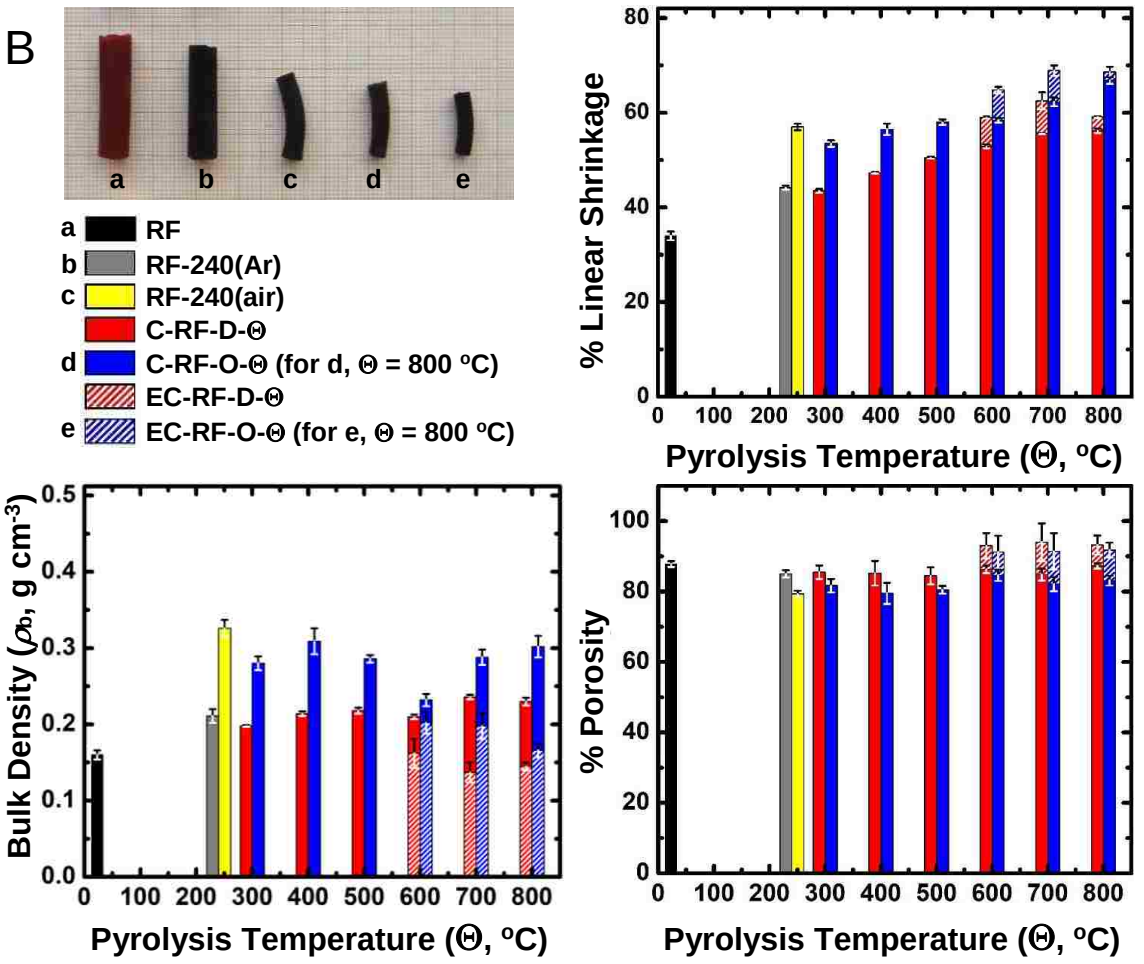

Figure 8. Photographs and general materials characterization data along pyrolysis and reactive etching of the **TPOL** (A) and **RF** (B) system. Linear shrinkage is relative to the molds. D refers to products from direct pyrolysis of as-prepared **RES**. O refers to products from pyrolysis of 240 °C/air-oxidized samples. Θ: pyrolysis temperature. Shaded segments of the bars indicate the values after reactive etching at 1000 °C of samples having been carbonized at Θ. (cont.)

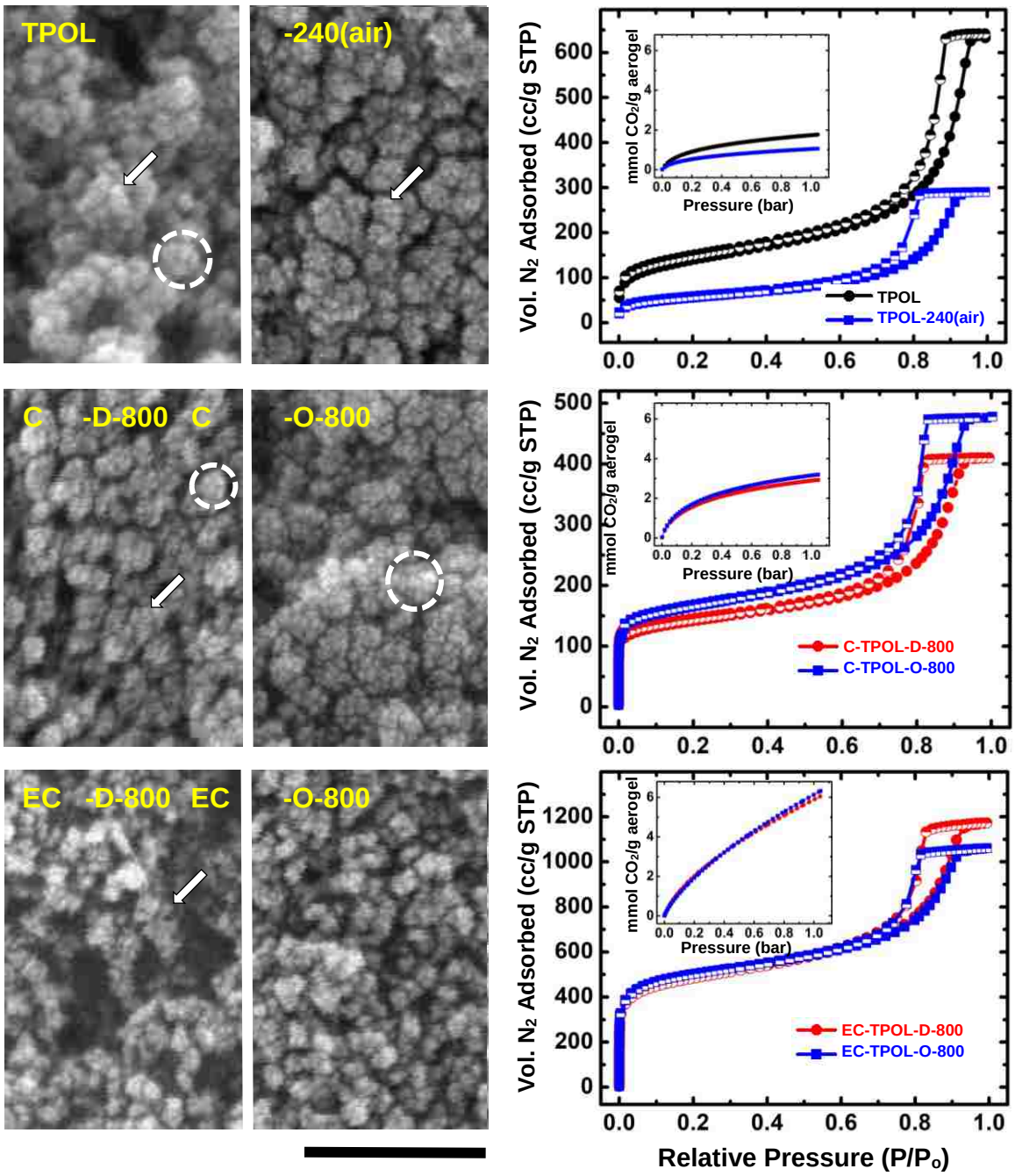

Figure 9. Representative SEM, N_2 sorption isotherms (77 K) and CO_2 sorption isotherms (0 °C - insets) exemplified by the **TPOL** system as follows: Top: **TPOL** and **TPOL-240(air)**; Middle: Carbonized **C-TPOL-D-800** (red) and **C-TPOL-O-800** (blue); Bottom: Etched samples corresponding to the samples in middle raw, **EC-TPOL-D-800** (red) and **EC-TPOL-O-800** (blue). SEM scale bar: 100 nm. (Corresponding data for the **FPOL**, **RF** and **PF** systems are shown in ESI, Appendix IX.)

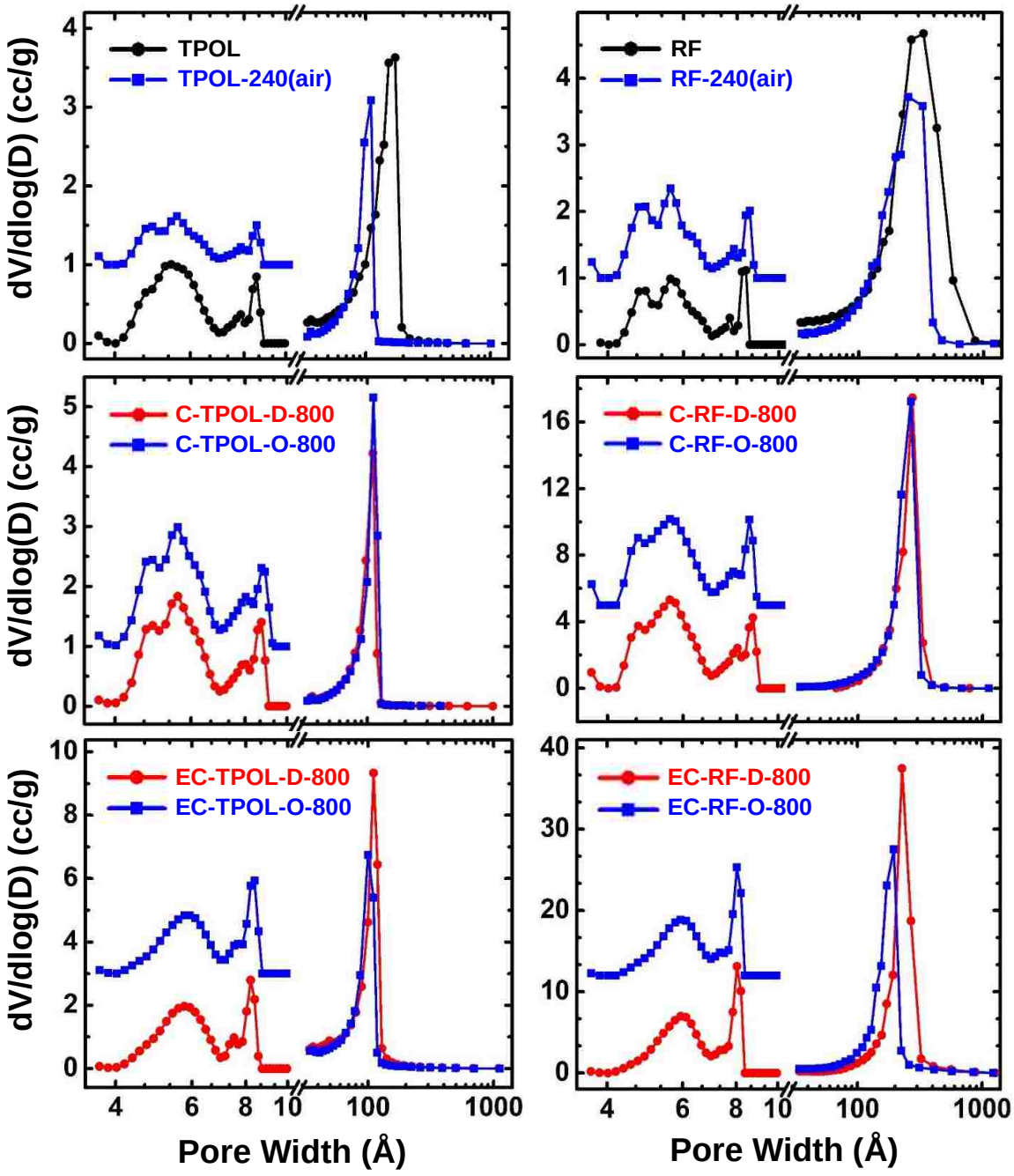

Figure 10. Pore size distributions in the meso and micropore range of samples as shown. Left: from the **TPOL** system; Right: from the **RF** system. Mesopore size distributions (curves at > 10 Å) from the BJH equation applied to N_2 sorption data. Micropore size distributions (curves at <10 Å, magnified 3× and offset for clarity) using a DFT model on CO_2 sorption data and assuming slit pores. (Data for the **FPOL** and **PF** systems are given in ESI, Appendix X.)

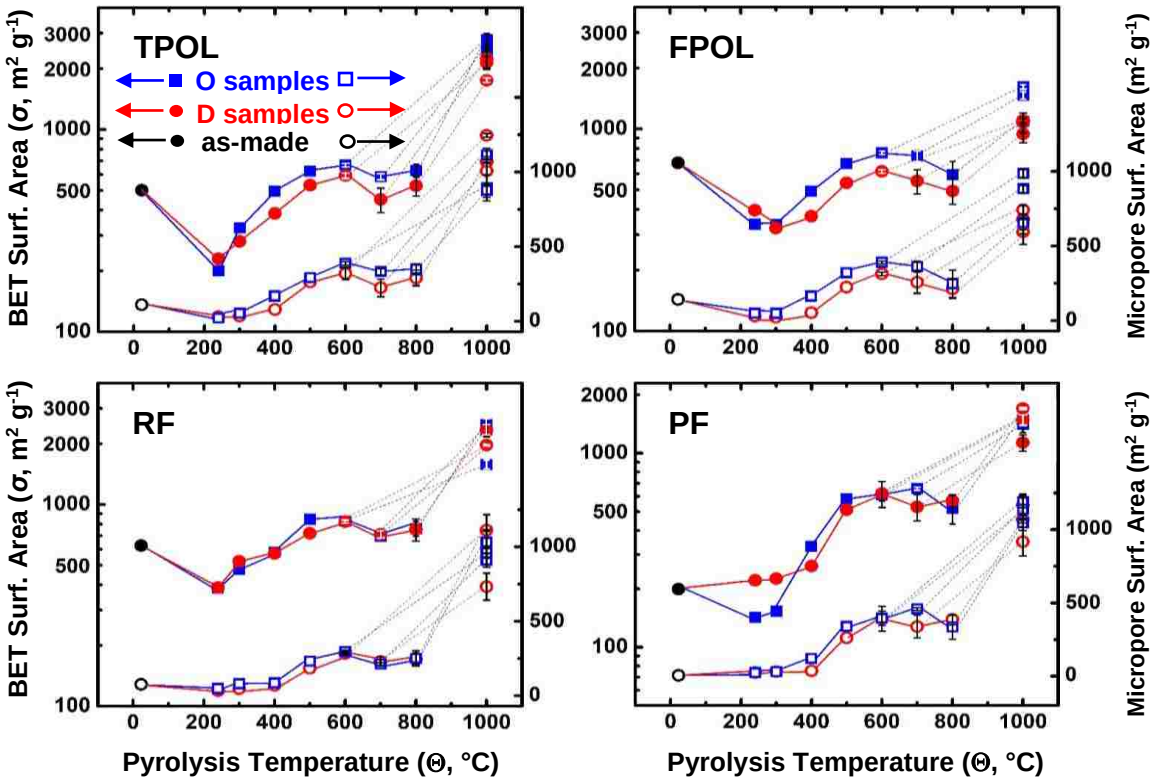

Figure 11. BET surface area data (upper curves, full symbols), and micropore surface area data (lower curves, open symbols) of all samples. Black: as-prepared samples. Red: samples from direct pyrolysis of as-prepared samples at the temperature indicated; Blue: samples from pyrolysis of samples oxidized in air at 240 ^{o}C. Dash-lines connect samples etched with CO_2 at 1000 ^{o}C with the corresponding carbonized samples. All data points are averages of three samples from different batches, run at different times. Errors bars mostly within the symbols.

ACKNOWLEDGEMENTS

We thank the Army Research Office for financial support under Award Number W911NF-14-1-0369. We also thank the Materials Research Center of the Missouri University of Science and Technology for support with materials characterization.

SUPPORTING INFORMATION

Appendix I. Formulations of RES Aerogels, Gelation Times and Pyrolytic Yields

Table S.I.1. Formulations and gelation times of the phenolic resin aerogels of this study [a]

sample	aldehyde							
	formaldehyde (F)				terephthalaldehyde (T)			
	mass (g) [b]	volume (mL)	mmol of F	C (M) [c]	mass (g)	volume (mL)	mmol	C (M) [c]
TPOL	---	---	---	---	3.16	2.29	23.6	0.419
FPOL	2.66	2.44	32.8	1.17	---	---	---	---
RF	0.520	0.477	6.41	0.497	---	---	---	---
PF	5.45	5.00	67.2	2.02	---	---	---	---

sample	phenolic compound											
	phenol (P)				resorcinol (R)				phloroglucinol (POL)			
	mass (g)	volume (mL)	mmol	C (M) [c]	mass (g)	volume (mL)	mmol	C (M) [c]	mass (g)	volume (mL)	mmol	C (M) [c]
TPOL	---	---	---	---	---	---	---	---	5.93	3.99	47.0	0.834
FPOL	---	---	---	---	---	---	---	---	2.07	0.672	16.4	0.583
RF	---	---	---	---	0.337	0.263	3.06	0.237	---	---	---	---
PF	3.15	2.94	33.5	1.01	---	---	---	---	---	---	---	---

[a] Volumes of P, R, T and POL were calculated based on their densities: R: 1.28 g cm^{-3}; T: 1.381 g cm^{-3}; POL: 1.488 g cm^{-3}; P: 1.07 g cm^{-3}. [b] Mass of the commercial solution of formaldehyde (37% w/w). Calculated from the volume and the density of that solution: 1.09 g cm^{-3}. [c] Molar concentration in the sol. [d] Calculated using density of 1,4-dioxane = 1.033 g cm^{-3}, and density of acetonitrile = 0.786 g cm^{-3}. [e] Calculated from the volume of the 12.1 N HCl solution and its density = 1.189 g cm^{-3}. [f] At 23 ºC. [g] At 80 ºC.

Table S.I.1. Formulations and gelation times of the phenolic resin aerogels of this study [a] (Cont.)

sample	solvent			
	acetonitrile		1,4-dioxane	
	mass (g) [d]	volume (mL)	mass (g) [d]	volume (mL)
TPOL	---	---	48.4	50.0
FPOL	---	---	24.20	25.0
RF	15.44	12.14	---	---
PF	---	---	24.20	25.0

sample	conc. HCl (12.1 N)			phenolic monomer/catalyst (mol/mol)	total monomer in the sol (% w/w)	gelation time
	volume (µL)	mass (g) [e]	mmol			
TPOL	35.7	0.0424	0.432	109	16	1 min [f]
FPOL	12.6	0.0150	0.152	108	11	10 min [f]
RF	30.0	0.0357	0.363	8.4	3.3	2 h [f]
PF	343	0.408	4.15	8.1	16	24 h [g]

[a] Volumes of P, R, T and POL were calculated based on their densities: R: 1.28 g cm^{-3}; T: 1.381 g cm^{-3}; POL: 1.488 g cm^{-3}; P: 1.07 g cm^{-3}. [b] Mass of the commercial solution of formaldehyde (37% w/w). Calculated from the volume and the density of that solution: 1.09 g cm^{-3}. [c] Molar concentration in the sol. [d] Calculated using density of 1,4-dioxane = 1.033 g cm^{-3}, and density of acetonitrile = 0.786 g cm^{-3}. [e] Calculated from the volume of the 12.1 N HCl solution and its density = 1.189 g cm^{-3}. [f] At 23 ºC. [g] At 80 ºC.

Table S.I.2. Gravimetric yields of pyrolysis products as shown [a]

Yield (% w/w) of:	From:			
	TPOL	**TPOL-240(air)**	**C-TPOL-D-Θ**	**C-TPOL-O-Θ**
TPOL-240(air)	89.83 ± 2.92			
C-TPOL-D-300	74.45 ± 2.36			
C-TPOL-O-300		98.91 ± 5.15		
C-TPOL-D-400	58.57 ± 3.55			
C-TPOL-O-400		88.92 ± 5.38		
C-TPOL-D-500	55.60 ± 3.95			
C-TPOL-O-500		72.71 ± 4.32		
C-TPOL-D-600	[b]			
C-TPOL-O-600		63.01 ± 1.78		
C-TPOL-D-700	[b]			
C-TPOL-O-700		58.17 ± 3.76		
C-TPOL-D-800	57.44 ± 1.73			
C-TPOL-O-800		53.93 ± 2.11		
EC-TPOL-D-600			25.25 ± 4.41	
EC-TPOL-O-600				16.41 ± 4.09
EC-TPOL-D-700			56.73 ± 5.44	
EC-TPOL-O-700				38.62 ± 6.20
EC-TPOL-D-800			44.35 ± 3.50	
EC-TPOL-O-800				41.85 ± 4.02

Yield (% w/w) of:	From:			
	FPOL	**FPOL-240(air)**	**C-FPOL-D-Θ**	**C-FPOL-O-Θ**
FPOL-240(air)	73.52 ± 5.65			
C-FPOL-D-300	89.60 ± 6.25			
C-FPOL-O-300		96.55 ± 1.46		
C-FPOL-D-400	78.09 ± 3.25			
C-FPOL-O-400		82.49 ± 3.97		
C-FPOL-D-500	66.05 ± 3.90			
C-FPOL-O-500		65.39 ± 3.97		
C-FPOL-D-600	54.20 ± 3.25			
C-FPOL-O-600		50.40 ± 2.88		
C-FPOL-D-700	49.28 ± 2.17			
C-FPOL-O-700		49.63 ± 3.14		
C-FPOL-D-800	53.89 ± 1.37			
C-FPOL-O-800		50.33 ± 2.21		
EC-FPOL-D-600			66.35 ± 4.76	
EC-FPOL-O-600				53.94 ± 5.59
EC-FPOL-D-700			70.44 ± 3.92	
EC-FPOL-O-700				72.39 ± 8.54
EC-FPOL-D-800			68.21 ± 5.31	
EC-FPOL-O-800				72.48 ± 6.90

[a] Data are averages from three samples. [b] Not measured.

Table S.I.2. Gravimetric yields of pyrolysis products as shown [a] (Cont.)

Yield (% w/w) of:	From:			
	RF	**RF-240(air)**	**C-RF-D-Θ**	**C-RF-O-Θ**
RF-240(air)	81.61 ± 0.25			
C-RF-D-300	67.58 ± 8.54			
C-RF-O-300		95.75 ± 8.77		
C-RF-D-400	63.53 ± 2.85			
C-RF-O-400		90.07 ± 4.54		
C-RF-D-500	52.82 ± 4.04			
C-RF-O-500		75.42 ± 5.42		
C-RF-D-600	[b]			
C-RF-O-600		52.64 ± 2.39		
C-RF-D-700	[b]			
C-RF-O-700		53.24 ± 3.99		
C-RF-D-800	54.02 ± 1.00			
C-RF-O-800		49.32 ± 3.50		
EC-RF-D-600			48.06 ± 5.84	
EC-RF-O-600				52.62 ± 3.46
EC-RF-D-700			35.20 ± 7.29	
EC-RF-O-700				37.30 ± 7.44
EC-RF-D-800			49.41 ± 3.92	
EC-RF-O-800				34.64 ± 3.40

Yield (% w/w) of:	From:			
	PF	**PF-240(air)**	**C-PF-D-Θ**	**C-PF-O-Θ**
PF-240(air)	99.87 ± 1.57			
C-PF-D-300	86.83 ± 4.14			
C-PF-O-300		93.65 ± 5.36		
C-PF-D-400	83.77 ± 3.59			
C-PF-O-400		76.30 ± 2.80		
C-PF-D-500	71.70 ± 5.07			
C-PF-O-500		65.82 ± 2.72		
C-PF-D-600	59.31 ± 2.57			
C-PF-O-600		52.22 ± 3.24		
C-PF-D-700	[b]			
C-PF-O-700		48.75 ± 1.63		
C-PF-D-800	61.30 ± 0.58			
C-PF-O-800		48.61 ± 1.72		
EC-PF-D-600			56.66 ± 3.14	
EC-PF-O-600				61.41 ± 5.75
EC-PF-D-700			68.05 ± 9.28	
EC-PF-O-700				78.52 ± 7.59
EC-PF-D-800			84.23 ± 5.28	
EC-PF-O-800				80.84 ± 5.41

[a] Data are averages from three samples. [b] Not measured.

Appendix II. Differential Scanning Calorimetry Data for the Four RES

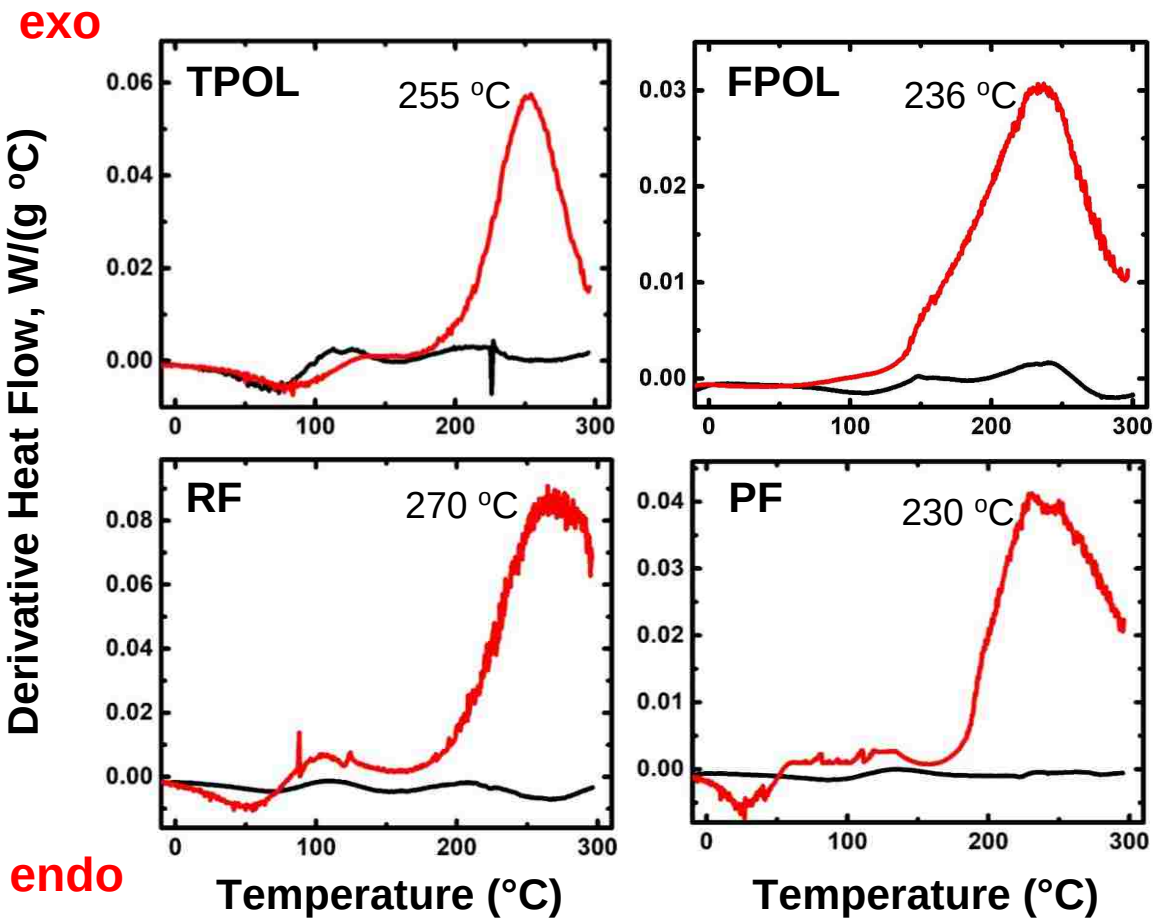

Figure S.II.1. All four **RES** aerogels show strong exotherms in air (red lines), and no major heat exchanges under N_2. (black lines)

Appendix III. FTIR Data

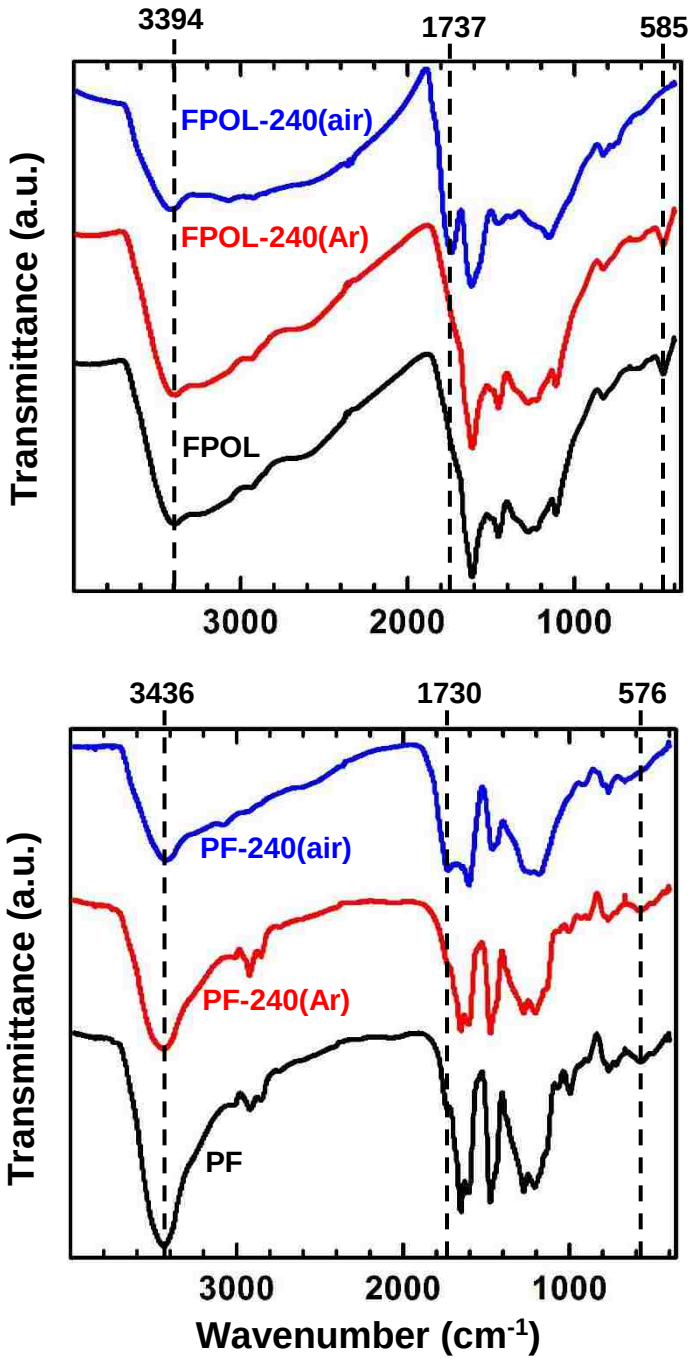

Figure S.III.1. FTIR spectra of as-prepared **FPOL** and **PF** (black lines), after heating at 240 ºC/Ar, (red lines) and after heating at 240 ºC/air (blue lines). (The corresponding spectra of **TPOL** and **RF** are shown in Figure 2 of the main article.)

A.

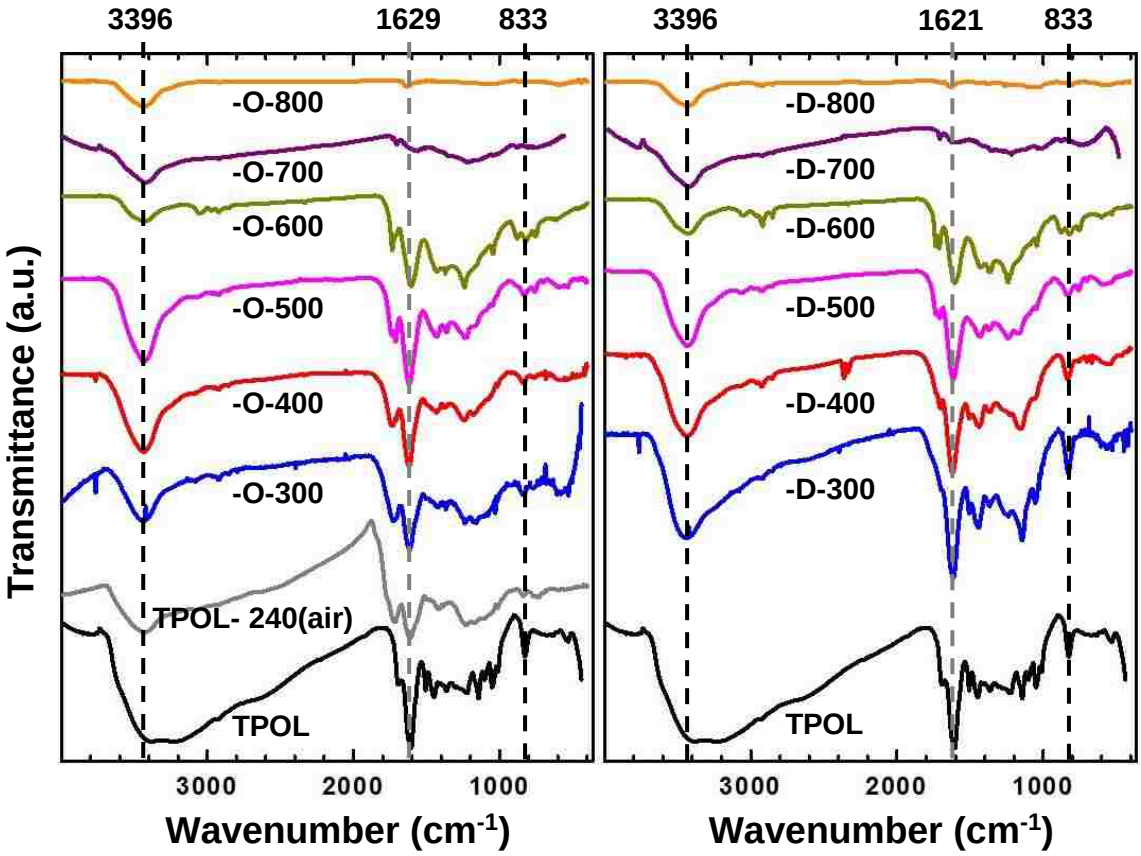

Figure S.III.2.A. FTIR spectra of **TPOL** and of air-oxidized **TPOL** (**TPOL-240(air)**) along pyrolysis at the temperatures (Θ) indicated in the format: –O-Θ and –D-Θ. ("D": Direct pyrolysis of **TPOL**; "O": Pyrolysis of the oxidized sample.) The absorptions at 3396 cm^{-1} and 1629 cm^{-1} survived pyrolysis at 800 ^{o}C/Ar.

B.

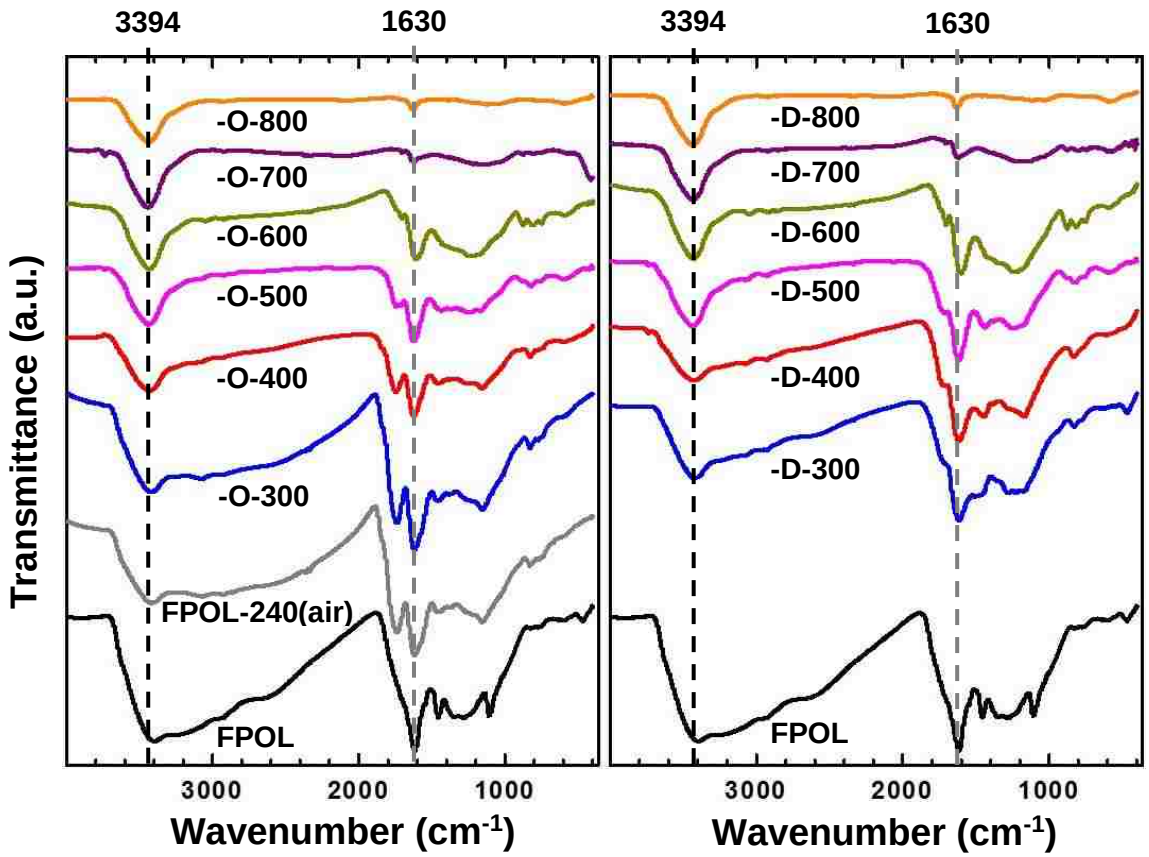

Figure S.III.2.B**.** FTIR spectra of **FPOL** and of air-oxidized **FPOL** (**FPOL-240(air)**) along pyrolysis at the temperatures (Θ) indicated in the format: –O-Θ and –D-Θ. ("D": Direct pyrolysis of **FPOL**; "O": Pyrolysis of the oxidized sample.) Dashed vertical lines mark the common absorptions surviving pyrolysis at 800 ºC/Ar. (Cont.)

C.

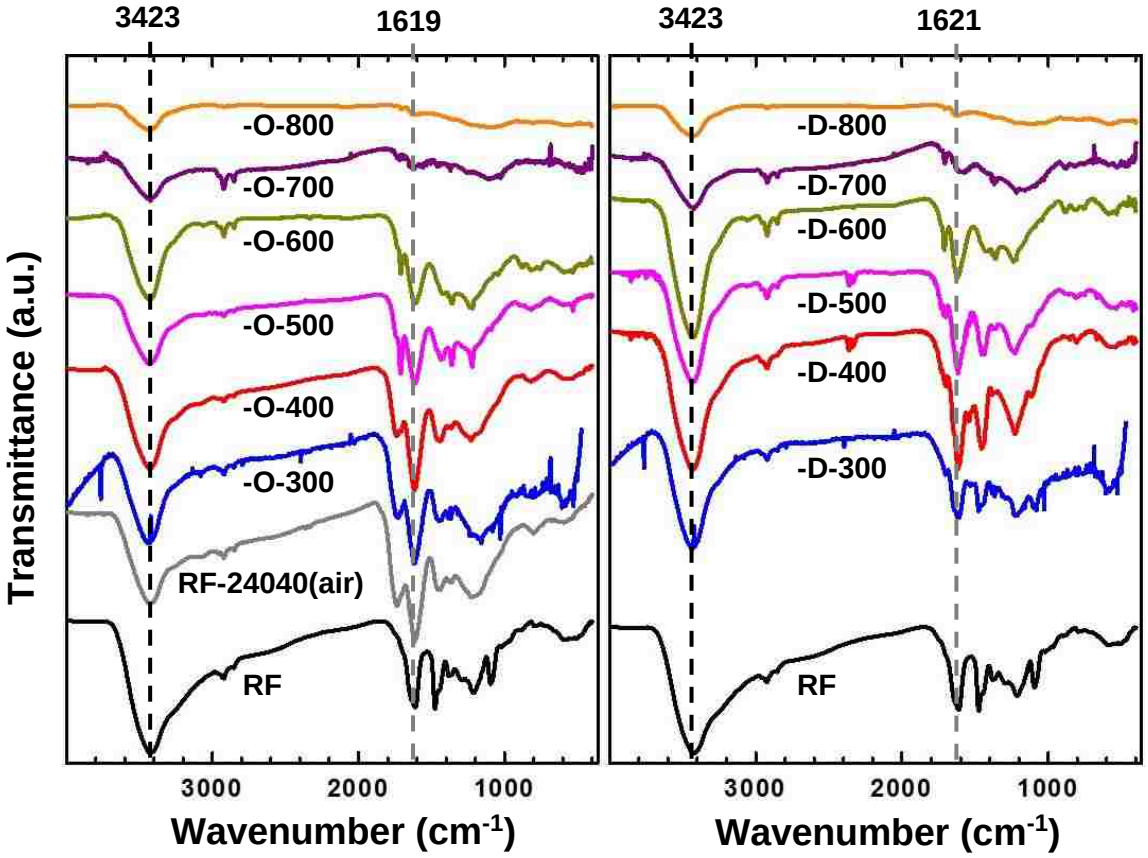

Figure S.III.2.C. FTIR spectra of **RF** and of air-oxidized **RF** (**RF-240(air)**) along pyrolysis at the temperatures (Θ) indicated in the format: –O-Θ and –D-Θ. ("D": Direct pyrolysis of **RF**; "O": Pyrolysis of the oxidized sample.) Dashed vertical lines mark the common absorptions surviving pyrolysis at 800 ^{o}C/Ar. (Cont.)

D.

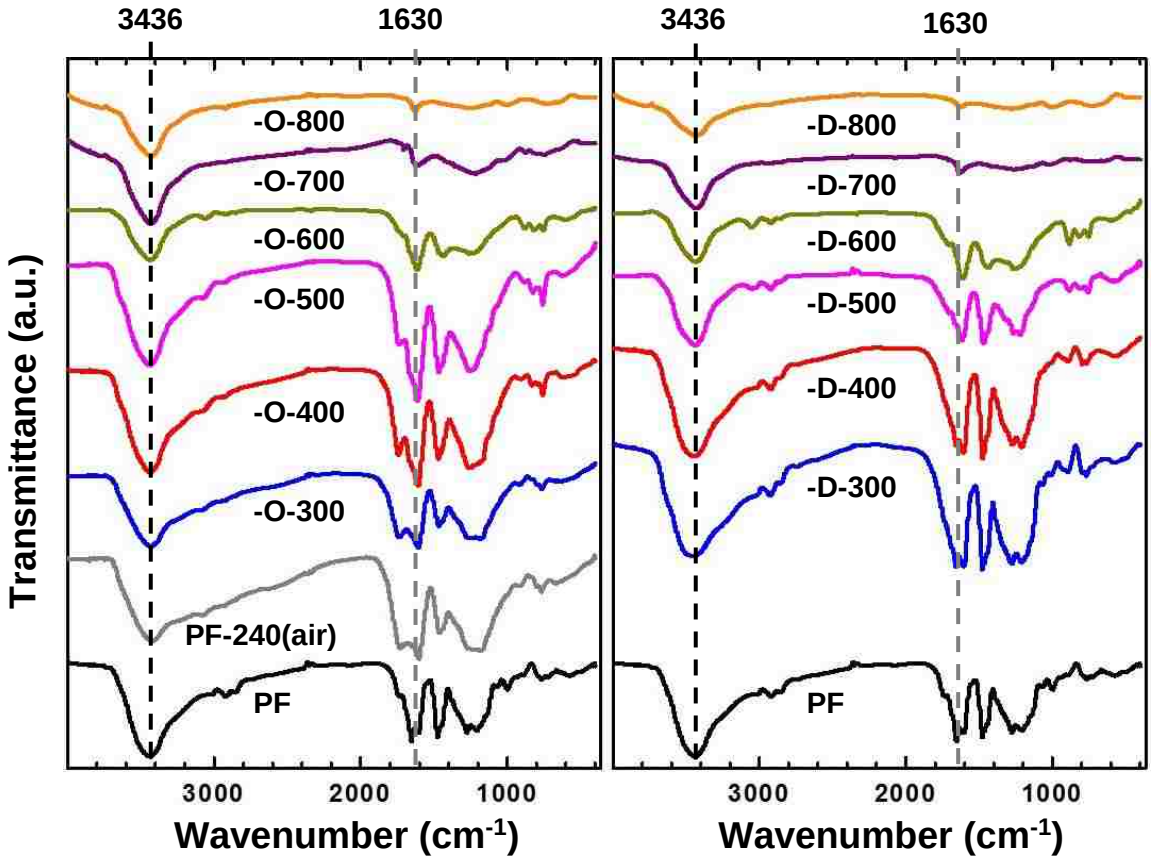

Figure S.III.2.D. FTIR spectra of **PF** and of air-oxidized **PF** (**PF-240(air)**) along pyrolysis at the temperatures (Θ) indicated in the format: –O-Θ and –D-Θ. ("D": Direct pyrolysis of **PF**; "O": Pyrolysis of the oxidized sample.) Dashed vertical lines mark the common absorptions surviving pyrolysis at 800 ^{o}C/Ar. (Cont.)

Appendix IV. O1s XPS Spectra

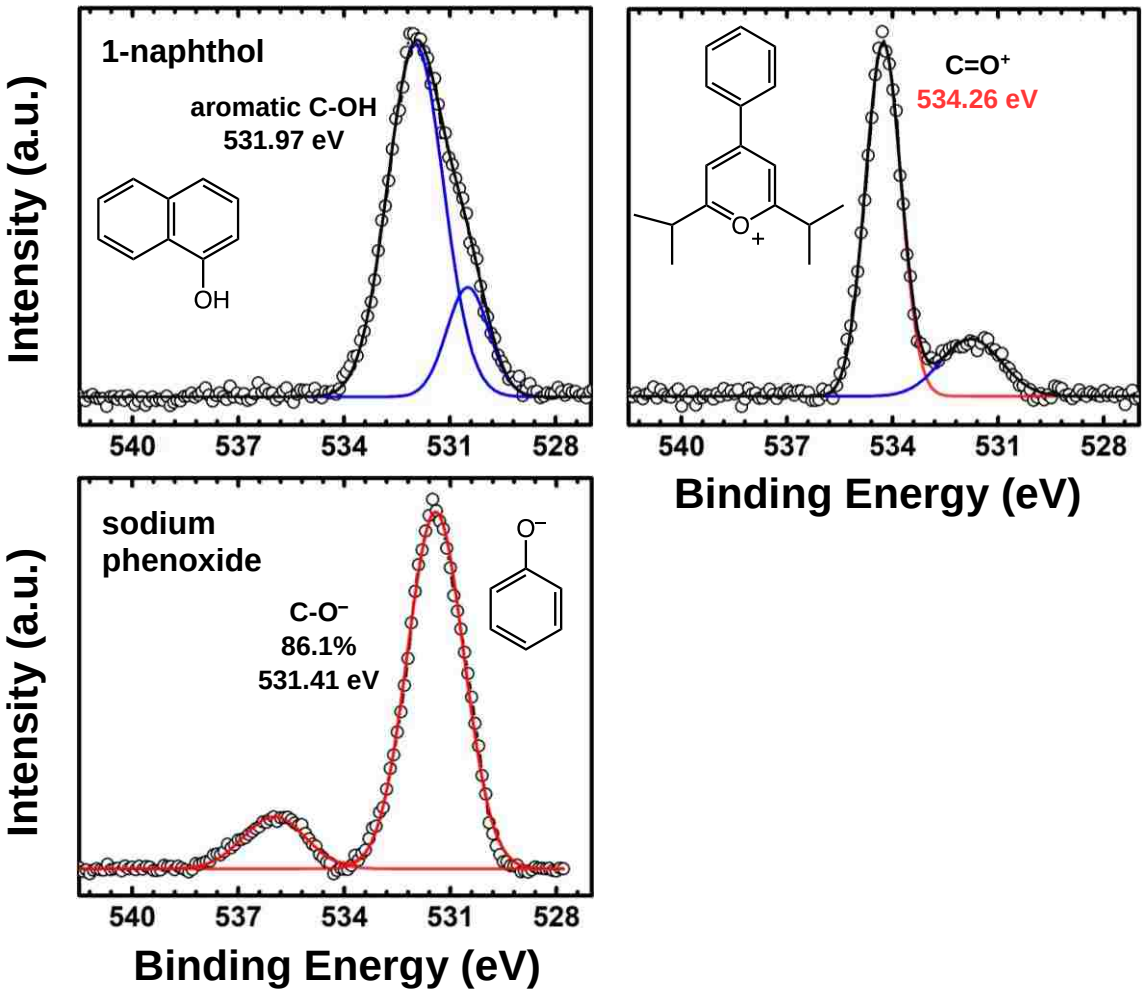

Figure S.IV.1. XPS control experiments: High-resolution O1s XPS spectra of the three compounds as indicated.

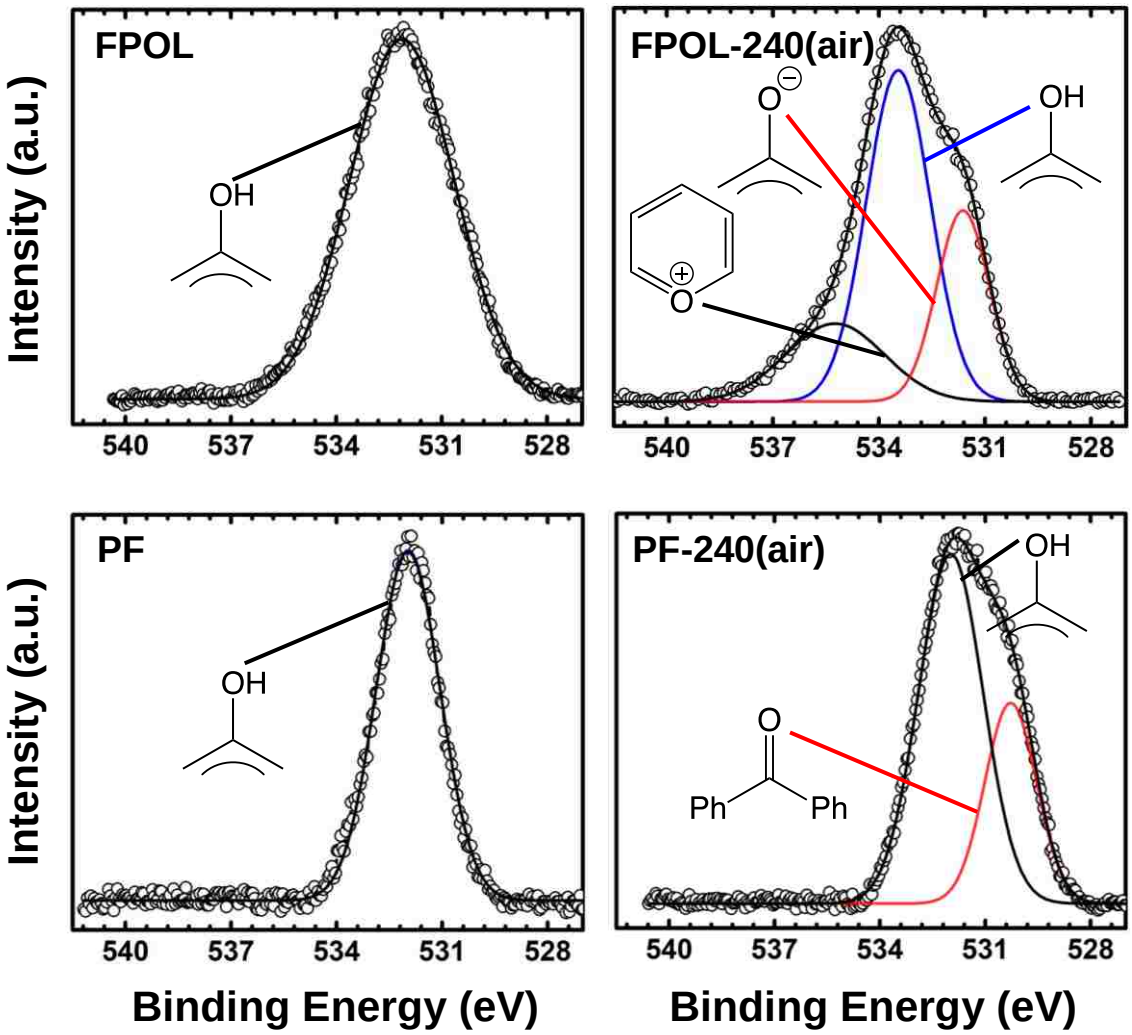

Figure S.IV.2. O1s XPS data for **FPOL** and **PF**, and their air-oxidation products as shown. (Similar spectra for **TPOL** and **RF** are shown in Figure 3 of the main article.)

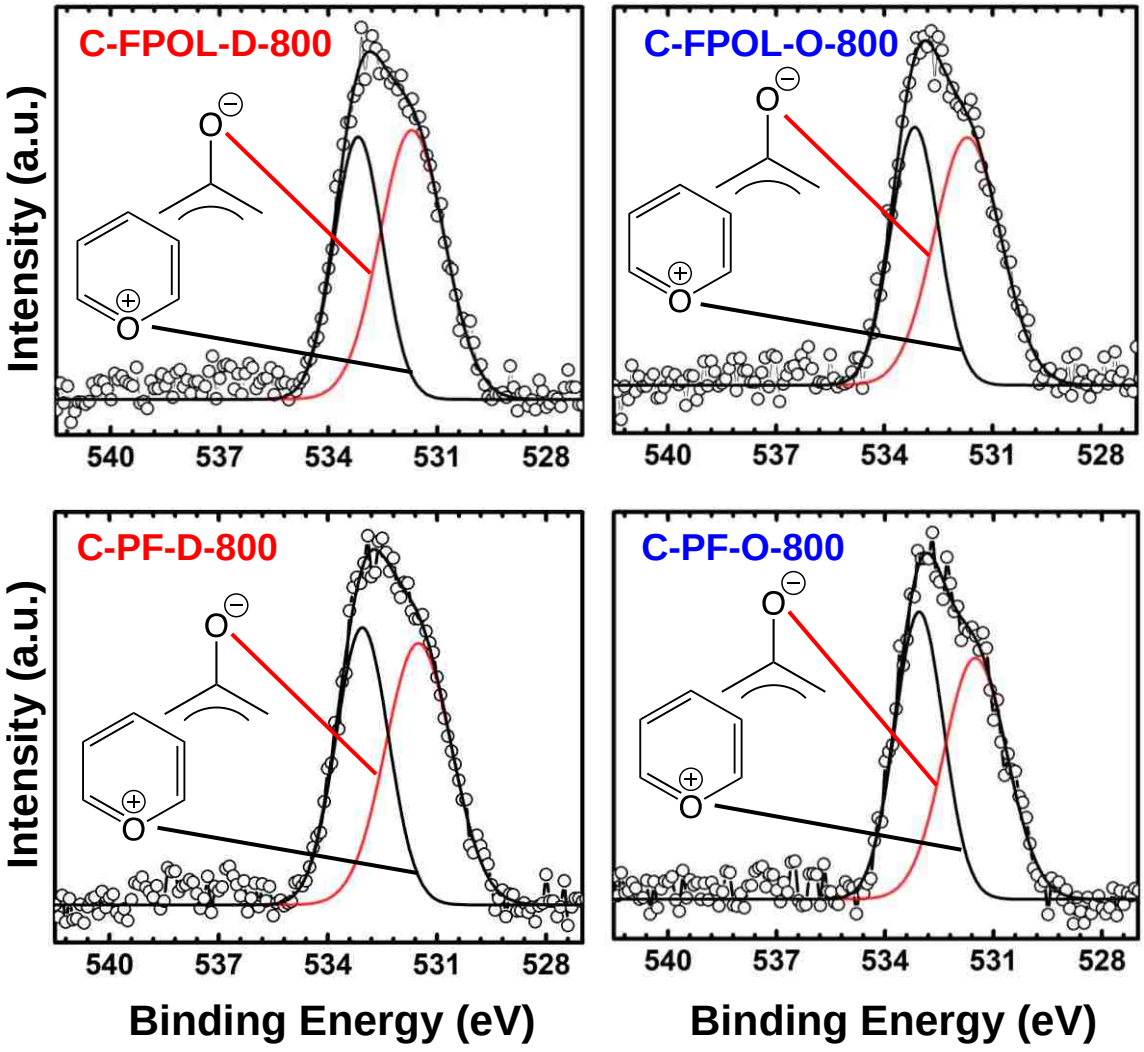

Figure S.IV.3. O1s XPS data from the 800 ºC-carbonized **C-FPOL-D-800** / **C-FPOL-O-800** and **C-PF-D-800** / **C-PF-O-800** pairs (top and bottom, respectively). (For the spectra of similar pairs from the **TPOL** and **RF** systems see Figure 7 of the main article.

Appendix V. Solid-state CPMAS ^{13}C NMR Spectra

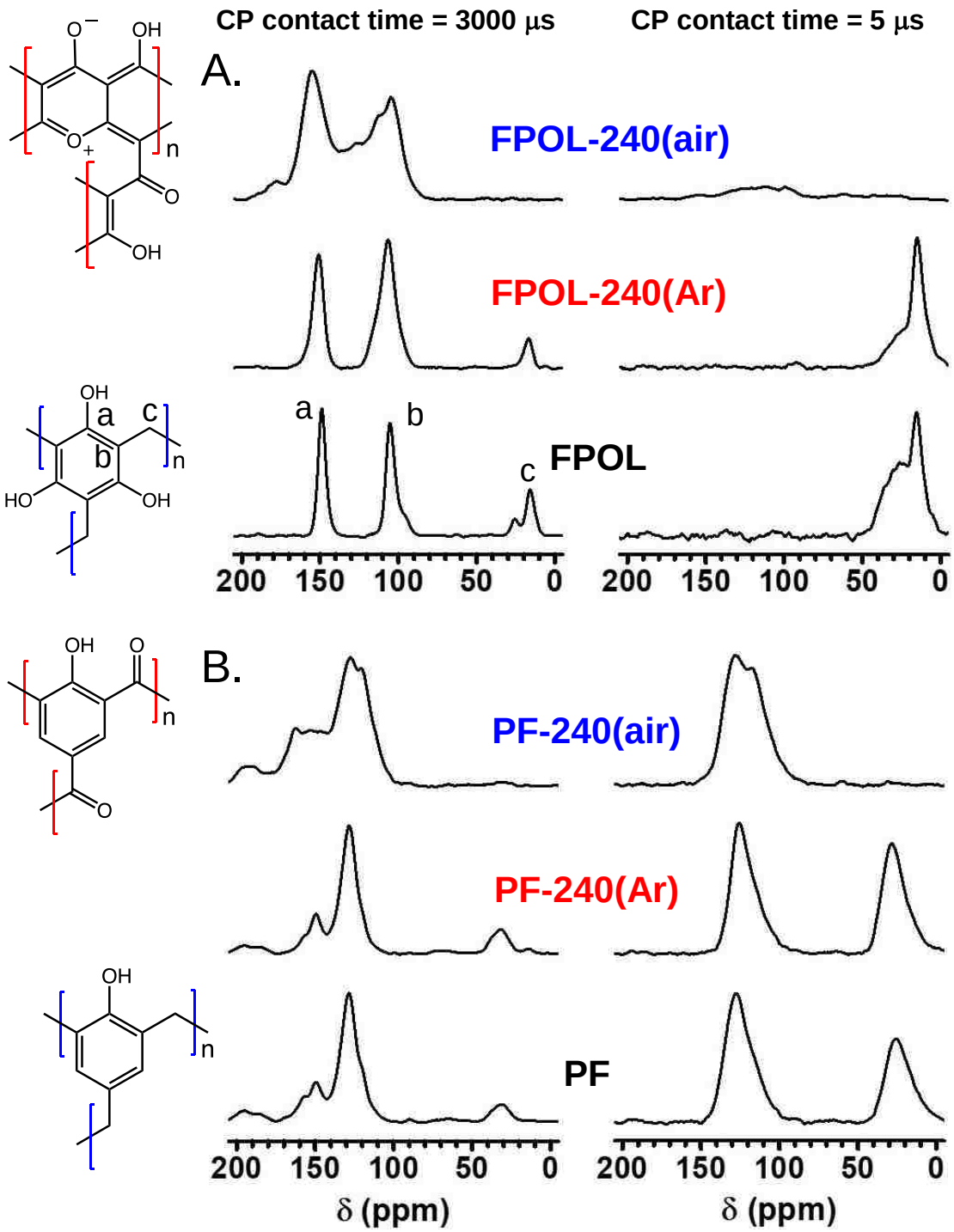

Figure S.V.1. Solid-state CPMAS ^{13}C NMR data for **FPOL** (A) and **PF** (B) and their pyrolyzed products at 240 ^{o}C under Ar or air, as shown.

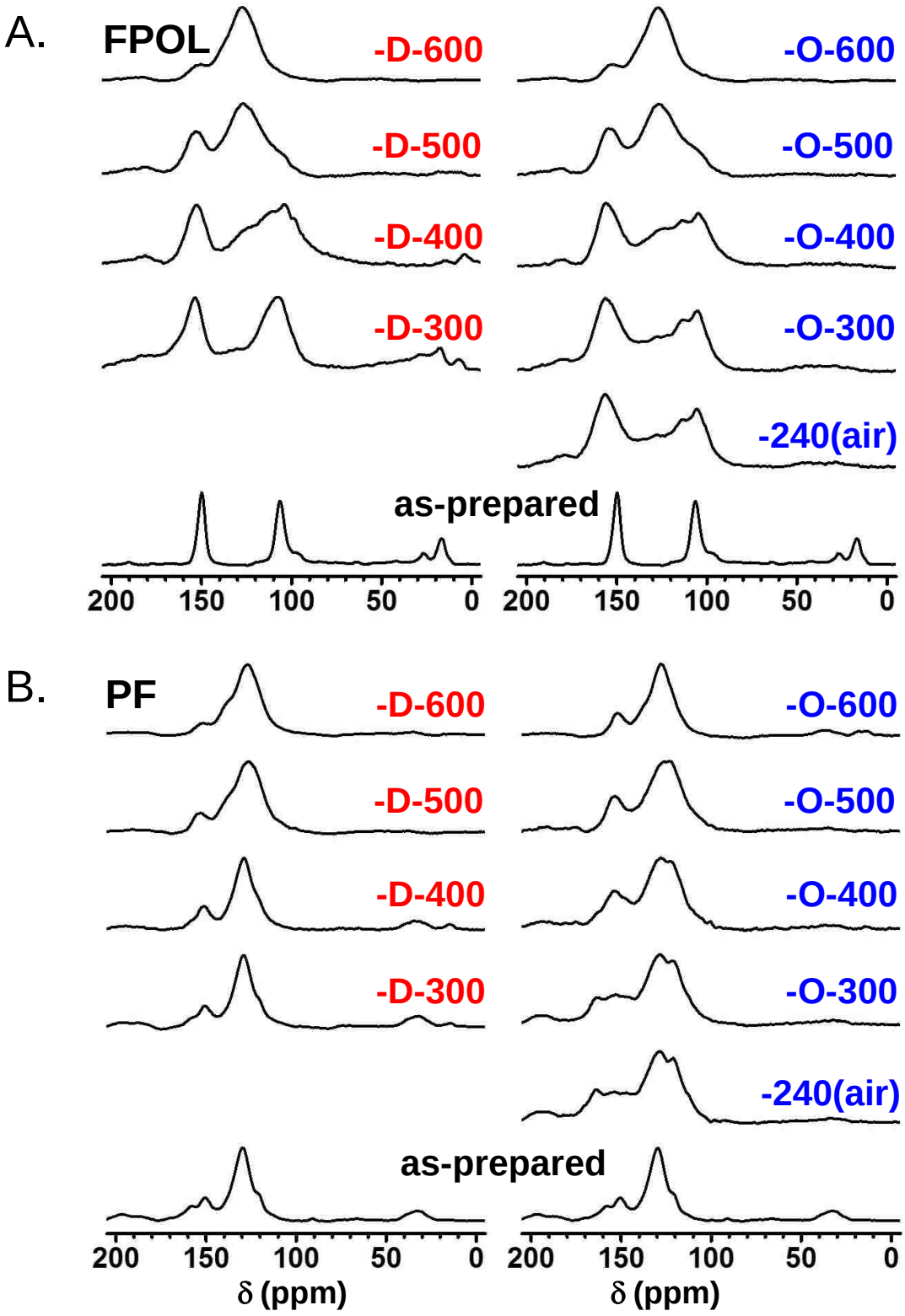

Figure S.V.2. Solid-state ^{13}C NMR data for **FPOL** (A) and **PF** (B) along pyrolysis as shown. (Similar spectra for **TPOL** and **RF** are shown in Figure 6 of the main article.)

Appendix VI. Air-oxidation Mechanism of FPOL

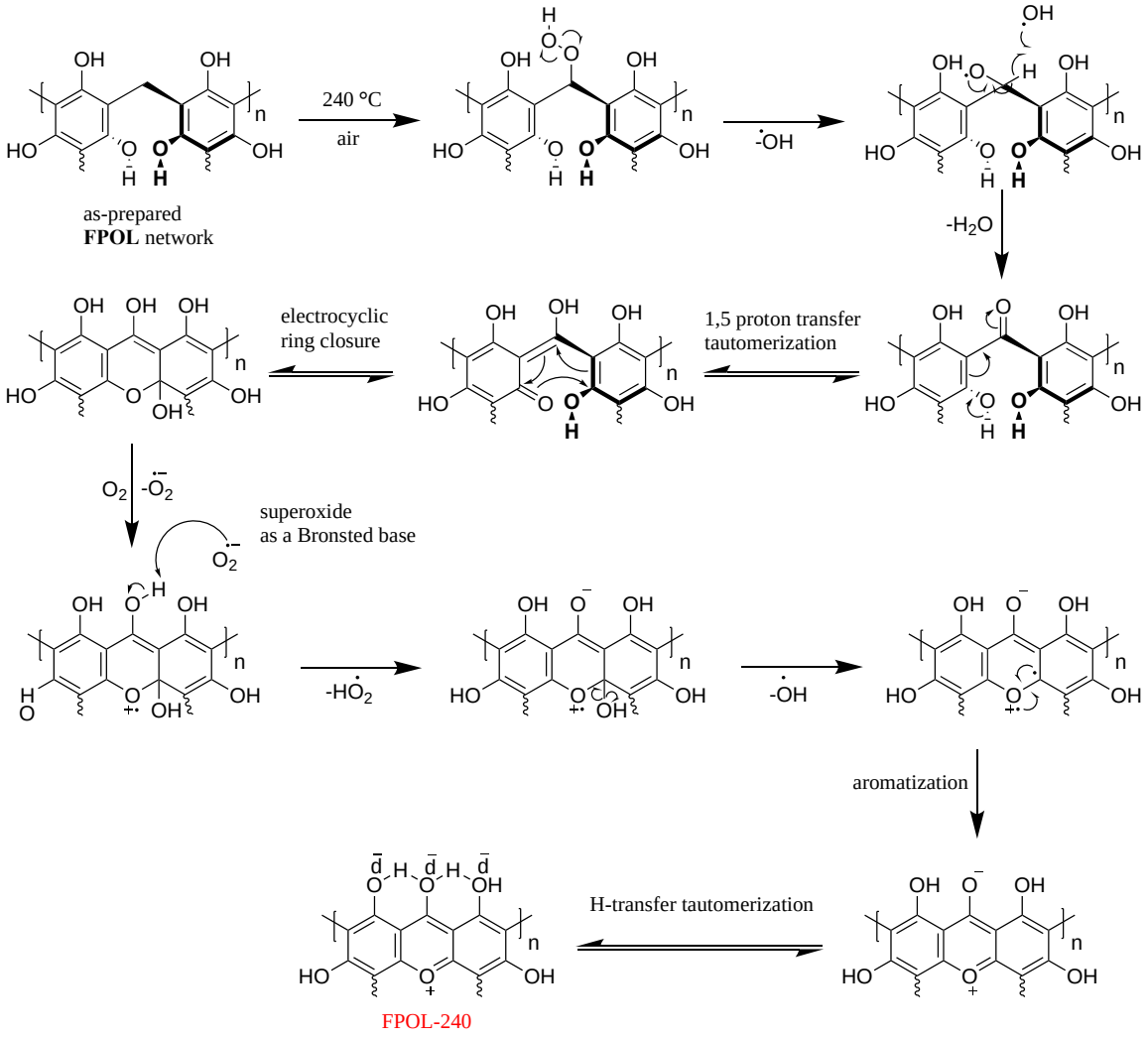

Appendix VII. Tables with Materials Characterization Data for All Samples

Table S.VII.1. Material characterization data of TPOL and all of its derivatives along air-oxidation, carbonization and etching

sample	linear shrinkage (%) [a, b]	bulk density, ρ_b (g cm^{-3}) [a]	skeletal density, ρ_s (g cm^{-3}) [c]	porosity, Π (% v/v)	specific pore volume (cm^3 g^{-1})				BET surf. area, σ [micropore] (m^2 g^{-1}) [h]	av. pore diameter (nm)	particle diameter, D, (nm) [j]
					V_{Total} $(1/\rho_b)$-$(1/\rho_s)$	$V_{1.7\text{-}300}$ (nm) [d]	$V_{>300}$ (nm) [e]	$V_{micropore}$ [f]		via $4\times V/\sigma$ [i]	
TPOL	32.2 ± 0.3	0.620 ± 0.009	1.434 ± 0.006	56.8 ± 0.8	0.92	0.91	0.00	$0.07 \pm 0.00_{04}$	501 [111]	7.32 [7.93]	8.35 ± 0.03
TPOL-240(Ar)	38.6 ± 0.6	0.635 ± 0.039	1.417 ± 0.002	55.2 ± 2.8	0.87	0.68	0.19	[g]	230 [31]	15.1 [11.7]	18.4 ± 0.03
TPOL-240(air)	46.1 ± 0.6	0.743 ± 0.014	1.538 ± 0.007	51.7 ± 1.0	0.70	0.46	0.20	$0.04 \pm 0.00_1$	200 [22]	13.9 [9.00]	19.5 ± 0.09
C-TPOL-D-300	40.0 ± 0.5	0.685 ± 0.007	1.394 ± 0.003	50.9 ± 0.6	0.74	0.74	0.00_2	[g]	280 [36]	10.6 [10.4]	15.4 ± 0.03
C-TPOL-O-300	44.7 ± 0.4	0.741 ± 0.013	1.479 ± 0.009	49.9 ± 1.1	0.67	0.66	0.01	[g]	326 [54]	8.26 [8.51]	12.4 ± 0.08
C-TPOL-D-400	43.4 ± 0.8	0.705 ± 0.012	1.379 ± 0.002	48.9 ± 0.9	0.69	0.72	0.00	[g]	385 [79]	7.20 [8.19]	11.3 ± 0.02
C-TPOL-O-400	46.8 ± 0.5	0.740 ± 0.002	1.452 ± 0.002	49.0 ± 0.2	0.66	0.71	0.00	[g]	495 [169]	5.35 [6.49]	8.35 ± 0.01
C-TPOL-D-500	47.2 ± 0.6	0.773 ± 0.017	1.397 ± 0.002	44.7 ± 1.2	0.58	0.56	0.02	[g]	531 [265]	4.35 [5.05]	8.09 ± 0.01
C-TPOL-O-500	49.2 ± 0.5	0.698 ± 0.001	1.430 ± 0.003	51.2 ± 0.2	0.73	0.71	0.02	[g]	624 [292]	4.70 [5.37]	6.72 ± 0.01
C-TPOL-D-600	48.9 ± 0.4	0.728 ± 0.034	1.454 ± 0.006	49.9 ± 2.4	0.69	0.55	0.14	[g]	592 ± 19 [320 ± 39]	$4.63 \pm 0.00_2$ [$4.58 \pm 0.00_2$]	6.97 ± 0.23
C-TPOL-O-600	51.6 ± 1.0	0.722 ± 0.024	1.474 ± 0.008	51.0 ± 1.7	0.71	0.51	0.20	[g]	666 ± 13 [388 ± 13]	$4.25 \pm 0.00_1$ [$4.04 \pm 0.00_1$]	6.11 ± 0.12
C-TPOL-D-700	51.8 ± 0.5	0.822 ± 0.017	1.693 ± 0.012	51.4 ± 1.3	0.63	0.48	0.15	[g]	451 ± 62 [225 ± 60]	5.55 ± 0.05 [4.98 ± 0.05]	7.86 ± 1.08
C-TPOL-O-700	53.9 ± 0.6	0.736 ± 0.018	1.708 ± 0.010	56.9 ± 1.3	0.77	0.46	0.31	[g]	585 ± 20 [332 ± 20]	$5.29 \pm 0.00_3$ [$3.99 \pm 0.00_3$]	6.00 ± 0.21
C-TPOL-D-800	53.4 ± 0.1	0.798 ± 0.008	1.794 ± 0.003	55.5 ± 0.5	0.70	0.52	0.06	$0.12 \pm 0.00_1$	527 ± 58 [292 ± 52]	5.29 ± 0.03 [5.20 ± 0.04]	6.35 ± 0.70
C-TPOL-O-800	52.8 ± 0.8	0.708 ± 0.039	1.776 ± 0.007	60.1 ± 2.2	0.85	0.62	0.10	$0.13 \pm 0.00_2$	628 ± 46 [349 ± 37]	5.41 ± 0.01 [4.77 ± 0.01]	5.38 ± 0.39

[a] Average of 5 samples. [b] Shrinkage = 100 × (mold diameter – sample diameter)/ (mold diameter). [c] Single sample, average of 50 measurements. [d] BJH-desorption cumulative pore volume. [e] Via $V_{>300} = V_{Total} - (V_{1.7\text{-}300} + V_{micropore})$. [f] $V_{micropore}$ was calculated with CO_2-sorption up to 760 Torr and relative pressure of 0.03 at 273 K via the Horvath-Kawazoe method. [g] Not measured. [h] Average of 3 samples. First number indicates the BET surface area; the number in the square bracket indicates the micropore area obtained by t-plot analysis. [i] For the first number, V was calculated via $V_{Total} = (1/\rho_b) - (1/\rho_s)$; for the number in brackets, V was calculated by the single-point adsorption method. [j] Via $D = 6 / (\rho_s \times \sigma)$.

Table S.VII.1. Material characterization data of TPOL and all of its derivatives along air-oxidation, carbonization and etching (Cont.)

sample	linear shrinkage (%) [a, b]	bulk density, ρ_b (g cm^{-3}) [a]	skeletal density, ρ_s (g cm^{-3}) [c]	porosity, Π (% v/v)	specific pore volume (cm^3 g^{-1})				BET surf. area, σ [micropore] (m^2 g^{-1}) [i]	av. pore diameter (nm)
					V_{Total} [d]	$V_{1.7\text{-}300}$ (nm) [e]	$V_{>300}$ (nm) [f]	$V_{micropore}$ [g]		via $4\times V/\sigma$ [j]
EC-TPOL-D-600	54.1 ± 0.1	0.333 ± 0.051	2.093 ± 0.005	84.1 ± 2.5	2.53	1.57	0.86	0.10 ± 0.00$_{03}$	2143 ± 165 [1246 ± 12]	4.71 ± 0.01 [3.88 ± 0.02]
EC-TPOL-O-600	56.6 ± 1.2	0.227 ± 0.083	2.221 ± 0.011	89.8 ± 3.8	3.96	1.72	2.10	0.14 ± 0.00$_{1}$	2778 ± 209 [894 ± 87]	5.69 ± 0.03 [3.63 ± 0.02]
EC-TPOL-D-700	54.9 ± 1.1	0.459 ± 0.089	1.962 ± 0.004	76.6 ± 4.5	1.67	1.69	0.00	[h]	2244 ± 228 [1007 ± 98]	2.97 ± 0.02 [3.45 ± 0.11]
EC-TPOL-O-700	54.9 ± 0.4	0.394 ± 0.062	1.994 ± 0.039	80.2 ± 4.0	2.04	0.76	1.28	[h]	2275 ± 140 [1113 ± 47]	3.58 ± 0.01 [2.89 ± 0.02]
EC-TPOL-D-800	54.4 ± 0.4	0.381 ± 0.035	2.082 ± 0.009	81.7 ± 1.8	2.14	1.34	0.55	0.25 ± 0.00$_{2}$	1752 ± 46 [1069 ± 12]	4.90 ± 0.00$_{2}$ [3.73 ± 0.01]
EC-TPOL-O-800	60.2 ± 1.0	0.422 ± 0.054	2.072 ± 0.008	79.6 ± 2.7	1.89	1.09	0.54	0.26 ± 0.00$_{3}$	2568 ± 75 [877 ± 48]	2.94 ± 0.00$_{1}$ [3.08 ± 0.03]

[a] Average of 5 samples. [b] Shrinkage = 100 × (mold diameter – sample diameter)/ (mold diameter). [c] Single sample, average of 50 measurements. [d] Calculated via $V_{Tot} = (1/\rho_b) - (1/\rho_s)$. [e] BJH-desorption cumulative pore volume. [f] Via $V_{>300} = V_{Total} - (V_{1.7\text{-}300} + V_{micropore})$. [g] $V_{micropore}$ was calculated with CO_2-sorption up to 760 Torr and relative pressure of 0.03 at 273 K via the Horvath-Kawazoe method. [h] Not measured. [i] Average of 3 samples. First number indicates the BET surface area; the number in the square bracket indicates the micropore area obtained by t-plot analysis. [j] For the first number, V was calculated via $V_{Total} = (1/\rho_b) - (1/\rho_s)$; for the number in brackets, V was calculated by the single-point adsorption method.

Table S.VII.2. Material characterization data of FPOL and all of its derivatives along air-oxidation, carbonization and etching

sample	linear shrinkage (%) [a, b]	bulk density, ρ_b (g cm^{-3}) [a]	skeletal density, ρ_s (g cm^{-3}) [c]	porosity, Π (% v/v)	specific pore volume (cm^3 g^{-1})				BET surf. area, σ [micropore] (m^2 g^{-1}) [h]	av. pore diameter (nm)	particle diameter, D, (nm) [j]
					V_{Total} $(1/\rho_b)$-$(1/\rho_s)$	$V_{1.7\text{-}300}$ (nm) [d]	$V_{>300}$ (nm) [e]	$V_{micropore}$ [f]		via $4\times V/\sigma$ [i]	
FPOL	41.9 ± 0.3	0.474 ± 0.007	1.508 ± 0.002	68.6 ± 0.5	1.45	1.38	0.00	0.08 ± 0.00$_1$	679 [142]	8.52 [8.54]	5.86 ± 0.01
FPOL-240(Ar)	47.5 ± 0.2	0.554 ± 0.015	1.505 ± 0.005	63.2 ± 1.1	1.14	1.05	0.09	[g]	396 [31]	11.5 [10.1]	10.1 ± 0.03
FPOL-240(air)	60.6 ± 0.2	0.824 ± 0.011	1.609 ± 0.007	48.8 ± 0.8	0.59	0.63	0.00	0.06 ± 0.0$_{002}$	338 [49]	7.02 [7.48]	11.0 ± 0.05
C-FPOL-D-300	48.4 ± 0.5	0.577 ± 0.005	1.487 ± 0.003	61.2 ± 0.4	1.06	1.03	0.03	[g]	323 [23]	13.1 [12.7]	12.5 ± 0.03
C-FPOL-O-300	60.4 ± 0.7	0.809 ± 0.015	1.610 ± 0.002	49.8 ± 0.9	0.61	0.61	0.00	[g]	337 [48]	7.30 [7.31]	11.1 ± 0.01
C-FPOL-D-400	52.6 ± 0.2	0.639 ± 0.006	1.499 ± 0.003	57.4 ± 0.5	0.90	0.94	0.00	[g]	370 [54]	9.71 [10.4]	10.8 ± 0.02
C-FPOL-O-400	62.8 ± 0.7	0.808 ± 0.020	1.581 ± 0.002	48.9 ± 1.3	0.61	0.56	0.05	[g]	493 [164]	4.91 [5.37]	7.70 ± 0.01
C-FPOL-D-500	54.5 ± 0.4	0.620 ± 0.010	1.472 ± 0.004	57.9 ± 0.7	0.93	0.84	0.09	[g]	541 [225]	6.90 [7.01]	7.53 ± 0.02
C-FPOL-O-500	64.4 ± 0.5	0.743 ± 0.009	1.543 ± 0.005	51.8 ± 0.7	0.70	0.60	0.10	[g]	674 [321]	4.14 [4.49]	5.77 ± 0.02
C-FPOL-D-600	57.3 ± 0.1	0.638 ± 0.008	1.540 ± 0.015	58.6 ± 1.2	0.92	0.79	0.13	[g]	617± 12 [314 ± 12]	5.96 ± 0.00$_1$ [6.12 ± 0.00$_2$]	6.31 ± 0.14
C-FPOL-O-600	66.8 ± 0.6	0.727 ± 0.015	1.560 ± 0.011	53.4 ± 1.3	0.73	0.62	0.11	[g]	761 ± 13 [391 ± 9]	3.86 ± 0.00$_1$ [4.24 ± 0.00$_1$]	5.05 ± 0.09
C-FPOL-D-700	59.4 ± 0.5	0.678 ± 0.015	1.738 ± 0.051	61.0 ± 3.5	0.90	0.74	0.16	[g]	553 ± 75 [257 ± 73]	6.51 ± 0.06 [6.19 ± 0.06]	6.24 ± 0.87
C-FPOL-O-700	68.0 ± 0.4	0.753 ± 0.011	1.776 ± 0.028	57.6 ± 1.9	0.76	0.68	0.08	[g]	736 ± 45 [362 ± 36]	4.16 ± 0.01 [4.23 ± 0.01]	4.59 ± 0.31
C-FPOL-D-800	60.5 ± 0.2	0.717 ± 0.012	1.884 ± 0.050	61.9 ± 3.2	0.86	0.72	0.04	0.10 ± 0.00$_1$	493 ± 70 [213 ± 65]	7.01 ± 0.07 [6.46 ± 0.07]	6.46 ± 0.93
C-FPOL-O-800	69.0 ± 0.5	0.793 ± 0.010	1.958 ± 0.019	59.5 ± 1.2	0.75	0.57	0.05	0.13 ± 0.00$_1$	594 ± 97 [247± 91]	5.05 ± 0.07 [4.48 ± 0.07]	5.16 ± 0.84

[a] Average of 5 samples. [b] Shrinkage = 100 × (mold diameter – sample diameter)/ (mold diameter). [c] Single sample, average of 50 measurements. [d] BJH-desorption cumulative pore volume. [e] Via $V_{>300} = V_{Total} - (V_{1.7\text{-}300} + V_{micropore})$. [f] $V_{micropore}$ was calculated with CO_2-sorption up to 760 Torr and relative pressure of 0.03 at 273 K via the Horvath-Kawazoe method. [g] Not measured. [h] Average of 3 samples. First number indicates the BET surface area; the number in the square bracket indicates the micropore area obtained by t-plot analysis. [i] For the first number, V was calculated via $V_{Total} = (1/\rho_b) - (1/\rho_s)$; for the number in brackets, V was calculated by the single-point adsorption method. [j] Via $D = 6 / (\rho_s \times \sigma)$.

Table S.VII.2. Material characterization data of FPOL and all of its derivatives along air-oxidation, carbonization and etching (Cont.)

sample	linear shrinkage (%) [a, b]	bulk density, ρ_b (g cm^{-3}) [a]	skeletal density, ρ_s (g cm^{-3}) [c]	porosity, Π (% v/v)	specific pore volume (cm^3 g^{-1})				BET surf. area, σ [micropore] (m^2 g^{-1}) [i]	av. pore diameter (nm)
					V_{Total} [d]	$V_{1.7\text{-}300}$ (nm) [e]	$V_{>300}$ (nm) [f]	$V_{micropore}$ [g]		via $4\times V/\sigma$ [j]
EC-FPOL-D-600	61.1 ± 0.1	0.540 ± 0.035	2.155 ± 0.021	74.9 ± 2.0	1.39	0.97	0.35	0.07 ± 0.00$_{03}$	1102 ± 34 [742 ± 27]	5.04 ± 0.00$_2$ [4.52 ± 0.00$_3$]
EC-FPOL-O-600	70.1 ± 0.2	0.518 ± 0.028	2.270 ± 0.036	77.2 ± 2.4	1.49	0.89	0.45	0.15 ± 0.00$_2$	1612 ± 40 [985 ± 26]	3.73 ± 0.00$_1$ [3.27 ± 0.00$_2$]
EC-FPOL-D-700	58.4 ± 1.4	0.525 ± 0.091	1.947 ± 0.009	73.0 ± 4.7	1.39	0.89	0.40	0.10 ± 0.00$_1$	1078 ± 121 [697 ± 97]	5.16 ± 0.03 [4.46 ± 0.07]
EC-FPOL-O-700	68.7 ± 0.2	0.525 ± 0.058	2.232 ± 0.019	76.5 ± 2.8	1.46	0.86	0.49	0.11 ± 0.00$_1$	1466 ± 61 [883 ± 24]	3.97 ± 0.00$_4$ [3.37 ± 0.01]
EC-FPOL-D-800	62.1 ± 0.4	0.595 ± 0.053	2.179 ± 0.020	72.7 ± 2.7	1.22	0.95	0.03	0.24 ± 0.00$_1$	943 ± 90 [595 ± 83]	5.18 ± 0.02 [4.73 ± 0.03]
EC-FPOL-O-800	70.0 ± 0.5	0.627 ± 0.078	2.114 ± 0.015	70.3 ± 3.8	1.12	0.71	0.14	0.27 ± 0.00$_4$	1088 ± 52 [657 ± 47]	4.12 ± 0.00$_5$ [3.56 ± 0.01]

[a] Average of 5 samples. [b] Shrinkage = 100 × (mold diameter – sample diameter)/ (mold diameter). [c] Single sample, average of 50 measurements. [d] Calculated via $V_{Total} = (1/\rho_b) - (1/\rho_s)$. [e] BJH-desorption cumulative pore volume. [f] Via $V_{>300} = V_{Total} - (V_{1.7\text{-}300} + V_{micropore})$. [g] $V_{micropore}$ was calculated with CO_2-sorption up to 760 Torr and relative pressure of 0.03 at 273 K via the Horvath-Kawazoe method. [h] Not measured. [i] Average of 3 samples. First number indicates the BET surface area; the number in the square bracket indicates the micropore area obtained by t-plot analysis. [j] For the first number, V was calculated via $V_{Total} = (1/\rho_b) - (1/\rho_s)$; for the number in brackets, V was calculated by the single-point adsorption method.

Table S.VII.3. Material characterization data of RF and all of its derivatives along air-oxidation, carbonization and etching

sample	linear shrinkage (%) [a, b]	bulk density, ρ_b (g cm^{-3}) [a]	skeletal density, ρ_s (g cm^{-3}) [c]	porosity, Π (% v/v)	specific pore volume (cm^3 g^{-1})				BET surf. area, σ [micropore] (m^2 g^{-1}) [h]	av. pore diameter (nm)	particle diameter, D, (nm) [j]
					V_{Total} $(1/\rho_b)-(1/\rho_s)$	$V_{1.7\text{-}300}$ (nm) [d]	$V_{>300}$ (nm) [e]	$V_{micropore}$ [f]		via $4\times V/\sigma$ [i]	
RF	34.0 ± 0.9	0.160 ± 0.006	1.310 ± 0.007	87.8 ± 0.8	5.49	2.34	3.09	0.06 ± 0.00$_1$	625 [77]	35.1 [15.4]	7.33 ± 0.04
RF-240(Ar)	44.2 ± 0.4	0.211 ± 0.009	1.411 ± 0.008	85.0 ± 1.0	4.03	2.14	1.89	[g]	387 [35]	41.7 [22.0]	11.0 ± 0.06
RF-240(air)	57.0 ± 0.7	0.326 ± 0.011	1.572 ± 0.006	79.3 ± 0.9	2.43	1.58	0.80	0.05 ± 0.00$_3$	385 [48]	25.3 [13.0]	9.91 ± 0.04
C-RF-D-300	43.5 ± 0.4	0.198 ± 0.001	1.365 ± 0.020	85.5 ± 1.9	4.32	4.22	0.10	[g]	523 [48]	33.0 [32.3]	8.40 ± 0.12
C-RF-O-300	53.5 ± 0.7	0.280 ± 0.009	1.533 ± 0.021	81.7 ± 1.9	2.92	1.41	1.51	[g]	478 [80]	24.4 [12.2]	8.19 ± 0.11
C-RF-D-400	47.3 ± 0.2	0.214 ± 0.003	1.448 ± 0.038	85.2 ± 3.5	3.98	3.89	0.09	[g]	571 [70]	27.9 [27.2]	7.26 ± 0.19
C-RF-O-400	56.5 ± 1.2	0.309 ± 0.017	1.505 ± 0.033	79.5 ± 3.0	2.57	2.36	0.21	[g]	579 [86]	17.8 [16.4]	6.89 ± 0.15
C-RF-D-500	50.5 ± 0.2	0.218 ± 0.004	1.404 ± 0.026	84.5 ± 2.4	3.87	3.86	0.01	[g]	720 [185]	21.5 [21.4]	5.94 ± 0.11
C-RF-O-500	58.0 ± 0.6	0.286 ± 0.005	1.466 ± 0.012	80.5 ± 1.1	2.81	2.77	0.04	[g]	844 [232]	13.3 [13.5]	4.85 ± 0.04
C-RF-D-600	52.9 ± 0.4	0.210 ± 0.003	1.536 ± 0.013	86.3 ± 1.1	4.11	2.25	1.86	[g]	823 ± 14 [284 ± 7]	20.0 ± 0.0$_{03}$ [19.2 ± 0.0$_1$]	4.75 ± 0.09
C-RF-O-600	58.4 ± 0.5	0.232 ± 0.008	1.506 ± 0.017	84.6 ± 1.6	3.65	3.04	0.61	[g]	827 ± 9 [296 ± 9]	17.6 ± 0.0$_{01}$ [15.0 ± 0.0$_1$]	4.82 ± 0.08
C-RF-D-700	55.6 ± 0.1	0.236 ± 0.003	1.556 ± 0.020	84.8 ± 1.7	3.59	3.34	0.25	[g]	712 ± 30 [230 ± 30]	20.2 ± 0.0$_2$ [19.0 ± 0.0$_2$]	5.42 ± 0.24
C-RF-O-700	62.3 ± 0.9	0.288 ± 0.010	1.612 ± 0.024	82.1 ± 2.0	2.85	2.62	0.23	[g]	697 ± 20 [213 ± 9]	16.4 ± 0.01 [15.5 ± 0.0$_2$]	5.34 ± 0.17
C-RF-D-800	56.2 ± 0.5	0.230 ± 0.005	1.805 ± 0.010	87.3 ± 0.8	3.79	3.73	0.00	0.12 ± 0.00$_2$	753 ± 94 [248 ± 38]	20.2 ± 0.2 [18.7 ± 0.3]	4.41 ± 0.55
C-RF-O-800	66.8 ± 0.7	0.302 ± 0.014	1.816 ± 0.017	83.4 ± 1.4	2.76	2.59	0.05	0.12 ± 0.00$_2$	760 ± 64 [251 ± 52]	14.5 ± 0.1 [14.1 ± 0.2]	4.35 ± 0.37

[a] Average of 5 samples. [b] Shrinkage = 100 × (mold diameter – sample diameter)/ (mold diameter). [c] Single sample, average of 50 measurements. [d] BJH-desorption cumulative pore volume. [e] Via $V_{>300} = V_{Total} - (V_{1.7\text{-}300} + V_{micropore})$. [f] $V_{micropore}$ was calculated with CO_2-sorption up to 760 Torr and relative pressure of 0.03 at 273 K via the Horvath-Kawazoe method. [g] Not measured. [h] Average of 3 samples. First number indicates the BET surface area; the number in the square bracket indicates the micropore area obtained by t-plot analysis. [i] For the first number, V was calculated via $V_{Total} = (1/\rho_b) - (1/\rho_s)$; for the number in brackets, V was calculated by the single-point adsorption method. [j] Via $D = 6 / (\rho_s \times \sigma)$.

Table S.VII.3. Material characterization data of RF and all of its derivatives along air-oxidation, carbonization and etching (Cont.)

sample	linear shrinkage (%) [a, b]	bulk density, ρ_b (g cm^{-3}) [a]	skeletal density, ρ_s (g cm^{-3}) [c]	porosity, Π (% v/v)	specific pore volume (cm^3 g^{-1})				BET surf. area, σ [micropore] (m^2 g^{-1}) [i]	av. pore diameter (nm)
					V_{Total} [d]	$V_{1.7\text{-}300}$ (nm) [e]	$V_{>300}$ (nm) [f]	$V_{micropore}$ [g]		via $4\times V/\sigma$ [j]
EC-RF-D-600	59.0 ± 0.2	0.162 ± 0.019	2.321 ± 0.059	93.0 ± 3.6	5.74	5.47	0.27	[h]	1970 ± 7 [1111 ± 7]	11.7 ± 0.0$_{004}$ [11.9 ± 0.0$_{001}$]
EC-RF-O-600	64.8 ± 0.7	0.202 ± 0.014	2.301 ± 0.078	91.2 ± 4.6	4.52	4.18	0.34	[h]	1582 ± 80 [911 ± 47]	11.4 ± 0.0$_1$ [11.1 ± 0.0$_2$]
EC-RF-D-700	62.5 ± 1.8	0.137 ± 0.013	2.281 ± 0.090	94.0 ± 5.4	6.86	5.37	1.49	[h]	2334 ± 164 [733 ± 91]	11.8 ± 0.0$_3$ [9.28 ± 0.04]
EC-RF-O-700	68.9 ± 1.1	0.198 ± 0.017	2.301 ± 0.088	91.4 ± 5.2	4.62	3.72	0.90	[h]	2341 ± 48 [959 ± 35]	7.89 ± 0.00$_2$ [7.19 ± 0.00$_3$]
EC-RF-D-800	59.1 ± 0.2	0.145 ± 0.005	2.147 ± 0.043	93.2 ± 2.7	6.43	6.36	0.00	0.44 ± 0.00$_1$	2355 ± 145 [1112 ± 105]	10.9 ± 0.0$_4$ [11.5 ± 0.0$_5$]
EC-RF-O-800	68.6 ± 1.1	0.166 ± 0.009	2.024 ± 0.030	91.8 ± 2.1	5.53	5.01	0.08	0.44 ± 0.00$_2$	2484 ± 161 [1030 ± 76]	8.91 ± 0.02 [8.69 ± 0.03]

[a] Average of 5 samples. [b] Shrinkage = 100 × (mold diameter – sample diameter)/ (mold diameter). [c] Single sample, average of 50 measurements. [d] Calculated via $V_{Tot} = (1/\rho_b) - (1/\rho_s)$. [e] BJH-desorption cumulative pore volume. [f] Via $V_{>300} = V_{Total} - (V_{1.7\text{-}300} + V_{micropore})$. [g] $V_{micropore}$ was calculated with CO_2-sorption up to 760 Torr and relative pressure of 0.03 at 273 K via the Horvath-Kawazoe method. [h] Not measured. [i] Average of 3 samples. First number indicates the BET surface area; the number in the square bracket indicates the micropore area obtained by t-plot analysis [j] For the first number, V was calculated via $V_{Total} = (1/\rho_b) - (1/\rho_s)$; for the number in brackets, V was calculated by the single-point adsorption method.

Table S.VII.4. Material characterization data of PF and all of its derivatives along air-oxidation, carbonization and etching

sample	linear shrinkage (%) [a, b]	bulk density, ρ_b (g cm^{-3}) [a]	skeletal density, ρ_s (g cm^{-3}) [c]	porosity, Π (% v/v)	specific pore volume (cm^3 g^{-1})				BET surf. area, σ [micropore] (m^2 g^{-1}) [h]	av. pore diameter (nm)	particle diameter, D, (nm) [j]
					V_{Total} $(1/\rho_b)$-$(1/\rho_s)$	$V_{1.7\text{-}300}$ (nm) [d]	$V_{>300}$ (nm) [e]	$V_{micropore}$ [f]		via $4\times V/\sigma$ [i]	
PF	35.1 ± 0.4	0.454 ± 0.011	1.257 ± 0.001	63.9 ± 0.9	1.41	1.19	0.19	0.03 ± 0.00$_{01}$	199 [6]	28.3 [23.9]	24.0 ± 0.02
PF-240(Ar)	38.3 ± 0.6	0.479 ± 0.011	1.266 ± 0.002	62.2 ± 0.9	1.30	1.16	0.14	[g]	221 [25]	23.5 [21.1]	21.4 ± 0.03
PF-240(air)	43.2 ± 0.4	0.652 ± 0.015	1.505 ± 0.002	56.7 ± 1.0	0.87	0.81	0.02	0.04 ± 0.00$_2$	142 [24]	24.5 [22.9]	28.1 ± 0.04
C-PF-D-300	39.1 ± 0.9	0.485 ± 0.029	1.274 ± 0.001	61.9 ± 2.3	1.28	1.14	0.14	[g]	226 [32]	22.6 [20.4]	20.8 ± 0.03
C-PF-O-300	44.2 ± 0.2	0.658 ± 0.015	1.486 ± 0.001	55.7 ± 1.0	0.85	0.84	0.01	[g]	153 [30]	22.1 [21.9]	26.4 ± 0.02
C-PF-D-400	39.3 ± 0.7	0.473 ± 0.014	1.266 ± 0.001	62.6 ± 1.1	1.32	1.20	0.12	[g]	262 [37]	20.2 [18.9]	18.1 ± 0.01
C-PF-O-400	47.6 ± 0.6	0.653 ± 0.045	1.438 ± 0.002	54.6 ± 3.1	0.84	0.81	0.03	[g]	333 [121]	10.0 [11.0]	12.5 ± 0.02
C-PF-D-500	44.4 ± 0.8	0.501 ± 0.018	1.265 ± 0.002	60.4 ± 1.4	1.21	1.02	0.19	[g]	511 [261]	9.44 [9.35]	9.28 ± 0.01
C-PF-O-500	48.6 ± 0.4	0.596 ± 0.014	1.408 ± 0.003	57.7 ± 1.0	0.97	0.90	0.07	[g]	580 [339]	6.67 [7.34]	7.35 ± 0.02
C-PF-D-600	48.8 ± 1.0	0.541 ± 0.017	1.428 ± 0.008	62.1 ± 1.4	1.15	0.88	0.27	[g]	620 ± 95 [392 ± 85]	7.41 ± 0.09 [6.83 ± 0.10]	6.78 ± 1.04
C-PF-O-600	51.3 ± 1.2	0.577 ± 0.033	1.461 ± 0.007	60.5 ± 2.3	1.05	0.82	0.23	[g]	609 ± 43 [395± 49]	6.89 ± 0.02 [7.10 ± 0.02]	6.74 ± 0.48
C-PF-D-700	51.6 ± 0.6	0.594 ± 0.018	1.721 ± 0.030	65.5 ± 2.3	1.10	0.83	0.27	[g]	529 ± 82 [339 ± 78]	8.34 ± 0.10 [7.35 ± 0.09]	6.59 ± 1.03
C-PF-O-700	54.5 ± 0.7	0.627 ± 0.021	1.725 ± 0.027	63.7 ± 2.2	1.02	0.86	0.16	[g]	657 ± 11 [459 ± 10]	6.18 ± 0.00$_1$ [6.46 ± 0.00$_1$]	5.29 ± 0.12
C-PF-D-800	52.3 ± 0.4	0.618 ± 0.015	1.962 ± 0.013	68.5 ± 1.1	1.11	0.82	0.16	0.13 ± 0.00$_1$	569 ± 41 [387 ± 36]	7.79 ± 0.02 [6.89 ± 0.02]	5.37 ± 0.11
C-PF-O-800	54.7 ± 0.7	0.640 ± 0.021	1.909 ± 0.010	66.5 ± 1.3	1.04	0.82	0.09	0.13 ± 0.00$_1$	519 ± 87 [335 ± 83]	8.01 ± 0.11 [7.46 ± 0.11]	6.06 ± 1.02

[a] Average of 5 samples. [b] Shrinkage = 100 × (mold diameter – sample diameter)/ (mold diameter). [c] Single sample, average of 50 measurements. [d] BJH-desorption cumulative pore volume. [e] Via $V_{>300} = V_{Total} - (V_{1.7\text{-}300} + V_{micropore})$. [f] $V_{micropore}$ was calculated with CO_2-sorption up to 760 Torr and relative pressure of 0.03 at 273 K via the Horvath-Kawazoe method. [g] Not measured. [h] Average of 3 samples. First number indicates the BET surface area; the number in the square bracket indicates the micropore area obtained by t-plot analysis. [i] For the first number, V was calculated via $V_{Total} = (1/\rho_b) - (1/\rho_s)$; for the number in brackets, V was calculated by the single-point adsorption method. [j] Via $D = 6 / (\rho_s \times \sigma)$.

Table S.VII.4. Material characterization data of PF and all of its derivatives along air-oxidation, carbonization and etching (Cont.)

sample	linear shrinkage (%) [a, b]	bulk density, ρ_b (g cm^{-3}) [a]	skeletal density, ρ_s (g cm^{-3}) [c]	porosity, Π (% v/v)	specific pore volume (cm^3 g^{-1})				BET surf. area, σ [micropore] (m^2 g^{-1}) [i]	av. pore diameter (nm)
					V_{Total} [d]	$V_{1.7\text{-}300}$ (nm) [e]	$V_{>300}$ (nm) [f]	$V_{micropore}$ [g]		via $4\times V/\sigma$ [j]
EC-PF-D-600	45.9 ± 1.0	0.516 ± 0.023	2.086 ± 0.011	75.3 ± 1.3	1.46	0.95	0.51	[h]	1488 ± 95 [1168 ± 74]	3.92 ± 0.01 [3.72 ± 0.01]
EC-PF-O-600	48.2 ± 1.0	0.523 ± 0.021	1.894 ± 0.005	72.4 ± 1.2	1.38	0.80	0.58	[h]	1488 ± 34 [1188 ± 36]	$3.72 \pm 0.00_1$ [3.63 ± 0.01]
EC-PF-D-700	53.3 ± 1.1	0.471 ± 0.058	1.867 ± 0.008	74.8 ± 3.2	1.59	0.90	0.69	[h]	1134 ± 111 [917 ± 97]	5.60 ± 0.03 [4.47 ± 0.03]
EC-PF-O-700	54.5 ± 1.6	0.517 ± 0.108	1.945 ± 0.010	73.4 ± 5.6	1.42	1.12	0.30	[h]	1408 ± 127 [1139 ± 92]	4.03 ± 0.02 [4.25 ± 0.04]
EC-PF-D-800	53.0 ± 0.6	0.544 ± 0.036	2.070 ± 0.008	73.7 ± 1.8	1.36	1.38	0.00	$0.22 \pm 0.00_1$	1701 ± 9 [1069 ± 4]	$3.19 \pm 0.00_{01}$ [$4.45 \pm 0.0_{01}$]
EC-PF-O-800	55.3 ± 0.3	0.544 ± 0.029	2.124 ± 0.007	74.4 ± 1.4	1.37	0.95	0.17	$0.25 \pm 0.00_1$	1483 ± 83 [1045 ± 51]	3.69 ± 0.01 [3.66 ± 0.01]

[a] Average of 5 samples. [b] Shrinkage = 100 × (mold diameter – sample diameter)/ (mold diameter). [c] Single sample, average of 50 measurements. [d] Calculated via $V_{Total} = (1/\rho_b) - (1/\rho_s)$. [e] BJH-desorption cumulative pore volume. [f] Via $V_{>300} = V_{Total} - (V_{1.7\text{-}300} + V_{micropore})$. [g] $V_{micropore}$ was calculated with CO_2-sorption up to 760 Torr and relative pressure of 0.03 at 273 K via the Horvath-Kawazoe method. [h] Not measured. [i] Average of 3 samples. First number indicates the BET surface area; the number in the square bracket indicates the micropore area obtained by t-plot analysis. [j] For the first number, V was calculated via $V_{Total} = (1/\rho_b) - (1/\rho_s)$; for the number in brackets, V was calculated by the single-point adsorption method.

Appendix VIII. All linear Shrinkage, Bulk (ρ_b) and Skeletal (ρ_s) Density, and Porosity (Π) Data in Graph Form

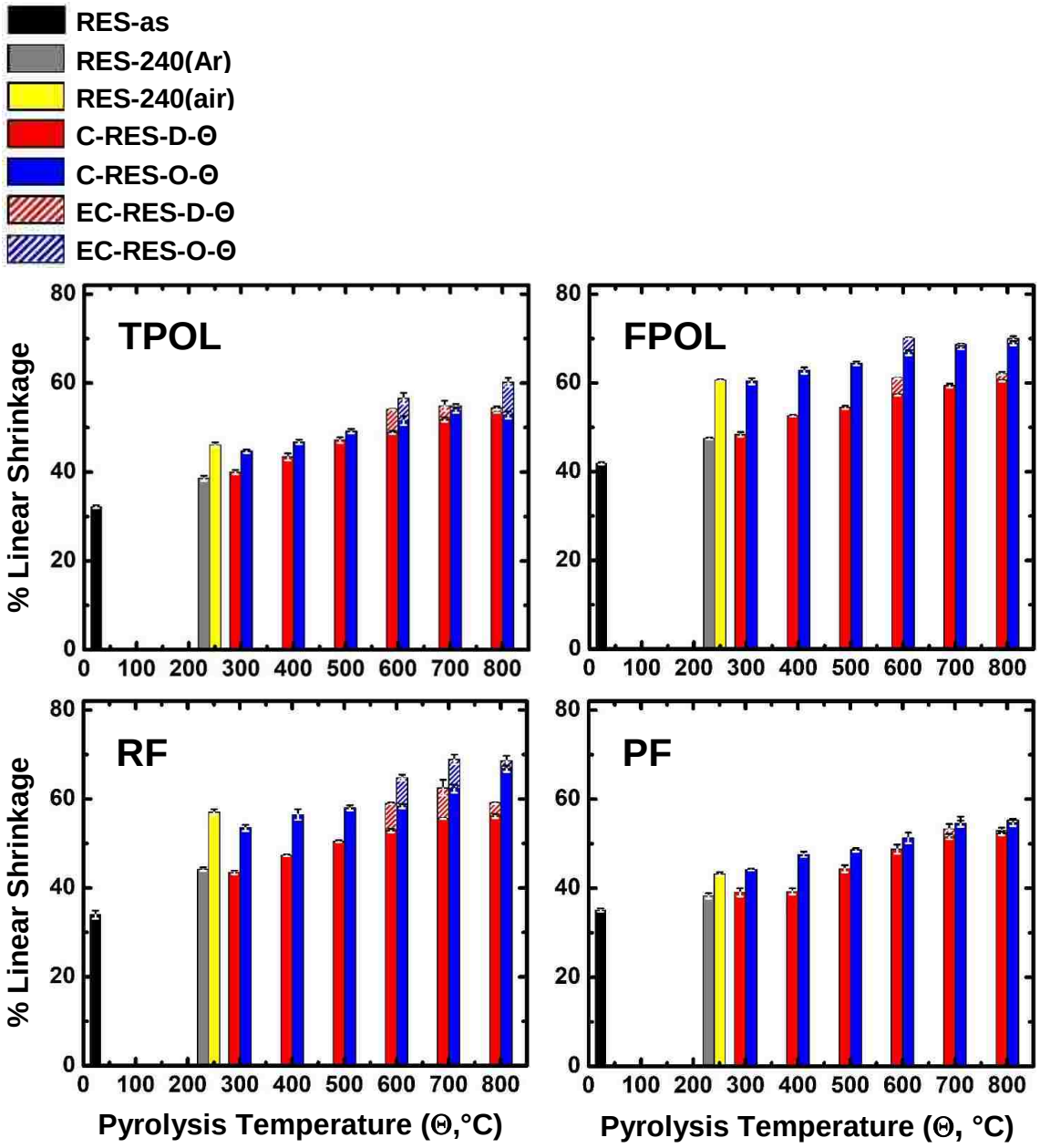

Figure S.VIII.1. Linear shrinkage relative to the molds of all samples along pyrolytic processing. D refers to the pyrolysis products of **RES** as-prepared. O refers to the pyrolysis products of **RES-240(air)**. Shaded areas refer to samples etched with CO_2 at 1000 ^oC.

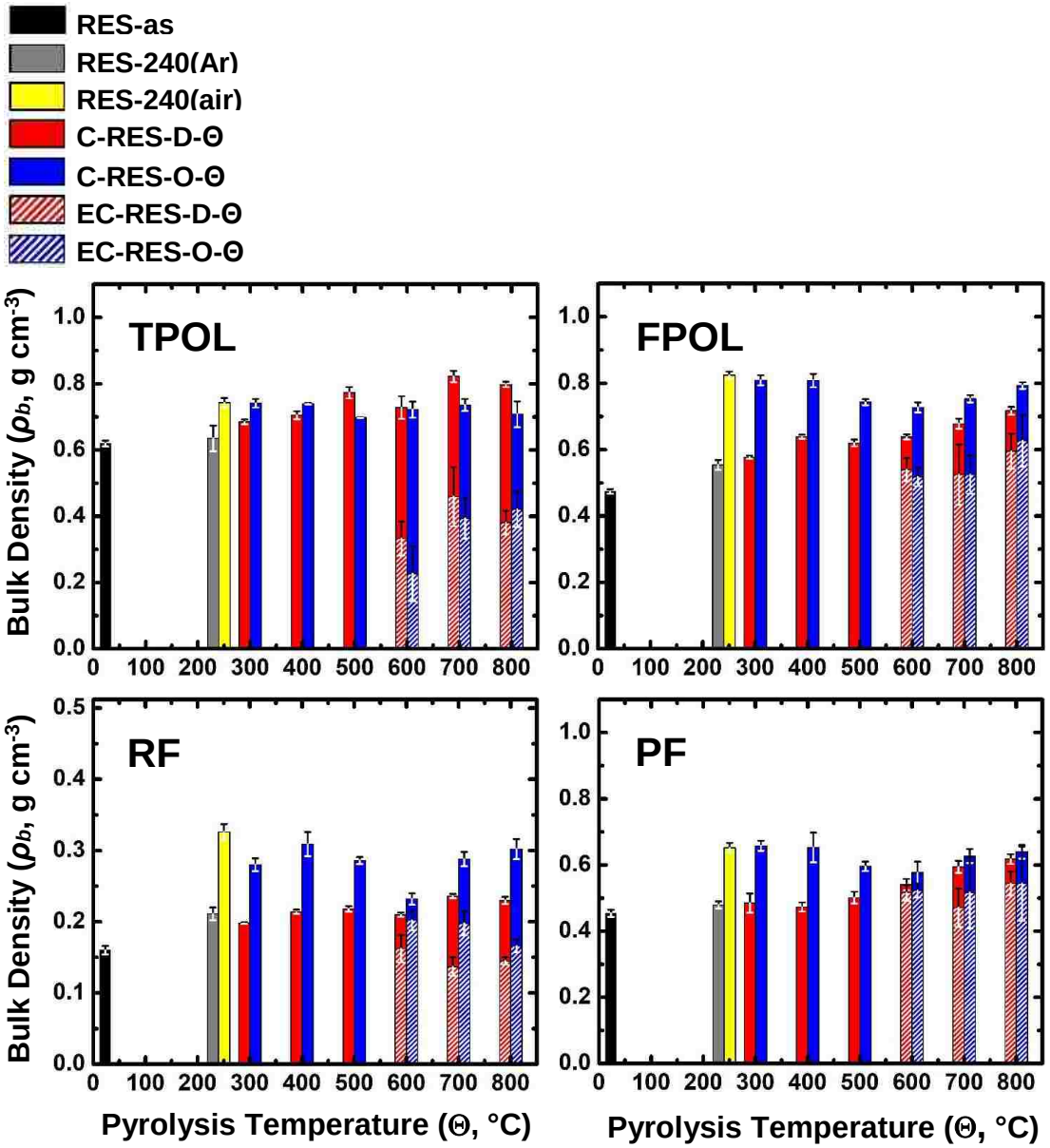

Figure S.VIII.2. Bulk density of all samples along pyrolytic processing. D refers to the pyrolysis products of **RES** as-prepared. O refers to the pyrolysis products of **RES-240(air)**. Shaded areas refer to samples etched with CO_2 at 1000 ^{o}C.

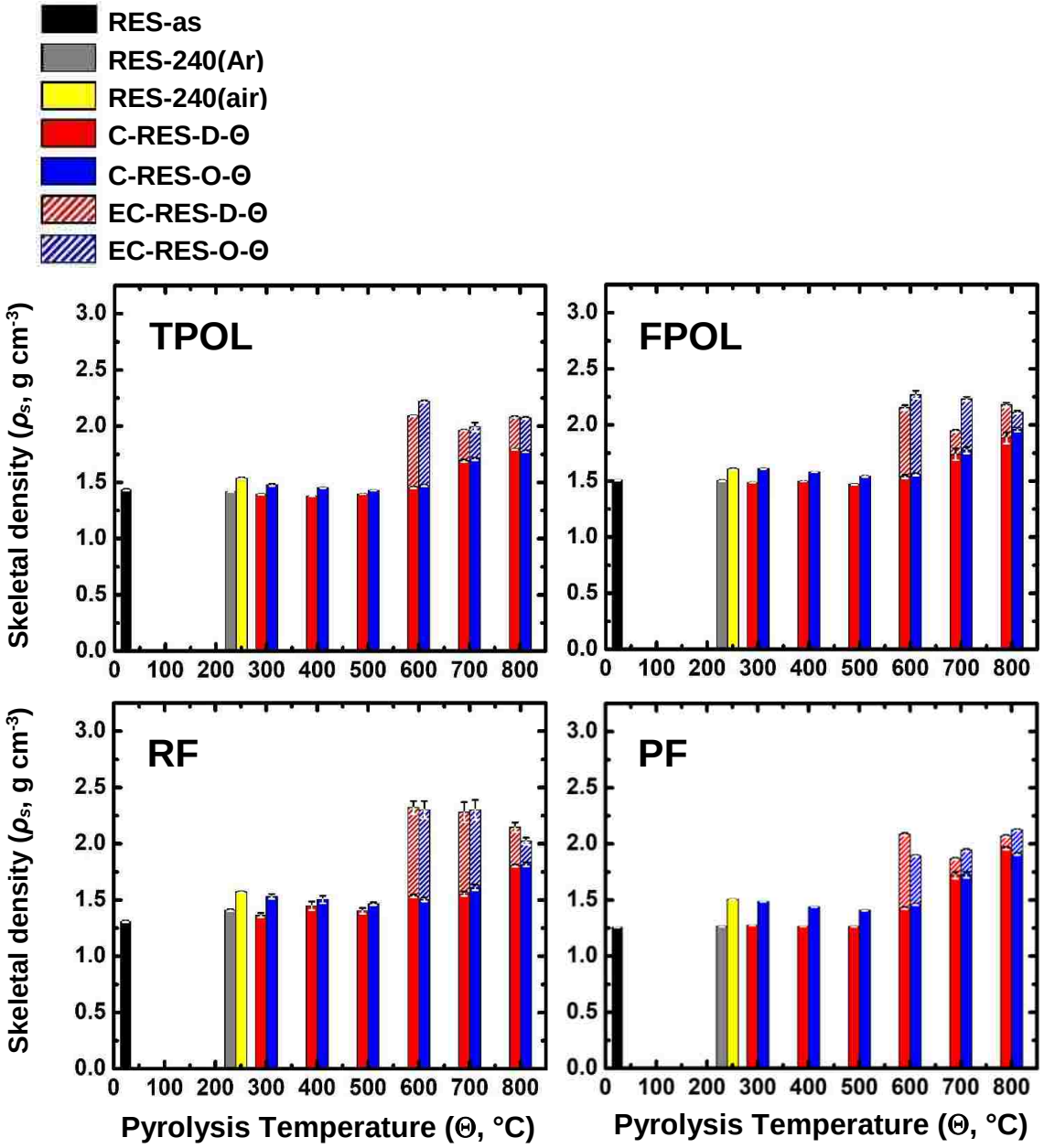

Figure S.VIII.3. Skeletal density of all samples along pyrolytic processing. D refers to the pyrolysis products of **RES** as-prepared. O refers to the pyrolysis products of **RES-240(air)**. Shaded areas refer to samples etched with CO_2 at 1000 ^{o}C.

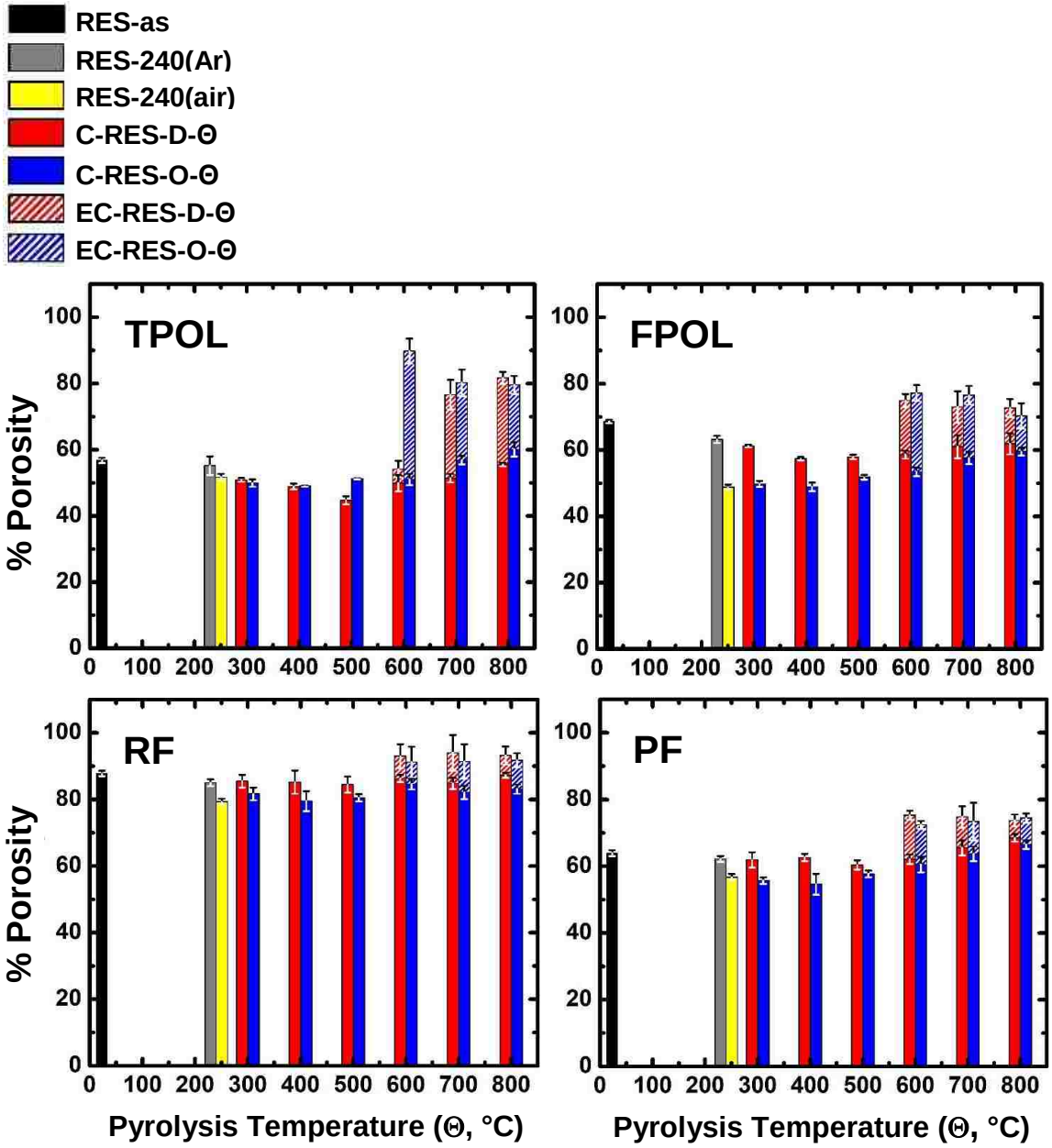

Figure S.VIII.4. Percent porosity (*Π*) of all samples along pyrolytic processing. D refers to the pyrolysis products of **RES** as-prepared. O refers to the pyrolysis products of **RES-240(air)**. Shaded areas refer to samples etched with CO_2 at 1000 ºC.

Appendix IX. SEM, N_2 Sorption and CO_2 Sorption Data

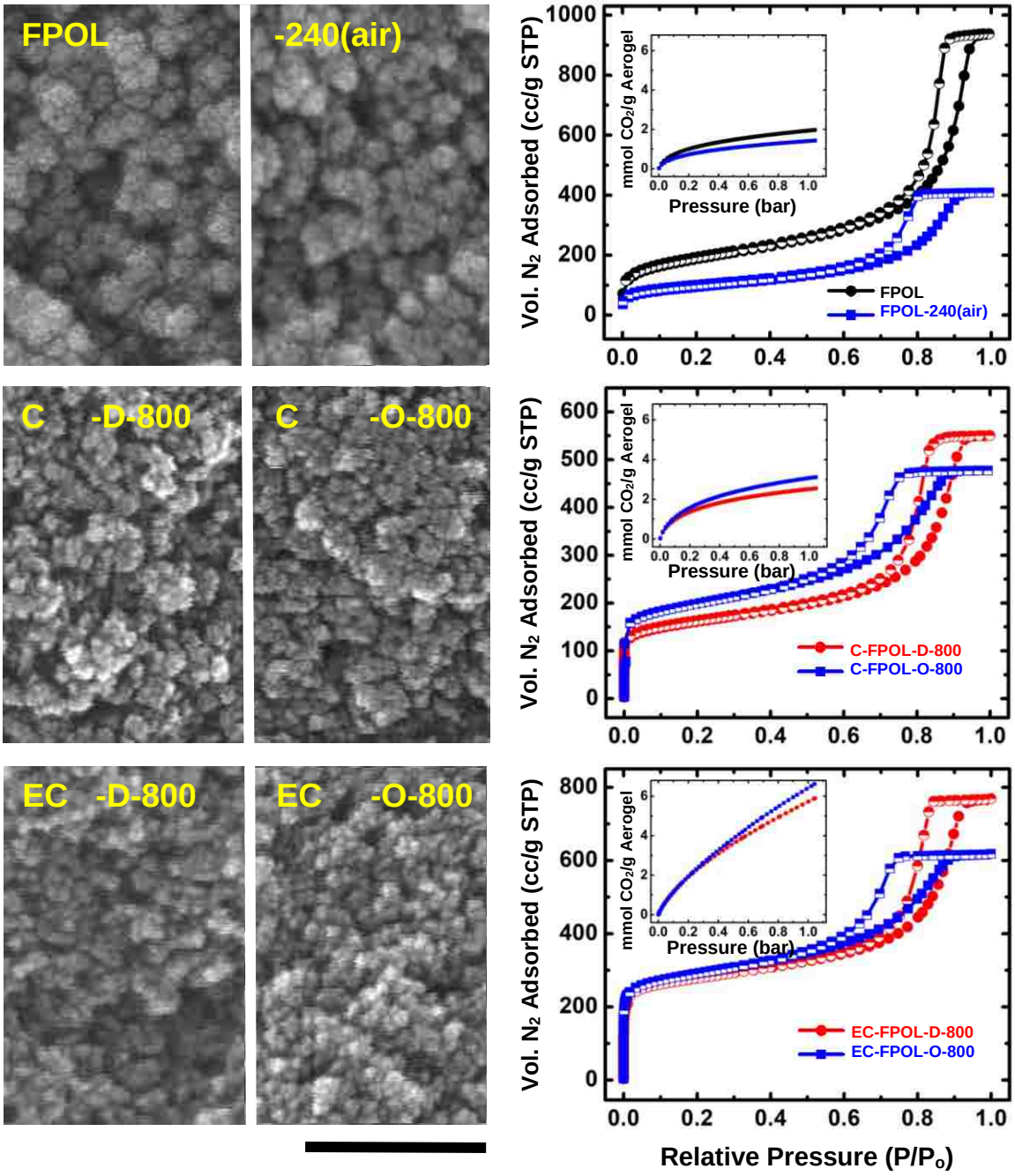

Figure S.IX.1. SEM, N_2 sorption isotherms (77 K) and CO_2 sorption isotherms (0 ^{o}C - insets) of: Top: **FPOL** and **FPOL-240(air)**; Middle: Carbonized **C-FPOL-D-800** (red) and **C-FPOL-O-800** (blue); Bottom: Etched samples corresponding to the samples in middle raw, **EC-FPOL-D-800** (red) and **EC-FPOL-O-800** (blue). SEM scale bar: 100 nm.

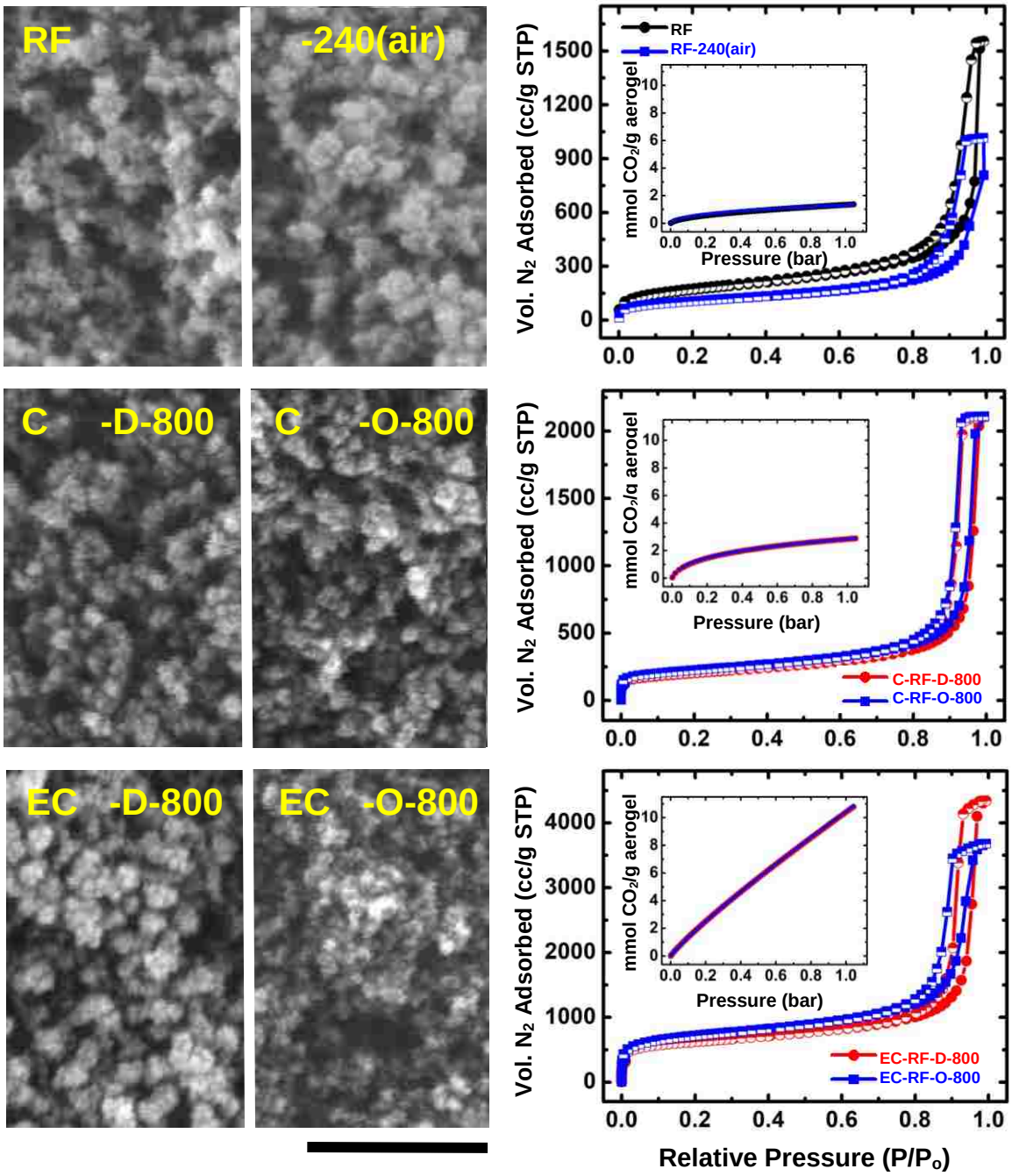

Figure S.IX.2. SEM, N_2 sorption isotherms (77 K) and CO_2 sorption isotherms (0 ^oC - insets) of: Top: **RF** and **RF-240(air)**; Middle: Carbonized **C-RF-D-800** (red) and **C-RF-O-800** (blue); Bottom: Etched samples corresponding to the samples in middle raw, **EC-RF-D-800** (red) and **EC-RF-O-800** (blue). SEM scale bar: 100 nm.

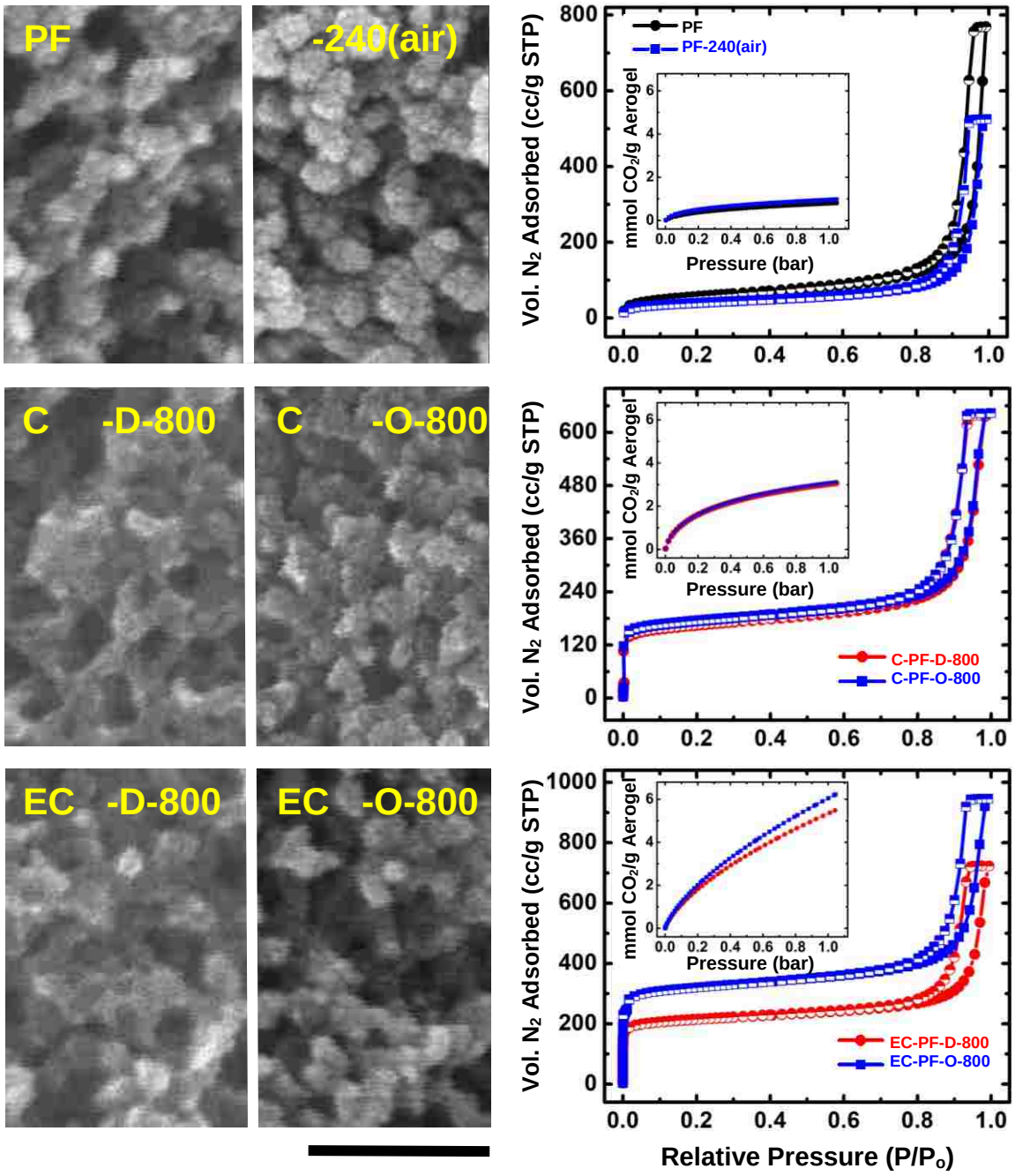

Figure S.IX.3. SEM, N_2 sorption isotherms (77 K) and CO_2 sorption isotherms (0 ^oC - insets) of: Top: **PF** and **PF-240(air)**; Middle: Carbonized **C-PF-D-800** (red) and **C-PF-O-800** (blue); Bottom: Etched samples corresponding to the samples in middle raw, **EC-PF-D-800** (red) and **EC-PF-O-800** (blue). SEM scale bar: 100 nm.

Appendix X. Meso and Micropore Size Distribution Data

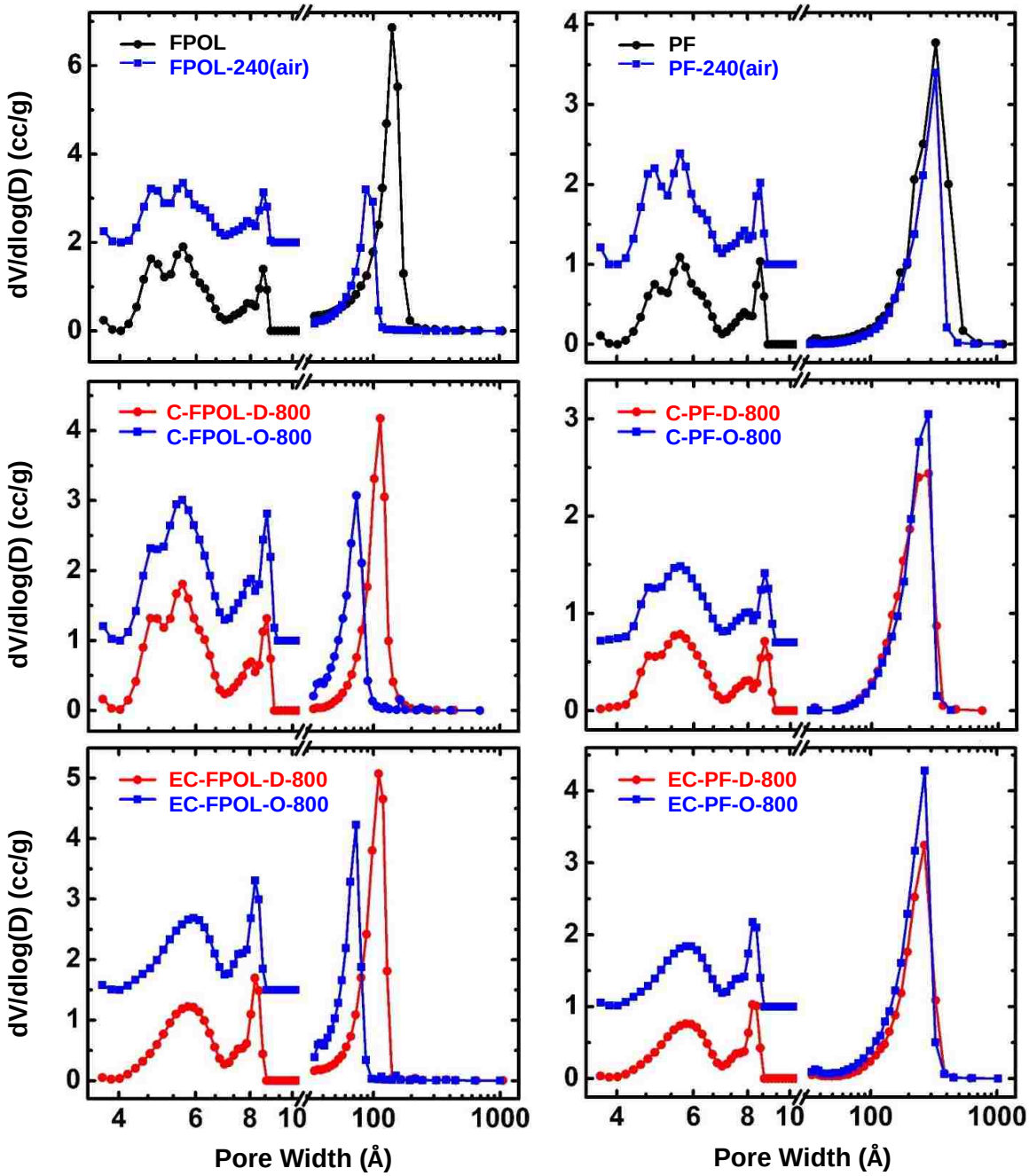

Figure S.X.1. Pore size distributions in the meso and micropore range of samples as shown (Left: from the **FPOL** system; Right: from the **PF** system). Mesopore size distributions (curves at > 10 Å) from the BJH equation applied to N_2 sorption data. Micropore size distributions (curves at <10 Å) using a DFT model on CO_2 sorption data and assuming slit pores. (The corresponding data for the **TPOL** and **RF** systems are shown in Figure 10 in the main article.)

REFERENCES

1. A. Gardziella, L. A. Pilato and A. Knop, *Phenolic Resins*, Springer-Verlag, Berlin (Germany), 2nd edn, 2000.

2. C. P. R. Nair, *Prog. Polym. Sci*., 2004, **29**, 401–498.

3. A. C. Pierre and G. M. Pajonk, *Chem. Rev*., 2002, **102**, 4243–4265.

4. N. Hüsing and U. Schubert, *Angew. Chem., Int. Ed*., 1998, **37**, 22–45.

5. R. W. Pekala, *J. Mater. Sci*., 1989, **24**, 3221–3227.

6. X. Lu, M. C. Arduini-Schuster, J. Kuhn, O. Nilsson, J. Fricke and R. W. Pekala, *Science*, 1992, **255**, 971**–**972.

7. R. W. Pekala and D. W. Schaefer, *Macromolecules*, 1993, **26**, 5487–5493.

8. S. A. Al-Muhtaseb and J. A. Ritter, *Adv. Mater*., 2003, **15**, 101–114.

9. W.-C. Li, A.-H. Lu and F. Schüth, *Chem. Mater*., 2005, **17**, 3620–3626.

10. C. Scherdel and G. Reichenauer, *Microporous and Mesoporous Materials*, 2009, **126**, 133–142.

11. N. Leventis, I. A. Elder, D. R. Rolison, M. L. Anderson and C. I. Merzbacher, *Chem. Mater*., 1999, **11**, 2837–2845.

12. N. Leventis, A.-M. M. Rawashdeh, I. A. Elder, J. Yang, A. Dass and C. Sotiriou-Leventis, *Chem. Mater*., 2004, **16**, 1493–1506.

13. B. A. Newcomb, *Composites Part A: Applied Science and Manufacturing*, 2016, **91**, 262–282.

14. L. Liu, C. Jia, J. He, F. Zhao, D. Fan, L. Xing, M. Wang, F. Wang, Z. Jiang and Y. Huang, *Comp. Sci. Tech*., 2015, **121**, 56–72.

15. J. Li, X. Huang and L. Chen, *J. Electrochem. Soc*., 2000, **147**, 2653**–**2657.

16. Y.-X. Wang and Q. Wang, *J. Appl. Polym. Sci*., 2007, **104**, 1255–1259.

17. K. E. Perepelkin, *Fibre Chemistry*, 2003, **35**, 409–416.

18. H. Ishida in *Handbook of Benzoxazine Resins*, ed, H. Ishida and T. Agag, Elsevier, New York, 2011, pp. 3–81.

19. T. Takeichi, T. Kawauchi and T. Agag, *Polym. J*., 2008, **40**, 1121–1131.

20. N. N. Ghosh, B. Kiskan and Y. Yagci, *Prog. Polym. Sci*., 2007, **32**, 1344–1391.

21. P. Lorjai, S. Wongkasemjit, T. Chaisuwan and A. M. Jamieson, *Polym. Degrad. Stab*., 2011, **96**, 708**–**718.

22. S. Mahadik-Khanolkar, S. Donthula, C. Sotiriou-Leventis and N. Leventis, *Chem. Mater*., 2014, **26**, 1303–1317.

23. A. G. Sadekar, S. S. Mahadik, A. N. Bang, Z. J. Larimore, C. A. Wisner, M. F. Bertino, A. K. Kalkan, J. T. Mang, C. Sotiriou-Leventis and N. Leventis, *Chem. Mater*., 2012, **24**, 26–47.

24. A. P. Katsoulidis and M. G. Kanatzidis, *Chem. Mater*., 2011, **23**, 1818–1824.

25. S. Mulik, C. Sotiriou-Leventis and N. Leventis, *Chem. Mater*., 2007, **19**, 6138–6144.

26. C. Scherdel and G. Reichenauer, *Microporous and Mesoporous Materials*, 2009, **126**, 133–142.

27. N. Leventis, S. Mulik and C. Sotiriou-Leventis, *Chem. Mater*., 2008, **20**, 6985–6997.

28. Z. Yoshida, H. Sugimoto and S. Yoneda, *Tetrahedron*, 1974, **30**, 2099–2105.

29. A. R. Katritzky, S. Sengupta and A. Dinculescu, *J. Heterocyclic Chemistry*, 1986, **23**, 169–171.

30. R. M. Silverstein, F. X. Webster and D. J. Kiemle, *Spectrometric Identification of Organic Compounds*, John Wiley & Sons, Inc. New York, 7th edn, 2005, pp. 87−88.

31. D. A. Pavia, G. M. Lampman, G. S. Kriz and J. R. Vyvyan, *Introduction to Spectroscopy*, Cengage Learning, Belmont, CA USA, 4th edn, 2009, pp. 15–104.

32. G. Socrates, *Infrared and Raman Characteristic Group Frequencies*, John Wiley & Sons, Inc. New York, 3rd edn, 2001, pp. 157–167.

33. A. Thangavel, C. Sotiriou-Leventis, R. Dawes and N. Leventis, *J. Org. Chem*., 2012, **77**, 2263–2271.

34. G. P. López, D. G. Castner and B. D. Ratner, *Surface and Interface Analysis*, 1991, **17**, 267–272.

35. D. Briggs and G. Beamson, *Analytical Chemistry*, 1993, **65**, 1517–1523.

36. A. Ganguly, S. Sharma, P. Papakonstantinou and J. Hamilton, *J. Phys. Chem. C*, 2011, **115**, 17009–17019.

37. R. Ciriello, A.; Guerrieri, F. Pavese and A. M. Salvi, *Analytical and Bioanalytical Chemistry*, 2008, **392**, 913–926.

38. M. Lawrinenko and D. A. Laird, *Green Chemistry*, 2015, **17**, 4628–4636.

39. C. M. Kim, H. S. Jeong and E. H. Kim, *Surface Science*, 2000, **459**, L457–L461.

40. L. Q. Wu, S. Q. Li, Y. C. Li, Z. Z. Li, G. D. Tang, W. H. Qi, L. C. Xue, L. L. Ding and X. S. Ge, *Applied Physics Letters*, 2016, **108**, 021905.

41. D. D. Werstler, *Polymer*, 1986, **27**, 757–764.

42. P. Sándor and L. Radics, *Org. Mag. Res*., 1981, **16**, 148–155.

43. A. M. Bello and L. P. Kotra, *Tetrahedron Letters*, 2003, **44**, 9271–9274.

44. A. R. Katritzky, Y.-K. Yang, B. Gabrielsen and J. Marquet, *J. Chem. Soc. Perkin Trans.*, 1984, **2**, 857–866.

45. J. Fossey, D. Lefort and J. Sorba, *Free Radicals in Organic Chemistry*, John Wiley & Sons, Inc, New York, 1995, p. 218.

46. J. March, *Advanced Organic Chemistry*, John Wiley & Sons, Inc, New York, 4th edn, 1992, pp. 705–706.

47. B. Saha and G. C. Schatz, *J. Phys. Chem. B*, 2012, **116**, 4684–4692.

48. Q. Chen, X. Jiang, Y. Bin and M. Matsuo, *Polym. J*., 2007, **39**, 568–578.

49. S. Naeem, V. Baheti, V. Tunakova, J. Militky, D. Karthik and B. Tomkova, *Carbon*, 2017, **111**, 439–447.

50. P. A. Webb and C. Orr, *Analytical Methods in Fine Particle Technology*, Micromeritics Instrument Corporation, Norcross, GA USA, 1997, pp. 80–81.

51. D. Lozano-Castelló, D. Cazorla-Amorós, A. Linares-Solano and A. M. Salvi, *Carbon*, 2004, **42**, 1231–1236.

52. B. B. Saha, S. Jribi, S. Koyama and I. I. El-Sharkawy, *J. Chem. Eng. Data*, 2004, **56**, 1974–1981.

53. G. Horvath and K. Kawazoe, *J. Chem. Eng. Jpn*., 1983, **16**, 470−475.

54. With regards to macroporosity, the case of **C-RF-D_**(or**_O**)**-800** and **EC-RF-D_**(or**_O**)**-800** was particularly interesting (ESI, Table S.VII.3) because, on one hand, owing to the low starting density of those materials, the V_{Total} values were always much higher than the values of all other corresponding carbons, on the other hand **RF**-derived carbons lacked completely any pores above >300 nm.

55. W. D. Harkins and G. Jura, *J. Am. Chem. Soc*., 1944**, 66**, 1362–1366.

56. P. A. Webb and C. Orr, *Analytical Methods in Fine Particle Technology*, Micromeritics Instrument Corporation, Norcross, GA USA, 1997, pp. 67–68.

57. H. Jiang, J. Wang, S. Wu, Z. Yuan, Z. Huc, R. Wu and Q. Liu, *Polymer Degradation and Stability*, 2012, **97**, 1527**–**1533.

58. L. Liu, J. Yang and Q. Meng, *J. Sol-Gel Sci. Technol.*, 2013, **67**, 304–311.

59. R. Banerjee, K. Patil and K. Khilar, *Can. J. Chem. Eng.* 2006, **84**, 328–337.

60. K. Ouchi, *Carbon*, 1966, **4**, 59–66.

61. Y. Yamashita and K. Ouchi, *Carbon*, 1981, **19**, 89–94.

62. A. M. Saeed, P. M. Rewatkar, H. Majedi Far, T. Taghvaee, S. Donthula, C. Mandal, C. Sotiriou-Leventis and N. Leventis, *ACS Appl. Mater. Interfaces*, 2017, **9**, 13520–13536.

II. EXCEPTIONALLY HIGH CO_2 ADSORPTION AT 273 K BY MICROPOROUS CARBONS FROM PHENOLIC AEROGELS: THE ROLE OF HETEROATOMS IN COMPARISON WITH CARBONS FROM POLYBENZOXAZINE AND OTHER ORGANIC AEROGELS

Hojat Majedi Far, Parwani M. Rewatkar, Suraj Donthula, Tahereh Taghvaee, Adnan Malik Saeed, Chariklia Sotiriou-Leventis* and Nicholas Leventis*

Department of Chemistry, Missouri University of Science and Technology, Rolla, MO 65409, U.S.A. *Correspondence: Tel.: 573-341-4391 (NL), 573-341-4353 (CSL). E-mail: leventis@mst.edu, cslevent@mst.edu

ABSTRACT

Phenolic aerogels containing oxygen, and other polymeric aerogels containing both oxygen and nitrogen (polybenzoxazine and a polyamide-polyimide-polyurea co-polymer) were converted to carbon aerogels (800 ^{o}C/Ar), and were etched with CO_2 (1000 ^{o}C). Etching opened closed pores and increased micropore volumes and size. Heteroatoms were retained in the terminal etched samples. All carbon aerogels were characterized chemically (CHN and XPS) and nanoscopically (gas-sorption) and were evaluated as CO_2 sorbers in terms of their capacity and selectivity towards CH_4, H_2 and N_2. CO_2 adsorption capacity was linked to microporosity. In most cases, monolayer coverage of micropore walls was enough to explain CO_2 uptake quantitatively. The interaction of CO_2 with micropore walls was evaluated via isosteric heats of adsorption, and was stronger with carbons containing only oxygen heteroatoms. The adsorption capacity of those carbons (5–6 mmol g^{-1}) was at par with the best carbon and polymeric

CO_2 adsorbers known in the literature, with one exception though: etched carbon aerogels from low-density resorcinol-formaldehyde aerogels showed a very high CO_2 uptake (14.8 ± 3.9 mmol g^{-1} at 273 K and 1 bar), which was attributed to a pore-filling process that proceeds beyond monolayer coverage whereas surface phenoxides engaged in a thermally-neutral carbonate forming reaction (surface-O^- --- + CO_2 ---> surface-O-(CO)-O^- --- + CO_2 ---> surface-O-(CO)-O-(CO)O^-) that continued until micropores were filled.

Keywords: phenolic aerogels, polybenzoxazine aerogels, CO_2 uptake, selectivity, isosteric heats of adsorption

Table of Contents Graphic:

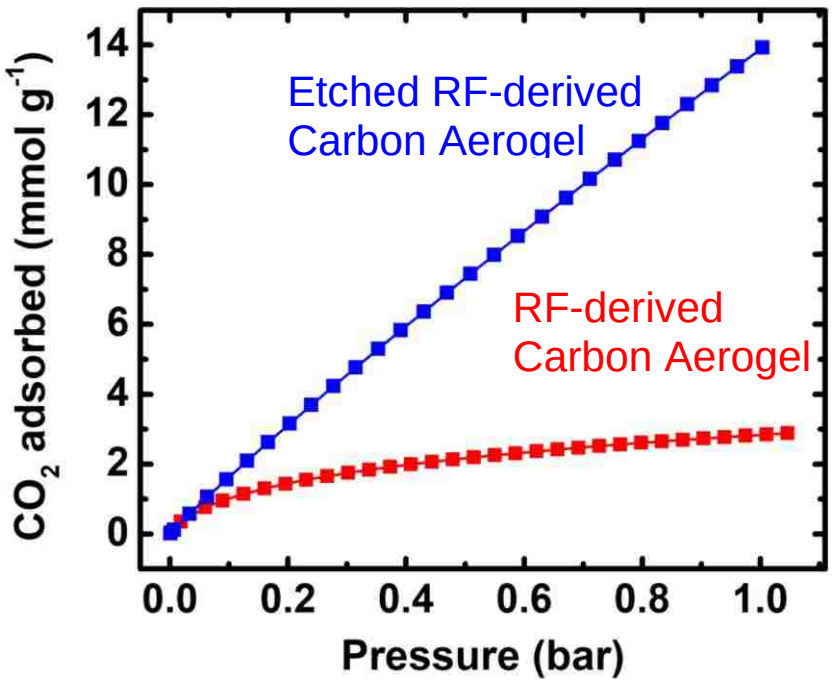

1. INTRODUCTION

For economic reasons, separation of CO_2 from both pre- and post-combustion gasses in power plants was already part of the process long before any anthropogenic contribution to global warming via massive release of green-house gasses like CO_2 in the atmosphere was a concern. Global warming has just brought the issue of carbon capture and sequestration (CCS) at the forefront of public awareness. CCS has an economic cost itself in terms of energy consumption in order to recycle the capturing agent and store CO_2. Thereby, research in the area stems from the need for CCS technologies that will bring the level of carbon-avoided closer to the carbon-captured.[1–3]

Currently, three main technologies are used to separate CO_2 from its emission sources: scrubbing solutions (mostly amines), solid sorbents, and membranes.[4] The advantage of solid sorbents is that they can tolerate wider temperature ranges, and they can be regenerated more easily, therefore their environmental footprint is lower. On the downside, their capture capacity is relatively low, and the goal has been to improve on that while maintaining selectivity.[5] Solid sorbent materials can be classified into two main groups: traditional porous sorbents that include activated carbons and zeolites, and novel synthetic materials.

Novel synthetic sorbent materials have been the focus of intense research interest in the last ~20 years because they bring the power of designed synthesis to implementing strategies that increase gas uptake and selectivity. Such strategies target enhanced surface areas, higher interaction energies with adsorbates of interest, tuned pore and particle sizes, surface modification by doping (e.g., with N), oxidation, fluorination, etc., and also via synthesis of porous hybrid materials.[5,6] Thus, not surprising, synthetic polymeric

porous sorbents cover an extremely broad range of materials that includes metal organic frameworks (MOFs),[7–9] hyper crosslinked polymers (HCPs),[10,11] conjugated microporous polymers (CMPs),[12,13] polymers with intrinsic microporosity (PIMs),[14,15] porous aromatic frameworks (PAFs),[16,17] covalent organic polymers (COPs),[18,19] covalent triazine-based frameworks (CTFs),[20] miroporous organic polymers (MOPs),[21,22] porous polymer frameworks (PPFs),[23] benzimidazole-linked polymers (BILPs),[24,25] etc.

The common target among all synthetic sorbent materials is free-volume microporosity, which is introduced by means of molecular rigidity at the monomer level. Oftentimes though, that molecular rigidity comes at a high cost: such monomers may be the result of multistep synthesis themselves from not readily available (therefore expensive) starting materials. In other instances, where starting materials may be easily available and inexpensive, e.g., case of MOFs, environmental sensitivity, for example to water, is an issue.[26,27] At last but not least, a perennial problem that faces materials in *all* those categories is that typically they are obtained as powders that must be re-packaged in useful forms that allow almost unobstructed passage of gasses, yet they provide long enough contact times for efficient adsorption. Ideally, such "useful forms" would be hybrids between monolithic chromatographic columns and catalytic converters. For all those reasons, designer polymeric adsorbers are not commonplace amongst practical solutions of the CSS problem, while in the meantime commercial products still rely on low-cost, high surface area, chemically inert, carbon-based materials made from natural sources.

One special type of high surface area carbons is referred to as carbon aerogels. They are produced from pyrolysis of an ever-increasing variety of carbonizable

polymeric aerogels, which in turn are synthesized via typical sol-gel chemistry. A very important attribute of the polymer-to-carbon aerogel route is that for rigidity and porosity the final carbon aerogels do not rely on the molecular rigidity of the monomer precursors of their parent polymeric aerogels, but rather on chemical transformations taking place during pyrolytic carbonization. Therefore, because the molecular rigidity requirement for making polymeric aerogels is not as strict as that for making the rigid framework of polymeric adsorbents, the selection of monomer precursors for polymeric aerogels is much less restrictive. Specifically, while molecular rigidity of organic/polymeric adsorbers typically requires expensive tetrafunctional monomers, crosslinking of polymeric chains, required for phase-separation during the sol-gel transition, can be achieved with just commodity-type trifunctional monomers. In addition, since there is a wide variety of polymeric aerogels that converge to carbon aerogels, selection of the specific chemistry may give carbon aerogels doped with heteroatoms in numerous functional group configurations, almost at will (e.g., pyridinic vs. pyridonic or nitroxide for nitrogen; pyrylium, carbonyl, or phenoxide for oxygen). A final, yet extremely important attribute of carbon aerogels is that they can be prepared easily as shaped monoliths with multiscale porosity with pore sizes ranging from macro to mirco pore-size regime, effectively being hybrids of monolithic chromatographic columns and catalytic converted as mentioned above, thus addressing also the requirement for packaging in useful forms.

The most well-known carbon aerogels have been obtained from pyrolysis of resorcinol-formaldehyde (**RF**) aerogels.[28,29] The backbone of **RF** aerogels is a phenolic resin; however, many other classes of polymeric aerogels yield carbon aerogels,

including polyureas,[30] polyamides,[31] polyimides,[32] polyurethanes,[33] and polybenzoxazines (**PBO**s).[34] The latter are considered a sub-class of phenolic aerogels with Mannich bridging between phenolic moieties rather than the typical methylene bridging of **RF** aerogels. **PBO** aerogels are particularly interesting materials: their curing in air triggers a ring-fusion aromatization process that increases their carbonization yield dramatically (from less than 30% to over 60%), and also rigidizes the polymeric backbone so that the resulting carbon aerogels are inherently mostly microporous materials.[34] With those findings about **PBO** aerogels as a point of departure, more recently we investigated the effect of air-oxidation on other more main-stream phenolic aerogels including **RF**, as well as phenol-formaldehyde (**PF**), pholoroglucinol-formaldehyde (**FPOL**), and pholoroglucinol-terephalaldehyde (**TPOL**) aerogels. Collectively, **PF**, **RF**, **FPOL** and **TPOL** aerogels are referred to as **RES** (Scheme 1). Only pholoroglucinol-based **FPOL** and **TPOL** aerogels would undergo oxidative ring fusion aromatization by heating at 240 ^{o}C in air, yet, unlike **PBO** aerogels, oxidative ring-fusion aromatization did not affect the carbonization yields and all four phenolic systems, irrespective of whether they were oxidized or not, converged to a common chemical composition at about 600 ^{o}C. Nevertheless, it was noted that carbon aerogels from the two systems that *did* undergo ring fusion aromatization (i.e., **TPOL** and **FPOL**) had consistently higher BET and micropore surface areas (up to 48%) than samples that were not subjected to oxidative aromatization.[35]

Those findings set the stage for the present study that was designed to explore the effect on CO_2 adsorption and selectivity of: (a) framework rigidization by oxidative ring fusion aromatization; (b) enhanced microporosity by reactive etching of carbon aerogels

with CO_2; and, (c) heteroatoms and their chemical context (i.e., the identity of functional groups that survived carbonization). Materials used for those purposes include monolithic carbon aerogels (designated as **C-polymer of origin**) and activated carbon aerogels (designated as **EC-polymer of origin**) from organic aerogels based on phenolic resin-type of polymers (**RES**), polybenzoxazine (**PBO**) from Ishida's monomer,[36–38] and a random copolymer of polyamide, polyurea, and polyimide (**PA**).[31] Monomers and abbreviations are summarized in Scheme 1. The uptake of CO_2 and CH_4 by etched carbons at near ambient temperatures and pressures were close to the upper end of the range reported for other adsorbers derived from similar organic polymers. Exceptionally high CO_2 uptake (14.8 ± 3.9 mmol g^{-1} at 273 K, 1 bar) was observed with etched **RF**-derived carbon aerogels. That value was higher than all porous CO_2 sorbents we are aware of in the literature under the same conditions. The highest selectivity towards CO_2/H_2 at 273 K was obtained with **C-PBO** aerogels (733 ± 58). The highest selectivity towards CO_2/N_2 was noted with **EC-PBO** aerogels (181 ± 51).

2. RESULTS AND DISCUSSION

2.1. CARBON AEROGEL SYNTHESIS AND CHARACTERIZATION

Synthesis and chemical characterization of all three types of polymeric aerogels used in this study (**RES**, **PBO** and **PA**) have been described in detail in the recent literature. All phenolic wet-gels and aerogels (**RES** and **PBO**) were prepared via acid (HCl)-catalyzed room temperature polymerization of the monomers.[34,35] **PA** aerogels were prepared via room-temperature reaction of (tris(4-isocyanatophenyl) methane) and pyromellitic acid (Scheme 1).[31]

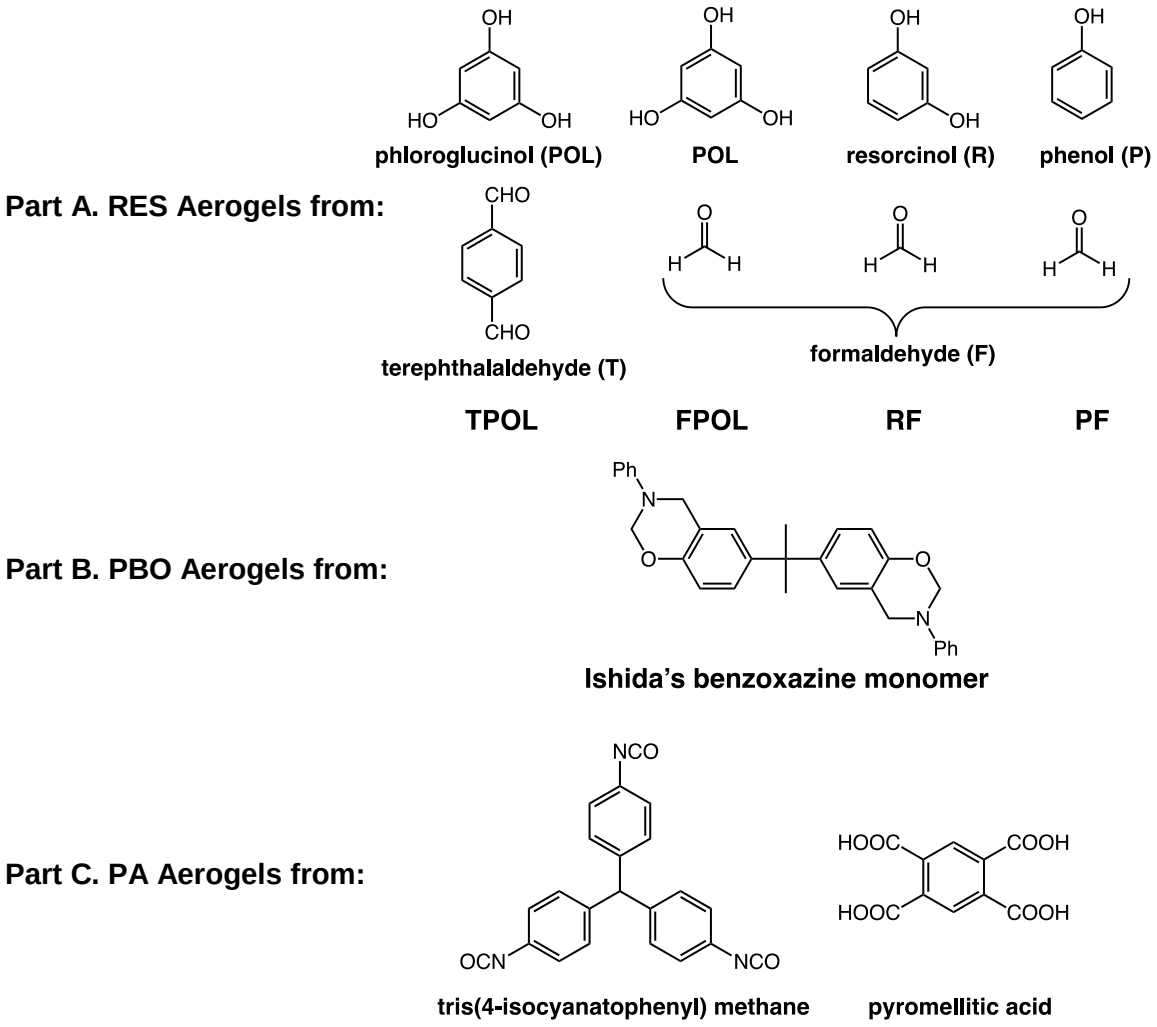

Scheme 1. Monomer precursors of the polymeric aerogels of this study (RES, PBO and PA).

RES aerogels were prepared with the same monomer concentrations as reported recently (TPOL: 16% w/w; FPOL: 11% w/w; RF: 3.3% w/w; and PF: 16% w/w). In certain control experiments, in order to match densities of the resulting carbons, **RF** aerogels were also prepared at 15% w/w of monomer concentration, and also **TPOL** aerogels were also prepared with 10% w/w of monomers. Those samples are referred to

as **RF$_{H\rho}$** and **TPOL$_{L\rho}$**, where Hρ and Lρ refer to the higher- and lower-densities of those samples, respectively. **PBO** and **PA** aerogels have been prepared previously at different monomer concentrations, but here we chose to use sols with 7.0 % w/w and 25% of monomers, respectively, because those aerogels yielded carbon aerogels with densities comparable to those from **RF** at 3.3 % w/w of monomers.

As summarized in Scheme 2, all as-prepared **RES** aerogels were either subjected to direct pyrolytic carbonization at 800 ^{o}C (the resulting carbon aerogels referred to as **C-RES-D**), or they were first subjected to an oxidative treatment at 240 ^{o}C/air followed by carbonization at 800 ^{o}C (samples referred to as **C-RES-O**). As noted in the Introduction, the only difference between **C-RES-D** and **C-RES-O** has been that the BET and micropore surface areas of the **C-RES-O** aerogels were consistently higher than those of **C-RES-D**.[35] The case of **PBO** aerogels is very different: as-prepared **PBO** aerogels must be subjected to oxidative ring-fusion aromatization (at 200 ^{o}C/air) before pyrolytic carbonization, otherwise carbonization yields are lower by about 30% w/w than those obtained from the air-cured samples.[34] That fact is reflected in Scheme 2 by showing that only aromatized **PBO** aerogels were considered for carbonization to **C-PBO** carbon aerogels. The carbonization process of **PA** aerogels is different from that of the phenolic aerogels and proceeds, at least at the early stages, via functional group interconversion that leads to CO_2 loss; oxidative aromatization was not relevant to those materials, thereby as-prepared **PA** aerogels were carbonized directly to **C-PA**. After pyrolytic carbonization, all types of C- samples were subjected to pyrolytic etching at 1000 ^{o}C for 3 h under a stream of flowing CO_2 (see Experimental section) and the resulting materials

are referred to as **EC-RES-D**, **EC-RES-O**, **EC-PBO** and **EC-PA**. (EC- stands for "etched.")

Yields of carbonization after processing according to Scheme 2 are summarized in Table S.1 of Appendix I in Supporting Information. **C-RES-D** were received at higher yields (41–56%) relative to their pre-oxidized counterparts (**C-RES-O**; 28–47%). As a group, all **C-RES-D**(or **O**) were received at lower yields than **C-PBO** (63%) and **C-PA** (57 %). No similar rules could be applied to the yield of the etching process. The yield of **EC-PBO** from **C-PBO** was only 27%, the yield of **EC-RF-D**(or **O**) from **C-RF-D**(or **O**) was higher (49% and 35%, respectively), while the yields of **EC-PA, EC-FPOL-D**(or **O**) **and EC-PF-D**(or **O**) from the corresponding C-systems were even higher (68–84%). Part of the variability in those yields is due to the fixed processing conditions. At a more basic level, yields of carbonization and etching are complicated functions of factors related to the pyrolytic conditions and structural parameters including the density of the material, the number of carbon rings per carbon atom, heteroatoms and fused rings.[39,40] In that context, and with all other factors being equal, we did notice a weak correlation between the skeletal densities of the C-materials (Table 1) and their yields of etching with CO_2: lower skeletal densities of C-aerogels were usually accompanied by lower yields of etching (Table S.1).

CHN analysis (Figure 1 and Table S.2 of Appendix II in Supporting Information) showed that pyrolysis products lost most of their hydrogen, consisted of ≥85% w/w of C, and retained a significant portion of their heteroatoms: O in the case of **C**(and **EC**)**-RES-O**, and O as well as N in the case of **C**(and **EC**)**-PBO** and **C**(and **EC**)**-PA**. With the exception of **C-PF**, after CO_2-etching the weight percent of carbon in **EC-RES-O**(and **D**)

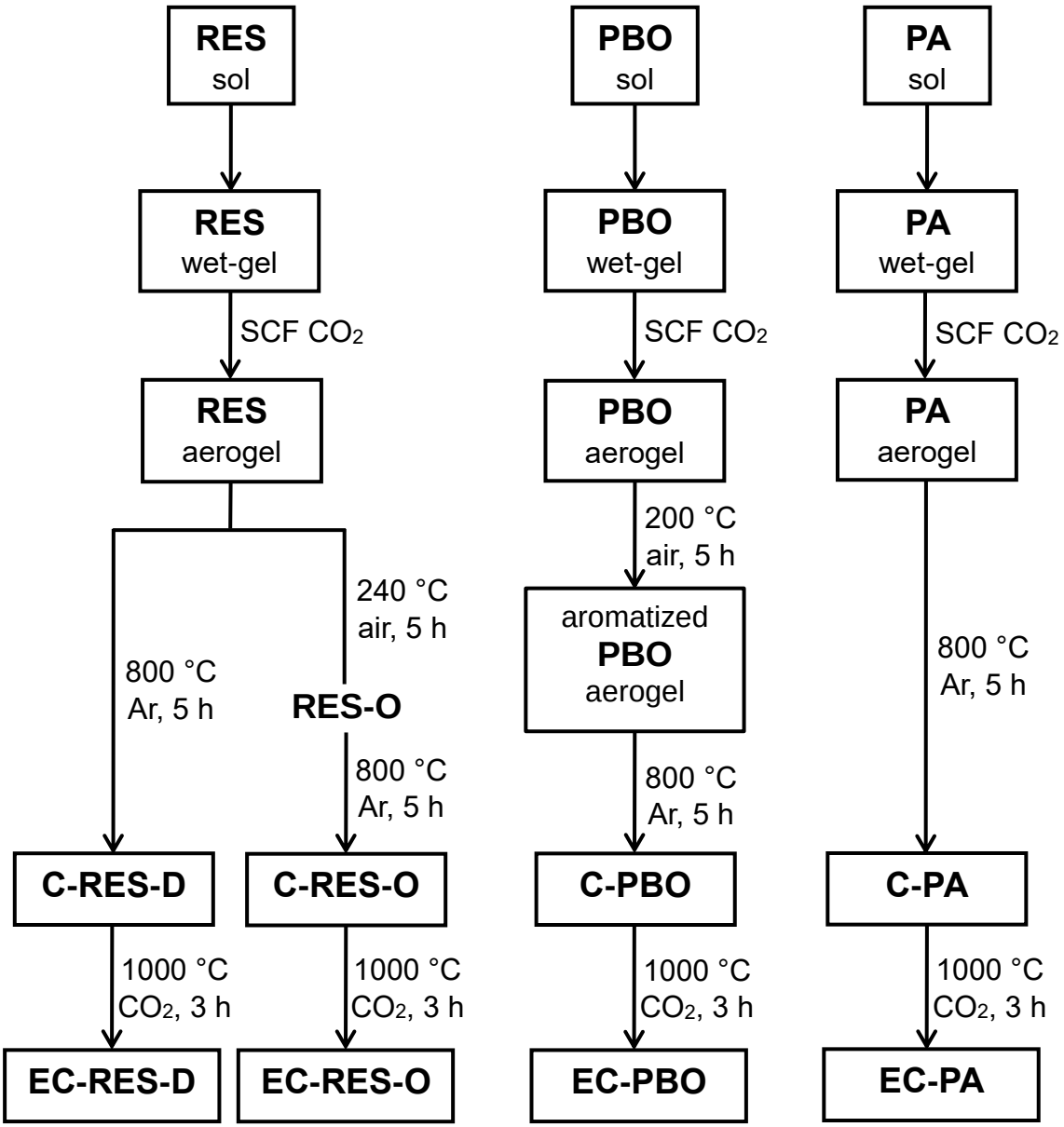

Scheme 2. Synthesis of the carbon aerogels of this study and their activated forms.

increased slightly, the amount of O decreased by an equivalent or slightly higher percentage, while H, already present in the C- samples, was mostly retained after etching, and its percent weight in the EC samples was generally at the same levels as in the

C-RES-O samples. (**EC-FPOL-O** contained almost no H and comprised an exception.). Turning to the **EC-PBO** and **EC-PA** systems, the former retained H and O but lost half of the N relative to **C-PBO**; the latter lost about half of both O and N present in **C-PA**, so that the O:N ratio remained about the same before and after etching.

The chemical identity of the heteroatoms in the C- and EC- carbons was probed with XPS. Figure 2 shows representative data. Spectra were fitted with Gaussian functions. As exemplified by the **RF** system, oxygen in all **C**(and **EC**)-**RES-O**(or **D**) was in equal amounts in the form of heteroaromatic pyrylium (O^+ at about 533 eV),[41] and charge-compensating phenoxide groups (O^- at about 532 eV),[42,43] as published recently for the C- aerogels.[35] Oxygen in **C**(and **EC**)-**PBO** was also in the form of pyrylium and C-O^-, whereas the latter probably overlaps with some C=O also at around 532 eV,[44,45] hence the somewhat highest intensity peak. Oxygen in **C**(and **EC**)-**PA** was in the form of pyrylium, C=O, as well as C-O^- and N^+-O^-.[46] The N1s XPS spectra of **C**(and **EC**)-**PBO** were deconvoluted into two peaks at about 398 eV and 401 eV, assigned to pyridinic and pyridonic N's, respectivey, in a 7:3 ratio in favor of the pyridonic functionality. The N1s XPS spectra of **C**(and **EC**)-**PA** carbons were richer in functionality than those of the **PBO**-derived carbons; according to Figure 2, in addition to pyridonic and pyridinic N's, those materials also included N in quaternary positions as well as in N^+-O^- groups,[47–51] which increased the amount of negative $–O^-$ in the O1s spectra relative to pyrylium oxygen (refer to the **EC-PA, O1s** frame in Figure 2).

Figure 3 shows representative samples along processing. General material characterization data for all aerogels and the derived carbons are summarized in Table 1. As-prepared **RES** aerogels shrunk more (32–42%) relative to their molds than **PBO** and

PA (12–13%). That initial shrinkage followed the samples after carbonization, and all **C-RES** samples shrunk 53–67%, while **C-PBO** and **C-PA** shrunk only 36–40%. As demonstrated by Figure 3, after etching the differential shrinkage was only nominal for almost all samples. The highest differential shrinkages were noted for **EC-TPOL-O** and **EC-FPOL-O**, yet they were still quite low at 7% and 9%, respectively.

Owing to different sol-concentrations, in combination with different shrinkages, bulk densities of as-prepared aerogels varied over a wide range (Table 1). Without going into unnecessary detail, after pyrolytic carbonization (with or without prior oxidation), bulk densities (and porosities) of **C-RES** and **EC-RES** carbons (with the exception of **C-RF** and **EC-RF**) converged into common ranges (Table 1).

Because of lower shrinkage, bulk densities of **PBO**- and **PA**-derived carbons were almost as low as the corresponding carbons derived from **RF**. By increasing the monomer concentration from 3.3% to 15% w/w, the densities of **C-RF$_H\rho$-O** and **EC-RF$_H\rho$-O** samples came to the same range as of all other **C-RES-O** and **EC-RES-O**, respectively. Similarly, bulk densities of carbons from lower concentration **TPOL** sols, **C-TPOL$_L\rho$-O** and **EC-TPOL$_L\rho$-O**, were in the range of the carbons from **RF** at 3.3 % w/w, **PBO** at 7% w/w and **PA** at 25% w/w.

Table 1 also shows that EC-samples had lower densities than the corresponding C-samples, consistent with mass loss and no (or very small) differential shrinkage during etching. Also, while **C-RES-O** were slightly denser than **C-RES-D**, that difference was practically eliminated after etching, and by comparison densities of **EC-RES-D** and **EC-RES-O** were closer to one another. All skeletal densities (ρ_s) of C-samples (i.e., **C-RES-D**, **C-RES-O**, **C-PBO** and **C-PA**) were <2.0 g cm^{-3} and relatively close to one another.

Table 1. Material Properties of Nanoporous Carbons and Etched Carbon Aerogels Derived from RES, PBO and PA Aerogels

sample	linear shrinkage (%) [a,b]	bulk density, ρ_b (g cm^{-3}) [a]	skeletal density, ρ_s (g cm^{-3}) [c]	porosity, Π (% v/v) [d]	specific pore volume (cm^3 g^{-1})		surface area (m^2 g^{-1})		average pore diam. (nm) via $4\times V/\sigma$ [h]	
					V_{Total} [e]	V_{max} [f]	BET, σ	micropore [g]	$V = V_{Total}$	$V = V_{max}$
TPOL	32.2 ± 0.3	0.620 ± 0.009	1.434 ± 0.006	56.8 ± 0.8	0.92 ± 0.01	0.99	501	111	7.32	7.93
C-TPOL-D	53.4 ± 0.1	0.798 ± 0.008	1.794 ± 0.003	55.5 ± 0.5	0.70 ± 0.01	0.68 ± 0.04	527 ± 58	292 ± 52	5.29 ± 0.03	5.20 ± 0.04
C-TPOL-O	52.8 ± 0.8	0.708 ± 0.039	1.776 ± 0.007	60.1 ± 2.2	0.85 ± 0.04	0.75 ± 0.02	628 ± 46	349 ± 37	5.41 ± 0.01	4.77 ± 0.01
EC-TPOL-D	54.4 ± 0.4	0.381 ± 0.035	2.082 ± 0.009	81.7 ± 1.8	2.14 ± 0.04	1.63 ± 0.13	1752 ± 46	1069 ± 12	4.90 ± 0.00	3.73 ± 0.01
EC-TPOL-O	60.2 ± 1.0	0.422 ± 0.054	2.072 ± 0.008	79.6 ± 2.7	1.89 ± 0.05	2.13 ± 0.06	2568 ± 75	877 ± 48	2.94 ± 0.00	3.08 ± 0.03
C-TPOL$_L\rho$-O	52.2 ± 0.2	0.511 ± 0.003	1.919 ± 0.044	73.4 ± 2.8	1.44 ± 0.04	1.08 ± 0.05	376 ± 7	115 ± 8	15.3 ± 0.00	11.5 ± 0.01
EC-TPOL$_L\rho$-O	59.1 ± 1.8	0.177 ± 0.029	2.171 ± 0.027	91.8 ± 2.2	5.19 ± 0.04	2.62 ± 0.22	2246 ± 179	1604 ± 337	9.24 ± 0.03	4.67 ± 0.03
FPOL	41.9 ± 0.3	0.474 ± 0.007	1.508 ± 0.002	68.6 ± 0.5	1.45 ± 0.01	1.45	679	142	8.52	8.54
C-FPOL-D	60.5 ± 0.2	0.717 ± 0.012	1.884 ± 0.050	61.9 ± 3.2	0.86 ± 0.05	0 .80 ± 0.04	493 ± 70	213 ± 65	7.01 ± 0.07	6.46 ± 0.07
C-FPOL-O	69.0 ± 0.5	0.793 ± 0.010	1.958 ± 0.019	59.5 ± 1.2	0.75 ± 0.02	0.66 ± 0.05	594 ± 97	247± 91	5.05 ± 0.07	4.48 ± 0.07
EC-FPOL-D	62.1 ± 0.4	0.595 ± 0.053	2.179 ± 0.020	72.7 ± 2.7	1.22 ± 0.06	1.11 ± 0.06	943 ± 90	595 ± 83	5.18 ± 0.02	4.73 ± 0.03
EC-FPOL-O	70.0 ± 0.5	0.627 ± 0.078	2.114 ± 0.015	70.3 ± 3.8	1.12 ± 0.08	0.97 ± 0.04	1088 ± 52	657 ± 47	4.12 ± 0.01	3.56 ± 0.01
RF	34.0 ± 0.9	0.160 ± 0.006	1.310 ± 0.007	87.8 ± 0.8	5.49 ± 0.01	2.41	625	77	35.1	15.4
C-RF-D	56.2 ± 0.5	0.230 ± 0.005	1.805 ± 0.010	87.3 ± 0.8	3.79 ± 0.01	3.25 ± 0.08	753 ± 94	248 ± 38	20.2 ± 0.2	18.7 ± 0.3
C-RF-O	66.8 ± 0.7	0.302 ± 0.014	1.816 ± 0.017	83.4 ± 1.4	2.76 ± 0.02	2.11 ± 0.41	760 ± 64	251 ± 52	14.5 ± 0.1	14.1 ± 0.2
EC-RF-D	59.0 ± 0.8	0.096 ± 0.005	2.147 ± 0.043	95.5 ± 2.8	9.95 ± 0.04	6.77 ± 0.48	2355 ± 145	1112 ± 105	10.9 ± 0.04	11.5 ± 0.05
EC-RF-O	66.4 ± 0.9	0.101 ± 0.008	2.024 ± 0.030	95.0 ± 2.1	9.41 ± 0.03	5.26 ± 0.37	2484 ± 161	1030 ± 76	8.91 ± 0.02	8.69 ± 0.03
C-RF$_H\rho$-O	55.6 ± 0.3	0.821 ± 0.009	1.750 ± 0.014	53.1 ± 1.0	0.65 ± 0.02	0.72 ± 0.05	628 ± 46	371 ± 30	4.12 ± 0.01	4.62 ± 0.02
EC-RF$_H\rho$-O	56.5 ± 0.5	0.461 ± 0.015	1.893 ± 0.017	75.6 ± 1.4	1.64 ± 0.02	1.88 ± 0.29	2237 ± 341	1280 ± 176	2.93 ± 0.03	3.35 ± 0.08
PF	35.1 ± 0.4	0.454 ± 0.011	1.257 ± 0.001	63.9 ± 0.9	1.41 ± 0.01	1.19	199	6	28.3	23.9
C-PF-D	52.3 ± 0.4	0.618 ± 0.015	1.962 ± 0.013	68.5 ± 1.1	1.11 ± 0.02	0.99 ± 0.01	569 ± 41	387 ± 36	7.79 ± 0.02	6.89 ± 0.02
C-PF-O	54.7 ± 0.7	0.640 ± 0.021	1.909 ± 0.010	66.5 ± 1.3	1.04 ± 0.02	0.97 ± 0.03	519 ± 87	335 ± 83	8.01 ± 0.11	7.46 ± 0.11
EC-PF-D	53.0 ± 0.6	0.544 ± 0.036	2.070 ± 0.008	73.7 ± 1.8	1.36 ± 0.04	1.89 ± 0.00	1701 ± 9	1069 ± 4	3.19 ± 0.00	4.45 ± 0.00
EC-PF-O	55.3 ± 0.3	0.544 ± 0.029	2.124 ± 0.007	74.4 ± 1.4	1.37 ± 0.03	1.36 ± 0.06	1483 ± 83	1045 ± 51	3.69 ± 0.01	3.66 ± 0.01

Table 1. Material Properties of Nanoporous Carbons and Etched Carbon Aerogels Derived from RES, PBO and PA Aerogels (Cont.)

sample	linear shrinkage (%) [a,b]	bulk density, ρ_b (g cm^{-3}) [a]	skeletal density, ρ_s (g cm^{-3}) [c]	porosity, Π (% v/v) [d]	specific pore volume (cm^3 g^{-1})		surface area (m^2 g^{-1})		average pore diam. (nm) via $4\times V/\sigma$ [h]	
					V_{Total} [e]	V_{max} [f]	BET, σ	micropore [g]	$V = V_{total}$	$V = V_{max}$
PBO	11.6 ± 0.4	0.207 ± 0.001	1.207 ± 0.006	82.9 ± 0.7	4.00 ± 1.21	0.19	66	2	239	11.6
C-PBO	36.1 ± 0.4	0.303 ± 0.004	1.658 ± 0.009	81.7 ± 0.7	2.70 ± 1.66	0.31 ± 0.02	492 ± 32	404 ± 34	21.9 ± 0.05	2.55 ± 2.70
EC-PBO	37.8 ± 2.0	0.137 ± 0.023	1.834 ± 0.040	92.5 ± 3.2	6.75 ± 1.83	1.30 ± 0.21	2284 ± 301	1008 ± 112	11.8 ± 0.10	2.28 ± 0.05
PA [i]	12.9 ± 0.5	0.330 ± 0.008	1.321 ± 0.002	75.0 ± 0.6	2.27 ± 0.01	0.12	46	6	198	10
C-PA [i]	39.9 ± 0.3	0.451 ± 0.013	1.870 ± 0.025	75.9 ± 1.8	1.68 ± 0.03	0.23	302	230	22.0	3.0
EC-PA [i]	45.1 ± 0.2	0.247 ± 0.001	2.264 ± 0.034	89.1 ± 2.0	3.60 ± 0.03	0.80	1394	1122	10	2.8

[a] Average of 5 samples. [b] All values relative to the molds. [c] Single sample, average of 50 measurements. [d] Via $\Pi = 100 \times (\rho_s-\rho_b)/\rho_s$. [e] $V_{Total} = (1/\rho_b) - (1/\rho_s)$. [f] V_{max}: single-point N_2 adsorption at 77 K as $P/P_0 \rightarrow 1.0$. [g] Via the *t*-plot method. [h] For V_{Total} and V_{max} refer to footnotes [e] and [f]. [i] Data taken from reference 31.

After etching, all skeletal densities increased to >2.0 g cm^{-3} (except that of **EC-PBO**, whose ρ_s value increased significantly relative to that of **C-PBO**, yet remained <2.0 g cm^{-3}). The increase of ρ_s upon etching suggests that all C-samples included close porosity that became accessible by CO_2-etching. Open porosity, Π, was calculated from bulk and skeletal density data via $\Pi=100\times(\rho_s-\rho_b)/\rho_s$. As expected, Π followed an inverse relationship with bulk density and it was higher for EC-samples than for C-samples. Porosities of the lowest density carbon aerogels that include **EC-RF-O**(or **D**), **EC-TPOL$_L\rho$-O**, **EC-PBO** and **EC-PA** were 95%, 92%, 93% and 89% respectively. Porosities of higher-density EC carbons were in the 70–80% range.

Scanning electron micrographs have been provided previously for all materials of this study.[31,34,35] Microscopically, all carbon aerogels consisted of loose assemblies of nanoparticles forming meso and macropores. Nanoparticles themselves were microporous. Microporosity, however, is not visible in SEM. A quantitative analysis of the pore structure is important for the evaluation of the materials of this study as CO_2 adsorbers. Thereby, meso and macroporosity were evaluated with medium pressure N_2-sorption porosimetry at 77 K. Microporosity was probed with low-pressure N_2-sorption at 77 K, and with CO_2 adsorption at 273 K.

At a high-level, the evaluation of open porosity (accessible from outside) was conducted by comparing the total pore volumes ($V_{Total} = (1/\rho_b) - (1/\rho_s)$) with V_{max} (the total volume of N_2 uptaken during N_2 sorption porosimetry as $P/P_0\rightarrow1$). Typical N_2 sorption isotherms of C and EC carbon aerogels are demonstrated in Figure 4 using as examples the low-density **RF** (prepared with 3.3% w/w monomer concentration) and the **PBO** systems. All V_{Total} and V_{max} data for all materials are included in Table 1. The

overall observation is that V_{Total} and V_{max} values were close to one another for all **C-RES-D**(or **O**) and **EC-RES-D**(or **O**) samples, irrespective of density, indicating that all those carbons lacked large macropores (with pore sizes >300 nm).[52] On the contrary, it was found that in all C and EC samples of **PBO** and **PA** $V_{Total}>>V_{max}$ indicating mostly macroporous materials.

BET surface areas, σ, were calculated from the medium pressure N_2 sorption data and they increased dramatically after carbonization, and especially after etching, reaching values in the range of 2300–2800 m^2 g^{-1} (cases of **EC-PBO**, **EC-RF-D**(and **O**) and **EC-TPOL-O** - see Table 1 and Figure 5). As suggested by the early (i.e., at low pressure) rapid increase of N_2 adsorption in the isotherms of Figure 4, carbon aerogels contained a significant amount of micropores. The surface area allocation to those micropores (for a quick overview refer to Figure 5) was evaluated using *t*-plot analysis according to the Harkins and Jura method.[53,54] For the samples with the highest BET surface areas, the surface area allocation to micropores was in the range of 34% (case of **EC-TPOL-O**) to 44–47% (cases of **EC-PBO**, **EC-RF-D**(and **O**)). Significantly for the discussion of Section 2.2, **EC-PBO** and **EC-RF-D**(and **O**) shared similar porosities, BET surface areas, and micropore areas.

Average pore sizes were calculated throughout via the $4V/\sigma$ method. For every range of pore sizes (macro, meso and micro), always two sets of pore volume data from two independent experiments were compared. Thus, macro and mesopores were evaluated by setting $V=V_{Total}$ or $V=V_{max}$. Consistent with the conclusion drawn from the pore volume data, pore sizes calculated from the two methods converged pairwise (i.e., for C- and EC- samples) for all **RES**–derived carbons, indicating (a) mesoporous

materials throughout (in fact, all pore sizes were <20 nm), and (b) that the etching process did not alter the relative 3D structure of the skeletal framework (a fact that was already inferred from shrinkage – Figure 3). In all **PBO**- and **PA**-derived carbon aerogels, pore sizes were calculated much larger for $V=V_{Total}$, than for $V=V_{max}$, indicating a higher contribution from larger macropores not probed by N_2 sorption (>300 nm).

Shifting attention to micropores, microporosity was evaluated independently with CO_2 adsorption at 273 K (Figure 6), and with low-pressure (LP) N_2 sorption at 77 K (from the early parts of the isotherms of Figure 4). Specific pore volumes from both sets of data (CO_2 and LP-N_2) were calculated using the Dubinin-Radushkevich (DR) method, which has been developed based on volume-filling of microporous carbons, by recognizing the fact that micropores are on the same order of magnitude as the adsorbate itself.[55–59] Typical plots according to the DR method are shown in Figure S.1 of Appendix III in the Supporting Information. Pore volumes and pore size distributions for pores <1 nm were evaluated from the CO_2 adsoprtion data using the DFT method.[60–62] Subsequently, micropore volumes from the DR(N_2) and the DR(CO_2) analyses were used in order to calculate average micropore sizes via the 4*V*/(surface area) method, where the denominator was set equal to the micropore surface area that was calculated from the *t*-plot method (see Table 1). All micropore volume and size data are provided in Table 2.

Micropore size distributions for all carbon aerogels of this study are shown in Figure S.2 of Appendix IV in the Supporting Information. First it is noted that independently of the parent polymers, all micropore size distributions of the C- and the EC-carbon aerogels looked similar to one another. It is also noted that the etching process had a smoothening effect on the micropore cavities as crevices observed in the C-samples

had disappeared after etching, and the overall distributions had moved to slightly larger sizes. Nevertheless, those data might be a deceptive description of the actual microporosity as the DFT pore volumes (<1 nm) were consistently only up to 50% of the micropore volume calculated by the DR method (see Table 2). It was concluded that samples included larger micropores not accounted for by the DFT method. Next, turning to micropore volumes by the DR method (Table 2), it was noted that either with LP-N_2 at 77 K, or with CO_2 at 273 K, pore volumes were generally numerically close (in strong support of the pore filling hypothesis), however with a couple of quite pronounced exceptions. First, the micropore volumes calculated via DR(CO_2) for **EC-RF-D** and **EC-RF-O** (1.3–1.4 $cm^3\ g^{-1}$) were not only double of the already high values calculated via DR(N_2), but they were also at least 3 × higher than what was found for any other sample. Those measurements were repeated numerous times with several samples from different batches prepared at different points in time as long as six months apart. Importantly, neither the etched samples from higher-bulk-density **RF**-derived samples (**EC-RF$_H\rho$-O**), nor those from lower-bulk-density **TPOL**-derived samples (**EC-TPOM$_L\rho$-O**) would match the high pore volumes noted in **EC-RF-D** and **EC-RF-O**. The pore volumes in those two cases (**EC-RF$_H\rho$-O** and **EC-TPOL$_L\rho$-O**) remained in the range of everything else, 0.33 $cm^3\ g^{-1}$ and 0.36 $cm^3\ g^{-1}$, respectively. Now, turning back to pore sizes, it is noted that average pore sizes from the DR(N_2) and DR(CO_2) data do fall outside the pore-distribution range reported by the DFT method, supporting that the majority of "micropores" were >1 nm in size. In fact, average pore sizes indicate that most of those pores do not fall into the category of micropores at all (<2 nm), but rather they should be classified as small mesopores. Nevertheless, they will still be referred to as "micropores"

Table 2. Micropore Analysis and CO_2 Uptake

sample	specific micropore volume ($cm^3\ g^{-1}$)			pore diameter (nm) via $4\times V/$(micropore area)[d]		CO_2 uptake (mmol g^{-1}) at 273 K, 1 bar			
	DR (N_2)[a]	DR (CO_2)[b]	DFT (CO_2)[c]	*V* from DR (N_2)	*V* from DR (CO_2)	measured	from surface areas		from DR (N_2)[g]
							BET[e]	micropore[f]	
TPOL	—	0.13 ± 0.00	0.06 ± 0.00	—	4.62 ± 0.00	1.74 ± 0.01	4.9	1.1	—
C-TPOL-D	0.22	0.22 ± 0.00	0.11 ± 0.00	3.05 ± 0.05	2.95 ± 0.05	2.87 ± 0.02	5.2	2.9	5.18
C-TPOL-O	0.21	0.23 ± 0.00	0.12 ± 0.00	2.40 ± 0.01	2.69 ± 0.02	3.11 ± 0.04	6.1	3.4	4.87
EC-TPOL-D	0.68	0.41 ± 0.01	0.12 ± 0.00	2.54 ± 0.00	1.55 ± 0.00	5.86 ± 0.05	17	10.4	15.76
EC-TPOL-O	0.87	0.43 ± 0.01	0.12 ± 0.01	3.98 ± 0.01	1.96 ± 0.00	6.20 ± 0.07	25	8.6	20.28
C-TPOL$_L\rho$-O	—	0.15 ± 0.00	0.07 ± 0.00	—	5.23 ± 0.01	1.99 ± 0.01	3.7	1.1	—
EC-TPOL$_L\rho$-O	—	0.36 ± 0.01	0.10 ± 0.00	—	0.91 ± 0.02	4.37 ± 0.06	22	15.7	—
FPOL	—	0.13 ± 0.00	0.06 ± 0.00	—	3.69 ± 0.00	1.93 ± 0.01	6.6	1.4	—
C-FPOL-D	0.30	0.18 ± 0.00	0.09 ± 0.00	5.6_8 ± 0.26	3.4_3 ± 0.16	2.49 ± 0.02	4.8	2.1	7.04
C-FPOL-O	0.17	0.23 ± 0.00	0.11 ± 0.00	2.7_2 ± 0.18	3.7_2 ± 0.25	3.05 ± 0.03	5.8	2.4	3.90
EC-FPOL-D	0.37	0.40 ± 0.01	0.12 ± 0.00	2.51 ± 0.02	2.70 ± 0.03	5.70 ± 0.02	9.2	5.8	8.69
EC-FPOL-O	0.42	0.44 ± 0.01	0.12 ± 0.01	2.56 ± 0.01	2.69 ± 0.01	6.40 ± 0.09	11	6.4	9.76
RF	—	0.09 ± 0.00	0.03 ± 0.00	—	4.65 ± 0.00	1.33 ± 0.01	6.1	0.75	—
C-RF-D	0.18	0.20 ± 0.00	0.10 ± 0.00	2.92 ± 0.03	3.28 ± 0.04	2.79 ± 0.05	7.4	2.4	4.22
C-RF-O	0.25	0.20 ± 0.00	0.10 ± 0.00	4.06 ± 0.09	3.21 ± 0.07	2.78 ± 0.05	7.4	2.5	5.93
EC-RF-D	0.63	1.3_3 ± 0.51	0.16 ± 0.03	2.25 ± 0.01	4.7_9 ± 0.37	$14._8$ ± 3.9	23	10.9	14.53
EC-RF-O	0.80	1.3_8 ± 0.43	0.14 ± 0.03	3.11 ± 0.01	5.3_6 ± 0.27	$13._7$ ± 2.7	24	10.1	18.61
C-RF$_H\rho$-O	—	0.30 ± 0.02	0.10 ± 0.00	—	2.34 ± 0.01	2.79 ± 0.02	6.1	3.6	—
EC-RF$_H\rho$-O	—	0.33 ± 0.01	0.09 ± 0.00	—	1.02 ± 0.01	3.79 ± 0.05	22	12.5	—
PF	—	0.06 ± 0.00	0.02 ± 0.00	—	[h]	0.79 ± 0.00	1.9	0.06	—
C-PF-D	0.09	0.23 ± 0.00	0.11 ± 0.00	0.92 ± 0.00	2.35 ± 0.01	3.02 ± 0.01	5.6	3.8	2.06
C-PF-O	0.06	0.23 ± 0.00	0.11 ± 0.00	0.74 ± 0.02	2.75 ± 0.08	3.07 ± 0.01	5.1	3.3	1.45
EC-PF-D	0.31	0.38 ± 0.00	0.12 ± 0.00	1.18 ± 0.00	1.40 ± 0.00	5.35 ± 0.04	17	10.4	7.31
EC-PF-O	0.43	0.42 ± 0.00	0.13 ± 0.00	1.64 ± 0.00	1.63 ± 0.00	6.03 ± 0.03	15	10.2	9.96
PBO	—	0.02 ± 0.00	0.01 ± 0.00	—	[h]	0.25 ± 0.03	0.64	0.02	—
C-PBO	0.20	0.21 ± 0.02	0.12 ± 0.01	2.02 ± 0.01	2.08 ± 0.02	2.9_5 ± 0.20	4.8	4.0	4.74
EC-PBO	0.71	0.32 ± 0.01	0.08 ± 0.01	2.82 ± 0.02	1.26 ± 0.01	3.2_6 ± 0.13	22	9.9	16.51
PA	—	0.06	0.03	—	[h]	0.80 [i]	0.45	0.06	—
C-PA	0.55	0.21	0.13	9.51	3.65	3.07 [i]	3.0	2.3	12.71
EC-PA	0.41	0.38	0.12	1.47	1.35	4.85 [i]	14	11.0	9.59

[a] Via the Dubinin-Radushkevich (DR) method from N_2 sorption data obtained at 77K using a low-pressure transducer ($P/P_\circ \leq 0.01$). Single experiments. [b] Via the DR method from CO_2 adsorption data at 273 K up to relative pressure of 0.015. Data are averages from at least 3 experiments, except for **EC-RF-D** and **EC-RF-O**, which are averages from 14 and 7 isotherms, respectively. [c] Like in [b] using the DFT method. Pore volumes are for pores <1 nm in size. [d] Calculated as indicated using the micropore surfaces areas calculated via the *t*-plot method. [e] Calculated by dividing the BET surface area over the CO_2 cross sectional area (0.17 nm^2), over Avogadro's number. [f] Calculated by dividing the the micropore surface area over the CO_2 cross sectional area (0.17 nm^2), over Avogadro's number. [g] Calculated by assuming that micropore volumes (see footnotes [a] and [b], respectively) are filled with liquid CO_2 (the density of liquid CO_2 at 273 K, was taken equal to the density of adsorbed CO_2 (1.023 g cm^{-3} – see text). [h] Micropore surface areas were too small ($\leq 6\ m^2\ g^{-1}$), samples practically had no microporosity. [i] Data from reference 31.

(in quotations) in reference to the methods they were probed with, namely LP-N_2 and CO_2 adsorption. Such "micropore" sizes calculated using pore volumes via the DR(N_2) method were about equal, or for several samples even larger, than the micropore volumes calculated via the DR(CO_2) method. The samples with the largest "micropore" volumes via CO_2 adsorption, that is **EC-RF-D** and **EC-RF-O**, were among the samples with the largest "micropores" as well (4.8 and 5.4 nm, respectively). By the same token, carbon samples prepared from higher-density **RF** aerogels, that is **C-RF$_{H\rho}$-O** and **EC-RF$_{H\rho}$-O**, showed significantly smaller pore sizes (2.3 nm and 1.0 nm, respectively).

In summary, as derived from properties probed by CO_2 sorption, **EC-RF-D** and **EC-RF-O** showed an increased aptitude for CO_2 uptake, which is discussed in the next section.

2.2. CO_2 UPTAKE BY THE CARBON AND ETCHED CARBON AEROGELS

The total CO_2 uptake at 273 K was taken from the isotherms of Figure 6 at 1 bar (P/P_o=0.03). (It is noted that all isotherms of Figure 6 are reversible with no hysteresis, but for simplicity only the adsorption branches are shown.) Results are presented in Table 2, along with uptake values calculated by assuming either: (a) monolayer coverage of the entire BET surface area with CO_2 (0.17 nm^2 per molecule[63]); or, (b) monolayer coverage of only the micropore surface area; or, (c) micropore filling with CO_2 in a state that resembles liquid CO_2 (the density of adsorbed CO_2 has been cited as 1.023 g cm^{-3},[64,65]). Experimental data and results from calculations are summarized in bar-graph form in Figure 7. (For calculating pore filling with CO_2 from pore volumes, only pore volumes by

the DR(N_2) method were considered; this is because the pore volume data from the DR(CO_2) method were not independent from the CO_2 uptake data.)

As noted in Figure 7 (red bars), etched samples in general uptook significantly more CO_2. **C-PBO** and **EC-PBO** comprised an exception with amounts of CO_2 uptaken by the two samples being about equal (3.0 and 3.3 mmol g^{-1}, respectively). Those amounts were generally low and comparable to the amounts uptaken by **C-RES-D**(and **O**) and **C-PA** (2.5–3.1 mmol g^{-1}). Focusing on EC-carbons now, the amount of CO_2 uptaken by **EC-PA** (4.85 mmol g^{-1}) was only slightly less than the amounts uptaken by most **EC-RES-O**(or **D**) (5.4–6.4 mmol g^{-1}), except by **EC-RF-O**(or **D**), which uptook 14–15 mmol g^{-1}. That amount of CO_2 uptaken was unusually high, but it was confirmed with numerous samples from different batches prepared and tested a few months apart from one another, and it represents the highest CO_2 uptake we are aware of among various microporous polymers and carbon-based adsorbers, including carbon nanotubes (CNTs).[66,67] (An extensive comparison of all EC-carbon aerogels of this study with other adsorbers from a literature survey is given in Figure S.3 of Appendix V in the Supporting Information.) Importantly, control samples from higher-density **RF** aerogels, i.e., **EC-RF$_{H}\rho$-O**, took up a lower amount of CO_2 (3.8 mmol g^{-1}) than the rest of **EC-RES-O** aerogels, including the other EC- control sample, **EC-TPOL$_{L}\rho$-O** (4.4 mmol g^{-1}), which was prepared from a lower-density **TPOL** aerogel precursor.

The amounts of uptaken CO_2 by *all* as-prepared C-type carbon aerogels (i.e., including all **C-RES**, as well as **C-PBO** and **C-PA**) correlated extremely well with monolayer coverage of the micropore surface areas (Figure 7 – compare corresponding red and shaded yellow bars). The amounts of CO_2 uptaken by all EC- samples, including

the high-uptake **EC-RF-D** and **EC-RF-O**, were significantly lower than those calculated both by monolayer coverage of the BET surface areas (Figure 7 – compare corresponding red and full yellow bars), and by filling the micropore volumes (Figure 7 – compare red and blue bars). With regards to monolayer coverage of the micropore surfaces, the experimental CO_2 uptake by N-containing **EC-PBO** and **EC-PA** fell also far behind. On the other hand, with the exception of **EC-RF-D**(and **O**), all other **EC-RES** aerogels showed an about equal (case of **EC-FPOL**), or again lower (cases of **EC-TPOL** and **EC-PF**) CO_2 uptake than what was calculated by monolayer coverage of the micropore surfaces. However, the case of **EC-RF-D**(and **O**) was particularly interesting: in those samples the amount of uptaken CO_2 was well above the amount needed for monolayer coverage of the micropores, in fact falling between the amounts calculated for monolayer coverage and pore filling by CO_2. Overall, either through the optic of surface coverage, or through pore filling, CO_2 uptake was a property related to micropores, and in some cases (most notable in **EC-RF-D**(and **O**)) it might have involved both the micropore surface area and the micropore volume. The highest CO_2 uptake was noted from carbon samples that contained only O as a heteroatom. It is also noteworthy that **EC-PBO**, with comparable density (Table 1), about equal BET and micropore surface areas (Figure 5), and about equal DR(N_2) micropore volumes (Table 2) to the highest-uptake **EC-RF-D** and **EC-RF-O**, showed a much *lower* CO_2 uptake capability. For further insight, we turned into an assessment of the interaction between adsorbate (CO_2) and adsorbent (carbon) via measurements of the isosteric heats of adsorption of CO_2 by all carbon aerogels of this study.[16]

2.3. CO_2 UPTAKE CAPACITY AND THE MECHANISM OF ADSORPTION

Isosteric heats of CO_2 adsorption, Q_{st}, as the negative of the differential change in the total enthalpy of a closed system, were calculated as a function of CO_2 uptake by employing Virial fitting of the CO_2 adsorption isotherms of each material at two different temperatures (273 K and 298 K – see Figure 6). The Virial fitting procedure is described in the Experimental section.[68] Figure S.4 of Appendix VI in Supporting Information shows typical plots used for Virial fitting, and Table S.3 gives all Virial coefficients for all carbon aerogels of this study.) Figure 8 shows the Q_{st} plots (i.e., calculated Q_{st} values vs. CO_2 uptake) of the C and EC carbon aerogels from the systems that showed extreme cases of CO_2 uptake (**RF, PBO** and **PA**). (Plots of Q_{st} vs. CO_2 uptake for the remaining carbons are shown in Figure S.5 of Appendix VII in Supporting Information.)

The energy of interaction of CO_2 with the surface of the adsorbate is referred to as Q_o and is given by the intercept of the Q_{st} plot at zero CO_2 uptake. It is accepted that higher Q_o values (>40 kJ mol^{-1}) correspond to chemisorption, lower values to physisorption.[69] Beyond interaction with the surface, Q_{st} plots may remain flat, curve down or curve up. Convex-down behavior is typically attributed to the fact that more favorable sites are occupied first.[70] Convex-up curves have been attributed to attractive interactions (e.g., van der Walls) between adsorbed molecules (CO_2-CO_2).[71] Irrespective of curving up or down, for most materials of this study, Q_{st} plots were rather insensitive to the number of polynomial terms used for Virial expansion. That was not true, however, for high-CO_2-uptake **EC-RF-O**(or **D**). For illustration, Figures 8 and S.5 show just two such curves marked with the number of polynomial terms (*m* and *n*) used for Virial fitting (see Experimental). At their end (i.e., at about 14 mmol of CO_2 adsorbed per gram of

carbon) those curves may end up at unrealistically high or low (negative) values. That breakdown of Virial fitting at high CO_2 uptake values is easy to visualize mathematically, if one considers the fact that Q_{st} depends on the amount of CO_2 uptaken raised to the power of the highest term in the polynomial expansion (see Experimental). What is important though is that despite divergence at high CO_2 uptake, the family of curves for **EC-RF-O** (Figures 8) and for **EC-RF-D** (Figure S.5) started at the same Q_o values respectively, and coincided up to about 4–5 mmol of CO_2 adsorbed per gram of carbon, which corresponds to about a monolayer coverage.

Q_o data are cited in Table S.4 of Appendix VIII in Supporting Information, and are compared in Figure 9 in bar-graph form. Q_o values of carbons containing N (i.e., **C**(and **EC**)-**PBO** and **C**(and **EC**)-**PA**) were significantly lower relative to all **EC-RES-D**(or **O**), and at about the same level as the Q_o values of the **C-RES-D**(and **O**) carbons (20 kJ mol^{-1} or less). In that regard, the Q_o values of **EC-RES-O**(or **D**) were in general <30 kJ mol^{-1}, except for the Q_o values of **EC-RF-O**(and **D**) that were found at 42 and 35 kJ mol^{-1}, respectively, and could be considered borderline cases for chemisorption.

Now, between **C-PA** and **EC-PA**, where the ratio of O:N remained about the same (Figure 1), the energy of interaction of CO_2 with the surface remained also about the same. Turning to **EC-PBO**, the weight percent of O remained the same relative to **C-PBO**, but N was reduced in half (Figure 1), and its identity shifted in favor of less-nucleophilic pyridonic at the expense of pyridinic N (80:20 vs 68:32 before etching, via XPS). By the same token, the interaction of CO_2 with **EC-PBO** was weaker (Q_o=12 kJ mol^{-1}) than its interaction with **C-PBO** (Q_o=19 kJ mol^{-1} – see Table S.4). It appears that the interaction of CO_2 with the surfaces of the carbons of this study depends strongly on

the heteroatoms, yet not in a way that correlates with the higher quadrupole moment of nitrogen-rich sites that would increase the binding affinity with quadrupolar CO_2.[19] In addition, adsorption of quadrupolar CO_2 in micropores is typically attributed to quadrupole interactions with the pore walls, and is favored by smaller micropores (yielding higher Q_o values[72]) where quadrupole fields come closer and interact stronger with the adsorbate.[73,74] This does not seem to be the case here: generally, EC samples have higher Q_o values than their C counterparts (except **EC-PBO**, Figure 9), but their smaller micropores are also wider (e.g., see Figure S.2). Considering all of the above together, an alternative mode of interaction of CO_2 with the surfaces of the specific aerogels may involve formation of carbamate with surface pyridinic/pyridonic nitrogens (Eq 1), or carbonate with phenoxide groups (Eq 2).

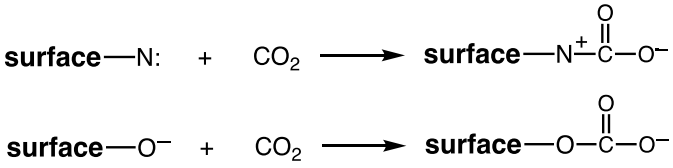

(1)

(2)

Equattions 1 and 2 are proposed based on extensive theoretical work on CO_2 capture via solution-phase formation of carbamate with, for example, methylamine, and follow the same enthalpic/entropic arguments.[75–77] Specifically, given that CO_2 entering micropores has already paid a severe entropic penalty,[78] and thus considering bond energies alone, Eq 1 is slightly endothermic (by about 17 kcal mol^{-1}), while Eq 2 is about energy-neutral. Those estimates support: (a) the higher Q_0 values for **RES**-derived carbons relative to those from **PBO** and **PA**, and (b) the much higher uptake of CO_2 by **EC-RF-D** and **EC-RF-O** relative to **EC-PBO**, which has practically identical material

properties with the former two, as discussed above. Our rough thermochemical calculation is in close agreement with the results of quantum mechanical calculations for the methylamine-CO_2 adduct, and was based on the bond energy of C=O, which is 173−181 kcal mol^{-1}, the bond energy of C−O, which is about half of the energy of C=O: 85−91 kcal mol^{-1}, and the bond energy of C–N, which is somewhat lower: 69–75 kcal mol^{-1}.[79]

As mentioned above, among RES-derived carbon aerogels, the Q_0 values of **C-RES-D**(or **O**) were lower than those of the corresponding **EC-RES-D**(or **O**), while the energies of interaction of **EC-RF-D**(and **O**) were higher than the rest of **EC-RES-D**(and **O**). The question is whether those two observations are related to one another, and whether they are also related to the high CO_2 uptake by **EC-RF-D**(and **O**). One probable cause for all three phenomena might be traced to the way micropores are filled, which in turn is related to the micropore size, and the fact that a monolayer coverage alone is sufficient to explain the uptake of CO_2 by all **RES**-derived carbon aerogels, except by **EC-RF-D**(and **O**) (Figure 7). The latter aerogels have displayed the largest “micropores” and “micropore” volumes (Table 2). Smaller micropores, as those identified with the DFT method (Figure S.2), are close to molecular dimensions. Monolayer coverage of those pores implies congestion and steric hindrance, which works against the thermal neutrality of Eq 2. By the same token, widening of those small micropores by etching (Figure S.2) should relieve congestion, and Q_o values should increase, as observed (Figure 9). It is speculated that after monolayer coverage of **EC-RF-D**(and **O**) micropores with CO_2 (at approximately 6 mmol g^{-1}), Eq 2 is followed by an isoenthalpic

cascade of reactions (see Eq 3). Just like Eq 2, Eq 3 is approximately energy-neutral as long as it refers to micropores, and

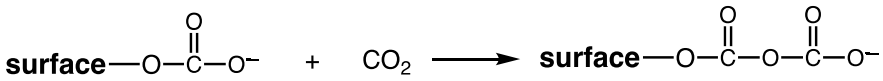

(3)

should continue until micropores are filled. Eq 3 implies that it is favorable for CO_2 to be adsorbed on CO_2, a fact supported by the upward trend of the Q_{st} plots as a function of uptaken CO_2, which is more pronounced in the etched samples. The fact that control samples **EC-RF$_H\rho$-O** and **EC-TPOL$_L\rho$-O** did not show a large uptake of CO_2 is consistent with their smaller "micropores." The size of small pores is related to the openness of the material that goes through the etching process, and to how thick its skeletal walls are, namely its bulk and skeletal densities and porosities.[21]

2.4. SELECTIVITY TOWARDS ADSORPTION OF CO_2 RELATIVE TO OTHER GASSES

High CO_2 uptake is necessary for efficient separation, but it is not sufficient.[5] High selectivity towards other gasses is also important for practical applications. Relevant to pre-combustion gas purification is selectivity toward CH_4 and H_2, and relevant to post-combustion CO_2 sequestration is selectivity towards N_2.[6] Figure 6 above included CH_4 and H_2 adsorption isotherms at 273 K of **C**(and **EC**)-**RF-O**, **C**(and **EC**)-**PBO** and **C**(and **EC**)-**PA**. Selectivity of adsorbents is often evaluated by comparing the initial slopes of the corresponding isotherms of two competing gases, assuming that at low coverage the uptake conforms Henry's law. However, in many cases isotherms deviate from linearity even at the lowest pressures. For example, isotherms of

microporous materials, or materials with heterogeneous microporous surfaces may show convex behavior starting from the beginning. In this work, isotherms at 273 K (Figure 6) were fitted with a Virial-type equation (different from the one used for the Q_{st}),[80,81] which was used to evaluate the Henry's constant, $K_{H,}$ for each gas as described under Methods in the Experimental section. Selectivities were calculated as the ratios of those values, and are presented together with the maximum gas uptake values in Table S.4 of Appendix VIII of the Supporting Information. The selectivities for selected carbon aerogels (**C**(and **EC**)**-RF-O**, **C**(and **EC**)**-PBO** and **C**(and **EC**)**-PA**) are shown and compared in bar-graph form in Figure 10. Data for all other systems are shown in the same format in Figure S.6 of Appendix IX in Supporting Information.

The uptake of N_2 and H_2 were quite low by all carbon aerogels of this study (Table S.4 and Figure 6), however the uptake of CH_4 could reach over 2.0 mmol g^{-1}. The latter has been attributed to the high polarizability of CH_4.[31,82,83] Qualitatively, low uptake of N_2 and H_2 creates shallow isotherms with low initial slopes (K_H values), thereby large differences from the initial slopes of the CO_2 adsorption isotherms, leading to high selectivities for CO_2 towards those two gasses. By the same token, selectivities for CO_2 towards methane were the lowest (typically $\leq$5). Although there were no definite trends in the selectivities before and after etching, the least variability was noted in the **PA**-derived carbons, and the most in the **PBO**-derived ones, probably reflecting the similarity or the difference, respectively, in the lining of micropores (refer to the O:N ratio in Figure 1).

Overall, the highest selectivities were observed towards H_2, next towards N_2 and finally towards CH_4. For reasons just described, the materials with the highest CO_2

uptake, **EC-RF-D** and **EC-RF- O**, showed also good selectivities towards H_2 (about 200:1), and also the best ones among all other materials of this study towards CH_4 (about 10:1). Concerning post-combustion CO_2-N_2 separation, the selectivity of those **RF**-derived carbons ranged on average around 70:1 (albeit with a large standard deviation of about ±20), and in that regard, all other things being equal (273 K, 1 bar) they were at par with organic cages (selectivity towards N_2 at 73:1),[84] amide networks based on tetraphenyl adamantane (58:1–74:1),[85] and AZO-COPs from tetrafunctional monomers (64:1–110:1).[19] In general, **EC-RES-D**(and **O**) show a good balance between high CO_2 adsorption capacity and selectivity toward other gasses.

3. CONCLUSIONS

We investigated CO_2 adsorption by various types of carbon aerogels. Emphasis was placed on microporosity in combination with the presence of heteroatoms (O and N). In that regard, we compared carbon aerogels coming from phenolic resins that contained only oxygen (**TPOL**, **FPOL**, **RF** and **PF**), and carbon aerogels coming from polymeric aerogels that contained both oxygen and nitrogen (**PBO** and **PA**). As demonstrated by carbon aerogels derived from resorcinol-formaldehyde (**RF**), and polybenzoxazine (**PBO**) aerogels with similar densities, porosities, micropore volumes, BET and micropore surface areas, the former materials that contained only oxygen were much better CO_2 adsorbers at 273 K, 1 bar (by 3–4 times) than the latter that contained both O and N. In fact, etched **RF**–derived carbon aerogels seem to have set a new level in terms of CO_2 uptake at 13–14 mmol g^{-1}. In most cases, CO_2 uptake could be associated with monolayer coverage of CO_2 on the microporous surfaces. In the case of etched **RF**-

derived carbons, however, data have shown that CO_2 uptake proceeds beyond monolayer coverage of the micropore surfaces. It is speculated that pore filling may be attributed to an isoenergetic processes: (1) surface-O^- + CO_2 ---> surface-O-(CO)-O^-, followed by (2) surface-O-(CO)-O^- + CO_2 ---> surface-O-(CO)-O-(CO)-O^- that continues until micropores are filled with CO_2. Beyond that point, further adsorption would entail a large entropic penalty. Although those surface processes amount to chemisorption, their energetic neutrality warrants reversibility that produces isotherms with no hysteresis, a feature desirable for regeneration purposes.[17] Overall, etched **RF**-derived carbon aerogels show a good balance between CO_2 adsorption capacity and selectivity towards other gases. A final point that may worth further investigation is the combination of decent adsorption capacities towards CH_4 (Table S.4) with relatively good selectivities towards H_2 (Figure 10), for CH_4/H_2 separation.

4. EXPERIMENTAL

4.1. MATERIALS

4.1.1. Gasses. Syphon grade CO_2 and N_2 at 99.999% purity, and Ar at 99.99999 % purity were purchased from Ozark Gas, Rolla, MO. H_2, CO_2 and CH_4 (all three gasses at 99.999% purity) were purchased from Air Gas, Rolla, MO.

4.1.2. Aerogel Synthesis. RES refers to the following phenolic resin aerogels:[35] phloroglucinol-terephthalaldehyde (**TPOL**), phloroglucinol-formaldehyde (**FPOL**), resorcinol-formaldehyde (**RF**), and phenol-formaldehyde (**PF**). All four wet-gel precursors were prepared in organic sols using HCl-catalysis.[86] As-prepared **RES** aerogels were either carbonized directly (see below), or were first treated for 5 h at 240

^{o}C in air. Carbons that were obtained by further pyrolysis at 800 ^{o}C (see below) are designated as –D or –O, for Direct and Oxidized, respectively. **PBO** refers to polybenzoxazine aerogels prepared from wet-gels obtained via room-temperature, HCl-catalyzed polymerization of Ishida's monomer in DMSO at 7% w/w concentration in the sol.[36–38] Before carbonization, PBO aerogels were cured for 5 h in air at 200 ^{o}C as described recently.[34] **PA** aerogels were also prepared at 25% w/w monomer concentration as described recently.[31]

4.1.3. Carbonization. All aerogels from above were carbonized in a tube furnace at 800 ^{o}C under flowing high purity Ar at 0.3 L min^{-1}. The resulting carbon aerogels are referred to as **C-RES**, **C-PBO** and **C-PA**.

4.1.4. Reactive Etching with CO_2. Carbon aerogels were etched with flowing CO_2 (0.3 L min^{-1}) at 1000 ^{o}C for 3 h. This process is also referred to as activation. The resulting Etched-Carbon aerogels are referred to as **EC-RES**, **EC-PBO** and **EC-PA**. For producing EC-carbons, right after the 5 h carbonization stay at 800 ^{o}C under Ar, the tube furnace was heated to 1000 ^{o}C under continuous flow of Ar, the flowing gas was switched to CO_2 for 3 h, and then back to Ar. All heating and cooling of the tube furnace was conducted at a rate of 2.5 ^{o}C min^{-1}.

4.2. METHODS

4.2.1. Drying Procedure. Wet-gels were dried in an autoclave (SPIDRY Jumbo Supercritical Point Dryer, SPI Supplies, Inc. West Chester, PA). Samples were placed into a special boat and were covered with acetone. The boat was loaded to the autoclave that was kept at 14 ^{o}C. The pressure vessel was closed, and liquid CO_2 was allowed in.

Acetone was drained out from the bottom of the autoclave while more liquid CO_2 was allowed in. Samples were left to equilibrate under liquid CO_2 for 30 min before liquid CO_2 was drained out again while it was simultaneously replenished with more liquid CO_2. That cycle was repeated until all acetone had been extracted out of the samples. Subsequently, the temperature of the autoclave was raised to 40 °C. After one hour at that temperature, supercritical fluid (SCF) CO_2 was vented off as a gas over a period of 5 h.

4.2.2. Oxidative Curing and Pyrolysis. Oxidative curing (ring-fusion aromatization) was conducted in a conventional convection oven. All pyrolyses were conducted under conditions described above in a MTI Corporation Model GSL1600X tube furnace equipped with an outer and an inner tube both of 99.8% pure alumina (outer tube: 1022 mm × 82 mm × 70 mm; inner tube: 610 mm × 61.45 mm × 53.55 mm; heating zone at set temperature: 457 mm).

4.2.3. CHN Elemental Analysis. It was conducted with an Exeter Analytical Model CE440 elemental analyzer, calibrated with acetanilide, urea, and glycine. The combustion furnace was operated at 1,050 ºC. All calibration standards and samples were run three times and results are given as averages. The oxygen content was calculated by subtracting %C+%H+%N from 100%.

4.2.4. XPS Analysis. It was carried out with a Kratos Axis 165 Photoelectron Spectroscopy System. Samples were mixed and ground together with Au powder (5% w/w) as internal reference. The mixture was compressed to pellets. Each pellet was placed on a piece of conductive carbon tape that was adhered to a stainless-steel sample holder. Samples were introduced into the analysis chamber one at a time and the chamber was evacuated at 10^{-8} Torr or lower. No ion sputtering was performed on any of

the samples. An Al monochromatic source at 150 watts was used for excitation. A charge neutralizer was used to reduce the effects of differential or sample charging. The analysis area was 700 × 300 microns. Elemental quantification calculations were based on broad survey results from single sweeps at higher sensitivity (Pass energy = 80) and were carried out with the Kratos Axis Vision processing software taking into consideration the appropriate relative sensitivity factors for the particular XPS system. High resolution elemental scans where carried out at a lower sensitivity (Pass energy = 20), using multiple sweeps to improve the signal-to-noise ratios. Deconvolution of N 1s and O 1s spectra was performed with Gaussian function fitting using the OriginPro 8.5.1 software package.

4.2.5. Physical Characterization. Bulk densities (ρ_b) were calculated from the weight and the physical dimensions of the samples. Skeletal densities (ρ_b) were measured using helium pycnometry on a Micromeritics AccuPyc II 1340 instrument.

4.2.6. Porosimetry and Gas Sorption Studies. Prior to analysis, all samples were degassed at 80 °C for 24 h in a vacuum oven. Subsequently, they were subjected to further degassing at 120 °C and a pressure below 20 mTorr for 12 h on a Micromeritics VacPrep061 sample degassing system. BET surface areas, σ, were determined via the Brunaue-Emmete-Teller (BET) method from medium-pressure N_2-sorption isotherms at 77 K using a TriStar II 3020 surface area and porosity analyzer. Micropore surface areas were calculated via *t*-plot analysis of the N_2-sorption isotherms using the Harkins and Jura model.[51,52] Average diameters of pores above 2 nm in size were calculated using the $4\times V/\sigma$ method, where the specific pore volume, V, was set equal either to $V_{\text{Total}} = (1/\rho_b) - (1/\rho_s)$, or to V_{max}, which is the single highest volume of N_2 adsorbed along the N_2-

sorption isotherm as $P/P_0 \rightarrow 1$. Micropore analysis was conducted with low-pressure N_2 sorption at 77 K using a Micromeritics ASAP 2020 instrument equipped with a low-pressure transducer, or with CO_2 adsorption up to 760 Torr (relative pressure $P/P_0 = 0.03$) at 273 K using the Micromeritics TriStar II 3020 system mentioned above. Prior to low-pressure N_2-sorption analysis at 77 K, a third degassing step was carried out under 1 μm Hg at 120 °C directly on the analysis port of the Micromeritics ASAP 2020 instrument (this step is critically important). Micropore volumes were determined either from the low-pressure N_2-sorption data at 77 K, or from the CO_2 adsorption data at 273 K by using the Dubinin-Radushkevich (DR) equation.[55–59] Average micropore sizes were calculated using again the 4×*V*/*micropore area* method, where the specific micropore volume, *V*, was set equal to the micropore volumes calculated via the DR model either from the low-pressure N_2 or the CO_2 adsorption data, and the micropore area was set equal to the micropore surface area obtained from the *t*-plot method. Micropore size distributions for pores <1 nm were obtained from the CO_2 adsorption data using the DFT method.[60–62]

Relative adsorption studies for CO_2, CH_4, N_2, and H_2 at 273 K up to 1 bar were performed on a Micromeritics TriStar II 3020. The total CO_2 uptake at 273 K was obtained from the same data used for micropore analysis. In order to calculate isosteric heats of CO_2 adsorption (Q_{st}) and isosteric heats at zero coverage (Q_0), CO_2 adsorption isotherms were also obtained at 298 K.

4.2.7. Calculation of Isosteric Heats of CO_2 Adsorption (Q_{st}). They were calculated via the Virial method.[68] For this, the CO_2 adsorption isotherms at 273 K and 298 K were fitted simultaneously with a Virial-type equation (Eq 4) using the OriginPro 8.5.1 software package.

$$\ln P = \ln N + \frac{1}{T}\sum_{i=0}^{m} a_i N^i + \sum_{i=0}^{n} b_i N^i \quad (4)$$

(P is pressure in Torr, N is the adsorbed amount in mmol g^{-1}, T is the absolute temperature, a_i and b_i are the Virial coefficients, and m and n are the number of coefficients needed in order to fit the isotherms adequately.) Using the least squares method, the values of m and n were gradually increased until the sum of the squared deviations of the experimental points from the fitted isotherm was minimized. Typically, $0 \leq m \leq 4$ and $0 \leq n \leq 2$, but generally most data were fitted well with $m = 4$ and $n = 2$. Exceptions were **EC-RF-D** and **EC-RF-O**, which showed a large sensitivity to the values of m and n, resulting in wide divergence of the respective Q_{st} plots for values of $N \geq 6$ (see Figures 8 and S.5). All Virial coefficients for all samples, along with key statistical parameters, are given in Appendix VI of the Supporting Information. The values of a_o to a_m were introduced into Eq 5 and isosteric heats of adsorption (Q_{st}) were calculated as a function of the surface coverage (N).

$$Q_{st} = -R\sum_{i=0}^{m} a_i N^i \quad (5)$$

(R is the universal gas constant (8.314 J mol^{-1} K^{-1}) and Q_{st} is given in kJ mol^{-1}.) The common term in Eq 5 for all N, Q_0, corresponds to $i = 0$ and is given by Eq 6.

$$Q_0 = -Ra_0 \quad (6)$$

Q_0 is the heat of adsorption as coverage goes to zero, and is a sensitive evaluator of the affinity of the adsorbate for the surface.[87]

4.2.8. Calculation of Adsorption Selectivities. Adsorption selectivities for one gas versus another were calculated as the ratios of the respective Henry's constants, K_H. The latter were calculated via another Virial model,[80,81,88] whereas the single-component adsorption isotherms for each gas at 273 K were fitted according to Eq 7.

$$\ln N = \ln P + K_1 + K_2 N + K_3 N^2 + \ldots = \ln P + \sum_{i=1}^{m} K_i N^{i-1} \quad (7)$$

Fitting was carried out using the least squares method by varying the number of terms, until a suitable number of terms, *m*, described the isotherms adequately. The coefficients K_1, K_2, ... K_m are characteristic constants for a given gas-solid system and temperature. The Henry's constant for each gas, K_H, is the limiting value of N/P as $P \rightarrow 0$, and is given by Eq 8.

$$K_H = \lim_{P \to 0} \left(\frac{N}{P}\right) \cong e^{K_1} \quad (8)$$

In order to calculate standard deviations, all isotherms obtained experimentally for each component were fitted individually. The K_H values from all isotherms were averaged, and the average values were used to calculate selectivities by taking the ratios. Standard deviations for the ratios were calculated using rules for propagation of error.

SUPPORTING INFORMATION: Supporting Information is available from the Wiley Online Library or from the author.

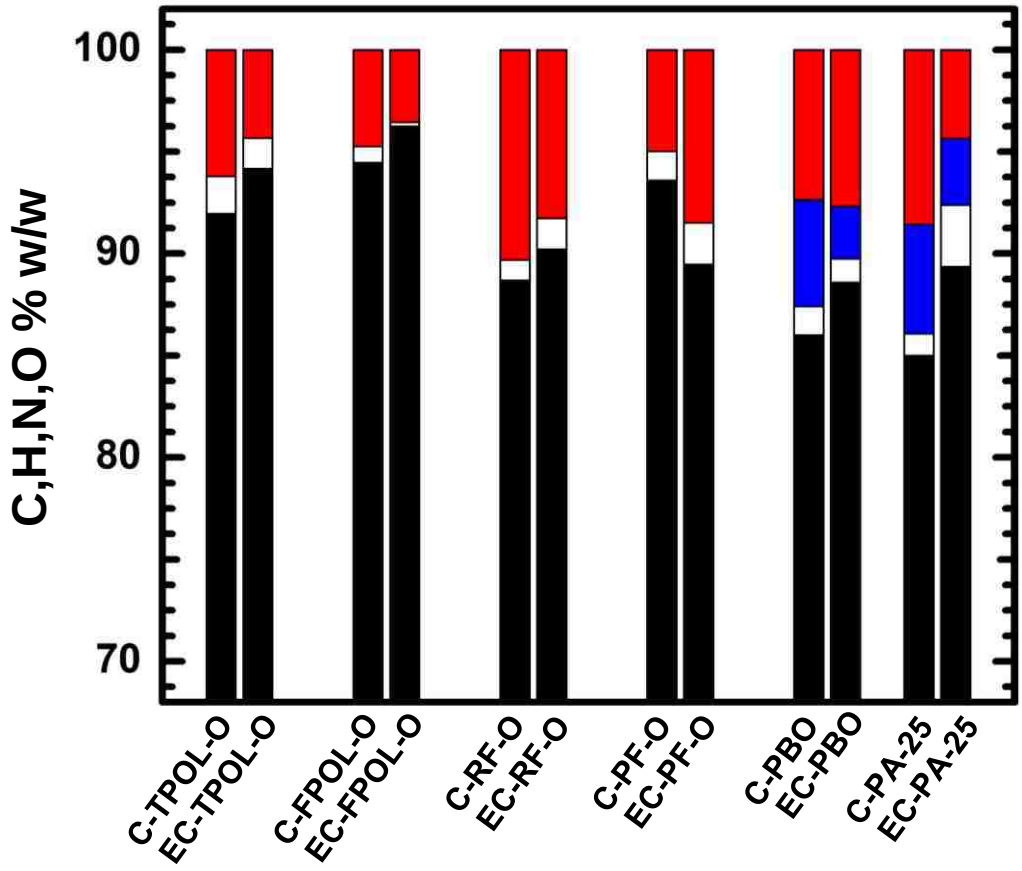

Figure 1. CHN analysis results for samples as shown. C: Black; H: White; N: Blue; O: Red. (For standard deviations refer to Table S.2 in Supporting Information)

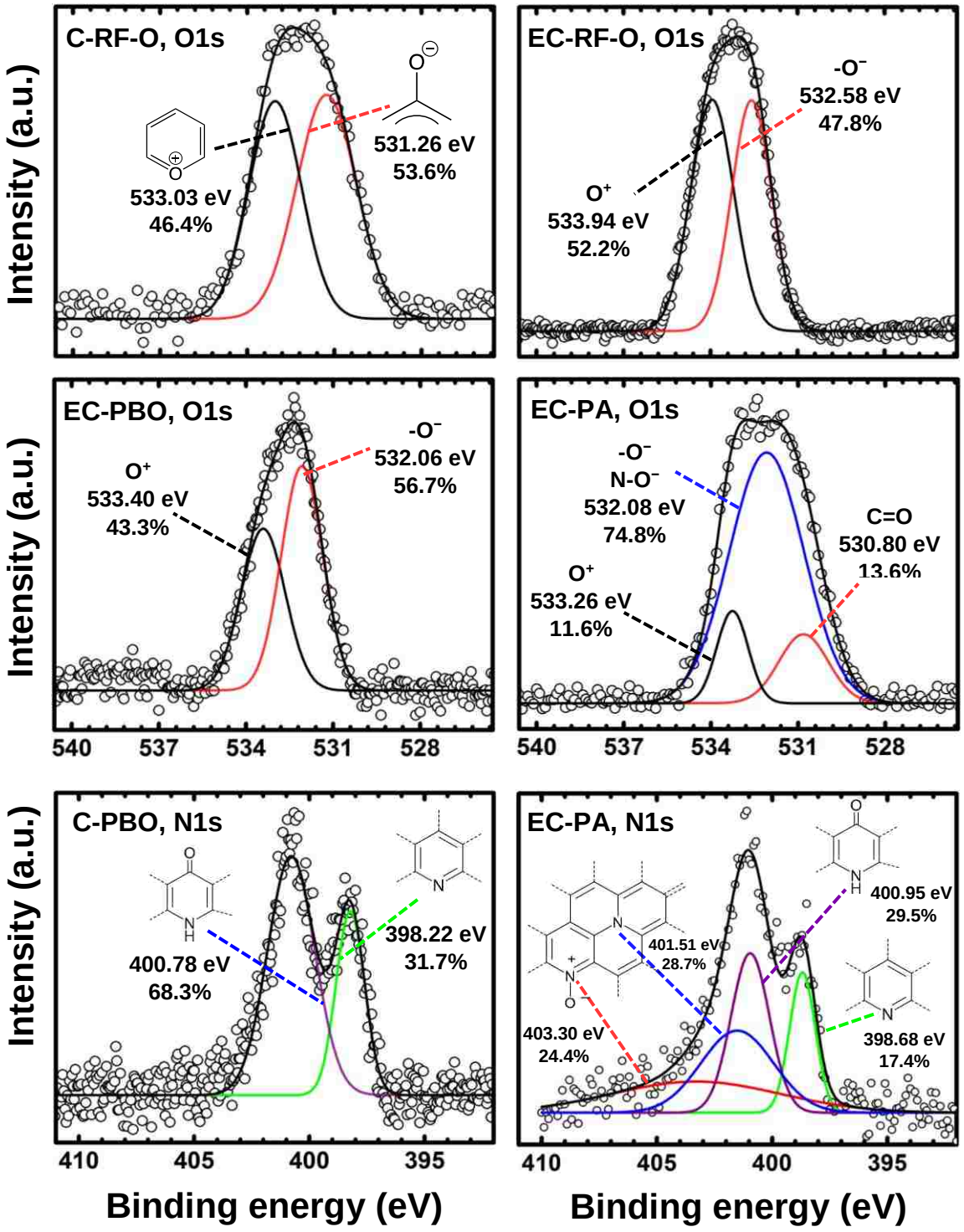

Figure 2. Representative XPS data of samples as shown. (Abbreviations: O^+ stands for the pyrylium cation, and $-O^-$ for the phenoxide anion, as shown in the first frame.)

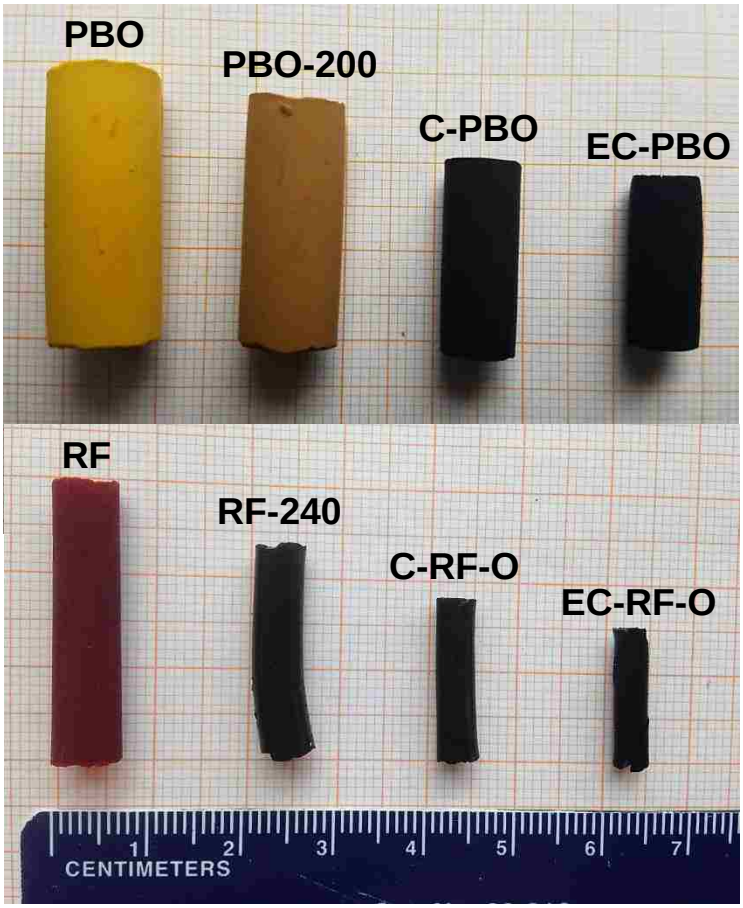

Figure 3. Photographs of **PBO** and **RF** aerogels along processing.

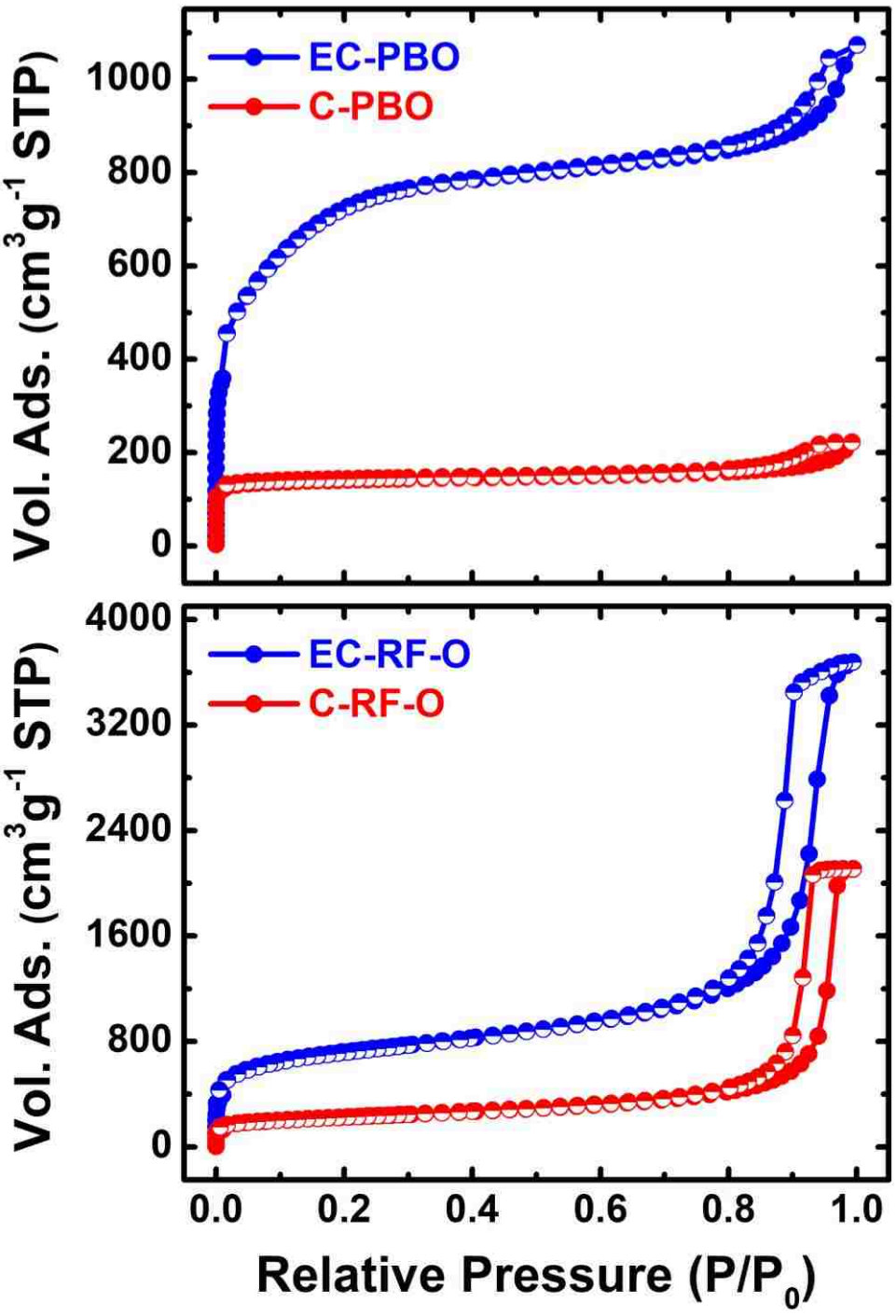

Figure 4. Representative low and medium pressure N_2-sorption isotherms of samples as shown.

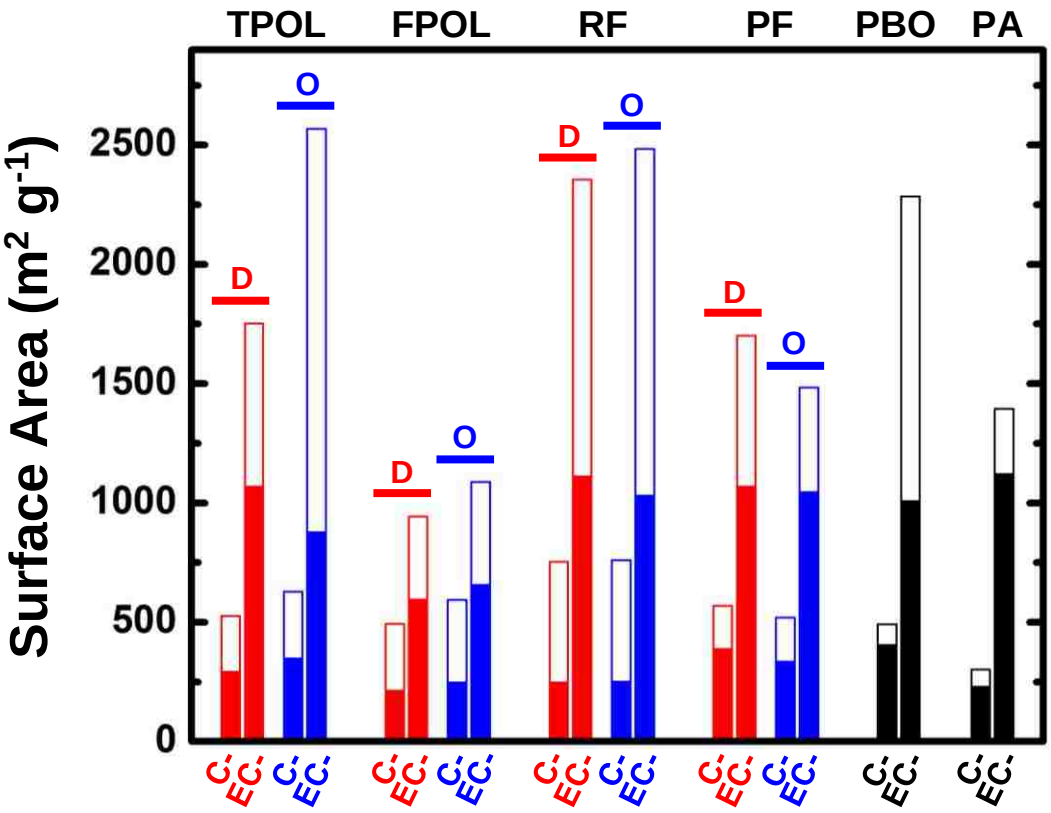

Figure 5. Surface areas by medium pressure N_2-sorption of all carbon aerogels of this study as shown. Full bars: BET surface area. Colored portion of the bars: Micropore (internal) surface area via t-plot analysis.

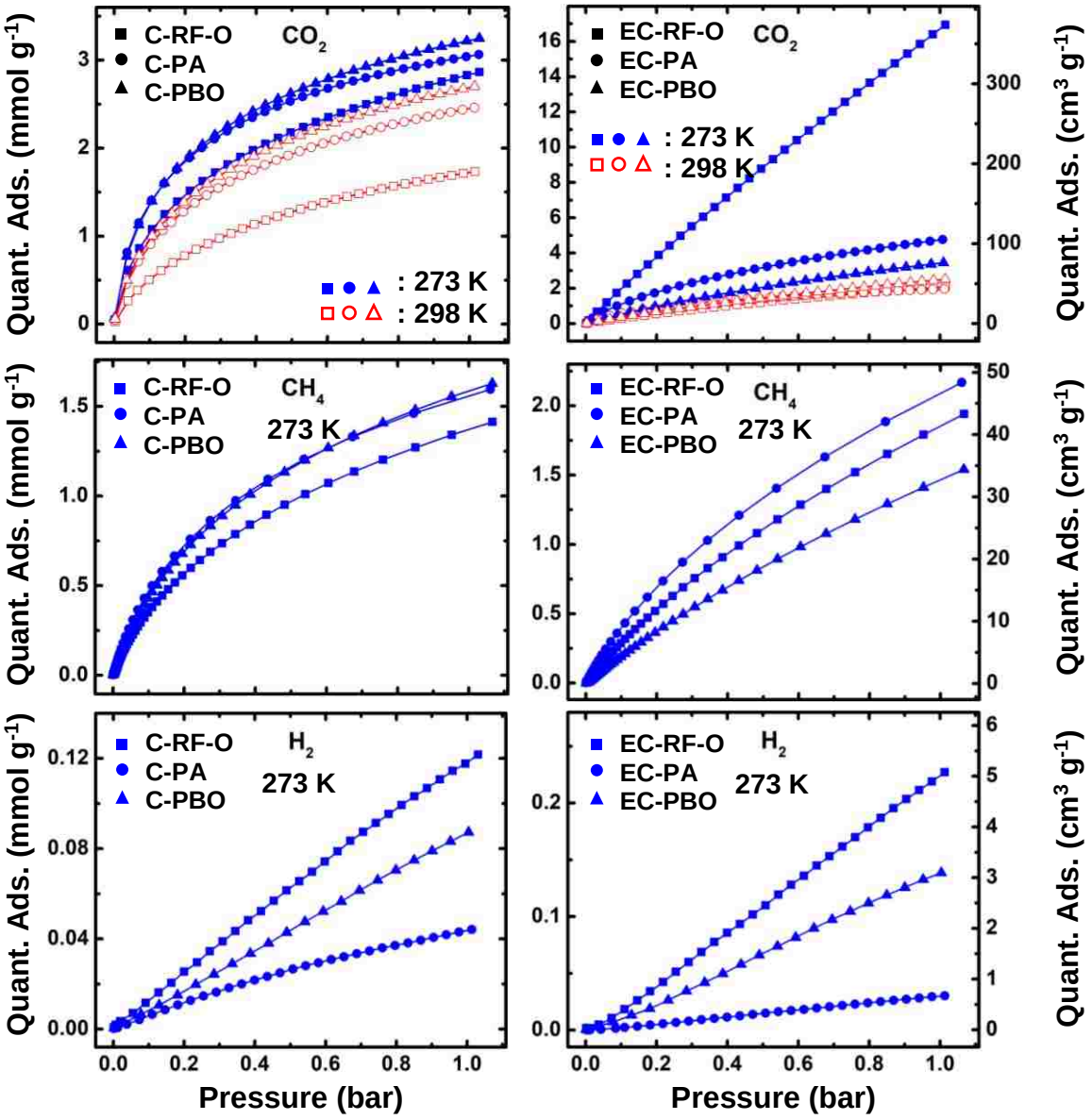

Figure 6. Representative adsorption isotherms by selected C and EC samples of CO_2 at two different temperatures (top); CH_4 at 273 K (middle); and, H_2 at 273 K (bottom).

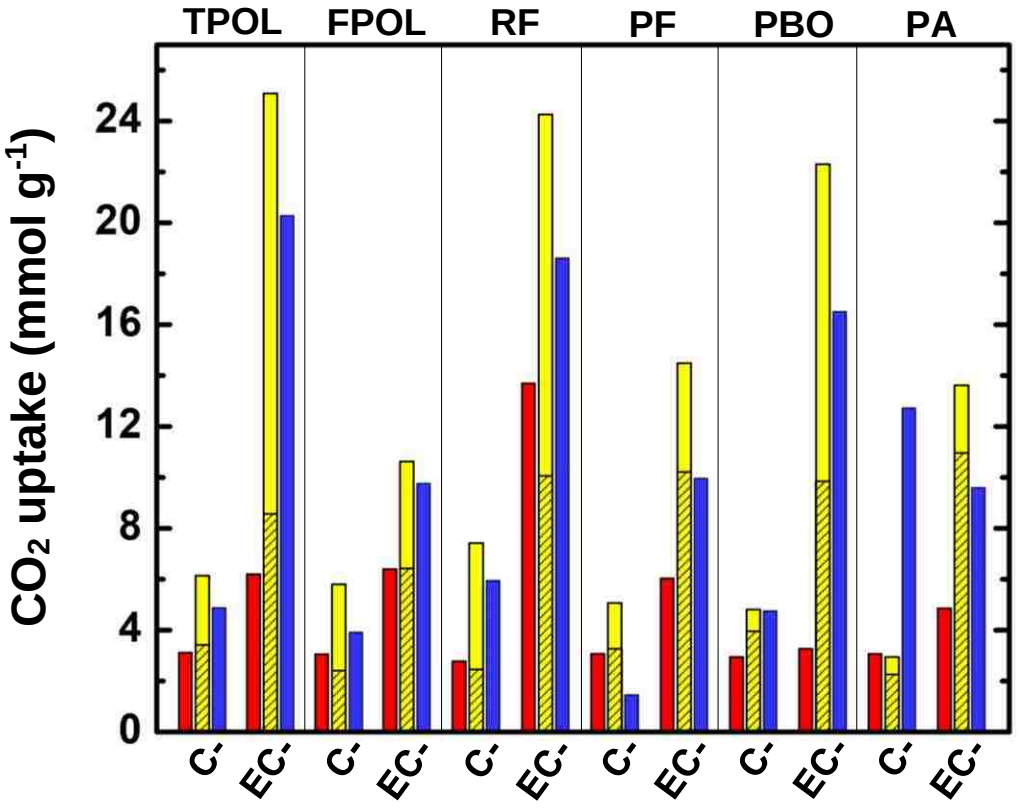

Figure 7. Experimental and calculated CO_2 uptake from carbon aerogels of this study. For clarity, aerogels systems are separated by thin black vertical lines. Red bars: Experimental values at P/P_o = 0.03 (1 bar). Yellow bars: Calculated from the BET surface area (full bars) or the micropore surface areas (shaded part of yellow bars) and the area occupied by each CO_2 molecule (0.17 nm^2). Blue bars: Calculated from the DR pore volumes [DR(N_2)] and the density of adsorbed CO_2 (see text). (For **RES**-derived carbon aerogels only the **C**(and **EC**)-**RES-O** samples are shown. Error bars are not shown for clarity – for standard deviations refer to Table 2.

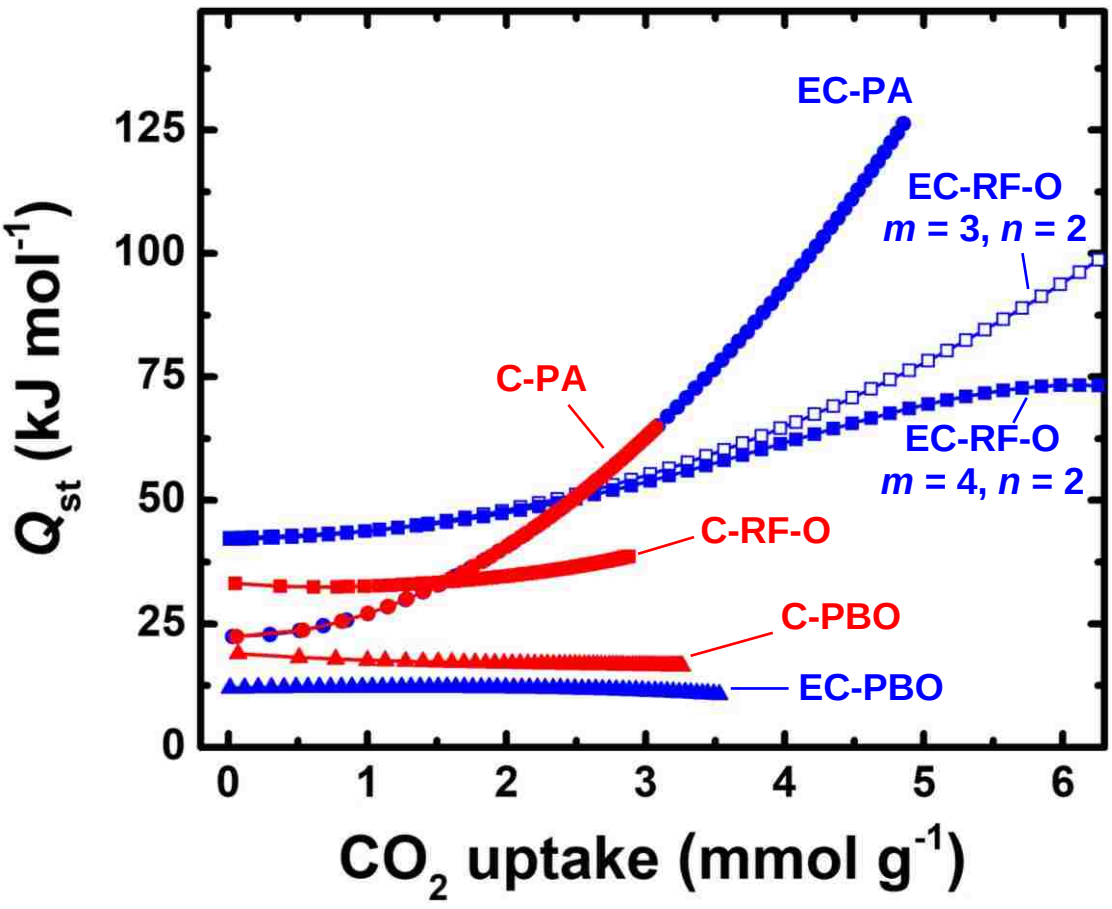

Figure 8. Representative isosteric heats of CO_2 adsorption (Q_{st}) on selected samples as a function of CO_2 uptake. Q_{st} plots have been calculated using Viral fitting with m=4 and n=2 (see Experimental). For a CO_2 uptake above 6 mmol g^{-1}, **EC-RF-O** shows a large sensitivity to the m, n value selection, and two such plots are shown with m, n values as indicated.

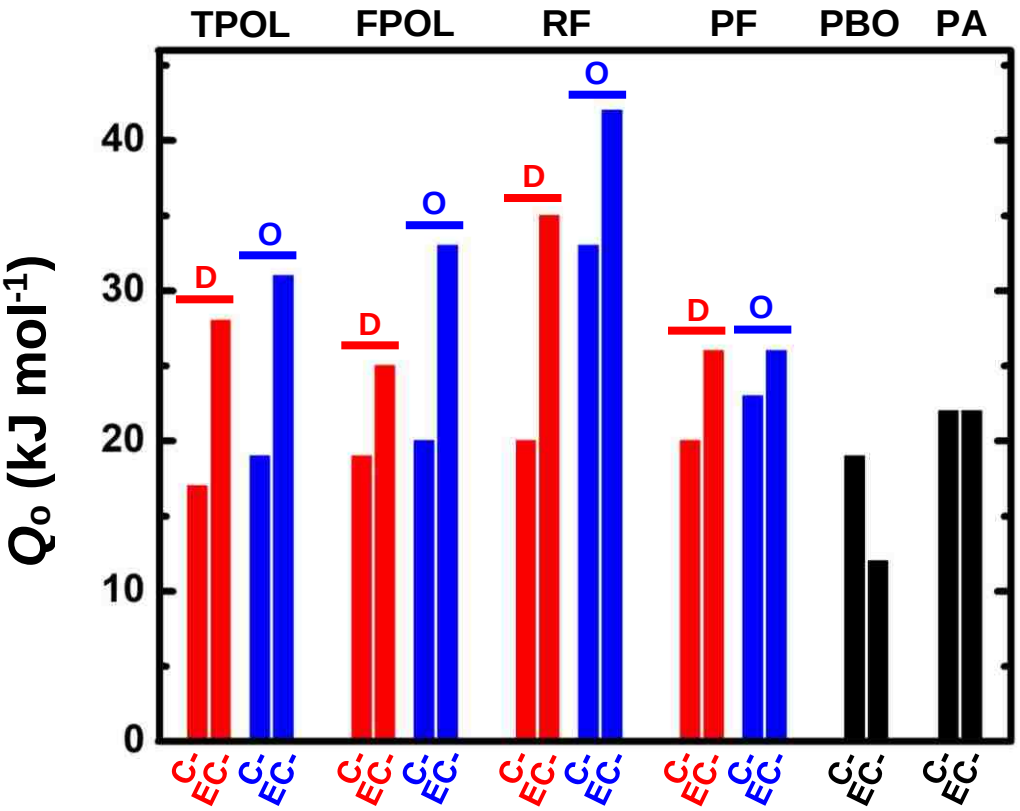

Figure 9. Comparison of the isosteric heats of adsorption at zero coverage (Q_0) of all carbon aerogels of this study. (Values taken from Table S.4 of Appendix VIII in Supporting Information.)

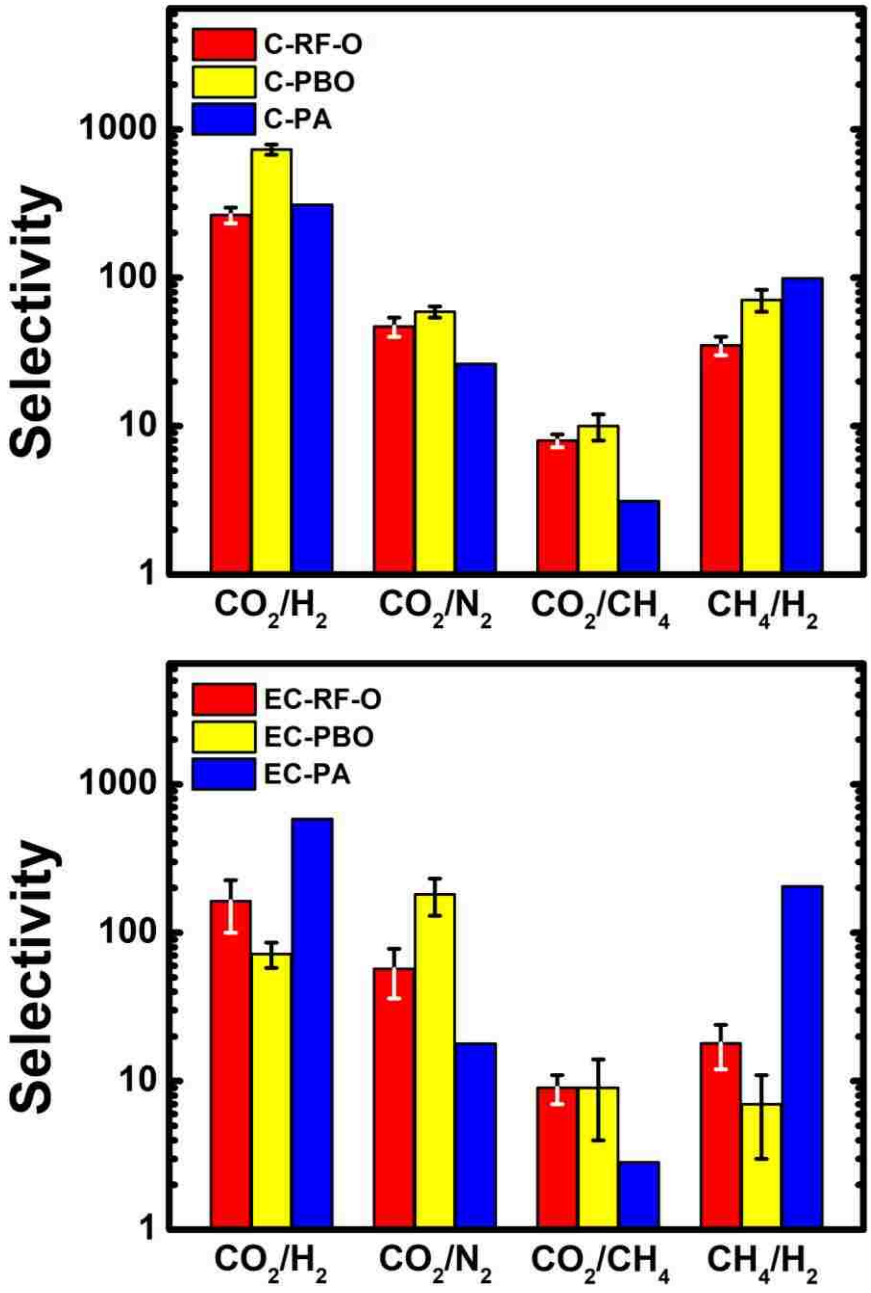

Figure 10. Relative selectivities at 273 K for the gasses shown of representative C- (top) and EC- (bottom) carbon aerogels derived from **RF** (red), **PBO** (yellow) and **PA** (blue) aerogels. Selectivities were calculated as the ratios of the corresponding Henry's constants obtained by Virial fitting of the isotherms at 273 K of Figure 6.

ACKNOWLEDGEMENTS

We thank the Army Research Office for financial support under Award Number W911NF-14-1-0369. We also thank the Materials Research Center of the Missouri University of Science and Technology for support with materials characterization.

SUPPORTING INFORMATION

Appendix I. Carbonization Yields

Table S.1. Carbonization yields from the corresponding precursors as indicated. Averages are from 3 samples at each formulation

TPOL system				
%Yield of:	**C-TPOL-D**	**C-TPOL-O**	**EC-TPOL-D**	**EC-TPOL-O**
From:	**TPOL**	**TPOL**	**C-TPOL-D**	**C-TPOL-O**
	41.24 ± 2.05	31.17 ± 1.33	44.35 ± 3.50	41.85 ± 4.02
FPOL system				
%Yield of:	**C-FPOL-D**	**C-FPOL-O**	**EC-FPOL-D**	**EC-FPOL-O**
From:	**FPOL**	**FPOL**	**C-FPOL-D**	**C-FPOL-O**
	50.00 ± 2.48	27.91 ± 1.46	68.21 ± 5.31	72.48 ± 6.90
RF system				
%Yield of:	**C-RF-D**	**C-RF-O**	**EC-RF-D**	**EC-RF-O**
From:	**RF**	**RF**	**C-RF-D**	**C-RF-O**
	43.41 ± 2.53	30.03 ± 1.99	49.41 ± 3.92	34.64 ± 3.40
PF system				
%Yield of:	**C-PF-D**	**C-PF-O**	**EC-PF-D**	**EC-PF-O**
From:	**PF**	**PF**	**C-PF-D**	**C-PF-O**
	55.68 ± 2.64	47.05 ± 2.07	84.23 ± 5.28	80.84 ± 5.41
PBO system				
%Yield of:	**C-PBO**		**EC-PBO**	
From:	**aromatized PBO**		**C-PBO**	
	62.68 ± 0.15		26.52 ± 1.62	
PA system				
%Yield of:	**C-PA**		**EC-PA**	
From:	**PA**		**C-PA**	
	57.32 ± 2.98		78.12 ± 1.84	

Appendix II. CHN Analysis Data

Table S.2. CHN elemental analysis data for carbon samples as shown. For carbonized **RES** only pre-oxidized samples were analyzed (**C-RES-O** and **EC-RES-O**). Averages are from 3 samples. (Oxygen was calculated from the difference from 100%)

Sample	% C	% H	% N	% O
C-TPOL-O	91.95 ± 0.32	1.85 ± 0.11	—	6.20 ± 0.06
EC-TPOL-O	94.17 ± 0.29	1.50 ± 0.11	—	4.33 ± 0.05
C-FPOL-O	94.46 ± 0.20	0.79 ± 0.02	—	4.75 ± 0.02
EC-FPOL-O	96.24 ± 0.42	0.20 ± 0.05	—	3.56 ± 0.09
C-RF-O	88.69 ± 0.21	1.00 ± 0.03	—	10.31 ± 0.02
EC-RF-O	90.21 ± 0.56	1.53 ± 0.18	—	8.26 ± 0.17
C-PF-O	93.58 ± 0.27	1.44 ± 0.09	—	4.98 ± 0.04
EC-PF-O	89.46 ± 0.38	2.05 ± 0.09	—	8.49 ± 0.08
C-PBO	86.00 ± 0.57	1.41 ± 0.04	5.24 ± 0.06	7.35 ± 0.17
EC-PBO	88.58 ± 0.28	1.17 ± 0.01	2.57 ± 0.02	7.68 ± 0.04
C-PA	85.00 ± 0.48	1.07 ± 0.08	5.36 ± 0.08	8.57 ± 0.12
EC-PA	89.35 ± 0.23	3.04 ± 0.67	3.26 ± 0.14	4.35 ± 0.26

Appendix III. Representative Dubinin-Radushkevich Plots

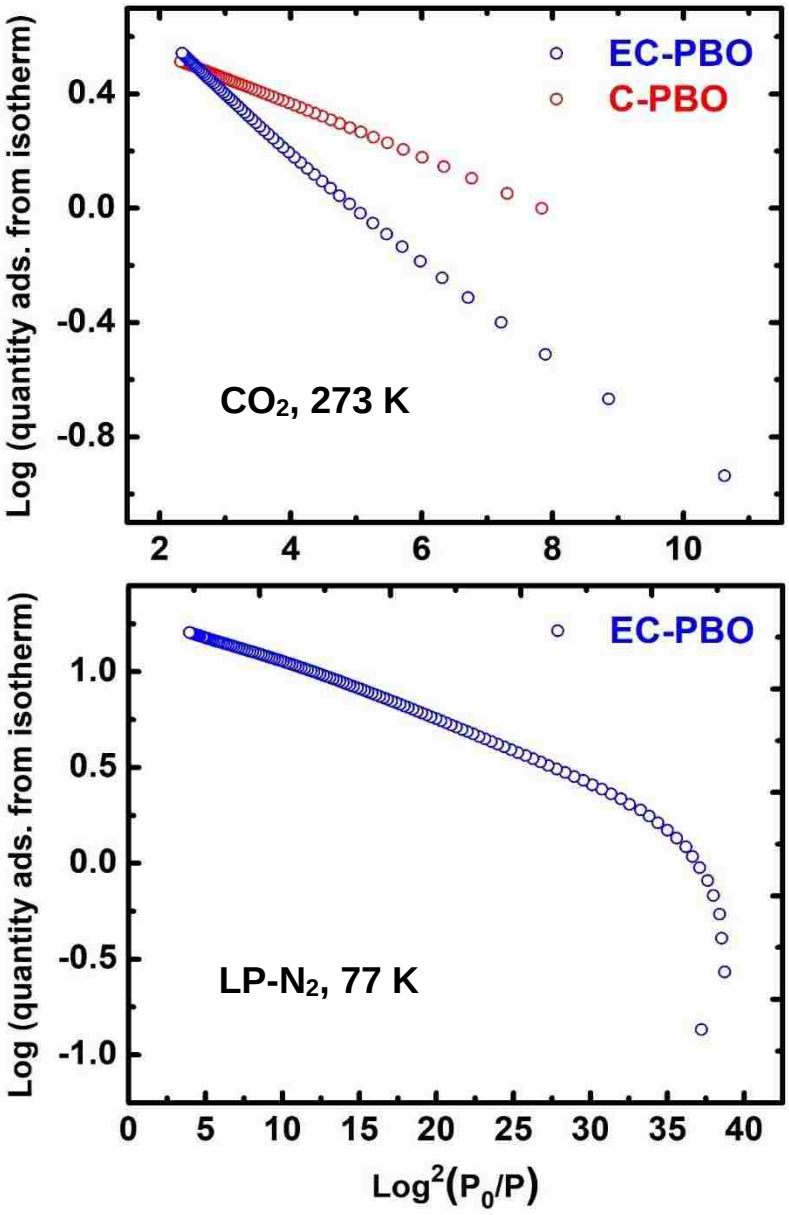

Figure S.1. Dubinin-Rudushkevich (DR) plots for **PBO**-derived carbon aerogels tested under conditions as shown (LP: Low Pressure). Micropore volumes were calculated from the intercepts by interpolating the linear parts of the plots.

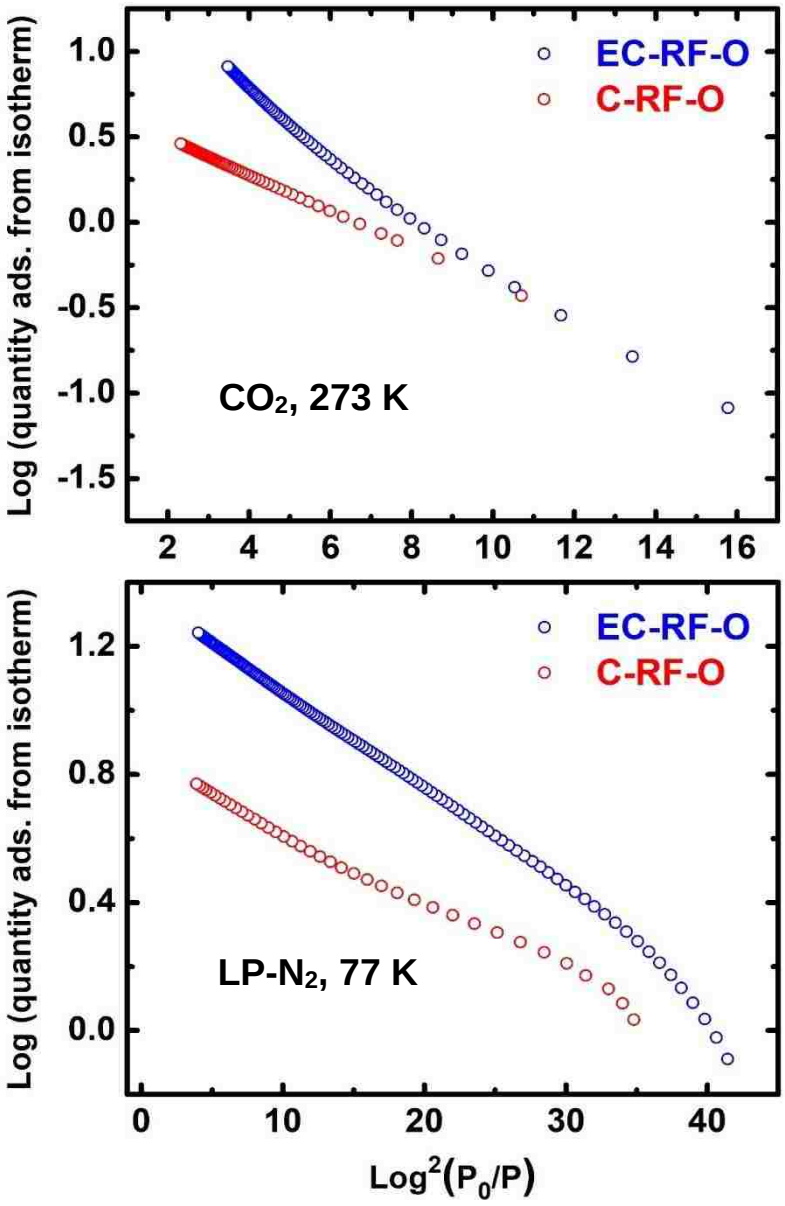

Figure S.1 Dubinin-Rudushkevich (DR) plots for selected **RF**-derived carbon aerogels tested under conditions as shown (LP: Low Pressure). Micropore volumes were calculated from the intercepts by interpolating the linear parts of the plots. (Cont.)

Appendix IV. Micropore Size Distribution by the DFT Method

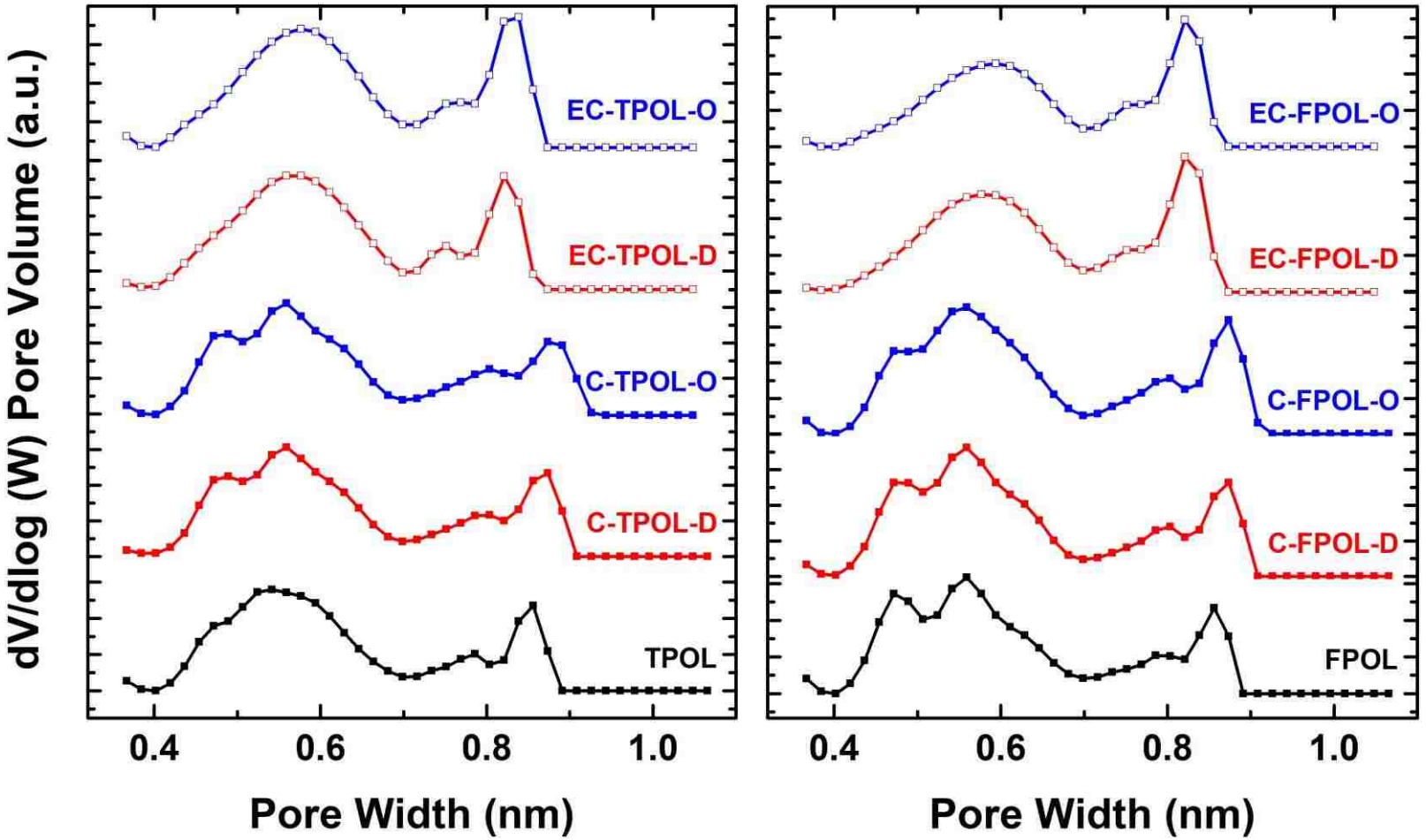

Figure S.2. Size distribution of micropores obtained by applying the DFT method on CO_2 adsorption data at 273 K up to 1 bar for samples as shown.

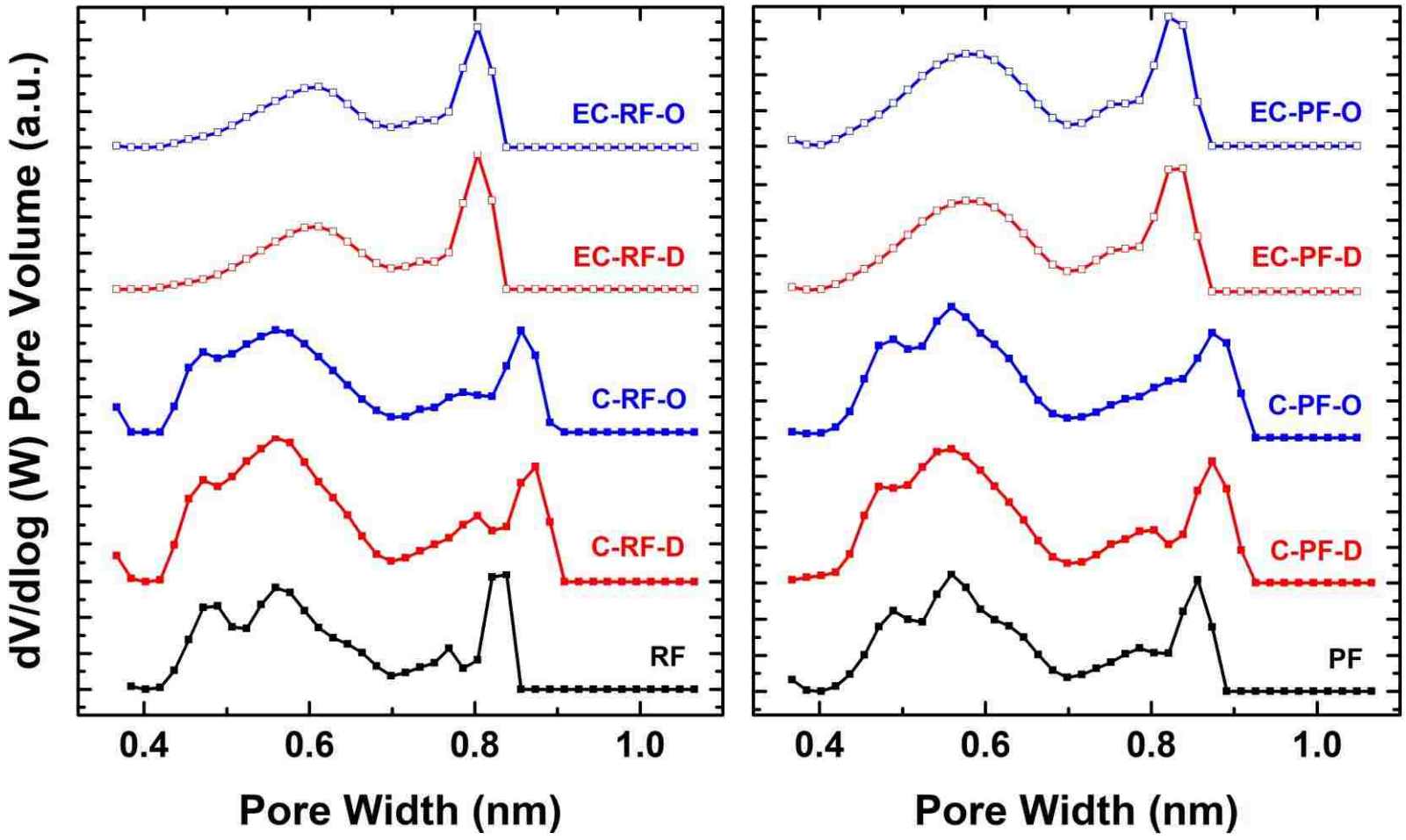

Figure S.2. Size distribution of micropores obtained by applying the DFT method on CO_2 adsorption data at 273 K up to 1 bar for samples as shown. (Cont.)

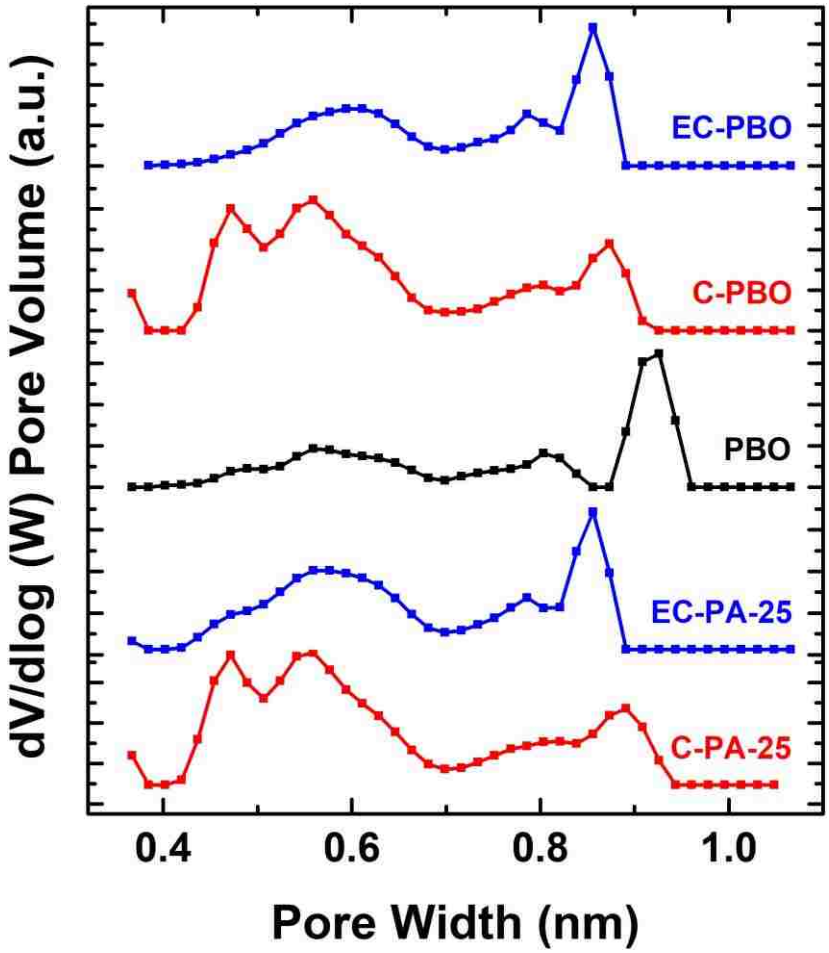

Figure S.2. Size distribution of micropores obtained by applying the DFT method on CO_2 adsorption data at 273 K up to 1 bar for samples as shown. (Cont.)

Appendix V. Comparison of CO_2 Uptake with Materials from the Literature

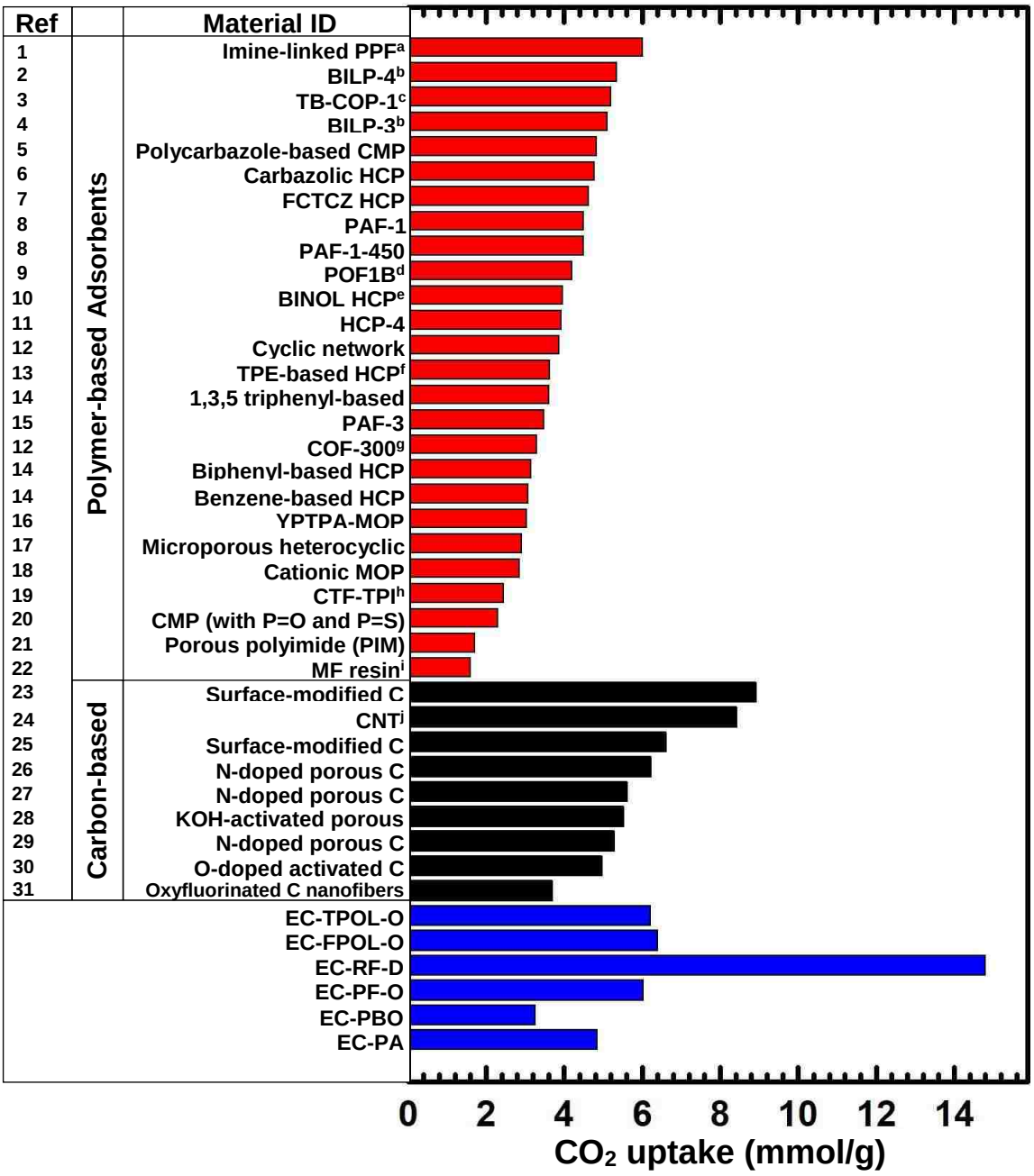

Figure S.3. Comparison of materials of this study with superior CO_2 sorbents at 1 bar and 273 K. [a] PPF: porous polymer framework; [b] benzimidazole-linked polymers; [c] Tröger's base COP; [d] polymeric organic framework; [e] binaphthol-based HCP; [f] tetraphenylethylene-based HCP; [g] covalent organic framework; [h] covalent triazine framework; [i] melamine-formaldehyde resin; [j] carbon nanotube. (For the references cited see Appendix X of this Supporting Information.)

Appendix VI. Virial Fitting of CO_2 Adsorption at 273 and 298 K

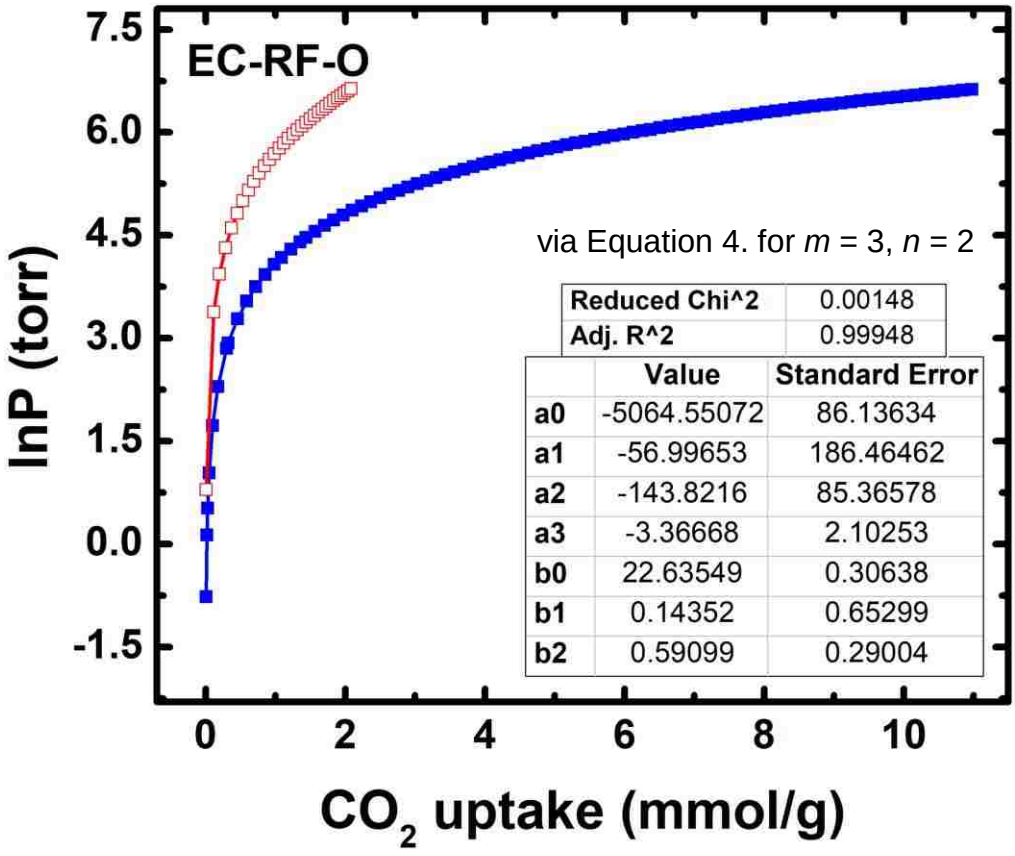

Figure S.4. Representative plots of CO_2 adsorption data at two different temperatures (blue: 273 K; red: 298 K). The two isotherms were fitted simultaneously using a Virial equation (refer to Equation 4 of the main article) for calculating the isosteric heats of adsorption, Q_{st}, as a function of CO_2 uptake.

Table S.3. Virial fitting parameters for calculating Q_{st} and Q_o for CO_2 from all C- and EC- aerogels. Data from isotherms at 273 K and 298 K (*m*, *n*: No. of terms used for Virial fitting)

C-TPOL-D (*m* = 4, *n* = 2)		
Parameters	**Value**	**Standard Error**
a_o	-2064.08604	39.7282
a_1	-331.11522	62.60313
a_2	265.68035	30.57424
a_3	-86.45602	13.12639
a_4	16.29732	2.62201
b_0	11.03024	0.13935
b_1	1.58508	0.21594
b_2	-0.41092	0.07751
$_{red}\chi^2$	1.16255×10^{-4}	
R^2	0.99993	
Q_o	17	

C-TPOL-O (*m* = 4, *n* = 2)		
Parameters	**Value**	**Standard Error**
a_o	-2257.35184	26.12724
a_1	-107.00605	39.04264
a_2	91.34715	17.6241
a_3	-24.83313	7.20762
a_4	4.87794	1.36075
b_0	11.61607	0.09166
b_1	1.05038	0.13541
b_2	-0.20446	0.04619
$_{red}\chi^2$	5.11272×10^{-5}	
R^2	0.99997	
Q_o	19	

EC-TPOL-D (*m* = 4, *n* = 2)		
Parameters	**Value**	**Standard Error**
a_o	-3404.92093	39.37812
a_1	-144.54366	62.548
a_2	-5.30072	22.12082
a_3	-1.63439	5.56026
a_4	0.59462	0.83732
b_0	16.10953	0.14215
b_1	1.02204	0.22892
b_2	-0.04862	0.07892
$_{red}\chi^2$	2.46135×10^{-4}	
R^2	0.99993	
Q_o	28	

EC-TPOL-O (*m* = 4, *n* = 2)		
Parameters	**Value**	**Standard Error**
a_o	-3701.5592	21.10578
a_1	461.05424	31.62063
a_2	-162.63173	10.56282
a_3	12.01227	3.44985
a_4	-1.00214	0.53632
b_0	17.28094	0.07621
b_1	-1.08732	0.11689
b_2	0.38325	0.0379
$_{red}\chi^2$	7.87553×10^{-5}	
R^2	0.99998	
Q_o	31	

C-TPOL$_{L\rho}$-O (*m* = 4, *n* = 2)		
Parameters	**Value**	**Standard Error**
a_o	-2428.6154	21.10125
a_1	241.72629	49.72417
a_2	4.69651	35.2298
a_3	-63.06804	22.56553
a_4	23.39503	6.69737
b_0	12.67392	0.07395
b_1	0.4529	0.17227
b_2	-0.01466	0.0925
$_{red}\chi^2$	3.42135×10^{-5}	
R^2	0.99998	
Q_o	20	

EC-TPOL$_{L\rho}$-O (*m* = 4, *n* = 2)		
Parameters	**Value**	**Standard Error**
a_o	-2223.51437	13.25834
a_1	381.93632	17.70456
a_2	-162.07335	6.91919
a_3	38.70741	2.07447
a_4	-4.5631	0.31829
b_0	11.93477	0.04645
b_1	-0.46604	0.06033
b_2	0.12754	0.01733
$_{red}\chi^2$	1.99099×10^{-5}	
R^2	0.99999	
Q_o	18	

Table S.3. Virial fitting parameters for calculating Q_{st} and Q_o for CO_2 from all C- and EC- aerogels. Data from isotherms at 273 K and 298 K (*m*, *n*: No. of terms used for Virial fitting) (Cont.)

C-FPOL-D (*m* = 4, *n* = 2)		
Parameters	**Value**	**Standard Error**
a_o	-2306.48621	37.47942
a_1	-317.25933	68.43603
a_2	269.53669	37.4412
a_3	-85.82294	19.23255
a_4	18.77444	4.46624
b_0	11.95335	0.13151
b_1	1.80726	0.23874
b_2	-0.51807	0.1005
$_{red}\chi^2$	1.01217×10^{-4}	
R^2	0.99994	
Q_o	19	

C-FPOL-O (*m* = 4, *n* = 2)		
Parameters	**Value**	**Standard Error**
a_o	-2428.66391	20.01324
a_1	222.40187	30.75707
a_2	27.01147	14.35734
a_3	-48.72958	5.95362
a_4	9.11159	1.15151
b_0	12.33055	0.07013
b_1	-0.2133	0.10624
b_2	0.17313	0.03712
$_{red}\chi^2$	3.08284×10^{-5}	
R^2	0.99998	
Q_o	20	

EC-FPOL-D (*m* = 4, *n* = 2)		
Parameters	**Value**	**Standard Error**
a_o	-3020.5397	45.07658
a_1	-87.47319	69.43017
a_2	-58.11599	23.57254
a_3	2.32972	7.6812
a_4	0.29154	1.2324
b_0	14.6989	0.16329
b_1	0.8978	0.25815
b_2	0.08717	0.08778
$_{red}\chi^2$	3.1675×10^{-4}	
R^2	0.99992	
Q_o	25	

EC-FPOL-O (*m* = 4, *n* = 2)		
Parameters	**Value**	**Standard Error**
a_o	-3918.97666	22.96489
a_1	391.84769	39.16362
a_2	-177.69949	14.58469
a_3	13.47392	4.20608
a_4	-1.1437	0.68037
b_0	18.16662	0.08287
b_1	-0.83819	0.14376
b_2	0.42317	0.05233
$_{red}\chi^2$	9.21369×10^{-5}	
R^2	0.99997	
Q_o	33	

C-RF-D (*m* = 4, *n* = 2)		
Parameters	**Value**	**Standard Error**
a_o	-2520.1642	11.76811
a_1	605.27018	19.4735
a_2	-211.07097	10.10349
a_3	30.99685	4.46114
a_4	-3.50812	0.93012
b_0	12.478	0.04121
b_1	-0.8891	0.06671
b_2	0.38028	0.025
$_{red}\chi^2$	9.9128×10^{-6}	
R^2	0.99999	
Q_o	20	

C-RF-O (*m* = 4, *n* = 2)		
Parameters	**Value**	**Standard Error**
a_o	-4011.75072	16.66278
a_1	350.96326	34.42767
a_2	-343.04305	18.42252
a_3	96.76335	5.96397
a_4	-16.2131	1.27016
b_0	17.79661	0.05816
b_1	0.3843	0.11948
b_2	0.42795	0.05686
$_{red}\chi^2$	1.7811×10^{-5}	
R^2	0.99999	
Q_o	33	

Table S.3. Virial fitting parameters for calculating Q_{st} and Q_o for CO_2 from all C- and EC- aerogels. Data from isotherms at 273 K and 298 K (*m*, *n*: No. of terms used for Virial fitting) (Cont.)

EC-RF-D (*m* = 3, *n* = 3)		
Parameters	**Value**	**Standard Error**
a_o	-4058.99689	50.1404
a_1	-985.83153	145.04978
a_2	202.49146	112.6477
a_3	-18.6782	24.8319
b_0	18.6351	0.17979
b_1	3.60322	0.51971
b_2	-0.70897	0.40502
b_3	0.06194	0.08968
$_{red}\chi^2$	2.93982×10^{-4}	
R^2	0.99990	
Q_o	34	

EC-RF-D (*m* = 3, *n* = 2)		
Parameters	**Value**	**Standard Error**
a_o	-4079.9819	39.70248
a_1	-895.47159	62.34444
a_2	126.1826	21.86049
a_3	-1.5363	0.78307
b_0	18.71089	0.14176
b_1	3.27781	0.21833
b_2	-0.4338	0.07246
$_{red}\chi^2$	2.91285×10^{-4}	
R^2	0.99990	
Q_o	34	

EC-RF-O (*m* = 4, *n* = 2)		
Parameters	**Value**	**Standard Error**
a_o	-5096.49151	81.43509
a_1	-94.16816	175.20015
a_2	-44.5252	86.65742
a_3	-43.35699	13.55354
a_4	6.02888	2.0216
b_0	22.77062	0.29069
b_1	0.08174	0.61233
b_2	0.52955	0.2726
$_{red}\chi^2$	0.0013	
R^2	0.99955	
Q_o	42	

EC-RF-O (*m* = 3, *n* = 2)		
Parameters	**Value**	**Standard Error**
a_o	-5064.55072	86.13634
a_1	-56.99653	186.46462
a_2	-143.8216	85.36578
a_3	-3.36668	2.10253
b_0	22.63549	0.30638
b_1	0.14352	0.65299
b_2	0.59099	0.29004
$_{red}\chi^2$	0.00148	
R^2	0.99948	
Q_o	42	

C-RF$_{H\rho}$-O (*m* = 4, *n* = 2)		
Parameters	**Value**	**Standard Error**
a_o	-1854.59796	40.5997
a_1	-156.43634	68.82708
a_2	290.91671	36.267
a_3	-150.63123	15.10141
a_4	28.64452	3.15343
b_0	10.57708	0.14237
b_1	0.65176	0.23452
b_2	-0.10241	0.08876
$_{red}\chi^2$	1.30168×10^{-4}	
R^2	0.99991	
Q_o	15	

EC-RF$_{H\rho}$-O (*m* = 4, *n* = 2)		
Parameters	**Value**	**Standard Error**
a_o	-1256.94754	19.35818
a_1	-150.09441	31.30609
a_2	2.08496	14.57245
a_3	-1.86758	4.69732
a_4	1.24357	0.84051
b_0	8.95602	0.06802
b_1	1.01587	0.10642
b_2	-0.09344	0.03666
$_{red}\chi^2$	4.4826×10^{-5}	
R^2	0.99997	
Q_o	10	

Table S.3. Virial fitting parameters for calculating Q_{st} and Q_o for CO_2 from all C- and EC- aerogels. Data from isotherms at 273 K and 298 K (*m*, *n*: No. of terms used for Virial fitting) (Cont.)

C-PF-D (*m* = 4, *n* = 2)		
Parameters	**Value**	**Standard Error**
a_o	-2356.11047	40.48019
a_1	-244.53912	62.17842
a_2	280.4581	28.20351
a_3	-117.33772	11.97601
a_4	20.22062	2.32869
b_0	12.16435	0.14198
b_1	0.96463	0.21681
b_2	-0.18326	0.07654
$_{red}\chi^2$	1.21901×10^{-4}	
R^2	0.99992	
Q_o	20	

C-PF-O (*m* = 4, *n* = 2)		
Parameters	**Value**	**Standard Error**
a_o	-2718.26564	42.60335
a_1	-219.51212	66.99755
a_2	211.69471	29.13963
a_3	-70.86644	12.27527
a_4	12.17909	2.38219
b_0	13.41543	0.14937
b_1	1.15155	0.23617
b_2	-0.27963	0.08614
$_{red}\chi^2$	1.35574×10^{-4}	
R^2	0.99991	
Q_o	23	

EC-PF-D (*m* = 4, *n* = 2)		
Parameters	**Value**	**Standard Error**
a_o	-3071.95072	23.00244
a_1	216.51544	34.13711
a_2	-91.95314	11.45907
a_3	0.57603	4.16953
a_4	0.62421	0.67412
b_0	14.95343	0.08335
b_1	-0.2012	0.12738
b_2	0.21704	0.04168
$_{red}\chi^2$	8.65249×10^{-5}	
R^2	0.99998	
Q_o	26	

EC-PF-O (*m* = 4, *n* = 2)		
Parameters	**Value**	**Standard Error**
a_o	-3107.9637	31.22559
a_1	98.39918	46.62711
a_2	-123.55132	15.25754
a_3	1.11031	4.78651
a_4	0.50099	0.74195
b_0	14.96823	0.11313
b_1	0.21284	0.1734
b_2	0.33145	0.05704
$_{red}\chi^2$	1.50298×10^{-4}	
R^2	0.99996	
Q_o	26	

C-PBO (*m* = 4, *n* = 2)		
Parameters	**Value**	**Standard Error**
a_o	-2298.23977	14.04213
a_1	280.79951	18.87439
a_2	-138.50379	8.19624
a_3	38.6447	3.05927
a_4	-4.11833	0.52508
b_0	11.12633	0.04918
b_1	0.32071	0.06439
b_2	0.0518	0.01972
$_{red}\chi^2$	1.23023×10^{-5}	
R^2	0.99999	
Q_o	19	

EC-PBO (*m* = 4, *n* = 2)		
Parameters	**Value**	**Standard Error**
a_o	-1447.42553	14.73266
a_1	-36.24602	29.09839
a_2	16.72061	15.71066
a_3	-2.28683	5.22846
a_4	1.14148	1.05856
b_0	10.10519	0.05167
b_1	0.40385	0.09858
b_2	-0.09957	0.04061
$_{red}\chi^2$	3.01251×10^{-5}	
R^2	0.99998	
Q_o	12	

Table S.3. Virial fitting parameters for calculating Q_{st} and Q_o for CO_2 from all C- and EC- aerogels. Data from isotherms at 273 K and 298 K (*m*, *n*: No. of terms used for Virial fitting) (Cont.)

C-PA (*m* = 5, *n* = 2)				**EC-PA (*m* = 5, *n* = 2)**		
Parameters	**Value**	**Standard Error**		**Parameters**	**Value**	**Standard Error**
a_o	-2637.00179	31.0257		a_o	-2696.53467	23.01278
a_1	-103.7966	45.92841		a_1	16.00876	40.98892
a_2	165.37504	42.00353		a_2	-592.41309	19.4743
a_3	-126.89657	33.78791		a_3	22.36671	8.69989
a_4	45.81131	12.85509		a_4	-2.01467	2.63168
a_5	-5.77277	1.7789		a_5	-0.01788	0.2859
b_0	12.50018	0.10861		b_0	13.44915	0.08067
b_1	1.01271	0.14623		b_1	0.81885	0.1432
b_2	-0.07586	0.04639		b_2	1.82888	0.0575
$_{red}\chi^2$	6.08467×10^{-5}			$_{red}\chi^2$	4.21652×10^{-5}	
R^2	0.99986			R^2	0.99989	
Q_o	22			Q_o	22	

Appendix VII. Q_{st} Plots for TPOL-, FPOL-, RF-, and PF-derived Carbon Aerogels

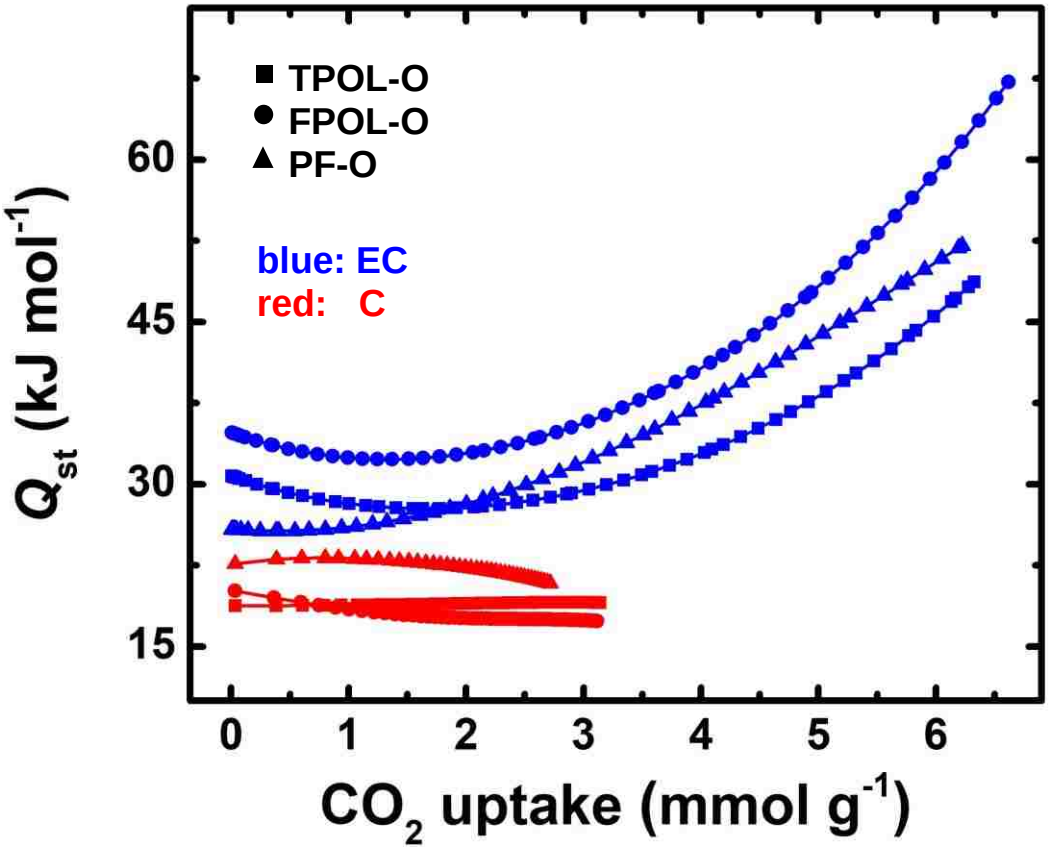

Figure S.5. Isosteric heats of CO_2 adsorption (Q_{st}) as a function of CO_2 uptake for **C**-(and **EC**)**RES-O** aerogels as shown. (For the Q_{st} plots of **C**-(and **EC**)**RF-O** aerogels refer to Figure 8 in the main article.)

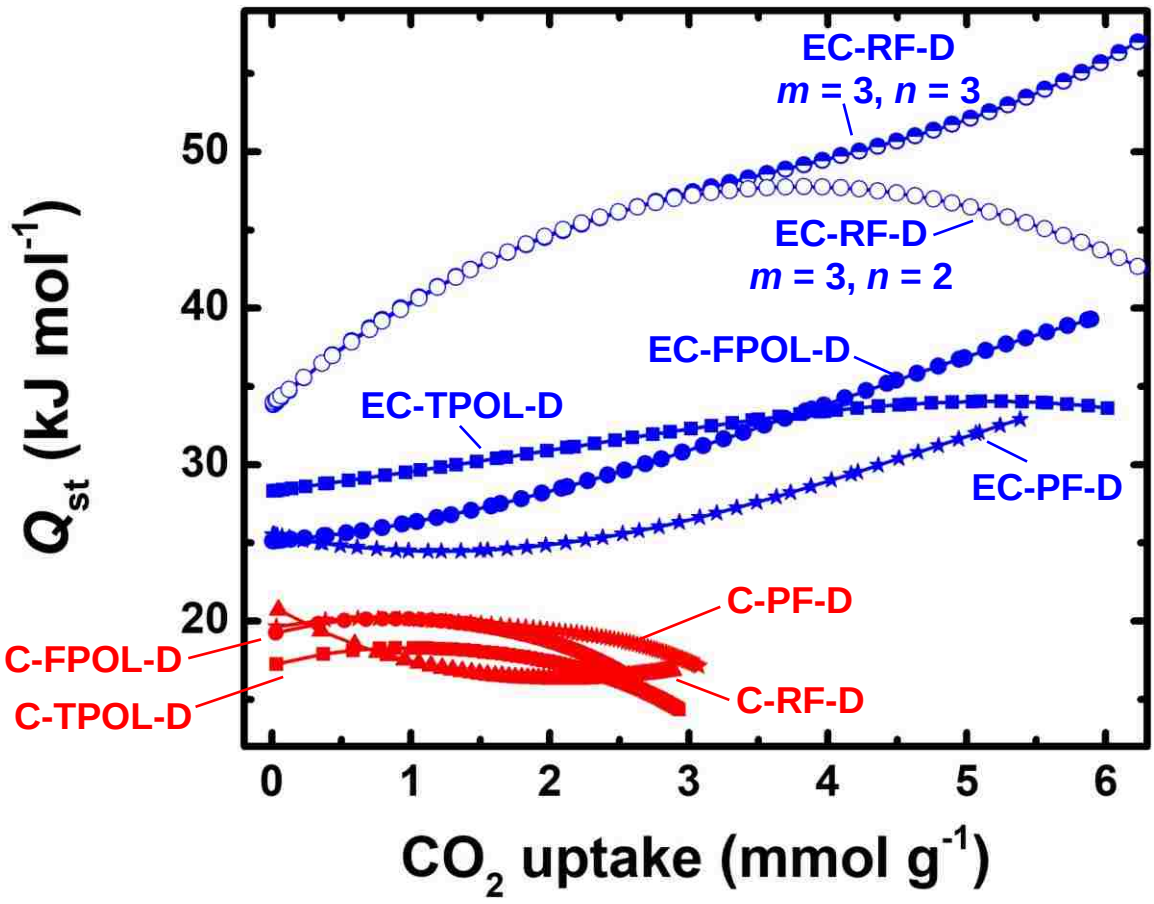

Figure S.5. (Continued) Isosteric heats of CO_2 adsorption (Q_{st}) as a function of CO_2 uptake of all **C-**(and **EC-**)**RES-D** samples as shown. Q_{st} plots have been calculated using Viral fitting with m=4 and n=2 (see Experimental). For CO_2 uptake above 6 mmol g^{-1}, **EC-RF-D** shows a large sensitivity to the m, n value selection; two such plots are shown using m and n values as indicated.

Appendix VIII. Q_o Values for CO_2 and Gas Selectivity Data

Table S.4. Gas Adsorption and Selectivity Data for CO_2, CH_4, N_2 and H_2 at 1 bar

sample	CO_2 uptake (mmol g^{-1}) [a]		Q_0 [b]	CH_4 uptake 273 K	N_2 uptake 273 K	H_2 uptake 273 K	Selectivity at 273 K [c]			
	273 K	298 K					CO_2/H_2	CO_2/N_2	CO_2/CH_4	CH_4/H_2
TPOL	1.74 ± 0.01	[d]	[e]	0.51 ± 0.00	0.08 ± 0.00	0.03 ± 0.00	538 ± 63	94 ± 8	15 ± 0.7	35 ± 4
C-TPOL-D	2.87 ± 0.02	2.28 ± 0.07	17	1.4$_2$ ± 0.11	0.49 ± 0.01	0.06 ± 0.00	410 ± 59	27 ± 1	5 ± 0.4	85 ± 14
C-TPOL-O	3.11 ± 0.04	2.47 ± 0.03	19	1.60 ± 0.02	0.52 ± 0.01	0.07 ± 0.00	334 ± 45	32 ± 3	5 ± 0.3	70 ± 9
EC-TPOL-D	5.86 ± 0.05	2.67 ± 0.05	28	1.9$_3$ ± 0.17	0.58 ± 0.01	0.09 ± 0.01	241 ± 8	21 ± 0.8	4 ± 0.1	62 ± 2
EC-TPOL-O	6.20 ± 0.07	2.85 ± 0.05	31	2.0$_1$ ± 0.16	0.61 ± 0.01	0.10 ± 0.01	166 ± 8	21 ± 0.8	4 ± 0.4	39 ± 4
C-TPOL$_L\rho$-O	1.99 ± 0.01	1.57 ± 0.00	20	[d]	[d]	[d]	[e]	[e]	[e]	[e]
EC-TPOL$_L\rho$-O	4.37 ± 0.06	3.10 ± 0.06	18	[d]	[d]	[d]	[e]	[e]	[e]	[e]
FPOL	1.93 ± 0.01	[d]	[e]	0.66 ± 0.00	0.16 ± 0.00	0.04 ± 0.01	546 ± 36	62 ± 8	10 ± 0.2	54 ± 4
C-FPOL-D	2.49 ± 0.02	1.96 ± 0.02	19	1.1$_9$ ± 0.10	0.37 ± 0.01	0.06 ± 0.00	718 ± 96	35 ± 2	5 ± 0.5	132 ± 22
C-FPOL-O	3.05 ± 0.03	2.35 ± 0.07	20	1.4$_7$ ± 0.14	0.45 ± 0.01	0.07 ± 0.01	438 ± 24	23 ± 1	6 ± 0.4	78 ± 6
EC-FPOL-D	5.70 ± 0.02	2.70 ± 0.02	25	2.02 ± 0.01	0.59 ± 0.01	0.12 ± 0.02	196 ± 22	22 ± 2	3 ± 0.1	60 ± 6
EC-FPOL-O	6.40 ± 0.09	2.52 ± 0.03	33	2.0$_2$ ± 0.12	0.54 ± 0.01	0.12 ± 0.04	230 ± 22	21 ± 0.8	5 ± 0.5	47 ± 6
RF	1.33 ± 0.01	[d]	[e]	0.31 ± 0.00	[d]	0.05 ± 0.01	538 ± 160	[e]	108 ± 8	5 ± 2
C-RF-D	2.79 ± 0.05	2.13 ± 0.09	20	1.38 ± 0.04	0.14 ± 0.04	0.11 ± 0.01	230 ± 25	53 ± 5	7 ± 1	33 ± 4
C-RF-O	2.78 ± 0.05	1.67 ± 0.05	33	1.36 ± 0.04	0.11 ± 0.04	0.11 ± 0.01	265 ± 32	48 ± 7	8 ± 0.8	35 ± 5
EC-RF-D	14.$_8$ ± 3.9	2.89 ± 0.24	35	1.93 ± 0.02	0.16 ± 0.03	0.20 ± 0.06	236 ± 43	82 ± 27	11 ± 2	22 ± 3
EC-RF-O	13.$_7$ ± 2.7	2.24 ± 0.30	42	1.92 ± 0.01	0.17 ± 0.03	0.20 ± 0.02	163 ± 63	57 ± 21	9 ± 2	18 ± 6
C-RF$_H\rho$-O	2.79 ± 0.02	2.29 ± 0.01	15	[d]	[d]	[d]	[e]	[e]	[e]	[e]
EC-RF$_H\rho$-O	3.79 ± 0.05	2.75 ± 0.03	10	[d]	[d]	[d]	[e]	[e]	[e]	[e]
PF	0.79 ± 0.00	[d]	[e]	0.18 ± 0.01	[d]	0.12 ± 0.04	15 ± 2	[e]	50 ± 4	0.3 ± 0.0$_5$
C-PF-D	3.02 ± 0.01	2.36 ± 0.01	20	1.49 ± 0.02	0.48 ± 0.00	0.06 ± 0.00	514 ± 69	29 ± 1	5 ± 0.2	103 ± 14
C-PF-O	3.07 ± 0.01	2.29 ± 0.01	23	1.53 ± 0.02	0.48 ± 0.00	0.06 ± 0.00	447 ± 43	30 ± 0.4	5 ± 0.1	89 ± 9
EC-PF-D	5.35 ± 0.04	2.75 ± 0.08	26	2.0$_2$ ± 0.12	0.65 ± 0.02	0.09 ± 0.01	184 ± 10	19 ± 1	3 ± 0.1	62 ± 3
EC-PF-O	6.03 ± 0.03	2.6$_8$ ± 0.10	26	2.1$_0$ ± 0.11	0.62 ± 0.02	0.10 ± 0.01	205 ± 14	20 ± 0.6	3 ± 0.1	61 ± 4
PBO	0.25 ± 0.03	[d]	[e]	[f]	[f]	[f]	[g]	[e]	[g]	[g]
C-PBO	2.9$_5$ ± 0.20	2.5$_0$ ± 0.15	19	1.4$_4$ ± 0.14	0.49 ± 0.00	0.08 ± 0.01	733 ± 58	59 ± 5	10 ± 2	71 ± 12
EC-PBO	3.2$_6$ ± 0.13	2.3$_2$ ± 0.14	12	1.46 ± 0.05	0.27 ± 0.01	0.11 ± 0.03	72 ± 14	181 ± 51	9 ± 5	7 ± 4
PA	0.80 [h]	[d]	[e]	0.19 [h]	[d]	[d]	[e]	[e]	10.5 [h]	[e]
C-PA	3.07 [h]	2.46	22	1.59 [h]	0.35 [h]	0.04 [h]	310 [h]	26.3 [h]	3.13 [h]	99.0 [h]
EC-PA	4.85 [h]	2.05	22	2.16 [h]	0.44 [h]	0.03 [h]	584 [h]	17.9 [h]	2.84 [h]	205 [h]

[a] All data are averages of at least 3 experiments, except **EC-RF-D** and **EC-RF-O**, which at 273 K are averages from 14 and 7 isotherms, respectively, and at 298 K data are averages from 11 and 9 isotherms, respectively. [b] Isosteric heats of adsorption at zero coverage, Q_0 (kJ mol^{-1}), using Virial fitting from CO_2 adsorption data at 273 K and 298 K (see Experimental). [c] Adsorption selectivities were calculated using Henry's law with data obtained from Virial-type fitting of adsorption isotherms at 273 K (see Experimental). Standard deviations in the K_H values were obtained by applying Virial fitting to all available isotherms. Errors in selectivities were calculated by applying propagation of error rules to the K_H ratios. [d] Not measured. [e] Not calculated. [f] Uptake of those gasses was negligible. [g] Not meaningful selectivities (see previous footnote). [h] Data from reference 32 (Appendix X).

Appendix IX. Comparison of Gas Selectivities by the Various Carbon Aerogels of this Study

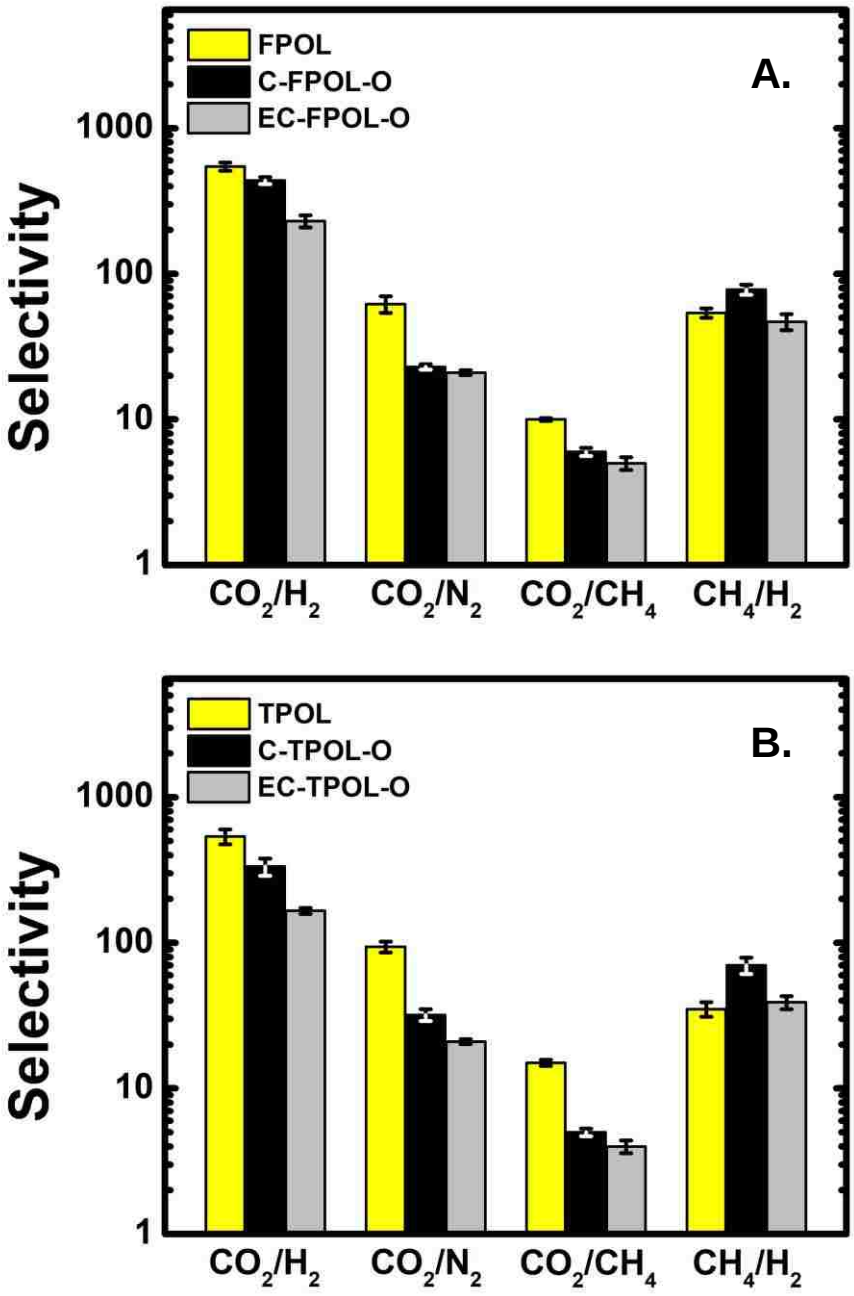

Figure S.6. Relative selectivities at 273 K for the gasses shown for as-prepared (yellow), C- (black), and EC- (grey) carbon aerogels derived from **TPOL-O** (A) and **FPOL-O** (B) aerogels.

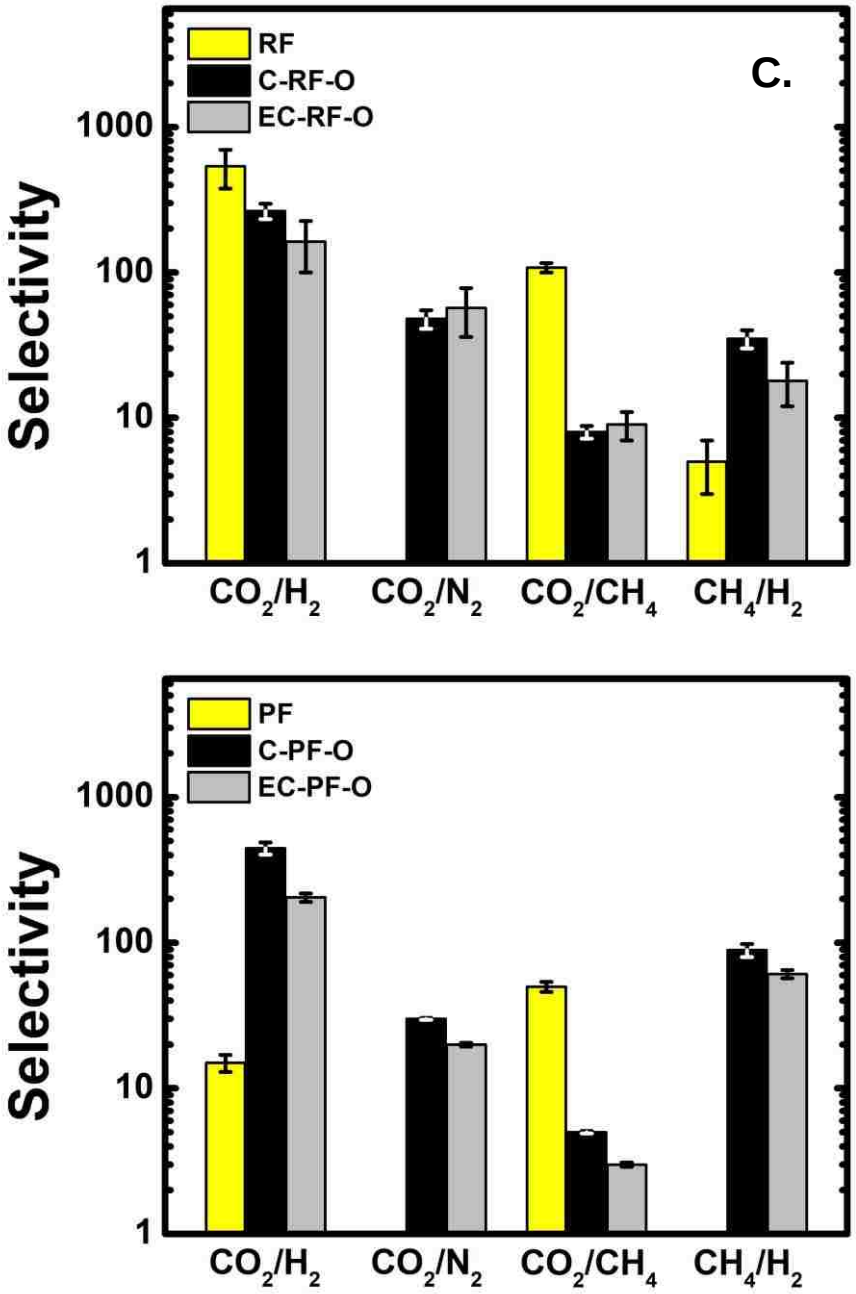

Figure S.6. (Continued) Relative selectivities at 273 K for the gasses shown for as-prepared (yellow), C- (black), and EC- (grey) carbon aerogels derived from **RF-O** (C) and **PF-O** (D) aerogels.

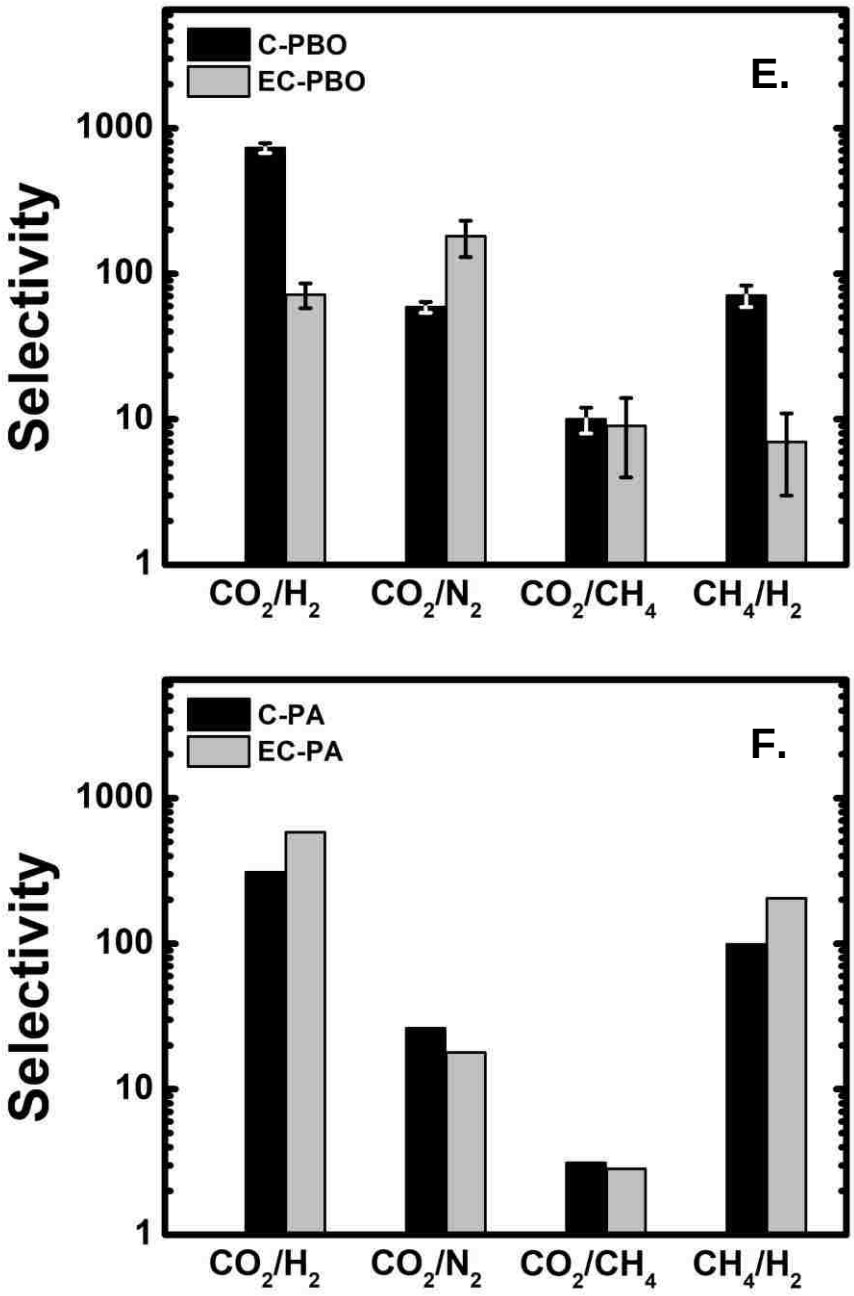

Figure S.6. (Continued) Relative selectivities at 273 K for the gasses shown for C- (black) and EC- (grey) carbon aerogels derived from **PBO** (E) and (F) **PA** (F) aerogels.

Appendix X. REFERENCES

1. Zhu, Y.; Long, H.; Zhang, W. Imine-Linked Porous Polymer Frameworks with High Small Gas (H_2, CO_2, CH_4, C_2H_2) Uptake and CO_2/N_2 Selectivity. *Chem. Mater.* **2013**, *25*, 1630–1635.

2. Rabbani, M. G.; El-Kaderi, H. M. Synthesis and Characterization of Porous Benzimidazole-Linked Polymers and Their Performance in Small Gas Storage and Selective Uptake. *Chem. Mater.* **2012**, *24*, 1511–1517.

3. Byun, J.; Je, S.-H.; Patel, H. A.; Coskun, A.; Yavuz, C. T. Nanoporous Covalent Organic Polymers Incorporating Troger's Base Functionalities for Enhanced CO_2 Capture. *J. Mater. Chem. A* **2014**, *2*, 12507–12512.

4. Rabbani, M. G.; Reich, T. E.; Kassab, R. M.; Jackson, K. T.; El-Kaderi, H. M. High CO_2 Uptake and Selectivity by Triptycene-Derived Benzimidazole-Linked Polymers. *Chem. Commun.* **2012**, *48*, 1141–1143.

5. Chen, Q.; Luo, M.; Hammershøj, P.; Zhou, D.; Han, Y.; Laursen, B. W.; Yan, C.-G.; Han, B.-H. Microporous Polycarbazole with High Specific Surface Area for Gas Storage and Separation. *J. Am. Chem. Soc.* **2012**, *134*, 6084–6087.

6. Zhu, X.; Mahurin, S. M.; An, S.-H.; Do-Thanh, C.-L.; Tian, C.; Li, Y.; Gill, L. W.; Hagaman, E. W.; Bian, Z.; Zhou, J.-H.; Hu, J.; Liu, H.; Dai, S. Efficient CO_2 Capture by a Task-Specific Porous Organic Polymer Bifunctionalized with Carbazole and Triazine Groups. *Chem. Commun.* **2014**, *50*, 7933–7936.

7. Yang, X.; Yu, M.; Zhao, Y.; Zhang, C.; Wang, X.; Jiang, J.-X. Hypercrosslinked Microporous Polymers Based on Carbazole for Gas Storage and Separation. *RSC Adv.* **2014**, *4*, 61051–61055.

8. Ben, T.; Li, Y.; Zhu, L.; Zhang, D.; Cao, D.; Xiang, Z.; Yao, X.; Qiu, S. Selective Adsorption of Carbon Dioxide by Carbonized Porous Aromatic Framework (PAF). *Energy Environ. Sci.* **2012**, *5*, 8370–8376.

9. Katsoulidis, A. P.; Kanatzidis, M. G. Phloroglucinol Based Microporous Polymeric Organic Frameworks with −OH Functional Groups and High CO_2 Capture Capacity. *Chem. Mater.* **2011**, *23*, 1818–1824.

10. Dawson, R.; Stevens, L. A.; Drage, T. C.; Snape, C. E.; Smith, M. W.; Adams, D. J.; Cooper, A. I. Impact of Water Coadsorption for Carbon Dioxide Capture in Microporous Polymer Sorbents. *J. Am. Chem. Soc.* **2012**, *134*, 10741–10744.

11. Martin, C. F.; Stockel, E.; Clowes, R.; Adams, D. J.; Cooper, A. I.; Pis, J. J.; Rubiera, F.; Pevida, C. Hypercrosslinked Organic Polymer Networks as Potential Adsorbents for Pre-Combustion CO_2 Capture. *J. Mater. Chem.* **2011**, *21*, 5475–5483.

12. Dawson, R.; Stockel, E.; Holst, J. R.; Adams, D. J.; Cooper, A. I. Microporous Organic Polymers for Carbon Dioxide Capture. *Energy Environ. Sci.* **2011**, *4*, 4239–4245.

13. Yao, S.; Yang, X.; Yu, M.; Zhang, Y.; Jiang, J.-X. High Surface Area Hypercrosslinked Microporous Organic Polymer Networks Based on Tetraphenylethylene for CO_2 Capture. *J. Mater. Chem. A* **2014**, *2*, 8054–8059.

14. Li, B.; Gong, R.; Wang, W.; Huang, X.; Zhang, W.; Li, H.; Hu, C.; Tan, B. A New Strategy to Microporous Polymers: Knitting Rigid Aromatic Building Blocks by External Cross-Linker. *Macromolecules* **2011**, *44*, 2410–2414.

15. Ben, T.; Pei, C.; Zhang, D.; Xu, J.; Deng, F.; Jing, X.; Qiu, S. Gas Storage in Porous Aromatic Frameworks (PAFs). *Energy Environ. Sci.* **2011**, *4*, 3991–3999.

16. Yang, X.; Yao, S.; Yu, M.; Jiang, J. X. Synthesis and Gas Adsorption Properties of Tetra-Armed Microporous Organic Polymer Networks Based on Triphenylamine. *Macromol. Rapid Commun.* **2014**, *35*, 834–839.

17. Luo, Y.; Li, B.; Wang, W.; Wu, K.; Tan, B. Hypercrosslinked Aromatic Heterocyclic Microporous Polymers: A New Class of Highly Selective CO_2 Capturing Materials. *Adv. Mater.* **2012**, *24*, 5703–5707.

18. Fischer, S.; Schimanowitz, A.; Dawson, R.; Senkovska, I.; Kaskel, S.; Thomas, A. Cationic Microporous Polymer Networks by Polymerisation of Weakly Coordinating Cations with CO_2-Storage Ability. *J. Mater. Chem. A* **2014**, *2*, 11825–11829.

19. Liebl, M. R.; Senker, J. Microporous Functionalized Triazine-Based Polyimides with High CO_2 Capture Capacity. *Chem. Mater.* **2013**, *25*, 970–980.

20. Chen, X.; Qiao, S.; Du, Z.; Zhou, Y.; Yang, R. Synthesis and Characterization of Functional Thienyl-Phosphine Microporous Polymers for Carbon Dioxide Capture. *Macromol. Rapid Commun.* **2013**, *34*, 1181–1185.

21. Luo, Y.; Li, B.; Liang, L.; Tan, B. Synthesis of Cost-Effective Porous Polyimides and Their Gas Storage Properties. *Chem. Commun.* **2011**, *47*, 7704–7706.

22. Wilke, A.; Weber, J. Hierarchical Nanoporous Melamine Resin Sponges with Tunable Porosity-Porosity Analysis and CO_2 Sorption Properties. *J. Mater. Chem.* **2011**, *21*, 5226–5229.

23. Wickramaratne, N. P.; Jaroniec, M. Importance of Small Micropores in CO_2 Capture by Phenolic Resin-Based Activated Carbon Spheres. *J. Mater. Chem. A* **2013**, *1*, 112–116.

24. Adeniran, B.; Mokaya, R. Low Temperature Synthesized Carbon Nanotube Superstructures with Superior CO_2 and Hydrogen Storage Capacity. *J. Mater. Chem. A* **2015**, *3*, 5148–5161.

25. Sevilla, M.; Fuertes, A. B. Sustainable Porous Carbons with a Superior Performance for CO_2 Capture. *Energy Environ. Sci.* **2011**, *4*, 1765–1771.

26. Sevilla, M.; Valle-Vigón, P.; Fuertes, A. B. N-Doped Polypyrrole-Based Porous Carbons for CO_2 Capture. *Adv. Funct. Mater.* **2011**, *21*, 2781–2787.

27. Liu, L.; Deng, Q.-F.; Hou, X.-X.; Yuan, Z.-Y. User-Friendly Synthesis of Nitrogen-Containing Polymer and Microporous Carbon Spheres for Efficient CO_2 Capture. *J. Mater. Chem.* **2012**, *22*, 15540–15548.

28. Wang, J.; Heerwig, A.; Lohe, M. R.; Oschatz, M.; Borchardt, L.; Kaskel, S. Fungi-Based Porous Carbons for CO_2 Adsorption and Separation. *J. Mater. Chem.* **2012**, *22*, 13911–13913.

29. Wang, J.; Senkovska, I.; Oschatz, M.; Lohe, M. R.; Borchardt, L.; Heerwig, A.; Liu, Q.; Kaskel, S. Highly Porous Nitrogen-Doped Polyimine-Based Carbons with Adjustable Microstructures for CO_2 Capture. *J. Mater. Chem. A* **2013**, *1*, 10951–10961.

30. Wang, J.; Krishna, R.; Wu, X.; Sun, Y.; Deng, S. Polyfuran-Derived Microporous Carbons for Enhanced Adsorption of CO_2 and CH_4. *Langmuir* **2015**, *31*, 9845–9852.

31. Bai, B. C.; Kim, J. G.; Im, J. S.; Jung, S.C.; Lee, Y.S. Influence of Oxyfluorination on Activated Carbon Nanofibers for CO_2 Storage. *Carbon Lett.* **2011**, *12*, 236–242.

32. Saeed, A. M.; Rewatkar, P. M.; Majedi Far, H.; Taghvaee, T.; Donthula, S.; Mandal, C.; Sotiriou-Leventis, C.; Leventis, N. Selective CO_2 Sequestration with Monolithic Bimodal Micro/Macroporous Carbon Aerogels Derived from Stepwise Pyrolytic Decomposition of Polyamide-Polyimide-Polyurea Random Copolymers. *ACS Appl. Mater. Interfaces* **2017**, *9*, 13520–13536.

REFERENCES

1. R. S. Haszeldine, Carbon Capture and Storage: How Green Can Black Be? *Science* **2009**, *325*, 1647–1652.

2. B. Smit, J. A. Reimer, C. M. Oldenburg, I. C. Bourg, *Introduction to Carbon Capture and Sequestration-The Berkeley Lectures on Energy*, Imperial College Press, London **2014**, Vol. 1, pp. 141–162.

3. M. Kanniche, R. Gros-Bonnivard, P. Jaud, J. Valle-Marcos, J.-M. Amann, C. Bouallou, Pre-combustion, Post-combustion and Oxy-combustion in Thermal Power Plant for CO_2 Capture, *Appl. Thermal Eng.* **2010**, *30*, 53–62.

4. B. Li, Y. Duan, D. Luebke, B. Morreale, Advances in CO_2 Capture Technology: A Patent Review, *Appl. Energy* **2013**, *102*, 1439–1447.

5. J. Wang, L. Huang, R. Yang, Z. Zhang, J. Wu, Y. Gao, Q. Wang, D. O'Hare, Z. Zhong, Recent Advances in Solid Sorbents for CO_2 Capture and New Development Trends, *Energy Environ. Sci.* **2014**, *7*, 3478–3518.

6. R. Dawson, A. I. Cooper, D. J. Adams, Chemical Functionalization Strategies for Carbon Dioxide Capture in Microporous Organic Polymers, *Polym. Int.* **2013**, *62*, 345–352.

7. J. Yu, L.-H. Xie, J.-R. Li, Y. Ma, J. M. Seminario, P. B. Balbuena, CO_2 Capture and Separations Using MOFs: Computational and Experimental Studies, *Chem. Rev.* **2017**, *117*, 9674–9754.

8. K. Sumida, D. L. Rogow, J. A. Mason, T. M. McDonald, E. D. Bloch, Z. R. Herm, T.-H. Bae, J. R. Long, Carbon Dioxide Capture in Metal–Organic Frameworks, *Chem. Rev.* **2012**, *112*, 724–781.

9. S. Keskin, T. M. V. Heest, D. S. Sholl, Can Metal-Organic Framework Materials Play a Useful Role in Large-Scale Carbon Dioxide Separations? *ChemSusChem* **2010**, *3*, 879–891.

10. S. Yao, X. Yang, M. Yu, Y. Zhang, J.-X. Jiang, High Surface Area Hypercrosslinked Microporous Organic Polymer Networks Based on Tetraphenylethylene for CO_2 Capture, *J. Mater. Chem. A* **2014**, *2*, 8054–8059.

11. M. P. Tsyurupa, V. A. Davankov, Hypercrosslinked Polymers: Basic Principle of Preparing the New Class of Polymeric Materials, *React. Funct. Polym.* **2002**, *53*, 193–203.

12. Y. Xu, S. Jin, H. Xu, A. Nagai, D. Jiang, Conjugated Microporous Polymers: Design, Synthesis and Application, *Chem. Soc. Rev.* **2013**, *42*, 8012–8031.

13. A. I. Cooper, Conjugated Microporous Polymers, *Adv. Mater.* **2009**, *21*, 1291–1295.

14. N. B. McKeown, Budd, P. M. Exploitation of Intrinsic Microporosity in Polymer-Based Materials, *Macromolecules* **2010**, *43*, 5163–5176.

15. P. M. Budd, B. S. Ghanem, S. Makhseed, N. B. McKeown, K. J. Msayib, C. E. Tattershall, Polymers of Intrinsic Microporosity (PIMs): Robust, Solution-Processable, Organic Nanoporous Materials, *Chem. Commun.* **2004**, 230–231.

16. T. Ben, Y. Li, L. Zhu, D. Zhang, D. Cao, Z. Xiang, X. Yao, S. Qiu, Selective Adsorption of Carbon Dioxide by Carbonized Porous Aromatic Framework (PAF), *Energy Environ. Sci.* **2012**, *5*, 8370–8376.

17. T. Ben, C. Pei, D. Zhang, J. Xu, F. Deng, X. Jing, S. Qiu, Gas Storage in Porous Aromatic Frameworks (PAFs), *Energy Environ. Sci.* **2011**, *4*, 3991–3999.

18. J. Byun, S.-H. Je, H. A. Patel, A. Coskun, C. T. Yavuz, Nanoporous Covalent Organic Polymers Incorporating Troger's Base Functionalities for Enhanced CO_2 Capture, *J. Mater. Chem. A* **2014**, *2*, 12507–12512.

19. H. A. Patel, S. H. Je, J. Park, Y. Jung, A. Coskun, C. T. Yavuz, Directing the Structural Features of N_2-Phobic Nanoporous Covalent Organic Polymers for CO_2 Capture and Separation, *Chem. - Eur. J.* **2014**, *20*, 772–780.

20. P. Kuhn, M. Antonietti, A. Thomas, Porous, Covalent Triazine-Based Frameworks Prepared by Ionothermal Synthesis, *Angew. Chem. Int. Ed.* **2008**, *47*, 3450–3453.

21. X. Yang, S. Yao, M. Yu, J. X. Jiang, Synthesis and Gas Adsorption Properties of Tetra-Armed Microporous Organic Polymer Networks Based on Triphenylamine, *Macromol. Rapid Commun.* **2014**, *35*, 834–839.

22. R. Dawson, E. Stockel, J. R. Holst, D. J. Adams, A. I. Cooper, Microporous Organic Polymers for Carbon Dioxide Capture, *Energy Environ. Sci.* **2011**, *4*, 4239–4245.

23. Y. Zhu, H. Long, W. Zhang, Imine-Linked Porous Polymer Frameworks with High Small Gas (H_2, CO_2, CH_4, C_2H_2) Uptake and CO_2/N_2 Selectivity, *Chem. Mater.* **2013**, *25*, 1630–1635.

24. M. G. Rabbani, T. E. Reich, R. M. Kassab, K. T. Jackson, H. M. El-Kaderi, High CO_2 Uptake and Selectivity by Triptycene-Derived Benzimidazole-Linked Polymers, *Chem. Commun.* **2012**, *48*, 1141–1143.

25. M. G. Rabbani, A. K. Sekizkardes, O. M. El-Kadri, B. R. Kaafarani, H. M. El-Kaderi, Pyrene-Directed Growth of Nanoporous Benzimidazole-Linked Nanofibers and Their Application to Selective CO_2 Capture and Separation, *J. Mater. Chem.* **2012**, *22*, 25409–25417.

26. P. Guo, D. Dutta, A. G. Wong-Foy, D. W. Gidley, A. J. Matzger, Water Sensitivity in Zn_4O-Based MOFs is Structure and History Dependent, *J. Am. Chem. Soc.* **2015**, *137*, 2651–2657.

27. P. M. Schoenecker, C. G. Carson, H. Jasuja, C. J. J. Flemming, K. S. Walton, Effect of Water Adsorption on Retention of Structure and Surface Area of Metal–Organic Frameworks, *Ind. Eng. Chem. Res.* **2012**, *51*, 6513–6519.

28. Y. Hanzawa, K. Kaneko, R. W. Pekala, M. S. Dresselhaus, Activated Carbon Aerogels, *Langmuir* **1996**, *12*, 6167–6169.

29. R. W. Pekala, D. W. Schaefer, Structure of Organic Aerogels. 1. Morphology and Scaling, *Macromolecules* **1993**, *26*, 5487–5493.

30. N. Leventis, C. Sotiriou-Leventis, N. Chandrasekaran, S. Mulik, Z. J. Larimore, H. Lu, G. Churu, J. T. Mang, Multifunctional Polyurea Aerogels from Isocyanates and Water. A Structure−Property Case Study, *Chem. Mater.* **2010**, *22*, 6692–6710.

31. A. M. Saeed, P. M. Rewatkar, H. Majedi Far, T. Taghvaee, S. Donthula, C. Mandal, C. Sotiriou-Leventis, N. Leventis, Selective CO_2 Sequestration with Monolithic Bimodal Micro/Macroporous Carbon Aerogels Derived from Stepwise Pyrolytic Decomposition of Polyamide-Polyimide-Polyurea Random Copolymers, *ACS Appl. Mater. Interfaces* **2017**, *9*, 13520–13536.

32. C. Chidambareswarapattar, L. Xu, C. Sotiriou-Leventis, N. Leventis, Robust Monolithic Multiscale Nanoporous Polyimides and Conversion to Isomorphic Carbons, *RSC Adv.* **2013**, *3*, 26459–26469.

33. G. Biesmans, A. Mertens, L. Duffours, T. Woignier, J. Phalippou, Polyurethane Based Organic Aerogels and Their Transformation into Carbon Aerogels, *J. Non-Cryst. Solids* **1998**, *225*, 64–68.

34. S. Mahadik-Khanolkar, S. Donthula, C. Sotiriou-Leventis, N. Leventis, Polybenzoxazine Aerogels. 1. High-Yield Room-Temperature Acid-Catalyzed Synthesis of Robust Monoliths, Oxidative Aromatization, and Conversion to Microporous Carbons, *Chem. Mater.* **2014**, *26*, 1303–1317.

35. H. Majedi Far, S. Donthula, T. Taghvaee, A. M. Saeed, Z. Garr, C. Sotiriou-Leventis, N. Leventis, Air-Oxidation of Phenolic Resin Aerogels: Backbone Reorganization, Formation of Ring-Fused Pyrylium Cations, and the Effect on Microporous Carbons with Enhanced Surface Areas, *RSC Adv.* **2017**, *7*, 51104–51120.

36. X. Ning, H. Ishida, Phenolic Materials via Ring-opening Polymerization: Synthesis and Characterization of Bisphenol-A Based Benzoxazines and their Polymers, *J. Polym. Sci., Part A: Polym. Chem.* **1994**, *32*, 1121–1129.

37. X. Ning, H. Ishida, Phenolic Materials via Ring-opening Polymerization of Benzoxazines: Effect of Molecular Structure on Mechanical and Dynamic Mechanical Properties, *J. Polym. Sci.:Part A: Polym. Chem.* **1994**, *32*, 921–927.

38. H. Ishida, Process for Benzoxazine Compounds in Solventless Systems, U.S. Patent No. 5,543,516 (1996).

39. M. A. Yahya, M. H. Manson, W. A. A. W. Zolkarnaini, N. S. Rusli, A. Aminuddin, K. Mohamad, F. A. M. Sabhan, A. A. A. Atik, L. N. Ozair, A Brief Review on Activated Carbon Derived from Agriculture By-product. Recent Advancement on Applied Physics, Industrial Chemistry and Chemical Technology *AIP Conf. Proc.* **1972**, 030023-1-030023-8.

40. Y. N. Sazanov, A. V. Gribanov, Criteria of Polymer Carbonization, *Russ. J. Appl. Chem.* **2009**, *82*, 473-482.

41. M. Lawrinenko, D. A. Laird, Anion Exchange Capacity of Biochar, *Green Chem.* **2015**, *17*, 4628–4636.

42. C. M. Kim, H. S. Jeong, E. H. Kim, NEXAFS and XPS Characterization of Molecular Oxygen Adsorbed on Ni (100) at 80 K, *Surf. Sci.* **2000**, *459*, L457–L461.

43. L. Q. Wu, S. Q. Li, Y. C. Li, Z. Z. Li, G. D. Tang, W. H. Qi, L. C. Xue, L. L. Ding, X. S. Ge, Presence of Monovalent Oxygen Anions in Oxides Demonstrated Using X-ray Photoelectron Spectra, *Appl. Phys. Lett.* **2016**, *108*, 021905.

44. G. P. López, D. G. Castner, B. D. Ratner, XPS O 1s Binding Energies for Polymers Containing Hydroxyl, Ether, Ketone and Ester Groups, *Surf. Interface Anal.* **1991**, *17*, 267–272.

45. A. Ganguly, S. Sharma, P. Papakonstantinou, J. Hamilton, Probing the Thermal Deoxygenation of Graphene Oxide Using High-Resolution In Situ X-ray-Based Spectroscopies, *J. Phys. Chem. C* **2011**, *115*, 17009–17019.

46. D. Briggs, G. Beamson, XPS Studies of the Oxygen 1s and 2s Levels in a Wide Range of Functional Polymers, *Anal. Chem.* **1993**, *65*, 1517–1523.

47. J. R. Pels, F. Kapteijn, J. A. Moulijn, Q. Zhu, K. M. Thomas, Evolution of Nitrogen Functionalities in Carbonaceous Materials During Pyrolysis, *Carbon* **1995**, *33*, 1641–1653.

48. M. Inagaki, M. Toyoda, Y. Soneda, T. Morishita, Nitrogen-Doped Carbon Materials, *Carbon* **2018**, *132*, 104–140.

49. J. Chen, Z. Mao, L. Zhang, Y. Tang, D. Wang, L. Bie, B. D. Fahlman, Direct Production of Nitrogen-Doped Porous Carbon from Urea via Magnesiothermic Reduction, *Carbon* **2018**, *130*, 41–47.

50. N. Hellgren, R. T. Haasch, S. Schmidt, L. Hultman, I. Petrov, Interpretation of X-ray Photoelectron Spectra of Carbon-Nitride Thin Films: New Insights from in Situ XPS, *Carbon* **2016**, *108*, 242–252.

51. I. K. Moon, J. Lee, H. Lee, Highly Qualified Reduced Graphene Oxides: the Best Chemical Reduction, *Chem. Commun.* **2011**, *47*, 9681–9683.

52. M. Thommes, K. Kaneko, A. V. Neimark, J. P. Olivier, F. Rodriguez-Reinoso, J. Rouquerol., K. S. W. Sing, Physisorption of Gases, with Special Reference to the Evaluation of Surface Area and Pore Size Distribution (IUPAC Technical Report), *Pure Appl. Chem.* **2015**, *87*, 1051–1069.

53. W. D. Harkins, G. Jura, Surfaces of Solids. XII. An Absolute Method for the Determination of the Area of a Finely Divided Crystalline Solid, *J. Am. Chem. Soc.* **1944**, *66*, 1362–1366.

54. P. A. Webb, C. Orr, *Analytical Methods in Fine Particle Technology*, Micromeritics Instrument Corporation, Norcross, GA **1997**, pp. 63–70.

55. M. M. Dubinin, Fundamentals of the Theory of Adsorption in Micropores of Carbon Adsorbents: Characteristics of Their Adsorption Properties and Microporous Structures, *Carbon* **1989**, *27*, 457–467.

56. P. A. Webb, C. Orr, *Analytical Methods in Fine Particle Technology*, Micromeritics Instrument Corporation, Norcross, GA **1997**, pp. 71–73.

57. F. Carrasco-Marin, M. V. Lopez-Ramon, C. Moreno-Castilla, Applicability of the Dubinin-Radushkevich Equation to Carbon Dioxide Adsorption on Activated Carbons, *Langmuir* **1993**, *9*, 2758–2760.

58. M. L. Pinto, A. S. Mestre, A. P. Carvalho, J. Pires, Comparison of Methods to Obtain Micropore Size Distributions of Carbonaceous Materials from CO_2 Adsorption Based on the Dubinin-Radushkevich Isotherm, *Ind. Eng. Chem. Res.* **2010**, *49*, 4726–4730.

59. J. Garrido, A. Linares-Solano, J. M. Martin-Martinez, M. Molina-Sabio, F. Rodriguez-Reinoso, R. Torregrosa, Use of Nitrogen vs. Carbon Dioxide in the Characterization of Activated Carbons, *Langmuir* **1987**, *3*, 76–81.

60. P. A. Webb, C. Orr, *Analytical Methods in Fine Particle Technology*, Micromeritics Instrument Corporation, Norcross, GA **1997**, pp. 81–87.

61. B. B. Saha, S. Jribi, S. Koyama, I. I. El-Sharkawy, Carbon Dioxide Adsorption Isotherms on Activated Carbons, *J. Chem. Eng. Data* **2011**, *56*, 1974–1981.

62. D. Lozano-Castelló, D. Cazorla-Amorós, A. Linares-Solano, Usefulness of CO_2 Adsorption at 273 K for the Characterization of Porous Carbons, *Carbon* **2004**, *42*, 1233–1242.

63. P. A. Webb, C. Orr, *Analytical Methods in Fine Particle Technology* Micromeritics Instrument Corporation, Norcross, GA **1997**, p. 61.

64. D. Cazorla-Amorós, J. Alcañiz-Monge, A. Linares-Solano, Characterization of Activated Carbon Fibers by CO_2 Adsorption, *Langmuir* **1996**, *12*, 2820–2824.

65. D. Cazorla-Amorós, J. Alcañiz-Monge, M. A. de la Casa-Lillo, A. Linares-Solano, CO_2 As an Adsorptive to Characteriza Carbon Molecular Sieves and Activated Carbons, *Langmuir* **1998**, *14*, 4589–4596.

66. M. Sevilla, A. B. Fuertes, Sustainable Porous Carbons with a Superior Performance for CO_2 Capture, *Energy Environ. Sci.* **2011**, *4*, 1765–1771.

67. N. P. Wickramaratne, M. Jaroniec, Importance of Small Micropores in CO_2 Capture by Phenolic Resin-Based Activated Carbon Spheres, *J. Mater. Chem. A* **2013**, *1*, 112–116.

68. L. Czepirski, J. JagieŁŁo, Virial-Type Thermal Equation of Gas-Solid Adsorption, *Chem. Eng. Sci.* **1989**, *44*, 797–801.

69. H. A. Patel, S. H. Je, J. Park, D. P. Chen, Y. Jung, C. T. Yavuz, A. Coskun, Unprecedented High-Temperature CO_2 Selectivity in N_2-phobic Nanoporous Covalent Organic Polymers, *Nat. Commun.* **2013**, *4*, 1357-1361.

70. S. Kayal, H. W. B. Teo, A. Chakraborty, Prediction of Phase Transitions by Investigating CO_2 Adsorption on 1% Lithium Doped MIL-101 (Cr) MOF with Anomalous Type Isosteric Heat of Adsorption, *Micropor. Mesopor. Mat.* **2016**, *236*, 21-27.

71. M. Murialdo, N. P. Stadie, C. C. Ahn, B. Fultz, Observation and Investigation of Increasing Isosteric Heat of Adsorption of Ethane on Zeolite-Templated Carbon, *J. Phys. Chem. C* **2015**, *119*, 944–950.

72. F. Svec, J. Germain, J. M. J. Frechet, Nanoporous Polymers for Hydrogen Storage, *Small* **2009**, *5*, 1098-1111.

73. P. Xydias, I. Spanopoulos, E. Klontzas, G. E. Froudakis, P. Trikalitis, Drastic Enhancement of the CO_2 Adsorption Properties in Sulfone-Functionalized Zr- and Hf-UiO-67 MOFs with Hierarchical Mesopores, *Inorg. Chem.* **2014**, *53*, 679-681.

74. X. Yang, M. Yu, Y. Zhao, C. Zhang, X. Wang, J.-X. Jiang, Hypercrosslinked Microporous Polymers Based on Carbazole for Gas Storage and Separation, *RSC Adv.* **2014**, *4*, 61051-61055.

75. A. Muelleman, J. Schell, S. Glazer, R. Glaser, Thermochemistry of a Biomimetic and Rubisco-Inspired CO_2 Capture System from Air, *C J. Carbon Res*. **2016,** *2*, 18–32.

76. R. Glaser, RuBisCO-Inspired Biomimetic Approaches to Reversible CO_2 Capture from Air. Metal Dependence of the H_2O/CO_2 Replacement Penalty, in *Advances in CO_2 Capture, Sequestration and Conversion*, (Eds: F. Jin, L.-N. He, Y. H. Hu), ACS Symposium Series, American Chemical Society: Washington, DC **2015**, Vol. 1194, pp. 265–293.

77. R. Glaser, P. O. Castello-Blindt, J. Yin, Biomimetic Approaches to Reversible CO_2 Capture from Air. *N*-Methylcarbaminic Acid Formation in Rubisco-Inspired Models, in *New and Future Developments in Catalysis. Activation of Carbon Dioxide*, (Ed: S. L. Suib), Elsevier, Amsterdam **2013**, pp. 501–534.

78. B. Smit, J. A. Reimer, C. M. Oldenburg, I. C. Bourg, *Introduction to Carbon Capture and Sequestration-The Berkeley Lectures on Energy*, Imperial College Press, London **2014**, Vol. 1, pp. 281–354.

79. *March's Advanced Organic Chemistry*, (Eds: M. B. Smith, J. March), John Wiley & Sons, Inc., Hoboken, NJ **2007**, pp. 3−31.

80. J. H. Cole, D. H. Everett, C. T. Marshall, A. R. Paniego, J. C. Powl, F. Rodriguez-Reinoso, Thermodynamics of the High Temperature Adsorption of Some Permanent Gases by Porous Carbons, *J. Chem. Soc., Faraday Trans. 1* **1974**, *70*, 2154–2169.

81. K. S. W. Sing, F. Rouquerol, J. Rouquerol, in *Adsorption by Powders and Porous Solids*, (Eds: F. Rouquerol, J. Rouquerol, K. S. W. Sing, P. Liewwllyn, G. Maurin), Academic Press, Oxford **2014**, pp. 159–163.

82. S. Bag, M. G. Kanatzidis, Chalcogels: Porous Metal−Chalcogenide Networks from Main-Group Metal Ions. Effect of Surface Polarizability on Selectivity in Gas Separation, *J. Am. Chem. Soc.* **2010**, *132*, 14951−14959.

83. P. Rallapalli, K. P. Prasanth, D. Patil, R. S. Somani, R. V. Jasra, H. C. Bajaj, Sorption Studies of CO_2, CH_4, N_2, CO, O_2 and Ar on Nanoporous Aluminum Terephthalate [MIL-53(Al)], *J. Porous Mater.* **2011**, *18*, 205−210.

84. Y. Jin, B. A. Voss, R. D. Noble, W. A. Zhang, Shape-Persistent Organic Molecular Cage with High Selectivity for the Adsorption of CO_2 over N_2, *Angew. Chem., Int. Ed.* **2010**, *49*, 6348−6351.

85. S. Zulfiqar, D. Mantione, O. El Tall, M. I. Sarwar, F. Ruipérez, A. Rothenberger, D. Mecerreyes, Nanoporous Amide Networks Based on Tetraphenyladamantane for Selective CO_2 Capture, *J. Mater. Chem. A* **2016**, *4*, 8190−8197.

86. S. Mulik, C. Sotiriou-Leventis, N. Leventis, Time-Efficient Acid-Catalyzed Synthesis of Resorcinol-Formaldehyde Aerogels, *Chem. Mater.* **2007**, *19*, 6138-6144.

87. S. Sircar, R. Mohr, C. Ristic, M. B. Rao, Isosteric Heat of Adsorption: Theory and Experiment, *J. Phys. Chem. B* **1999**, *103*, 6539–6546.

88. P. Carrott, K. Sing, Multilayer Adsorption of Nitrogen and Alkanes by Non-porous Carbons and Silicas, *Pure Appl. Chem.* **1989**, *61*, 1835–1840.

SECTION

2. CONCLUSIONS

Four polymeric aerogels: TPOL, FPOL, RF, and PF were synthesized via an acid-catalyzed gelation of phenolic compounds: phenol (P), resorcinol (R), phloroglucinol (P) with aldehydes: formaldehyde (F) and terephthalaldehyde (T) in organic solvents in order to study the carbonization process.

In Paper I phenolic resin-based organic aerogels were converted to carbon through two routes. In one route, they were directly pyrolyzed at 800 °C/Ar, while in the other, they were subjected to an oxidative heating step at 240 °C/air prior to pyrolysis at 800 °C/Ar. Subsequently, all carbons were activated (etched) by exposing them to CO_2 gas at 1000 °C, which resulted in significant increase in their surface areas. N_2 sorption analysis showed that carbons obtained from the oxidative pathway in TPOL and FPOL systems exhibit higher total and micropore surface areas in comparison to the carbons that were directly pyrolyzed. However, unlike polybenzoxazine aerogels where the oxidation step (200 °C/air) is necessary for high-yield carbonization, the carbonization yields of carbons from the two routes were not too different from each other. Spectroscopic studies such as XPS, ^{13}C NMR, FTIR, and CHN analysis revealed that at 240 °C/air ring-fusion aromatization, similar to PAN fibers takes place. The oxidized polymeric backbone includes fused pyrylium rings ($C{=}O^{+}$), and charge-compensating phenoxides ($C{-}O^{-}$). That ring fusion and aromatization thereafter rigidizes the polymeric backbone and creates microporosity and carbons with higher surface areas than those obtained by direct-pyrolysis of as-made materials. In the case of RF and PF aerogels,

curing at 240 °C/air oxidized only the bridging $–CH_2-$ groups, forming carbonyl groups (C=O). Ring fusion aromatization did not take place. Consequently, the surface areas of carbons from the two routes were close to one another. An interesting observation was made which showed that all carbons, regardless of their precursors and their carbonization routes, converged to a common structure consisting of stacked 6-membered aromatic rings with surface pyrylium ($C=O^+$) and phenoxide ($C–O^-$) ions. The significance of these studies is that wherever ring-fusion aromatization takes place at the early stages of carbonization, it is beneficial to the properties of final carbons; it produces high-yield carbons (from PBO aerogels) or improves the surface areas (in TPOL- and FPOL-derived carbon aerogels).

In Paper II the utility of carbons and etched carbons obtained from the four phenolic resin aerogels (TPOL, FPOL, RF, and PF) were investigated in CO_2 sequestration as applied to postcombustion techniques. The inspiration for that was their high micropore surface areas obtained after etching at 1000 °C/CO_2. Etched carbons from TPOL, FPOL, and PF showed CO_2 uptakes as high as 6 mmol g^{-1} at 273 K and 1 bar, close to the values reported for the best porous polymeric or carbon-based adsorbents under the same conditions. However, RF showed an exceptionally high CO_2 uptake of 14.8 ± 3.9 mmol g^{-1}, which was attributed to the high micropore volume due to the opening of closed pores developed after the etching process. In addition, CO_2 interacts with the phenoxide within the micropore walls through an energy-neutral reaction beyond a multilayer coverage. Since those materials contained only oxygen functional groups ($C=O^+$, and $C–O^-$), the CO_2 adsorption data were compared with carbons obtained from polybenzoxazine and a polyamide-polyimide-polyurea copolymer aerogel, which contain

nitrogen in addition to oxygen functional groups. In summary, the results confirmed the importance of large accessible micropore volumes to CO_2 molecules at close to ambient temperatures and pressures and the benefit of oxygen over nitrogen functional groups in porous sorbents. In addition, they show relatively high CO_2 selectivity toward CH_4, N_2, and H_2, a requirement for designing superior CO_2 adsorbents. Therefore, these materials could be viable candidates in separation techniques such as column chromatographic packing materials, and sorbents for separation of CO_2 from CH_4 and N_2 relevant to post-combustion, or CO_2 from H_2 in pre-combustion gas sequestration techniques.

APPENDIX A.

PHENOLIC RESINS

The term “resin” refers to any synthetic polymer which is adhesive, film-forming or show other useful properties.

Phenolic resins are a class of resins, which are formed by the polycondensation of phenol or phenol derivatives with aldehyde (often formaldehyde), and elimination of water.[1,2]

In 1909, Baekeland introduced the first polymer by developing the first fully synthetic plastic, Bakelite. He carried out the polycondensation of phenol with formaldehyde to form a crosslinked thermosetting plastic. Bakelite belongs to a class of organic materials named “phenolic resins”.

Historically, phenolic resins were used as thermosets and electrical insulating polymers. Subsequently, implementation of new organic reactions led to the development of other types of phenolic resins with various useful applications such as: adhesives, printing ink binders, waterborne paints, temperature-resistant binders, and laminated plastics. Commercialized resins include: unsaturated polyester resins, alkyd resins, emulsion polymers, amino resins for surface coatings, polyurethane resins, polyamide-epichlorohydrin resins, formaldehyde resins, and urea formaldehyde.[3]

Among aldehydes, formaldehyde is the most important starting material in phenolic resin applications. Acetaldehyde and butyraldehyde are rarely used; furfural is also sometimes used to prepare dark brown to black resins.

The phenols that have been used in the commercial production of phenolic resins are either substituted or unsubstituted. Phenol and resorcinol are the widely used unsubstituted ones. Substituted phenols include: ortho-cresol, meta-cresol, para-cresol, para-phenylphenol, para-tert-butylphenol, para-tert-amylphenol, para-tert-octylphenol,

para-nonylphenol, and 4,4'-(propane-2, 2-diyl) diphenol (bisphenol A). The structures of those aldehydes and phenols are given in Scheme 1.[4]

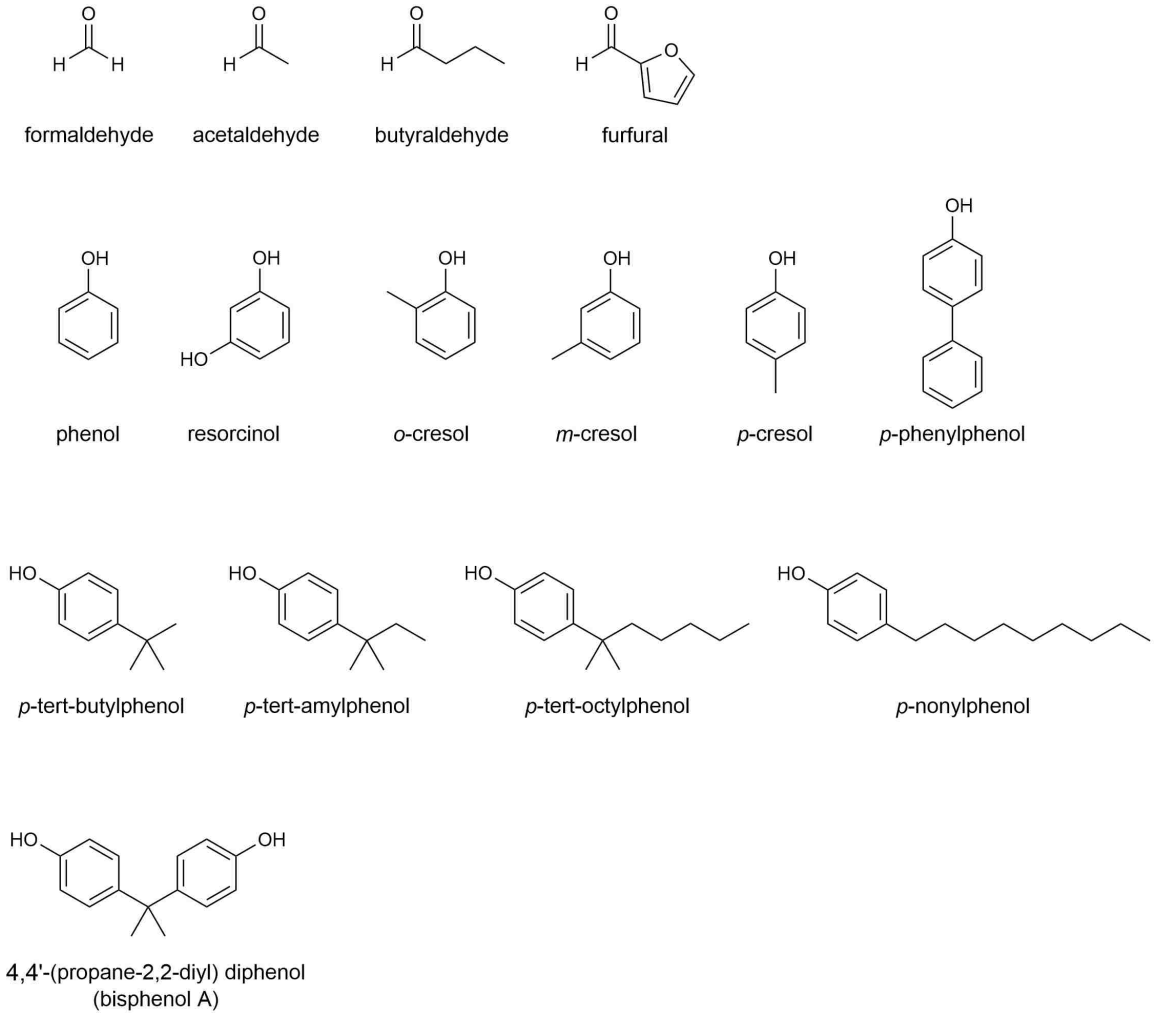

Scheme 1. Structures of aldehydes and phenols that are normally used in the commercial production of phenolic resins.

In phenolic resins, depending on the presence of either methylene ether ($–CH_2OCH_2–$) or methylene ($–CH_2–$) bridges between aromatic rings they are classified as “resol” and “novolac”, respectively. In resols, the polymerization is based-catalyzed,

whereas in novolac the polymerization is carried out in acidic media. As an example, phenol reacts with formaldehyde in basic/acidic conditions to form resol/novolac types of phenol-formaldehyde (PF) resins. If the excess of F is used the resulting PF polymer is a resol, and if the excess of P is used, it will produce a novolac PF.[5]

A detailed spectroscopic study of PF polymerization reveals that the structure of resol differs from novolac in that it consists of both methylene ether and methylene in contrast to the only methylene bridges in novolac. Scheme 2 shows those structures in the case of PF resins.[4,6,7]

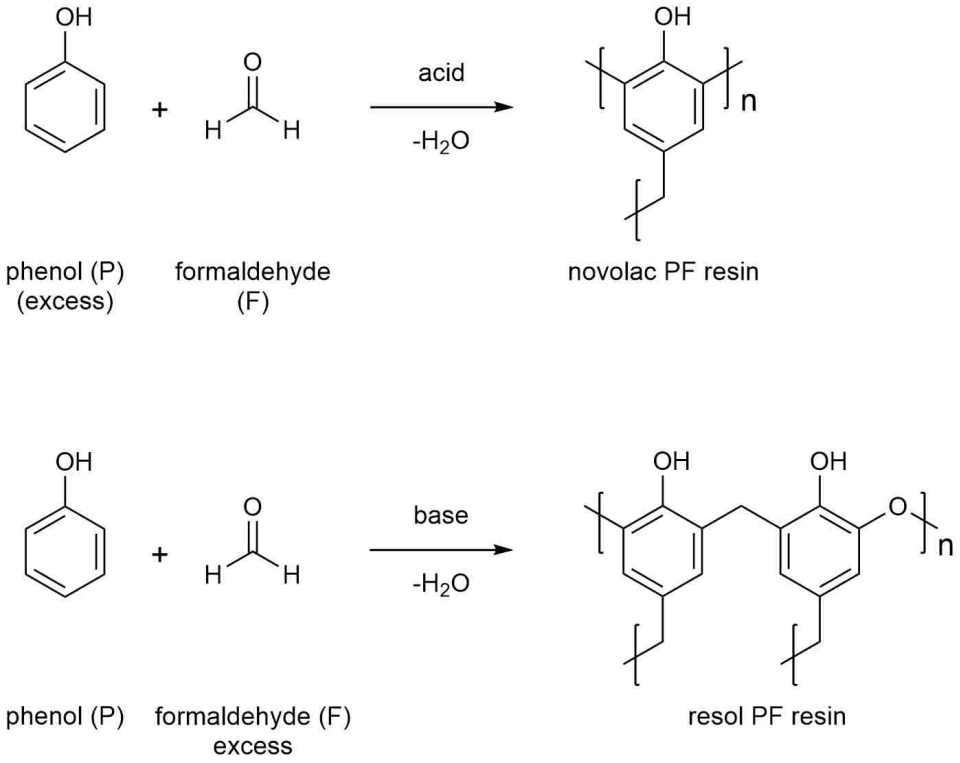

Scheme 2. Chemical structures of novolac and resol PF resins. Resol resins contain dimethylene ether in addition to methylene bridges.

REFERENCES

1. Gardziella, A.; Pilato, L. A.; Knop, A. *Phenolic Resins*, 2nd ed.; Springer: Berlin, 2000.

2. Nair, C. P. R. Advances in Addition-Cure Phenolic Resins. *Prog. Polym. Sci.* **2004**, *29*, 401–498.

3. Ottenbourgs, B.; Adriaensens, P.; Carleer, R.; Vanderzande, D.; Gelan, J. Quantitative Carbon-13 Solid-State N.M.R. and FT–Raman Spectroscopy in Novolac Resins. *Polymer* **1998**, *39*, 5293–5300.

4. Fry, J. S.; Merriam, C. N.; Boyd, W. H. Chemistry and Technology of Phenolic Resins and Coatings. In *Applied Polymer Science*; ACS Symposium Series, 2nd ed.; American Chemical Society: Washington, DC, 1985; Vol. 285; pp 1141–1158.

5. Lu, K. -T.; Luo, K. -M.; Lin, S. -H.; Su, S. -H.; Hu, K. -H. The Acid-Catalyzed Phenol-Formaldehyde Reaction: Critical Runaway Conditions and Stability Criterion. *Process Saf. Environ. Prot.* **2004**, *82*, 37–47.

6. Rego, R.; Adriaensens, P. J.; Carleer, R. A.; Gelan, J. M. Fully Quantitative Carbon-13 NMR Characterization of Resol Phenol-Formaldehyde Prepolymer Resins. *Polymer* **2004**, *45*, 33–38.

7. Zhang, X.; Looney, M. G.; Solomon, D. H.; Whittaker, A. K. The Chemistry of Novolac Resins: 3. ^{13}C and ^{15}N N.M.R. Studies of Curing with Hexamethylenetetramine. *Polymer* **1997**, *38*, 5835–5848.

APPENDIX B.

C 1s XPS DATA

The C 1s x-ray photoelectron spectroscopy (XPS) data of all materials studied in this dissertation are shown in Figure 1. The peaks were internally calibrated with respect to the Au ($4f_{7/2}$) peak at 84.0 eV, which was mixed in 5% with the sample powder before the experiment. The peak assignments were performed by using three compounds as external references: 1-naphthol, 2,6-diisopropyl-4-phenylpyrylium, and sodium phenoxide and also literature. The peaks observed at binding energies of 284.16, 285.02, 285.46, 285.74, 286.36, and 287.12 were assigned to aromatic carbon (C=C), pyrylium carbon ($C=O^+$), aliphatic carbon (C–C), carbon bonded to hydroxyl group (C–OH), phenoxide carbon ($C–O^-$), and carbonyl (C=O) respectively. Table 1 summarizes the average binding energies corresponding to those peaks from all samples.

It is interesting to note that the XPS spectra of all C- and EC- samples are identical to one another, showing graphitic carbon peak at 284 eV, pyrylium carbon ($C=O^+$) at 285 eV, phenoxide carbon ($C–O^-$) at 286 eV, and π–π satellite peak at ~ 290 eV, the latter of which is due to the presence of highly conjugated systems after carbonization and etching.

Table1. Average binding energies (eV) from C 1s XPS spectra corresponding to different types of carbon

carbon species	binding energy (eV)
C=C	284.16 ± 0.60
$C=O^+$	285.02 ± 0.47
C–C	285.46 ± 0.85
C–OH	285.74 ± 1.39
$C–O^-$	286.36 ± 0.96
C=O	287.12 ± 0.03

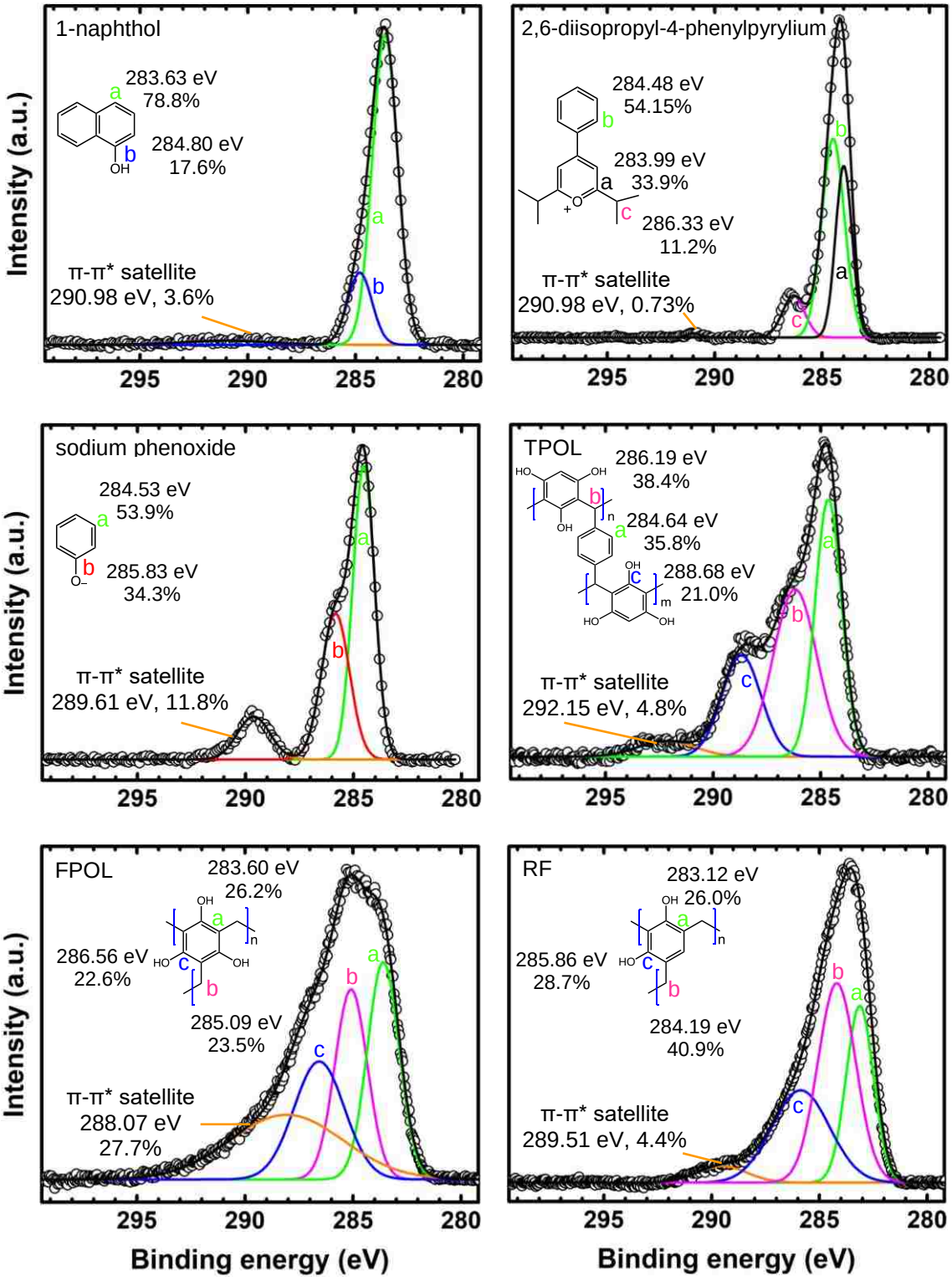

Figure 1. C 1s XPS spectra of the indicated samples.

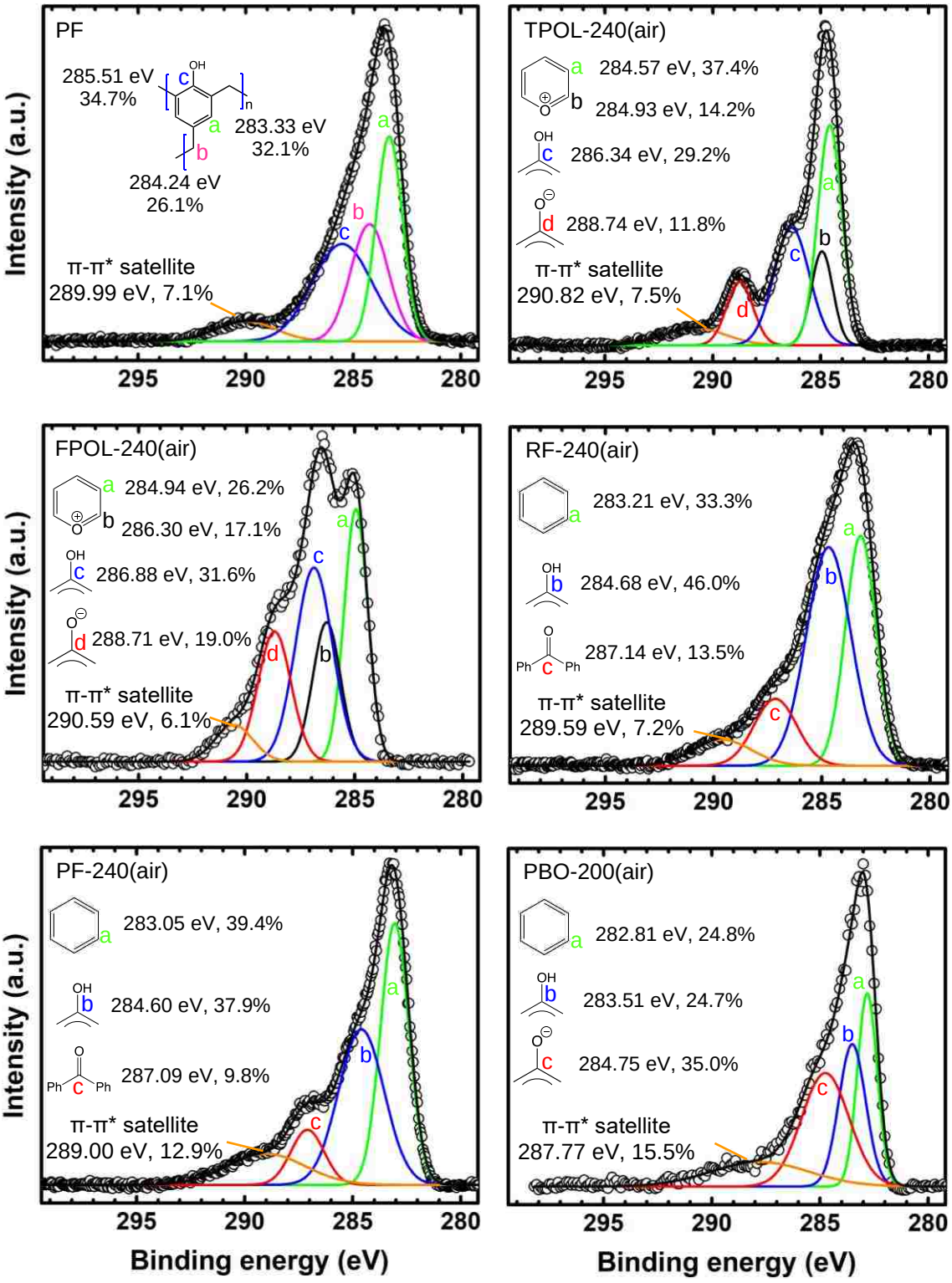

Figure 1. C 1s XPS spectra of the indicated samples. (Cont.)

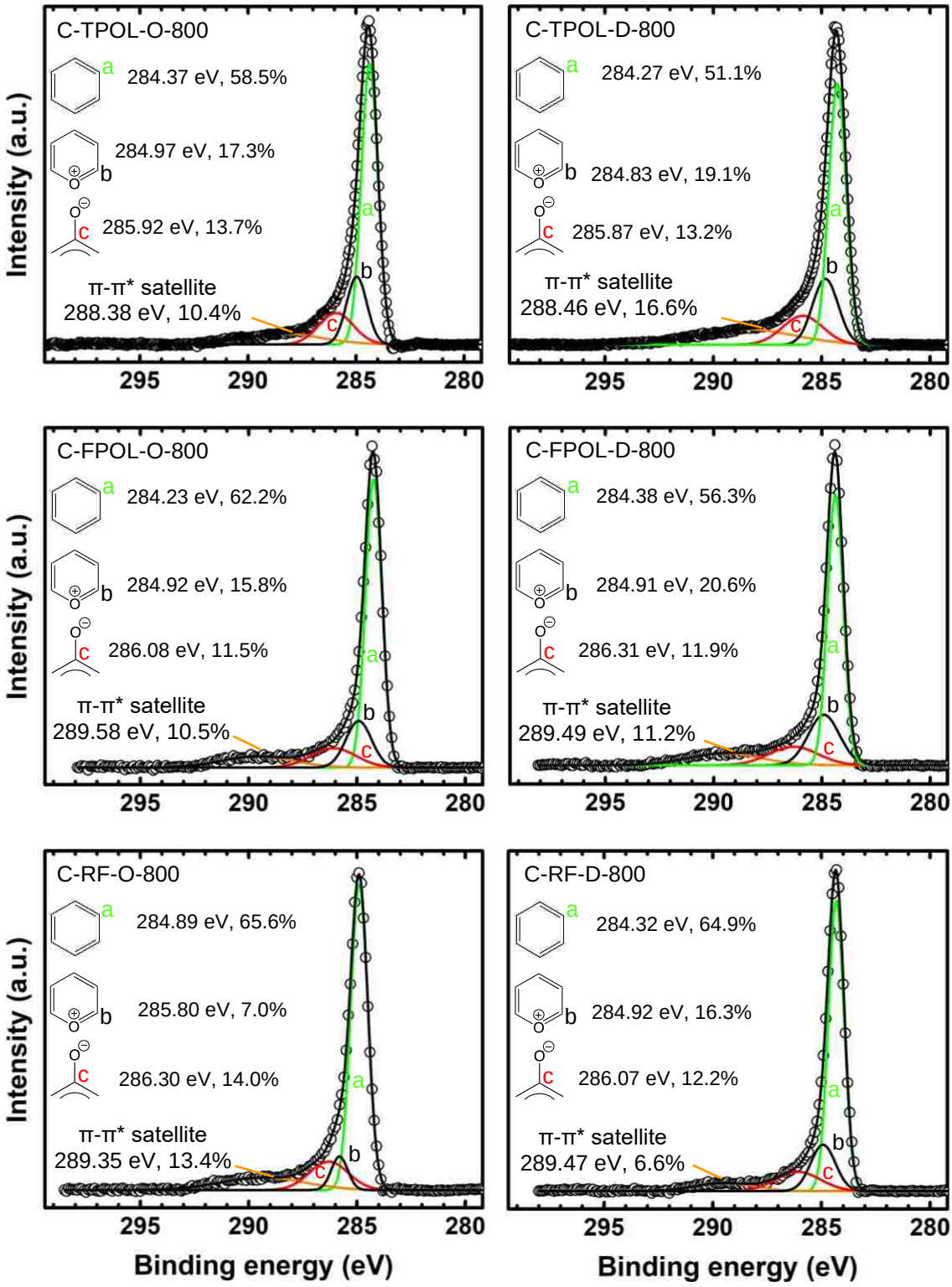

Figure 1. C 1s XPS spectra of the indicated samples. (Cont.)

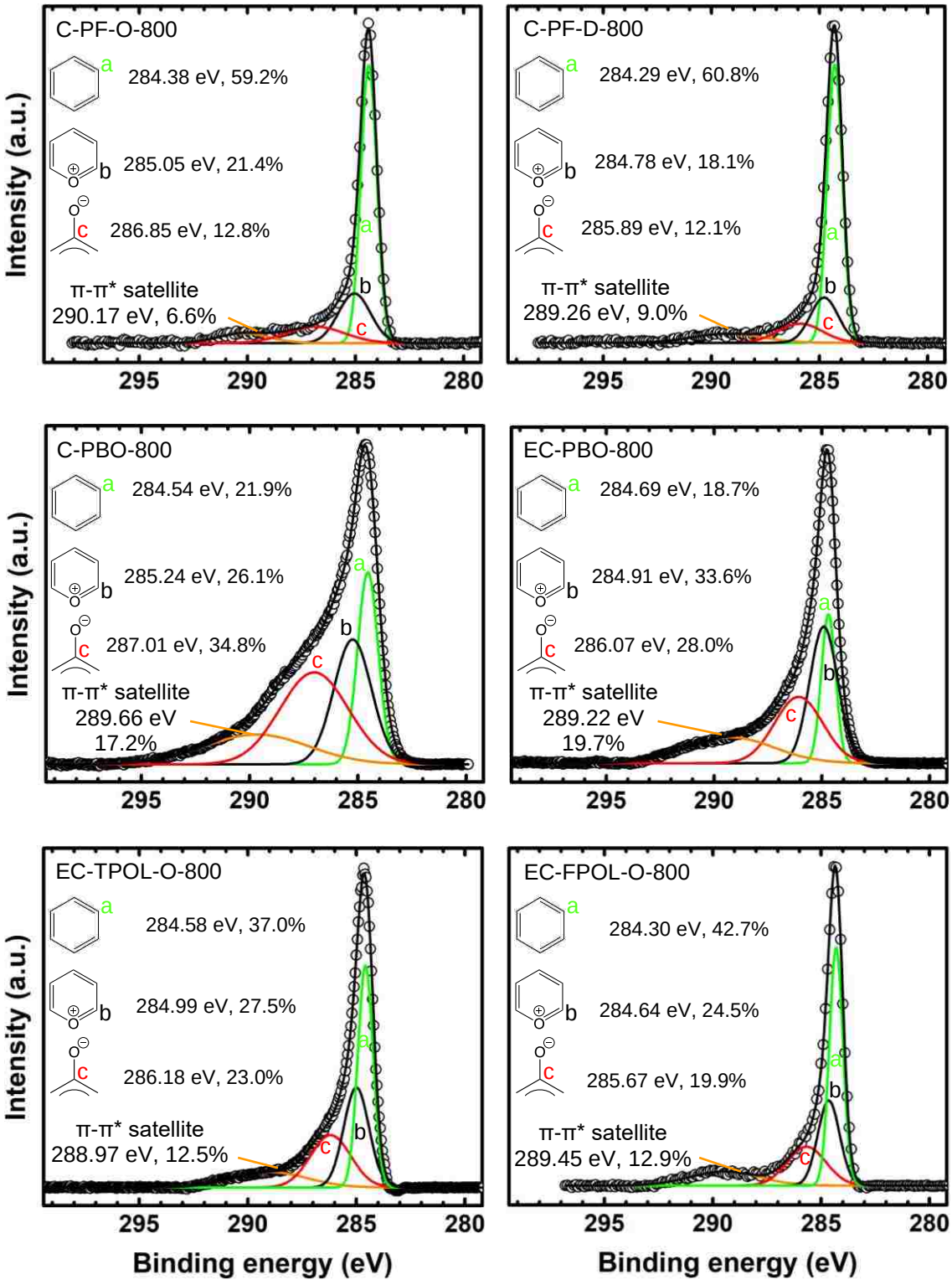

Figure 1. C 1s XPS spectra of the indicated samples. (Cont.)

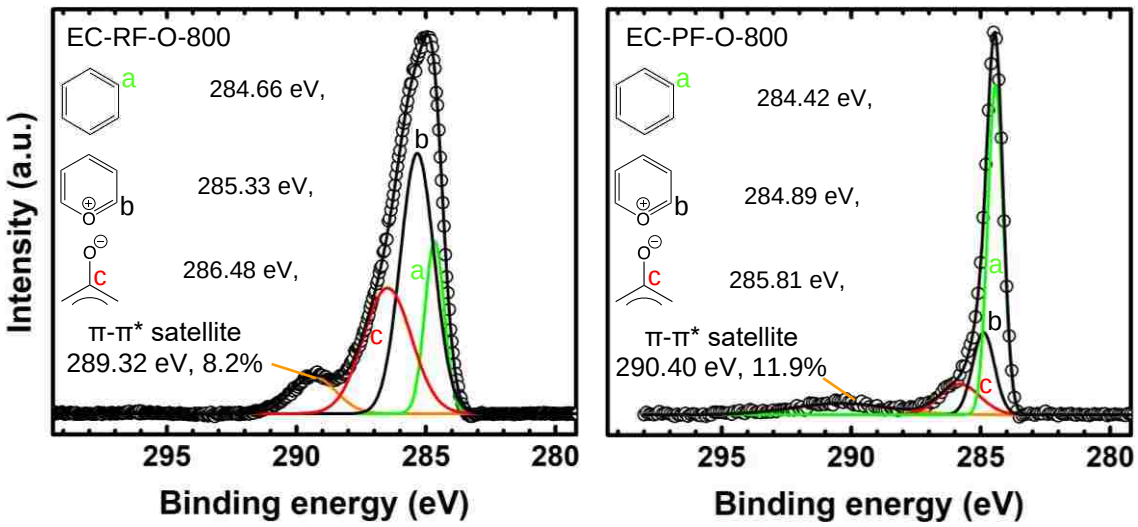

Figure 1. C 1s XPS spectra of the indicated samples. (Cont.)

REFERENCES

1. Yun, J.; Chen, L.; Zhang, X.; Feng, J.; Liu, L. The Effect of Introducing B and N on Pyrolysis Process of High Ortho Novolac Resin. *Polymers* **2016**, *8*, 35.

2. Lawrinenko, M.; Laird, D. A. Anion Exchange Capacity of Biochar. *Green Chem.* **2015**, *17*, 4628–4636.

3. Wang, P.; Liu, Z.-G.; Chen, X.; Meng, F.-L.; Liu, J.-H.; Huang, X.-J. UV Irradiation Synthesis of an Au-Graphene Nanocomposite with Enhanced Electrochemical Sensing Properties. *J. Mater. Chem. A* **2013**, *1*, 9189–9195.

4. Ganguly, A.; Sharma, S.; Papakonstantinou, P.; Hamilton, J. Probing the Thermal Deoxygenation of Graphene Oxide Using High-Resolution In Situ X-Ray-Based Spectroscopies. *J. Phys. Chem. C* **2011**, *115*, 17009–17019.

5. Haubner, K.; Murawski, J.; Olk, P.; Eng, L. M.; Ziegler, C.; Adolphi, B.; Jaehne, E. The Route to Functional Graphene Oxide. *ChemPhysChem* **2010**, *11*, 2131–2139.

6. Georgiou, P.; Walton, J.; Simitzis, J. Surface Modification of Pyrolyzed Carbon Fibres by Cyclic Voltammetry and Their Characterization with XPS and Dye Adsorption. *Electrochim. Acta* **2010**, *55*, 1207–1216.

7. Hueso, J. L.; Espinós, J. P.; Caballero, A.; Cotrino, J.; González-Elipe, A. R. XPS Investigation of the Reaction of Carbon with NO, O_2, N_2 and H_2O Plasmas. *Carbon* **2007**, *45*, 89–96.

8. Desimoni, E.; Casella, G. I.; Morone, A.; Salvi, A. M. XPS Determination of Oxygen-Containing Functional Groups on Carbon-Fibre Surfaces and the Cleaning of These Surfaces. *Surf. Interface Anal.* **1990**, *15*, 627–634.

APPENDIX C.

THE ANALYSIS OF VIRIAL FITTINGS APPLIED TO THE CO_2 ADSORPTION ISOTHERMS

For the calculation of the isosteric heats of adsorption, the adsorption isotherms at 273 K and 298 K were fit using the virial equation

$$\ln P = \ln N + \frac{1}{T}\sum_{i=0}^{m} a_i N^i + \sum_{i=0}^{n} b_i N^i \quad (1)$$

with N being the CO_2 uptake in mmol g^{-1}, T the temperature (273 or 298 K in this case) and a and b the polynomial approximations (parameters). The virial equation is based on two assumptions, namely

$$\left[\frac{\partial \ln P}{\partial \left(\frac{1}{T}\right)}\right]_N = \mathrm{g}\,(N) \quad (2)$$

and

$$\left[\frac{\partial g\,(N)}{\partial\,(T)}\right]_N = 0 \quad (3)$$

The adsorption isosteres are linear and g (*N*) is a polynomial function that is independent of temperature and depends only on the uptake.

The values of *m* and *n* were varied until the best statistical coefficients, i.e., highest R^2 and lowest reduced χ^2, were obtained. A systematic analysis of the different number of parameters was done, from *m* = 5, *n* = 5 to *m* = 1, *n* = 0 for C-RF-D, EC-RF-D, C-RF-O, and EC-RF-O samples. The R^2 and reduced χ^2 for all the different virial fits are listed in Tables 1–4.

Table 1. Coefficients of determination (R^2), reduced χ^2, and Q_0 for calculating the isosteric heats of adsorption using Equation (1) for C-RF-O

m	n	R^2	red. χ^2	Q_0 (kJ mol^{-1})
5	5	1.00000	2.00×10^{-7}	32.60
5	4	1.00000	5.04×10^{-7}	32.67
5	3	1.00000	7.34×10^{-7}	32.59
5	2	0.99996	1.64×10^{-5}	33.29
5	1	0.99993	3.10×10^{-5}	32.57
5	0	0.99861	5.83×10^{-4}	36.09
4	5	1.00000	4.77×10^{-7}	32.67
4	4	1.00000	1.84×10^{-6}	32.55
4	3	1.00000	1.91×10^{-6}	32.60
4	2	0.99996	1.79×10^{-5}	33.32
4	1	0.99992	3.52×10^{-5}	32.52
4	0	0.99855	6.10×10^{-4}	36.11
3	5	1.00000	8.30×10^{-7}	32.57
3	4	1.00000	1.86×10^{-6}	32.59
3	3	0.99997	1.21×10^{-5}	32.34
3	2	0.99984	6.86×10^{-5}	33.59
3	1	0.99970	9.78×10^{-5}	32.56
3	0	0.99850	6.30×10^{-4}	36.05
2	5	0.99997	1.24×10^{-5}	33.16
2	4	0.99997	1.35×10^{-5}	33.19
2	3	0.99985	6.20×10^{-5}	33.53
2	2	0.99939	2.56×10^{-4}	32.60
2	1	0.99939	2.57×10^{-4}	33.00
2	0	0.99845	6.51×10^{-4}	35.98
1	5	0.99990	4.15×10^{-5}	32.14
1	4	0.99989	4.61×10^{-5}	32.11
1	3	0.99973	1.13×10^{-4}	32.19
1	2	0.99940	2.52×10^{-4}	32.73
1	1	0.99554	0.00188	30.61
1	0	0.99114	0.00373	36.61

Table 2. Coefficients of determination (R^2), reduced χ^2, and Q_0 for calculating the isosteric heats of adsorption using Equation (1) for EC-RF-O

m	n	R^2	red. χ^2	Q_0 (kJ mol^{-1})
5	5	0.99983	4.97×10^{-4}	46.77
5	4	0.99972	8.06×10^{-4}	45.25
5	3	0.99964	0.00104	43.65
5	2	0.99962	0.00108	42.92
5	1	0.99955	0.00128	41.45
5	0	0.99914	0.00245	44.58
4	5	0.99972	8.04×10^{-4}	45.25
4	4	0.99971	8.20×10^{-4}	45.45
4	3	0.99959	0.00118	43.60
4	2	0.99955	0.00130	42.37
4	1	0.99952	0.00136	41.50
4	0	0.99914	0.00247	44.56
3	5	0.99964	0.00102	43.71
3	4	0.99959	0.00117	43.60
3	3	0.99958	0.00120	43.83
3	2	0.99948	0.00148	42.11
3	1	0.99945	0.00156	41.12
3	0	0.99884	0.00330	44.84
2	5	0.99963	0.00105	43.09
2	4	0.99955	0.00128	42.46
2	3	0.99948	0.00147	42.11
2	2	0.99947	0.00152	42.31
2	1	0.99938	0.00176	40.72
2	0	0.99862	0.00395	44.73
1	5	0.99957	0.00123	41.66
1	4	0.99954	0.00133	41.68
1	3	0.99946	0.00154	41.22
1	2	0.99939	0.00176	40.73
1	1	0.99937	0.00180	40.87
1	0	0.99858	0.00407	44.99

Table 3. Coefficients of determination (R^2), reduced χ^2, and Q_0 for calculating the isosteric heats of adsorption using Equation (1) for C-RF-D

m	n	R^2	red. χ^2	Q_o (kJ mol^{-1})
5	5	1.00000	3.42×10^{-7}	20.31
5	4	1.00000	9.30×10^{-7}	20.44
5	3	1.00000	9.69×10^{-7}	20.40
5	2	0.99997	1.01×10^{-5}	20.93
5	1	0.99983	5.09×10^{-5}	19.77
5	0	0.99881	5.68×10^{-5}	20.13
4	5	1.00000	9.26×10^{-7}	20.44
4	4	1.00000	9.15×10^{-7}	20.44
4	3	1.00000	9.52×10^{-7}	20.40
4	2	0.99997	9.91×10^{-6}	20.93
4	1	0.99984	5.00×10^{-5}	19.77
4	0	0.99982	5.59×10^{-5}	20.13
3	5	1.00000	1.00×10^{-6}	20.39
3	4	1.00000	9.86×10^{-7}	20.39
3	3	0.99999	3.09×10^{-6}	20.38
3	2	0.99996	1.22×10^{-5}	20.92
3	1	0.99983	5.13×10^{-5}	19.76
3	0	0.99981	5.70×10^{-5}	20.12
2	5	0.99998	7.26×10^{-6}	20.83
2	4	0.99998	7.16×10^{-6}	20.83
2	3	0.99997	9.42×10^{-6}	20.83
2	2	0.99954	1.41×10^{-4}	20.82
2	1	0.99942	1.77×10^{-4}	19.67
2	0	0.99941	1.81×10^{-4}	20.03
1	5	0.99977	6.91×10^{-5}	19.40
1	4	0.99978	6.79×10^{-5}	19.40
1	3	0.99977	6.88×10^{-5}	19.41
1	2	0.99935	1.97×10^{-4}	19.40
1	1	0.99594	0.00123	19.31
1	0	0.99598	0.00122	19.73

Table 4. Coefficients of determination (R^2), reduced χ^2, and Q_0 for calculating the isosteric heats of adsorption using Equation (1) for EC-RF-D

m	n	R^2	red. χ^2	Q_o (kJ mol^{-1})
5	5	0.99995	1.39×10^{-4}	34.74
5	4	0.99993	1.89×10^{-4}	34.07
5	3	0.99993	1.87×10^{-4}	33.92
5	2	0.99993	1.92×10^{-4}	34.23
5	1	0.99990	2.75×10^{-4}	35.22
5	0	0.99788	0.00609	42.22
4	5	0.99994	1.87×10^{-4}	34.08
4	4	0.99992	2.24×10^{-4}	34.21
4	3	0.99991	2.48×10^{-4}	33.65
4	2	0.99991	2.65×10^{-4}	34.14
4	1	0.99987	3.73×10^{-4}	35.28
4	0	0.99792	0.00599	42.21
3	5	0.99994	1.84×10^{-4}	33.99
3	4	0.99991	2.46×10^{-4}	33.67
3	3	0.99990	2.94×10^{-4}	33.75
3	2	0.99990	2.91×10^{-4}	33.92
3	1	0.99984	4.66×10^{-4}	35.28
3	0	0.99791	0.00601	42.22
2	5	0.99994	1.63×10^{-4}	34.45
2	4	0.99990	2.92×10^{-4}	34.90
2	3	0.99985	4.41×10^{-4}	35.65
2	2	0.99951	0.00140	38.18
2	1	0.99984	4.58×10^{-4}	35.29
2	0	0.99753	0.00711	42.51
1	5	0.99991	2.65×10^{-4}	35.26
1	4	0.99987	3.65×10^{-4}	35.28
1	3	0.99984	4.59×10^{-4}	35.24
1	2	0.99984	4.52×10^{-4}	35.26
1	1	0.99983	5.00×10^{-4}	35.27
1	0	0.99739	0.00751	42.84

After fitting the Equation (1) to the absolute uptakes, the parameters a's and b's obtained were used to calculate the isosteric heats of adsorption using Equation (4)

$$Q_{st} = -R \sum_{i=0}^{m} a_i N^i \quad (4)$$

as a function of the CO_2 uptake (mmol g^{-1}) where R is the universal gas constant of 8.314 J mol^{-1} K^{-1}. The first term in Equation 4 corresponding to $i = 0$ is given by Equation 5

$$Q_0 = -R\, a_0 \quad (5)$$

Q_0 is the heat of adsorption at zero coverage.

Figures 1–4 show the plots of Q_{st} vs CO_2 uptakes for C-RF-O, EC-RF-O, C-RF-D, and EC-RF-D samples respectively. As can be seen, the Q_{st} plots of C-RF-O and C-RF-D samples are rather insensitive to m and n. On the other hand, the Q_{st} plots of the high-CO_2 uptake samples (EC-RF-O and EC-RF-D) show an extreme sensitivity, diverging after about 6 mmol g^{-1}, reaching very high values (positive or negative). Nevertheless, all those curves start from the same Q_0 value (except for the non-realistic case of $n = 0$) and coincide to about 4–5 mmol g^{-1}. This means that the isosteres are less linear at the higher uptakes, which means that some of the assumptions in the virial equation might not be appropriate at high adsorption ranges.

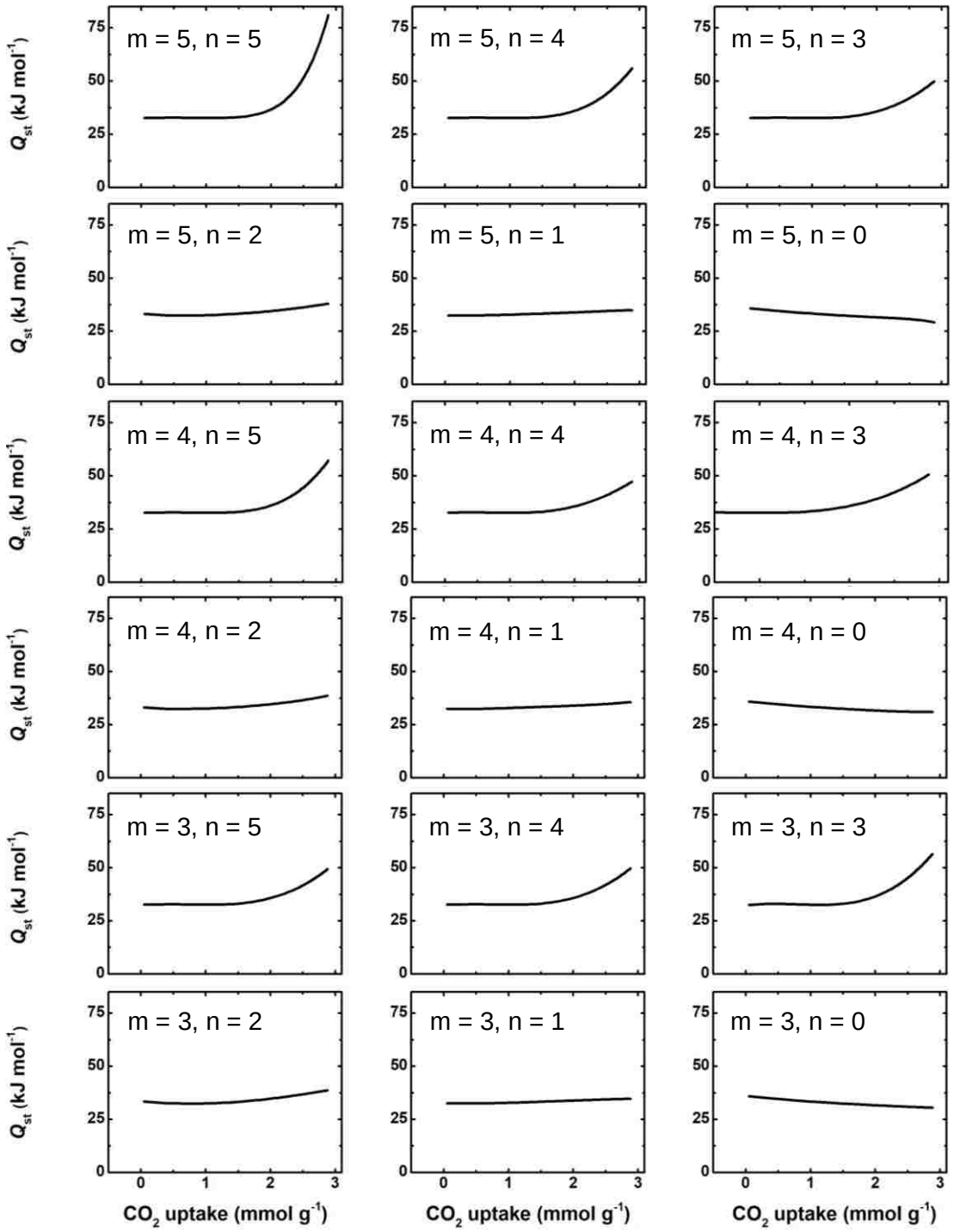

Figure 1. The isosteric heats of adsorption calculated using Equation (4) for different values of *m* and *n* as indicated for C-RF-O.

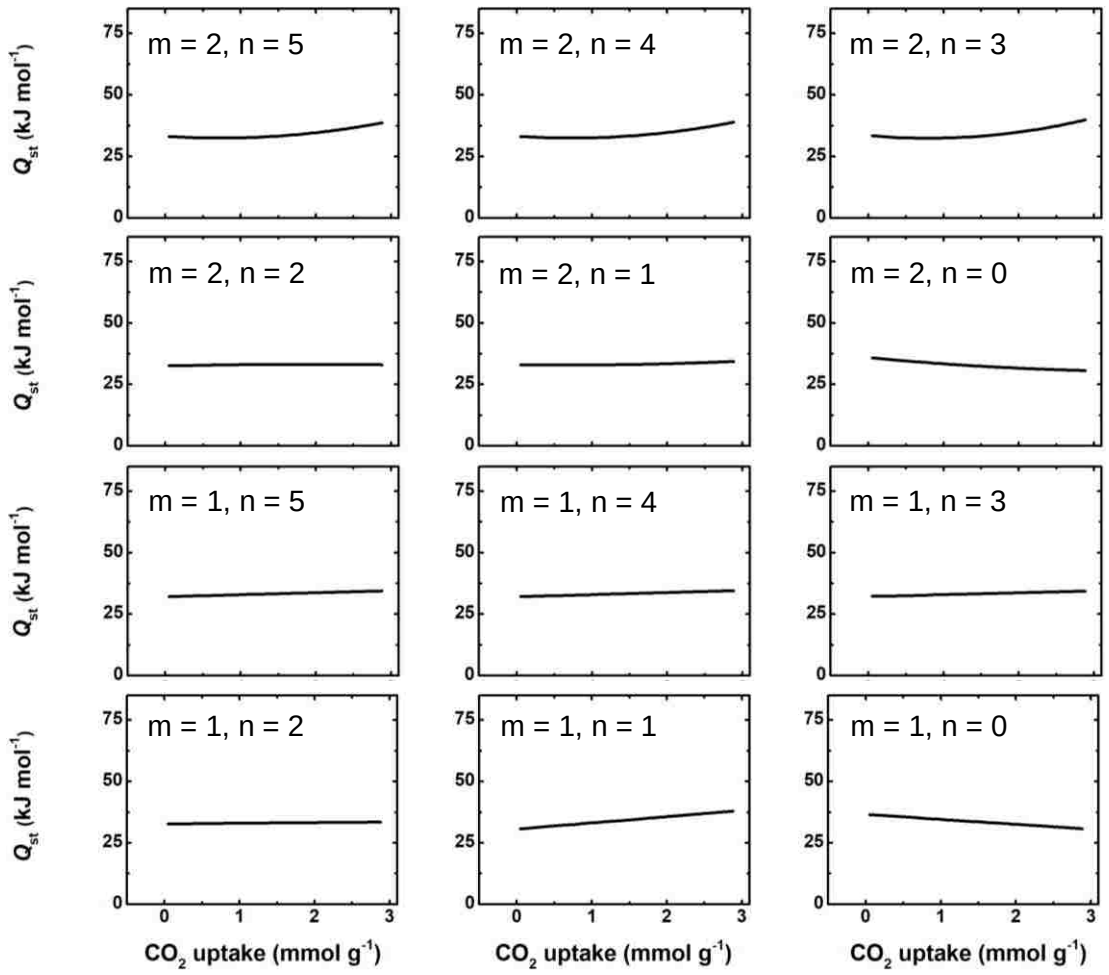

Figure 1. The isosteric heats of adsorption calculated using Equation (4) for different values of *m* and *n* as indicated for C-RF-O. (Cont.)

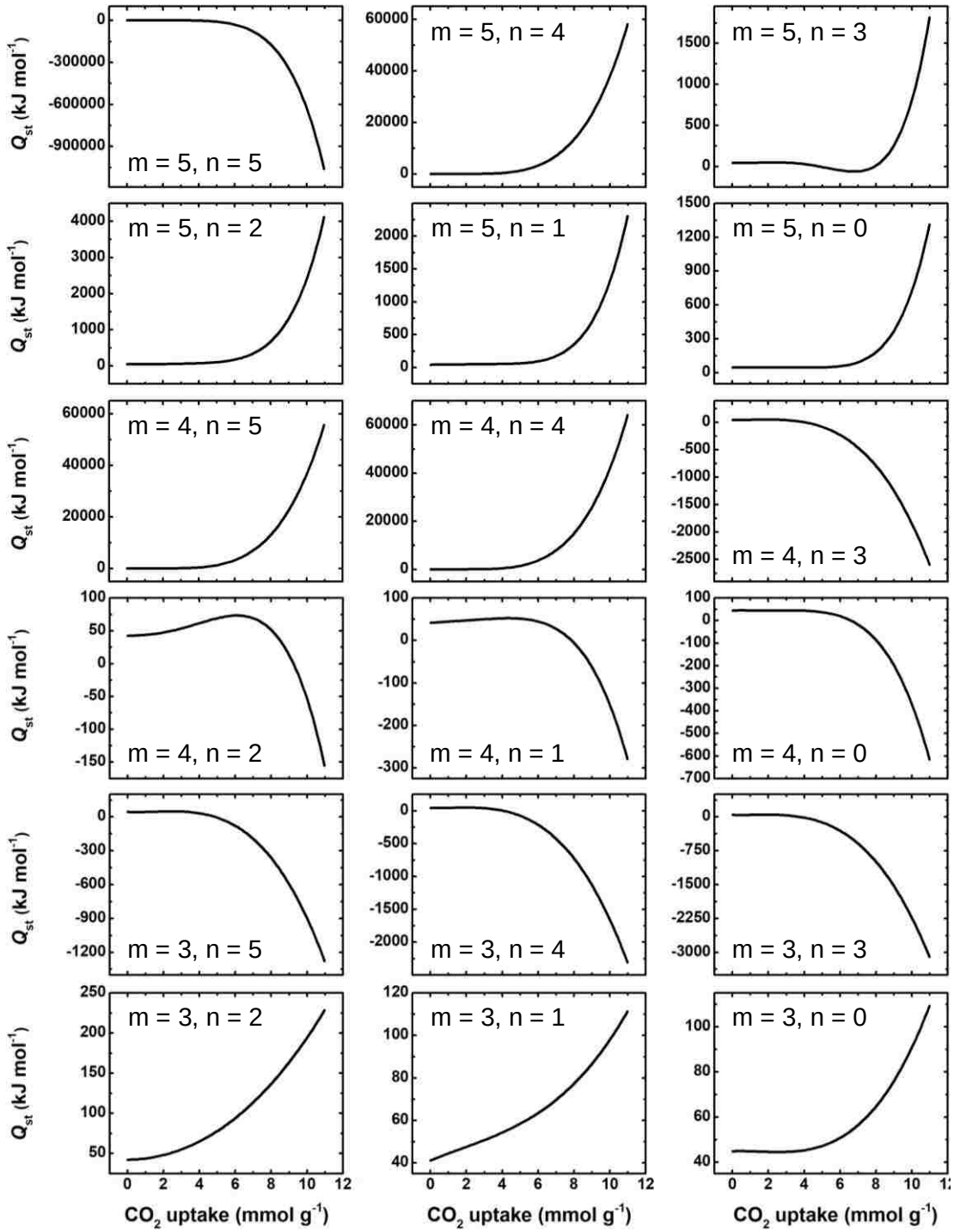

Figure 2. The isosteric heats of adsorption calculated using Equation (4) for different values of *m* and *n* as indicated for EC-RF-O.

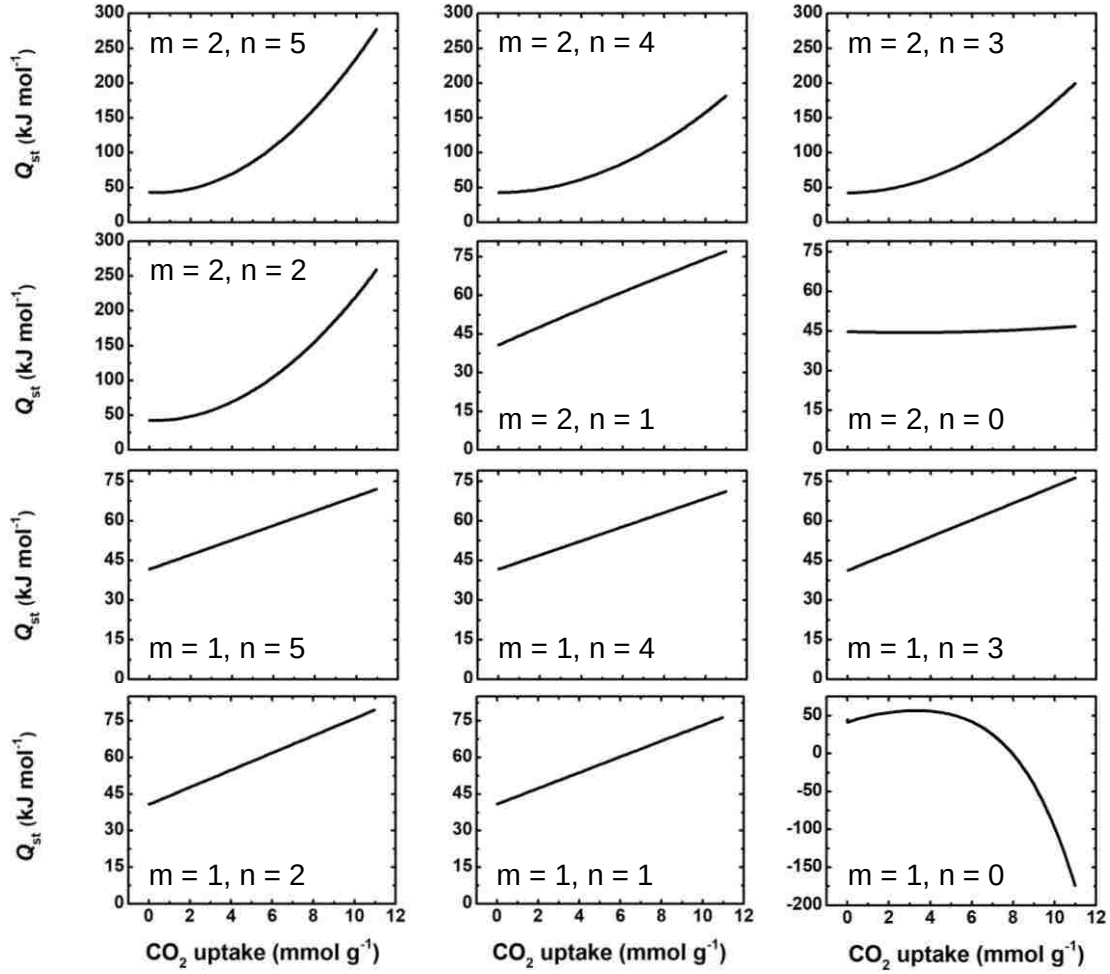

Figure 2. The isosteric heats of adsorption calculated using Equation (4) for different values of *m* and *n* as indicated for EC-RF-O. (Cont.)

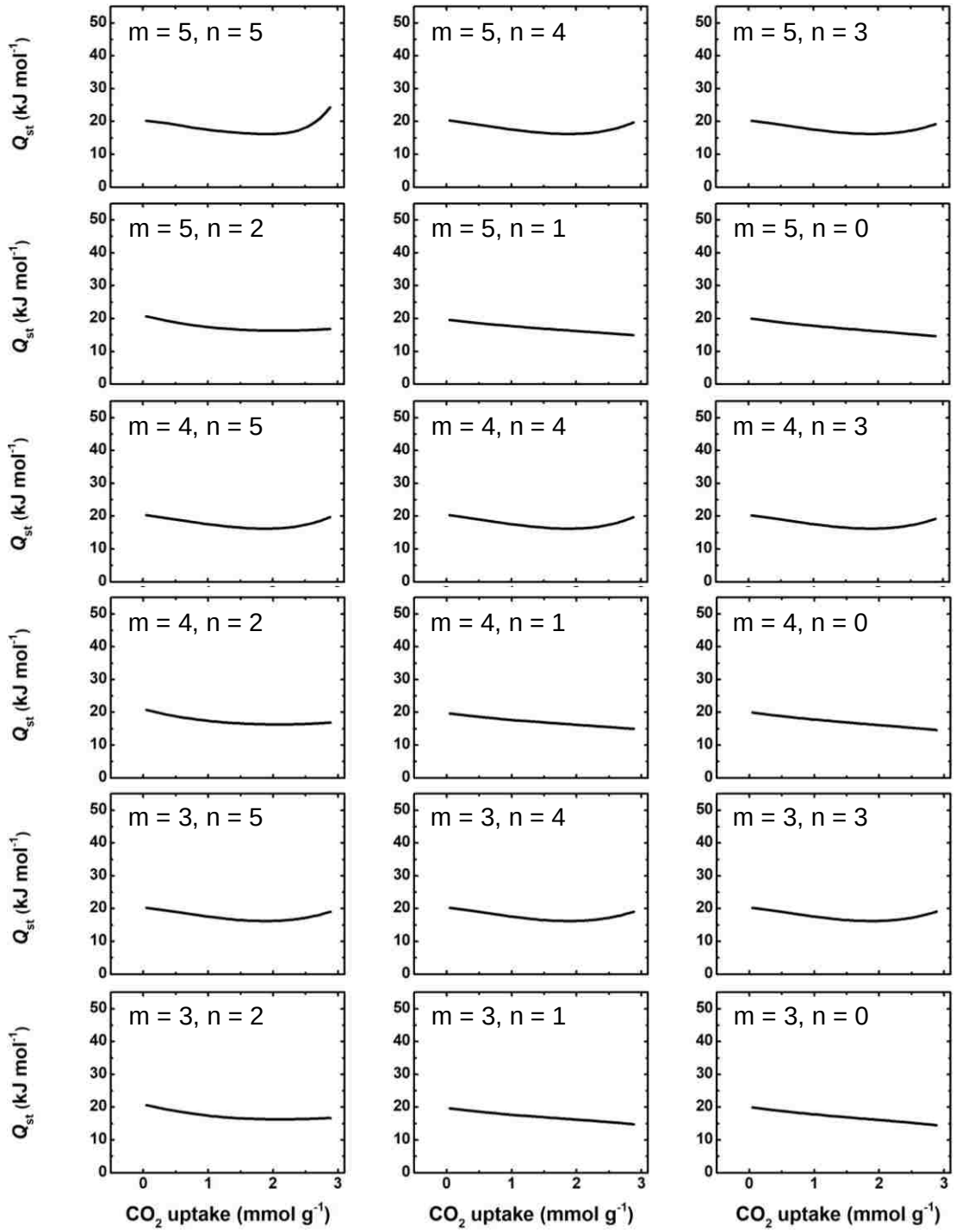

Figure 3. The isosteric heats of adsorption calculated using Equation (4) for different values of *m* and *n* as indicated for C-RF-D.

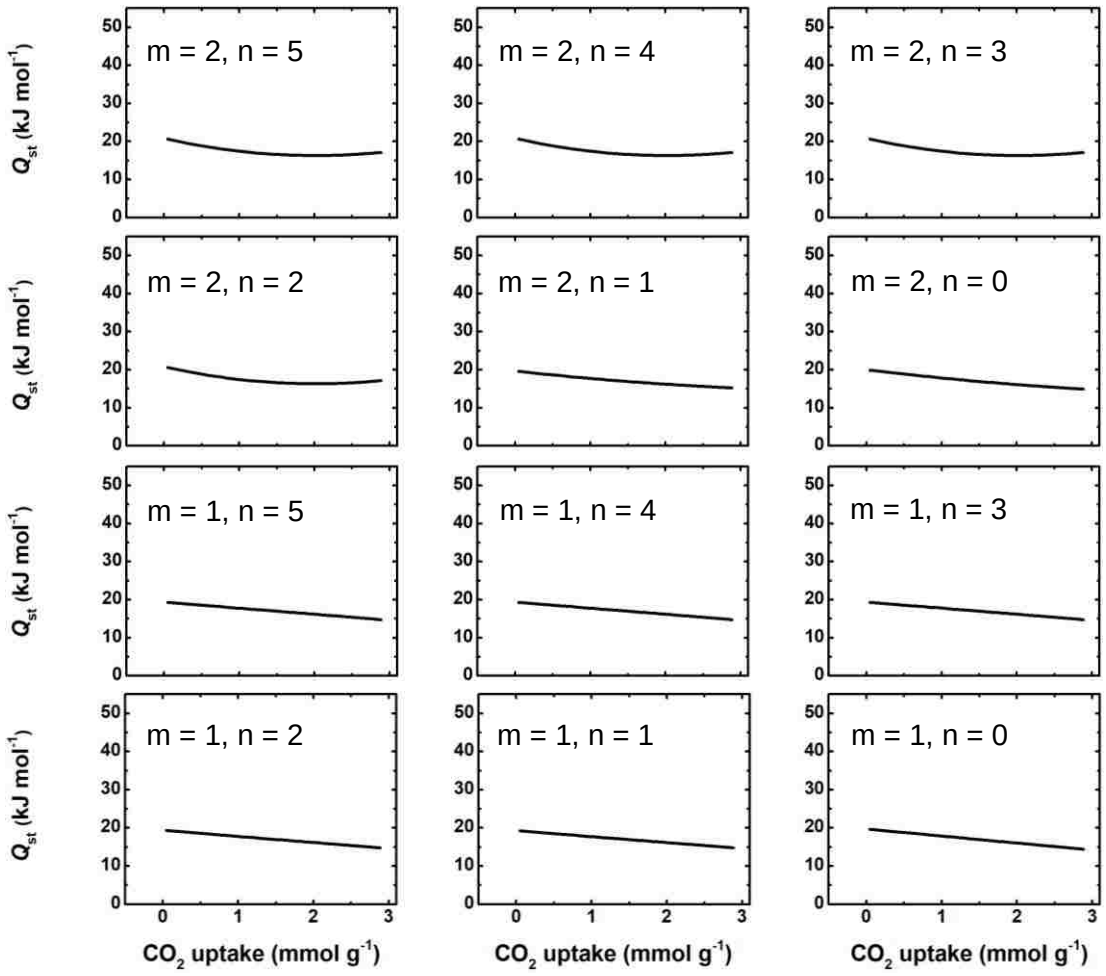

Figure 3. The isosteric heats of adsorption calculated using Equation (4) for different values of *m* and *n* as indicated for C-RF-D. (Cont.)

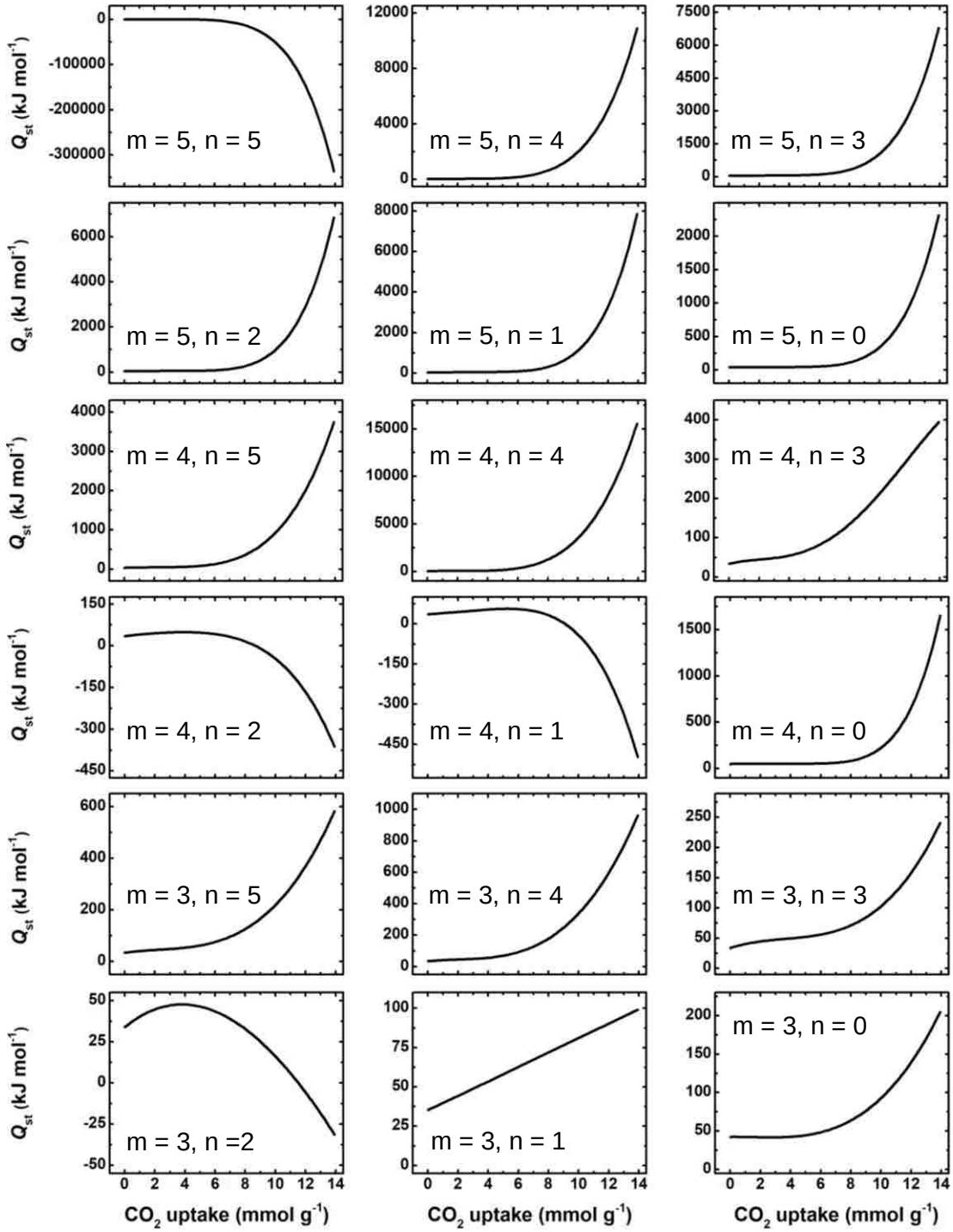

Figure 4. The isosteric heats of adsorption calculated using Equation (4) for different values of *m* and *n* as indicated for EC-RF-D.

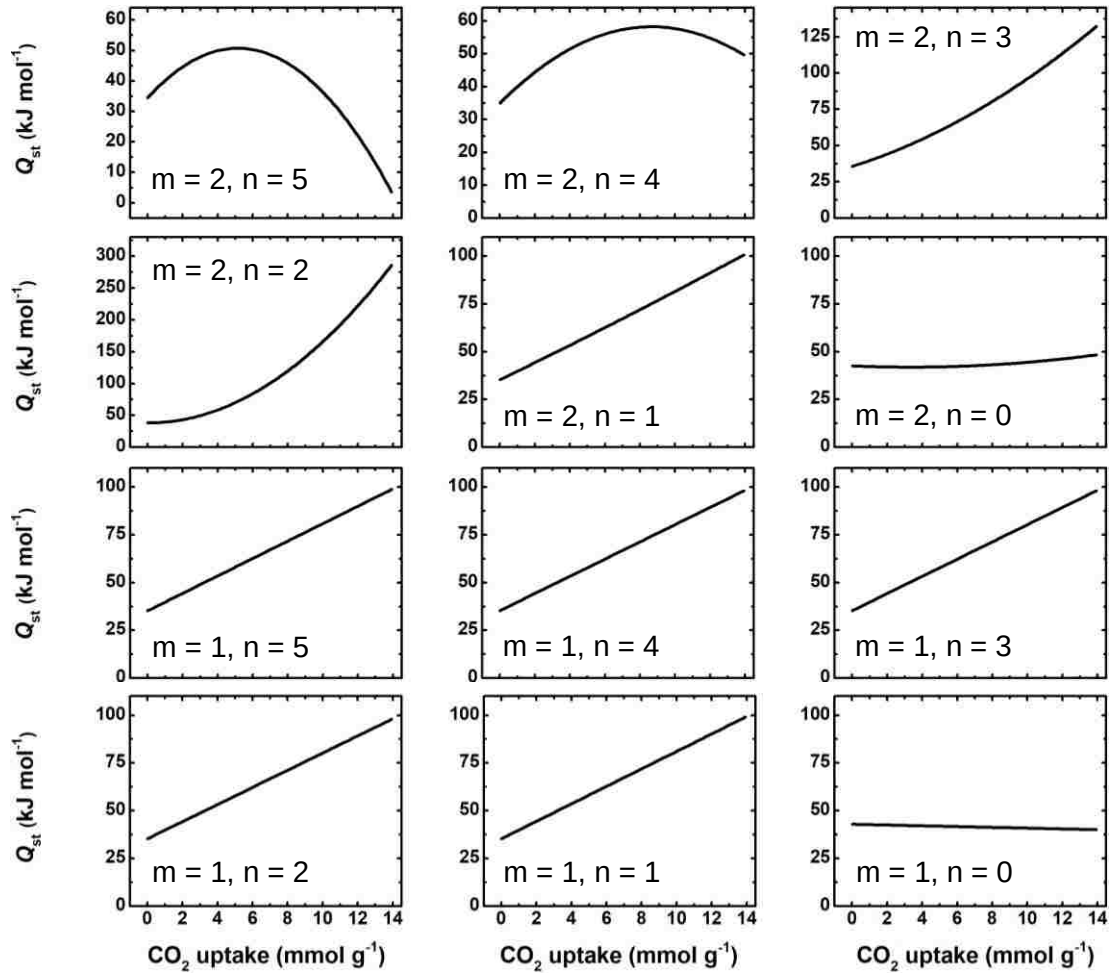

Figure 4. The isosteric heats of adsorption calculated using Equation (4) for different values of *m* and *n* as indicated for EC-RF-D. (Cont.)

BIBLIOGRAPHY

1. Vareda, J. P.; Lamy-Mendes, A.; Durães, L. A Reconsideration on the Definition of the Term Aerogel Based on Current Drying Trends. *Microporous Mesoporous Mater*. **2018**, *258*, 211–216.

2. Rechberger, F.; Niederberger, M. Synthesis of Aerogels: from Molecular Routes to 3-Dimensional Nanoparticle Assembly. *Nanoscale Horizons* **2017**, *2*, 6–30.

3. Fricke, J.; Emmerling, A. Aerogels-Recent Progress in Production Techniques and Novel Applications. *J. Sol-Gel Sci. Technol*. **1998**, *13*, 299–303.

4. Gesser, H. D.; Goswami, P. C. Aerogels and Related Porous Materials. *Chem. Rev*. **1989**, *89*, 765–788.

5. Hüsing, N.; Schubert, U. Aerogels-Airy Materials: Chemistry, Structure, and Properties. *Angew. Chem. Int. Ed*. **1998**, *37*, 22–45.

6. Fricke, J.; Emmerling, A. Aerogels. *J. Am. Ceram. Soc*. **1992**, *75*, 2027–2035.

7. Leventis, N.; Donthula, S.; Mandal, C.; Ding, M. S.; Sotiriou-Leventis, C. Explosive versus Thermite Behavior in Iron(0) Aerogels Infiltrated with Perchlorates. *Chem. Mater*. **2015**, *27*, 8126–8137.

8. Mahadik-Khanolkar, S.; Donthula, S.; Bang, A.; Wisner, C.; Sotiriou-Leventis, C.; Leventis, N. Polybenzoxazine Aerogels. 2. Interpenetrating Networks with Iron Oxide and the Carbothermal Synthesis of Highly Porous Monolithic Pure Iron(0) Aerogels as Energetic Materials. *Chem. Mater*. **2014**, *26*, 1318–1331.

9. Hrubesh, L. W. Aerogel Applications. *J. Non-Cryst. Solids* **1998**, *225*, 335–342.

10. Fesmire, J. E. Aerogel Insulation Systems for Space Launch Applications. *Cryogenics* **2006**, *46*, 111–117.

11. Fricke, J. Aerogels and Their Applications. *J. Non-Cryst. Solids* **1992**, *147–148*, 356–362.

12. Schmidt, M.; Schwertfeger, F. Applications for Silica Aerogel Products. *J. Non-Cryst. Solids* **1998**, *225*, 364–368.

13. Fricke, J.; Tillotson, T. Aerogels: Production, Characterization, and Applications. *Thin Solid Films* **1997**, *297*, 212–223.

14. Carlson, G.; Lewis, D.; McKinley, K.; Richardson, J.; Tillotson, T. Aerogel Commercialization: Technology, Markets and Costs. *J. Non-Cryst. Solids* **1995,** *186*, 372–379.

15. Herrmann, G.; Iden, R.; Mielke, M.; Teich, F.; Ziegler, B. On the Way to Commercial Production of Silica Aerogel. *J. Non-Cryst. Solids* **1995**, *186*, 380–387.

16. Brinker, C. J.; Scherer, G. W. *Sol-Gel Science: The Physics and Chemistry of Sol-Gel Processing*, 1st ed.; Academic Press: San Diego, 1990.

17. Pierre, A. C.; Pajonk, G. M. Chemistry of Aerogels and Their Applications. *Chem. Rev.* **2002**, *102*, 4243–4265.

18. Leventis, N. Three-Dimensional Core-Shell Superstructures: Mechanically Strong Aerogels. *Acc. Chem. Res.* **2007**, *40*, 874–884.

19. Capadona, L. A.; Meador, M. A. B.; Alunni,A.; Fabrizio, E. F.; Vassilaras, P.; Leventis, N. Flexible, Low-Density Polymer Crosslinked Silica Aerogels. *Polymer* **2006**, *47*, 5754–5761.

20. Zhang, G.; Dass, A.; Rawashdeh, A.-M. M.; Thomas, J.; Counsil, J. A.; Sotiriou-Leventis, C.; Fabrizio, E. F.; Ilhan, F.; Vassilaras, P.; Scheiman, D. A.; McCorkle, L.; Palczer, A.; Johnston, J. C.; Meador, M. A.; Leventis, N. Isocyanate-Crosslinked Silica Aerogel Monoliths: Preparation and Characterization. *J. Non-Cryst. Solids* **2004**, *350*, 152–164.

21. Leventis, N.; Sotiriou-Leventis, C.; Zhang, G.; Rawashdeh, A.-M. M. Nanoengineering Strong Silica Aerogels. *Nano Lett.* **2002**, *2*, 957–960.

22. (a) Pekala, R. W. Organic Aerogels from the Polycondensation of Resorcinol with Formaldehyde. *J. Mater. Sci.* **1989**, *24*, 3221–3227. (b) Pekala, R. W. Low Density, Resorcinol-Formaldehyde Aerogels. U.S. Patent No. 4,873,218, 1989. (c) Lu, X.; Arduini-Schuster, M. C.; Kuhn, J.; Nilsson, O.; Fricke, J.; Pekala, R. W. Thermal Conductivity of Monolithic Organic Aerogels. *Science* **1992**, *255*, 971–972. (d) Pekala, R. W.; Schaefer, D. W. Structure of Organic Aerogels. 1. Morphology and Scaling. *Macromolecules* **1993**, *26*, 5487–5493. (e) Inorganic and Organic Aerogels. *MRS Bulletin* **1990**, *15*, 30–36.

23. (a) Pekala, R. W.; Alviso, C. T. A New Synthetic Route to Organic Aerogels. *MRS Proc.* **1990**, *180*, 791–795. (b) Ruben, G. C.; Pekala, R. W. High-Resolution Transmission Electron Microscopy of the Nanostructure of Melamine-Formaldehyde Aerogels. *J. Non-Cryst. Solids* **1995**, *186*, 219–231.

24. Mulik, S.; Sotiriou-Leventis, C.; Leventis, N. Time-Efficient Acid-Catalyzed Synthesis of Resorcinol-Formaldehyde Aerogels. *Chem. Mater*. **2007**, *19*, 6138–6144.

25. Mulik, S.; Sotiriou-Leventis, C. Resorcinol-Formaldehyde Aerogels. In *Aerogels Handbook*; Aegerter, M. A., Leventis, N., Koebel, M. M., Eds.; Springer: New York, **2011**, pp 215–234.

26. (a) Yoldas, B. E.; Annen, M. J.; Bostaph, J. Chemical Engineering of Aerogel Morphology Formed under Nonsupercritical Conditions for Thermal Insulation. *Chem. Mater*. **2000**, *12*, 2475–2484. (b) Alviso, C. T.; Pekala, R. W.; Gross, J.; Lu, X.; Caps, R.; Fricke, J. Resorcinol-Formaldehyde and Carbon Aerogel Microspheres. *MRS Proc*. **1996**, *431*, 521–525.

27. (a) Scherdel, C.; Gayer, R.; Slawik, T.; Reichenauer, G.; Scherb, T. Organic and Carbon Xerogels Derived from Sodium Carbonate Controlled Polymerisation of Aqueous Phenol-formaldehyde Solutions. *J. Porous Mater*. **2011**, *18*, 443–450. (b) Shitta-Bey, G. O.; Mirzaeian, M.; Hall, P. J. Effect of Composition, Solvent Exchange Liquid and Drying Method on the Porous Structure of Phenol-Formaldehyde Gels. *J. Sol-Gel Sci. Technol*. **2011**, *57*, 178–184. (c) Scherdel, C.; Gayer, R.; Reichenauer, G. Porous Organic and Carbon Xerogels Derived from Alkaline Aqueous Phenol-Formaldehyde Solutions. *J. Porous Mater*. **2012**, *19*, 351–360. (d) Wu, D.; Fu, R.; Sun, Z.; Yu, Z. Low-Density Organic and Carbon Aerogels from the Sol-Gel Polymerization of Phenol with Formaldehyde. *J. Non-Cryst. Solids* **2005**, *351*, 915–921.

28. Li, W.; Guo, S. Preparation of Low-Density Carbon Aerogels from a Cresol/Formaldehyde Mixture. *Carbon* **2000**, *38*, 1520–1523.

29. Fu, R.; Zheng, B.; Liu, J.; Dresselhaus, M. S.; Dresselhaus, G.; Satcher, J. H.; Baumann, T. F. The Fabrication and Characterization of Carbon Aerogels by Gelation and Supercritical Drying in Isopropanol. *Adv. Funct. Mater*. **2003**, *13*, 558–562.

30. Pekala, R. W.; Alviso, C. T.; Lu, X.; Gross, J.; Fricke, J. New Organic Aerogels Based upon a Phenolic-Furfural Reaction. *J. Non-Cryst. Solids* **1995**, *188*, 34–40.

31. Mahadik-Khanolkar, S.; Donthula, S.; Sotiriou-Leventis, C.; Leventis, N. Polybenzoxazine Aerogels. 1. High-Yield Room-Temperature Acid-Catalyzed Synthesis of Robust Monoliths, Oxidative Aromatization, and Conversion to Microporous Carbons. *Chem. Mater*. **2014**, *26*, 1303–1317.

32. Majedi Far, H.; Donthula, S.; Taghvaee, T.; Saeed, A. M.; Garr, Z.; Sotiriou-Leventis, C.; Leventis, N. Air-Oxidation of Phenolic Resin Aerogels: Backbone Reorganization, Formation of Ring-Fused Pyrylium Cations, and the Effect on Microporous Carbons with Enhanced Surface Areas. *RSC Adv*. **2017**, *7*, 51104–51120.

33. Sadekar, A. G.; Mahadik, S. S.; Bang, A. N.; Larimore, Z. J.; Wisner, C. A.; Bertino, M. F.; Kalkan, A. K.; Mang, J. T.; Sotiriou-Leventis, C.; Leventis, N. From 'Green' Aerogels to Porous Graphite by Emulsion Gelation of Acrylonitrile. *Chem*. *Mater*. **2012**, *24*, 26–47.

34. Bang, A.; Buback, C.; Sotiriou-Leventis, C.; Leventis, N. Flexible Aerogels from Hyperbranched Polyurethanes: Probing the Role of Molecular Rigidity with Poly(Urethane Acrylates) versus Poly(Urethane Norbornenes). *Chem*. *Mater*. **2014**, *26*, 6979–6993.

35. (a) Saeed, A. M.; Wisner, C. A.; Donthula, S.; Majedi Far, H.; Sotiriou-Leventis, C.; Leventis, N. Reuseable Monolithic Nanoporous Graphite-Supported Nanocatalysts (Fe, Au, Pt, Pd, Ni, and Rh) from Pyrolysis and Galvanic Transmetalation of Ferrocene-Based Polyamide Aerogels. *Chem*. *Mater*. **2016**, *28*, 4867–4877. (b) Leventis, N.; Chidambareswarapattar, C.; Mohite, D. P.; Larimore, Z. J.; Lu, H.; Sotiriou-Leventis, C. Multifunctional Porous Aramids (Aerogels) by Efficient Reaction of Carboxylic Acids and Isocyanates. *J*. *Mater*. *Chem*. **2011**, *21*, 11981–11986.

36. (a) Chidambareswarapattar, C.; Xu, L.; Sotiriou-Leventis, C.; Leventis, N. Robust Monolithic Multiscale Nanoporous Polyimides and Conversion to Isomorphic Carbons. *RSC Adv*. **2013**, *3*, 26459–26469. (b) Leventis, N.; Sotiriou-Leventis, C.; Mohite, D. P.; Larimore, Z. J.; Mang, J. T.; Churu, G.; Lu, H. Polyimide Aerogels by Ring-Opening Metathesis Polymerization (ROMP). *Chem*. *Mater*. **2011**, *23*, 2250–2261. (c) Chidambareswarapattar, C.; Larimore, Z.; Sotiriou-Leventis, C.; Mang, J. T.; Leventis, N. One-Step Room-Temperature Synthesis of Fibrous Polyimide Aerogels from Anhydrides and Isocyanates and Conversion to Isomorphic Carbons. *J*. *Mater*. *Chem*. **2010**, *20*, 9666–9678.

37. (a) Leventis, N.; Chidambareswarapattar, C.; Bang, A.; Sotiriou-Leventis, C. Cocoon-in-Web-Like Superhydrophobic Aerogels from Hydrophilic Polyurea and Use in Environmental Remediation. *ACS Appl*. *Mater*. *Interfaces* **2014**, *6*, 6872–6882. (b) Leventis, N.; Sotiriou-Leventis, C.; Chandrasekaran, N.; Mulik, S.; Larimore, Z. J.; Lu, H.; Churu, G.; Mang, J. T. Multifunctional Polyurea Aerogels from Isocyanates and Water. A Structure-Property Case Study. *Chem*. *Mater*. **2010**, *22*, 6692–6710. (c) Leventis, N.; Sotiriou-Leventis, C.; Chandrasekaran, N.; Mulik, S.; Chidambareswarapattar, C.; Sadekar, A.; Mohite, D.; Mahadik, S. S.; Larimore, Z. J.; Lu, H.; Churu, G.; Mang, J. T. Isocyanate-Derived Organic Aerogels: Polyureas, Polyimides, Polyamides. *MRS Proc*. **2011**, *1306*, mrsf10–1306-bb03–01.

38. (a) Chidambareswarapattar, C.; McCarver, P. M.; Luo, H.; Lu, H.; Sotiriou-Leventis, C.; Leventis, N. Fractal Multiscale Nanoporous Polyurethanes: Flexible to Extremely Rigid Aerogels from Multifunctional Small Molecules. *Chem. Mater.* **2013**, *25*, 3205–3224. (b) Biesmans, G.; Mertens, A.; Duffours, L.; Woignier, T.; Phalippou, J. Polyurethane Based Organic Aerogels and Their Transformation into Carbon Aerogels. *J. Non-Cryst. Solids* **1998**, *225*, 64–68.

39. (a) Bang, A.; Mohite, D.; Saeed, A. M.; Leventis, N.; Sotiriou-Leventis, C. Polydicyclopentadiene Aerogels from First- versus Second-Generation Grubbs' Catalysts: a Molecular versus a Nanoscopic Perspective. *J. Sol-Gel Sci. Technol.* **2015**, *75*, 460–474. (b) Mohite, D. P.; Mahadik-Khanolkar, S.; Luo, H.; Lu, H.; Sotiriou-Leventis, C.; Leventis, N. Polydicyclopentadiene Aerogels Grafted with PMMA: I. Molecular and Interparticle Crosslinking. *Soft Matter* **2013**, *9*, 1516–1530. (c) Mohite, D. P.; Mahadik-Khanolkar, S.; Luo, H.; Lu, H.; Sotiriou-Leventis, C.; Leventis, N. Polydicyclopentadiene Aerogels Grafted with PMMA: II. Nanoscopic Characterization and Origin of Macroscopic Deformation. *Soft Matter* **2013**, *9*, 1531–1539.

40. (a) Scherdel, C.; Reichenauer, G. Carbon Xerogels Synthesized via Phenol-Formaldehyde Gels. *Microporous and Mesoporous Mater.* **2009**, *126*, 133–142. (b) Wu, D.; Fu, R. Requirements of Organic Gels for a Successful Ambient Pressure Drying Preparation of Carbon Aerogels. *J. Porous Mater.* **2008**, *15*, 29–34. (c) Kong, F.-M.; LeMay, J. D.; Hulsey, S. S.; Alviso, C. T.; Pekala, R. W. Gas Permeability of Carbon Aerogels. *J. Mater. Res.* **1993**, *8*, 3100–3105.

41. Hou, K.; Zhang, A.; Gu, L.; Liu, M.; Guo, X. Efficient Synthesis and Sulfonation of Ordered Mesoporous Carbon Materials. *J. Colloid Interface Sci.* **2012**, 377, 18–26.

42. Baumann, T. F.; Worsley, M. A.; Han, T. Y.-J.; Satcher, J. H. High Surface Area Carbon Aerogel Monoliths with Hierarchical Porosity. *J. Non-Cryst. Solids* **2008**, *354*, 3513–3515.

43. Li, W.-C.; Lu, A.-H.; Schüth, F. Preparation of Monolithic Carbon Aerogels and Investigation of Their Pore Interconnectivity by a Nanocasting Pathway. *Chem. Mater.* **2005**, *17*, 3620–3626.

44. Li, W.-C.; Lu, A.-H.; Schüth, F. Preparation of Monolithic Carbon Aerogels and Investigation of Their Pore Interconnectivity by a Nanocasting Pathway. *Chem. Mater.* **2005**, *17*, 3620–3626.

45. Al-Muhtaseb, S. A.; Ritter, J. A. Preparation and Properties of Resorcinol-Formaldehyde Organic and Carbon Gels. *Adv. Mater.* **2003**, *15*, 101–114.

46. Reichenauer, G.; Emmerling, A.; Fricke, J.; Pekala, R. W. Microporosity in Carbon Aerogels. *J. Non-Cryst. Solids* **1998**, *225*, 210–214.

47. Tamon, H.; Ishizaka, H.; Araki, T.; Okazaki, M. Control of Mesoporous Structure of Organic and Carbon Aerogels. *Carbon* **1998**, *36*, 1257–1262.

48. Fung, A. W. P.; Reynolds, G. A. M.; Wang, Z. H.; Dresselhaus, M. S.; Dresselhaus, G.; Pekala, R. W. Relationship between Particle Size and Magnetoresistance in Carbon Aerogels Prepared under Different Catalyst Conditions. *J. Non-Cryst. Solids* **1995**, *186*, 200–208.

49. Mulik, S.; Sotiriou-Leventis, C.; Leventis, N. Macroporous Electrically Conducting Carbon Networks by Pyrolysis of Isocyanate-Cross-Linked Resorcinol-Formaldehyde Aerogels. *Chem. Mater.* **2008**, *20*, 6985–6997.

50. Wang, J.; Angnes, L.; Tobias, H.; Roesner, R. A.; Hong, K. C.; Glass, R. S.; Kong, F. M.; Pekala, R. W. Carbon Aerogel Composite Electrodes. *Anal. Chem.* **1993**, *65*, 2300–2303.

51. Li, X.; Nilsson, O.; Fricke, J. Thermal and Electrical Conductivity of Monolithic Carbon Aerogels. *J. Appl. Phys.* **1993**, *73*, 581–584.

52. Radovic, L. R. *Chemistry and Physics of Carbon*. Ed.; CRC Press: Florida, 2003; Vol. 28; p 75.

53. Biener, J.; Stadermann, M.; Suss, M.; Worsley, M. A.; Biener, M. M.; Baumann, T. F. Advanced Carbon Aerogels for Energy Applications. In *Carbon-Based Nanomaterials and Hybrids: Synthesis, Properties, and Commercial Applications*; Fecht, H. -J., Bruhne, K., Gluche, P., Eds.; Pan Stanford Publishing: Singapore, 2014; pp 49–77.

54. Lu, A. -H.; Hao, G. -P.; Zhang, X. -Q. Porous Carbons for Carbon Dioxide Capture. In *Porous Materials for Carbon Dioxide Capture, Green Chemistry and Sustainable Technology*; Lu, A. H., Dai, S., Eds.; Springer: New York, 2014; pp 15−77.

55. Wei, X.; Jiang, X.; Wei, J.; Gao, S. Functional Groups and Pore Size Distribution Do Matter to Hierarchically Porous Carbons as High-Rate-Performance Supercapacitors. *Chem. Mater.* **2016**, *28*, 445–458.

56. Pekala, R. W.; Farmer, J. C.; Alviso, C. T.; Tran, T. D.; Mayer, S. T.; Miller, J. M.; Dunn, B. Carbon Aerogels for Electrochemical Applications. *J. Non-Cryst. Solids* **1998**, *225*, 74–80.

57. Saliger, R.; Fischer, U.; Herta, C.; Fricke, J. High Surface Area Carbon Aerogels for Supercapacitors. *J. Non-Cryst. Solids* **1998**, *225*, 81–85.

58. Mayer, S. T.; Pekala, R. W.; Kaschmitter, J. L. The Aerocapacitor: An Electrochemical Double-Layer Energy-Storage Device. *J. Electrochem. Soc.* **1993**, *140*, 446–451.

59. Moreno-Castilla, C.; Maldonado-Hódar, F. J. Carbon Aerogels for Catalysis Applications: An Overview. *Carbon* **2005**, *43*, 455–465.

60. Pierson, H. O. *Handbook of Carbon, Graphite, Diamond and Fullerenes*; Noyes Publications: New Jersey, 1993; p 87.

61. Rahaman, M. S. A.; Ismail, A. F.; Mustafa, A. A Review of Heat Treatment on Polyacrylonitrile Fiber. *Polym. Degrad. Stab.* **2007**, *92*, 1421–1432.

62. Pierson, H. O. *Handbook of Carbon, Graphite, Diamond and Fullerenes*; Noyes Publications: New Jersey, 1993; p 123.

63. (a) Jiang, H.; Wang, J.; Wu, S.; Yuan, Z.; Hu, Z.; Wu, R.; Liu, Q. The Pyrolysis Mechanism of Phenol Formaldehyde Resin. *Polym. Degrad. Stab.* **2012**, *97*, 1527–1533. (b) Ouchi, K. Infra-Red Study of Structural Changes During the Pyrolysis of a Phenol-Formaldehyde Resin. *Carbon* **1966**, *4*, 59–66. (c) Chien, J. C. W.; Kiang, J. K. Y. Polymer Reactions, 8. Oxidative Pyrolysis of Poly(propylene). *Makromol. Chem. Phys.* **1980**, *181*, 47–57. (d) Chien, J. C. W.; Kiang, J. K. Y. Pyrolysis and Oxidative Pyrolysis of Polypropylene. In *Stabilization and Degradation of Polymers*; Allara, D. L., Hawkins, W. L., Eds.; American Chemical Society: 1978; Vol. 169, pp 175–197. (e) Cullis, C. F.; Laver, H. S. The Thermal Degradation and Oxidation of Polybutadiene. *Eur. Polym. J.* **1978**, *14*, 571–573. (f) Blazsó, M. Recent Trends in Analytical and Applied Pyrolysis of Polymers. *J. Anal. Appl. Pyrolysis* **1997**, *39*, 1–25. (g) Sobeih, K. L.; Baron, M.; Gonzalez-Rodriguez, J. Recent Trends and Developments in Pyrolysis-Gas Chromatography. *J. Chromatogr. A* **2008**, *1186*, 51–66. (h) Wang, F. C.-Y. Polymer Analysis by Pyrolysis Gas Chromatography. *J. Chromatogr. A* **1999**, *843*, 413–423.

64. Kim, M.-A.; Jang, D.; Tejima, S.; Cruz-Silva, R.; Joh, H.-I.; Kim, H. C.; Lee, S.; Endo, M. Strengthened PAN-Based Carbon Fibers Obtained by Slow Heating Rate Carbonization. *Sci. Rep.* **2016**, *6*, 1–7.

65. Bashir, Z. A Critical Review of the Stabilisation of Polyacrylonitrile. *Carbon* **1991**, *29*, 1081–1090.

66. Newcomb, B. A. Processing, Structure, and Properties of Carbon Fibers. *Composites Part A* **2016**, *91*, 262–282.

67. Saha, B.; Schatz, G. C. Carbonization in Polyacrylonitrile (PAN) Based Carbon Fibers Studied by ReaxFF Molecular Dynamics Simulations. *J. Phys. Chem. B* **2012**, *116*, 4684–4692.

68. Jenkins, G. M.; Kawamura, K. *Polymeric Carbons: Carbon Fibre, Glass and Char*, Cambridge University Press: New York, 1976; pp 11–35.

69. Leventis, N.; Donthula, S. HCl-Catalyzed Polymerization of Benzoxazine and Chemical Transformations Along Pyrolysis to Microporous Carbons. In *Advanced and Emerging Polybenzoxazine Science and Technology*; Ishida, H., Froimowicz, P., Eds.; Elsevier: Amsterdam, 2016; pp 673–695.

70. Rufford, T. E.; Hulicova-Jurcakova, D.; Khosla, K.; Zhu, Z.; Lu, G. Q. Microstructure and Electrochemical Double-Layer Capacitance of Carbon Electrodes Prepared by Zinc Chloride Activation of Sugar Cane Bagasse. *J. Power Sources* **2010**, *195*, 912–918.

71. Rodriguez-Reinoso, F.; Linares-Solano, A. Microporous Structure of Activated Carbons as Revealed by Adsorption Methods. In *Chemistry and Physics of Carbon*; Thrower, P. A., Ed.; Marcel Dekker: New York, 1989; Vol. 21; p 35.

72. Saeed, A. M.; Rewatkar, P. M.; Majedi Far, H.; Taghvaee, T.; Donthula, S.; Mandal, C.; Sotiriou-Leventis, C.; Leventis, N. Selective CO_2 Sequestration with Monolithic Bimodal Micro/Macroporous Carbon Aerogels Derived from Stepwise Pyrolytic Decomposition of Polyamide-Polyimide-Polyurea Random Copolymers. *ACS Appl. Mater. Interfaces* **2017**, *9*, 13520–13536.

73. Rahman, F. A.; Aziz, M. M. A.; Saidur, R.; Bakar, W. A. W. A.; Hainin, M. R.; Putrajaya, R.; Hassan, N. A. Pollution to Solution: Capture and Sequestration of Carbon Dioxide (CO_2) and Its Utilization as a Renewable Energy Source for a Sustainable Future. *Renew. Sustain. Energy Rev.* **2017**, *71*, 112–126.

74. Aminu, M. D.; Nabavi, S. A.; Rochelle, C. A.; Manovic, V. A Review of Developments in Carbon Dioxide Storage. *Appl. Energy* **2017**, *208*, 1389–1419.

75. Dawson, R.; Cooper, A. I.; Adams, D. J. Chemical Functionalization Strategies for Carbon Dioxide Capture in Microporous Organic Polymers. *Polym. Int.* **2013**, *62*, 345–352.

76. Wang, J.; Huang, L.; Yang, R.; Zhang, Z.; Wu, J.; Gao, Y.; Wang, Q.; O'Hare, D.; Zhong, Z. Recent Advances in Solid Sorbents for CO_2 Capture and New Development Trends. *Energy Environ. Sci.* **2014**, *7*, 3478–3518.

77. Wang, J.; Krishna, R.; Wu, X.; Sun, Y.; Deng, S. Polyfuran-Derived Microporous Carbons for Enhanced Adsorption of CO_2 and CH_4. *Langmuir* **2015**, *31*, 9845–9852.

78. Haszeldine, R. S. Carbon Capture and Storage: How Green Can Black Be? *Science* **2009**, *325*, 1647–1652.

79. (a) http://www.c2es.org/content/international-emissions/ accessed 10/12/2018 (b) https://www.epa.gov/sites/production/files/2018-01/documents/2018_complete_report.pdf accessed 10/12/2018

80. (a) https://www.co2.earth/daily-CO_2 accessed 10/12/2018 (b) Wennersten, R.; Sun, Q.; Li, H. The Future Potential for Carbon Capture and Storage in Climate Change Mitigation – an Overview from Perspectives of Technology, Economy and Risk. *J. Cleaner Production* **2015**, *103*, 724–736. (c) Ben, T.; Pei, C.; Zhang, D.; Xu, J.; Deng, F.; Jing, X.; Qiu, S. Gas Storage in Porous Aromatic Frameworks (PAFs). *Energy Environ. Sci.* **2011**, *4*, 3991–3999. (d) IPCC (Intergovernmental Panel on Climate Change). 2013. Climate change 2013: The physical science basis. *Working Group I Contribution to the IPCC Fifth Assessment Report.* Cambridge University Press, Cambridge, United Kingdom.

81. Smit, B.; Reimer, J. A.; Oldenburg, C. M.; Bourg, I. C. *The Berkeley Lectures on Energy, Introduction to Carbon Capture and Sequestration*; Imperial College Press: London, 2014; Vol. 1; pp 141–162.

82. Metz, B.; Davidson, O.; Coninck, H. D.; Loos, M.; Meyer, L. In *IPCC Special Report on Carbon Dioxide Capture and Storage, Prepared by Working Group III of the Intergovernmental Panel on Climate Change*; Eds.; Cambridge University Press: Cambridge, United Kingdom, 2005; Summary for Policymakers, pp 3–16.

83. Kanniche, M.; Gros-Bonnivard, R.; Jaud, P.; Valle-Marcos, J.; Amann, J. -M.; Bouallou, C. Pre-Combustion, Post-Combustion and Oxy-Combustion in Thermal Power Plant for CO_2 Capture. *Appl. Therm. Eng.* **2010**, *30*, 53–62.

84. Arenillas, A.; Smith, K. M.; Drage, T. C.; Snape, C. E. CO_2 Capture Using Some Fly Ash-Derived Carbon Materials. *Fuel* **2005**, *84*, 2204–2210.

85. Wu, D.; Xu, F.; Sun, B.; Fu, R.; He, H.; Matyjaszewski, K. Design and Preparation of Porous Polymers. *Chem. Rev.* **2012**, *112*, 3959–4015.

86. (a) Duan, X.; Wang, H.; Cui, Y.; Yang, Y.; Wang, Z.; Chen, B.; Qian, G. A New NbO Type Metal-Organic Framework for High Acetylene and Methane Storage. *RSC Adv.* **2015**, *5*, 84446–84450. (b) Mulfort, K. L.; Farha, O. K.; Malliakas, C. D.; Kanatzidis, M. G.; Hupp, J. T. An Interpenetrated Framework Material with Hysteretic CO_2 Uptake. *Chem. -Eur. J.* **2010**, *16*, 276–281. (c) Keskin, S.; Heest, T. M. V.; Sholl, D. S. Can Metal-Organic Framework Materials Play a Useful Role in Large-Scale Carbon Dioxide Separations? *ChemSusChem* **2010**, *3*, 879–891. (d) Horcajada, P.; Chalati, T.; Serre, C.; Gillet, B.; Sebrie, C.; Baati, T.; Eubank, J. F.; Heurtaux, D.; Clayette, P.; Kreuz, C.; Chang, J.-S.; Hwang, Y. K.; Marsaud, V.; Bories, P.-N.; Cynober, L.; Gil, S.; Férey, G.; Couvreur, P.; Gref, R. Porous Metal-Organic-Framework Nanoscale Carriers as a Potential Platform for Drug Delivery and Imaging. *Nat. Mater.* **2009**, *9*, 172–178.

87. (a) Yao, S.; Yang, X.; Yu, M.; Zhang, Y.; Jiang, J. -X. High Surface Area Hypercrosslinked Microporous Organic Polymer Networks Based on Tetraphenylethylene for CO_2 Capture. *J. Mater. Chem. A* **2014**, *2*, 8054–8059. (b) Wang, J.; Huang, J.; Wu, X.; Yuan, B.; Sun, Y.; Zeng, Z.; Deng, S. Effect of Nitrogen Group on Selective Separation of CO_2/N_2 in Porous Polystyrene. *Chem. Eng. J.* **2014**, *256*, 390–397. (c) Woodward, R. T.; Stevens, L. A.; Dawson, R.; Vijayaraghavan, M.; Hasell, T.; Silverwood, I. P.; Ewing, A. V.; Ratvijitvech, T.; Exley, J. D.; Chong, S. Y.; Blanc, F.; Adams, D. J.; Kazarian, S. G.; Snape, C. E.; Drage, T. C.; Cooper, A. I. Swellable, Water-and Acid-Tolerant Polymer Sponges for Chemoselective Carbon Dioxide Capture. *J. Am. Chem. Soc.* **2014**, *136*, 9028–9035. (d) Dawson, R.; Ratvijitvech, T.; Corker, M.; Laybourn, A.; Khimyak, Y. Z.; Cooper, A. I.; Adams, D. J. Microporous Copolymers for Increased Gas Selectivity. *Polym. Chem.* **2012**, *3*, 2034–2038.

88. (a) Xu, Y.; Jin, S.; Xu, H.; Nagai, A.; Jiang, D. Conjugated Microporous Polymers: Design, Synthesis and Application. *Chem. Soc. Rev.* **2013**, *42*, 8012–8031. (b) Dawson, R.; Adams, D. J.; Cooper, A. I. Chemical Tuning of CO_2 Sorption in Robust Nanoporous Organic Polymers. *Chem. Sci.* **2011**, *2*, 1173–1177. (c) Chen, L.; Honsho, Y.; Seki, S.; Jiang, D. Light-Harvesting Conjugated Microporous Polymers: Rapid and Highly Efficient Flow of Light Energy with a Porous Polyphenylene Framework as Antenna. *J. Am. Chem. Soc.* **2010**, *132*, 6742–6748. (d) Schmidt, J.; Werner, M.; Thomas, A. Conjugated Microporous Polymer Networks via Yamamoto Polymerization. *Macromolecules* **2009**, *42*, 4426–4429.

89. (a) McKeown, N. B.; Budd, P. M. Exploitation of Intrinsic Microporosity in Polymer-Based Materials. *Macromolecules* **2010**, *43*, 5163–5176. (b) Ghanem, B. S.; Msayib, K. J.; McKeown, N. B.; Harris, K. D. M.; Pan, Z.; Budd, P. M.; Butler, A.; Selbie, J.; Book, D.; Walton, A. A Triptycene-Based Polymer of Intrinsic Microposity that Displays Enhanced Surface Area and Hydrogen Adsorption. *Chem. Commun.* **2007**, *0*, 67–69. (c) McKeown, N. B.; Gahnem, B.; Msayib, K. J.; Budd, P. M.; Tattershall, C. E.; Mahmood, K.; Tan, S.; Book, D.; Langmi, H. W.; Walton, A. Towards Polymer-Based Hydrogen Storage Materials: Engineering Ultramicroporous Cavities within Polymers of Intrinsic Microporosity. *Angew. Chem. Int. Ed.* **2006**, *45*, 1804–1807. (d) McKeown, N. B.; Budd, P. M. Polymers of Intrinsic Microporosity (PIMs): Organic Materials for Membrane Separations, Heterogeneous Catalysis and Hydrogen Storage. *Chem. Soc. Rev.* **2006**, *35*, 675–683.

90. (a) Ben, T.; Li, Y.; Zhu, L.; Zhang, D.; Cao, D.; Xiang, Z.; Yao, X.; Qiu, S. Selective Adsorption of Carbon Dioxide by Carbonized Porous Aromatic Framework (PAF). *Energy Environ*. *Sci*. **2012**, *5*, 8370–8376. (b) Ben, T.; Pei, C.; Zhang, D.; Xu, J.; Deng, F.; Jing, X.; Qiu, S. Gas Storage in Porous Aromatic Frameworks (PAFs). *Energy Environ*. *Sci*. **2011**, *4*, 3991–3999. (c) Ren, H.; Ben, T.; Wang, E.; Jing, X.; Xue, M.; Liu, B.; Cui, Y.; Qiu, S.; Zhu, G. Targeted Synthesis of a 3D Porous Aromatic Framework for Selective Sorption of Benzene. *Chem*. *Commun*. **2010**, *46*, 291–293. (d) Ben, T.; Ren, H.; Ma, S.; Cao, D.; Lan, J.; Jing, X.; Wang, W.; Xu, J.; Deng, F.; Simmons, J. M.; Qiu, S.; Zhu, G. Targeted Synthesis of a Porous Aromatic Framework with High Stability and Exceptionally High Surface Area. *Angew*. *Chem*. *Int*. *Ed*. **2009**, *48*, 9457–9460.

91. (a) Byun, J.; Je, S.-H.; Patel, H. A.; Coskun, A.; Yavuz, C. T. Nanoporous Covalent Organic Polymers Incorporating Troger's Base Functionalities for Enhanced CO_2 Capture. *J*. *Mater*. *Chem*. *A* **2014**, *2*, 12507–12512. (b) Patel, H. A.; Je, S. H.; Park, J.; Jung, Y.; Coskun, A.; Yavuz, C. T. Directing the Structural Features of N_2-Phobic Nanoporous Covalent Organic Polymers for CO_2 Capture and Separation. *Chem*. *-Eur*. *J*. **2014**, *20*, 772–780. (c) Patel, H. A.; Karadas, F.; Byun, J.; Park, J.; Deniz, E.; Canlier, A.; Jung, Y.; Atilhan, M.; Yavuz, C. T. Highly Stable Nanoporous Sulfur-Bridged Covalent Organic Polymers for Carbon Dioxide Removal. *Adv*. *Funct*. *Mater*. **2013**, *23*, 2270–2276. (d) Patel, H. A.; Karadas, F.; Canlier, A.; Park, J.; Deniz, E.; Jung, Y.; Atilhan, M.; Yavuz, C. T. High Capacity Carbon Dioxide Adsorption by Inexpensive Covalent Organic Polymers. *J*. *Mater*. *Chem*. **2012**, *22*, 8431–8437.

92. Kuhn, P.; Antonietti, M.; Thomas, A. Porous, Covalent Triazine-Based Frameworks Prepared by Ionothermal Synthesis. *Angew*. *Chem*. *Int*. *Ed*. **2008**, *47*, 3450–3453.

93. (a) Yang, X.; Yao, S.; Yu, M.; Jiang, J. X. Synthesis and Gas Adsorption Properties of Tetra-Armed Microporous Organic Polymer Networks Based on Triphenylamine. *Macromol*. *Rapid Commun*. **2014**, *35*, 834–839. (b) Li, B.; Gong, R.; Wang, W.; Huang, X.; Zhang, W.; Li, H.; Hu, C.; Tan, B. A New Strategy to Microporous Polymers: Knitting Rigid Aromatic Building Blocks by External Cross-Linker. *Macromolecules* **2011**, *44*, 2410–2414. (c) Dawson, R.; Stockel, E.; Holst, J. R.; Adams, D. J.; Cooper, A. I. Microporous Organic Polymers for Carbon Dioxide Capture. *Energy Environ*. *Sci*. **2011**, *4*, 4239–4245. (d) Jiang, J.-X.; Cooper, A. Microporous Organic Polymers: Design, Synthesis, and Function. In *Functional Metal-Organic Frameworks: Gas Storage, Separation and Catalysis*; Schröoder, M., Ed.; Springer: Berlin and Heidelberg, Germany, 2010; pp 1–33.

94. Zhu, Y.; Long, H.; Zhang, W. Imine-Linked Porous Polymer Frameworks with High Small Gas (H_2, CO_2, CH_4, C_2H_2) Uptake and CO_2/N_2 Selectivity. *Chem*. *Mater*. **2013**, *25*, 1630–1635.

95. (a) Rabbani, M. G.; Reich, T. E.; Kassab, R. M.; Jackson, K. T.; El-Kaderi, H. M. High CO_2 Uptake and Selectivity by Triptycene-Derived Benzimidazole-Linked Polymers. *Chem*. *Commun*. **2012**, *48*, 1141–1143. (b) Rabbani, M. G.; Sekizkardes, A. K.; El-Kadri, O. M.; Kaafarani, B. R.; El-Kaderi, H. M. Pyrene-Directed Growth of Nanoporous Benzimidazole-Linked Nanofibers and Their Application to Selective CO_2 Capture and Separation. *J*. *Mater*. *Chem*. **2012**, *22*, 25409–25417. (c) Rabbani, M. G.; El-Kaderi, H. M. Template-Free Synthesis of a Highly Porous Benzimidazole-Linked Polymer for CO_2 Capture and H_2 Storage. *Chem*. *Mater*. **2011**, *23*, 1650–1653.

96. (a) Guo, P.; Dutta, D.; Wong-Foy, A. G.; Gidley, D. W.; Matzger, A. J. Water Sensitivity in Zn4O-Based MOFs is Structure and History Dependent. *J*. *Am*. *Chem*. *Soc*. **2015**, *137*, 2651–2657. (b) Schoenecker, P. M.; Carson, C. G.; Jasuja, H.; Flemming, C. J. J.; Walton, K. S. Effect of Water Adsorption on Retention of Structure and Surface Area of Metal-Organic Frameworks. *Ind*. *Eng*. *Chem*. *Res*. **2012**, *51*, 6513–6519.

VITA

Hojat Majedi Far graduated from University of Zabol, Iran and received his Bachelor of Science in Chemistry in 2005. He then moved to Tehran to study toward his Master degree at Kharazmi University. He received his MSc. Degree in Physical Chemistry in 2009 with his research focusing on the *spectroscopy of diatomic molecules*. In the Spring of 2012 he began his PhD studies at Missouri S&T and joined Dr. Chariklia Sotiriou-Leventis's research group in the summer of 2013. His research project was on the synthesis of phenolic resin aerogels and study of their carbonization process. Hojat had two papers as first author, one of which was published in *RSC Advances* in 2017, and another in *Macromolecular Chemistry and Physics* in 2018. During his PhD, he collaborated with his colleagues, which resulted in co-authoring three papers published in *Chemistry of Materials*, and *ACS Applied Materials and Interfaces*. He has presented the results of his research in four regional and two national ACS meetings. He received his Doctor of Philosophy in Chemistry from Missouri S&T in December 2018.